Marius Andersen

An Experimental and Numerical Study of Thermoplastics at Large Deformations

Marius Andersen

Doctoral thesis

NTNU
Norwegian University of
Science and Technology
Thesis for the Degree of
Philosophiae Doctor
Faculty of Engineering Science and Technology
SFI Structural Impact Laboratory

◻ NTNU
Norwegian University of
Science and Technology

◻ NTNU
Norwegian University of
Science and Technology

◼ NTNU

Marius Andersen

An Experimental and Numerical Study of Thermoplastics at Large Deformations

Thesis for the Degree of Philosophiae Doctor

Trondheim, June 2016

Norwegian University of Science and Technology
Faculty of Engineering Science and Technology
SFI Structural Impact Laboratory

NTNU
Norwegian University of
Science and Technology

Abstract

This thesis has examined the mechanical behavior of HDPE and PVC at large strains and at low to intermediate strain rates. This examination has been done by analyzing experimental results from uniaxial tension and compressions tests, where the test data has been evaluated through a combination of improved measurement techniques, simplified 1D material models and FEM simulations. Strains beyond the natural draw limit of HDPE have been achieved in uniaxial tension by utilizing a custom-made tension sample.

DIC has been used to measure local deformation of test samples. Extra attention has been paid to the measurements of local strains as the neck forms and propagates in uniaxial tension. To this end, a custom implementation of a DIC algorithm has been presented, where the use of higher order elements has been shown to enable a more precise determination of the location of the neck. This has facilitated the development of a systematic approach for defining the section of a sample first experiencing necking and accurately measuring the deformation of this cross section with an infinitesimal length. An edge tracing algorithm has also been developed, allowing for the determination of additional geometrical properties of the section first experiencing necking.

The improved measurement technique has allowed for the precise determination of stress and strain behavior of both materials at large strains. The measurement and calculation of the evolution of volumetric strain in uniaxial tension has been a central topic in this thesis, and it has been shown that a traditional approach to the calculation of volumetric strain can lead to results that severely misrepresent the actual material behavior. To this end an alternative equation for calculating the volumetric strain has been proposed and validated. With this improved method, it has been shown that the polymers investigated in this thesis exhibit a highly non-linear increase in volume when subjected to uniaxial tension. This volumetric growth has also been shown to depend on strain rate in the case of HDPE. Adiabatic heating has also been quantified by the use of a thermal camera, and it has been shown that adiabatic heating significantly affects mechanical properties even at intermediate strain rates.

The experimental results have been incorporated into a FEM material model. Through thermo-mechanically coupled simulations, the material model has been shown to accurately

capture thermal softening and the non-linear volumetric growth. The simulations have also revealed discrepancies in the assumption that hardening in polymers is primarily entropic elastic. This assumption does not appear to be consistent with the measured generated heat found from experiments, and in the case of PVC it was shown that all hardening had to be assumed to be dissipative in order to achieve temperatures similar to those measured in the experiments.

Acknowledgements

My supervisors for the work on this thesis have been Professor Arild Holm Clausen and Professor Odd Sture Hopperstad. I would like to thank them both for the fantastic balance of freedom and structure they have provided me with throughout my work on this thesis. They have been as curious as me, and I am pretty sure a future supervisor will be less enthusiastic when I show him or her that I have been working within a different field for a month.

I would also like to thank my colleagues at the department of Structural Engineering and especially at SIMLab for creating an environment defined by curiosity, discussion and a willingness to help each other. I could not imagine a better setting for conducting research. Trond Auestand deserves a special mention for all his support on my experimental work.

This thesis could probably have been written without any contributions from my friends. In fact, it could probably have been finished in a more timely fashion. They have however made the difference between living and staying alive. A special thanks goes to Bjørn and Friday rice porridge.

Finally, I would like to thank my family. My mom and dad have always encouraged openness and exploration. These values have formed how I think. My girlfriend Maria has through her grace, patience and thoughtfulness been an invaluable support throughout my work on this thesis. I assume I owe her something for all the strange hours I have spent at work, but I have never looked more forward to repaying a debt.

Table of Contents

1 Introduction

1.1 Background

The use of polymers in load-carrying or shock absorbing components is widespread and still increasing. During the recent years, it has become common to apply finite element method simulations as a tool in the design process of such structures, including the parts made of polymers. Advances in the modeling of these materials have however not kept up with the increased usage, and so there appears to be a gap between the wide field of applications and the ability to predict material behavior.

Early modeling of polymers has been done by making similar assumptions as those made for metals, a field where the physical mechanisms are well mapped into the mathematical sphere. This was at least partly due to a lack of experimental data for polymers, as traditional experimental set-ups provided a very narrow insight into the large deformation range. Material models for metals would typically contain features such as the von Mises yield criterion, the associated flow rule, and pressure-insensitive material behavior. These assumptions are normally not fulfilled for polymers. In particular, it might quickly become apparent as one moves into the large deformation range that the framework of metal plasticity is unsuited and that the fundamental assumptions made for metals do not apply. The most obvious distinctions between metals and polymers are that some polymers exhibit plastic volume change during deformation, yielding of polymers can dependent on the hydrostatic stress state, viscous effects related to strain rate and temperature are more prominent, and polymers exhibit an entropy-elastic stiffness contribution at large strains.

The mechanical properties of polymers have to be characterized through experimental tests. Indeed, there are two purposes with test campaigns. Firstly, the main features of the response of the material have to be explored to get an idea of whether it dilates, is pressure sensitive, has a strong entropic stiffness, etc. Such information is relevant in the development of constitutive models for finite element simulations. Next, mechanical tests are required for calibration of the material parameters involved in the model at hand. The strategy for model development and parameter identification is similar for metals. The most widely applied

1

loading mode for metals is uniaxial tension. Most ductile metals experience strain hardening after yielding, and the onset of necking occurs often late in the deformation process. Exploiting that the plastic deformation of metals is isochoric, i.e. volume preserving, this calls for an experimental protocol where an extensometer is sufficient to measure the strains up to necking. After necking, local strain measurements in the neck are required.

The typical experimental procedures for tension tests on metals cannot be transferred to all types of polymers. An important reason is that the onset of necking often comes at comparatively small deformations. Another issue is that the dilatation makes it necessary to abandon the classical formula giving true stress as function of the nominal stress and strain, i.e. $\sigma_{true} = \sigma_{nom}(1 + \varepsilon_{nom})$. Yet, the design of tension test samples as recommended by standards for mechanical testing of polymers is strongly influenced by the geometrical shapes applied for tensile testing of metals [1]. Indeed, the main concern for such standards are often determination of the initial elastic stiffness and yield stress, while neither the response at large strains nor determination of relevant parameters for use in finite element simulations are usually addressed.

Hence, new protocols for doing experiments on polymers, including the design of test samples as well as instrumentation, were required. For determination of the response, the use of optical measurement techniques represents the biggest modern breakthrough for measuring post-necking behavior. This was pioneered by G'sell et al. [2], using an in situ technique. Their method is based on tracking the displacement of a pattern of dots hand painted on the surface of a material test specimen. These dots will move as the sample deforms, and the relative movement of the dots will constitute a local deformation measurement. The technique does however require that the sample localizes at the center of the dot pattern, and it is hence necessary to machine a small imperfection that triggers the localization. This thesis will use a different, more general, video-based technique called digital image correlation (DIC) [3]. The technique requires that the material sample is sprayed with a random speckled pattern before the test and photographed hundreds of times during the deformation process with a digital camera. During the postprocessing of the pictures, an element mesh is assigned to an area of the test specimen on the first picture, representing an undeformed configuration. The DIC algorithm then deforms the mesh in the subsequent pictures so that the inverse of the

2

transformations of the regions, defined by the elements, matches the undeformed elements speckled pattern as closely as possible. The result is a continuous deformation field throughout the mesh with as many deformation configurations as there are pictures. The elements typically confine a region of a few hundred pixels out of a picture that is comprised of 5 Mpixels, resulting in a theoretical number of elements equal to about 5000. When taking into account the complexity and size of the nonlinear problem, it is clear that the DIC algorithm can be quite computationally heavy, and thus the data processing is usually done after the test is performed. This limits the use of DIC as an in-situ feed-back tool of the test conditions, where control of the local strain rate is a relevant example. Despite this drawback, DIC is well suited for measuring large strains over a non-homogenous field, and has earlier been used for quantifying the deformation of polymers by for example Parsons et al. [4] and Jerabek et al. [5]. Maturing of the technique as well as SIMLab developing its own DIC software [6] hold promise for a more in depth analysis of the large strain behavior of polymers.

When it comes to design of the sample for tensile testing of polymers, a typical dog-bone test specimen with a long gauge part is in many ways incompatible with an accurate determination of the ultimate strains during the deformation process with DIC because resolution is lost when the pictures have to cover the entire stretching of a rather long sample. Thus, it is advantageous to look at alterative designs in order to facilitate measurements of large strains with DIC. Another aspect related to material tests is uniaxial compression. This type of test has been more widely applied for polymers than for metals, partly due to the challenges of necking and dilatation associated with tension. Yet, there are also drawbacks with compression tests, in particular friction and barreling. For a large number of practical applications, tension is the most important mode, in particular when it comes to large deformations, because thin parts subject to compression are likely to buckle at comparatively small strains.

The aim with studies on the mechanical behavior of polymers is to provide information for numerical simulations with the finite element method. This thesis is a continuation of previous work done on polymers at SIMLab, where the initial contribution on material modeling was a hyperelastic-viscoplastic constitutive relation proposed by Polanco-Loria et

al. [7]. They further developed the idea, originally proposed by Haward and Thackray [8], that the response of glassy polymers can be split into the three stages; energy-elasticity, viscous flow and then entropic-elasticity with increased deformation. The Haward-Thackray model had already been refined by Boyce et al. [9, 10], Tervoort et al. [11], Wu and Buckley [12], Dupaix and Boyce [13], Richeton et al. [14] and Anand et al. [15], to mention a few, while Polanco-Loria et al. [7] introduced the pressure sensitive yield criterion proposed by Raghava et al. [16] and a non-associated flow rule. This enabled the model to account for the difference in yield stress observed when varying the hydrostatic stress, and also presented the possibility to describe plastic volume change in a more flexible way than an associated flow rule manages. Despite the number of mechanisms included in the model, it has a relatively small number of calibration parameters. This is to make it a viable model for use in industrial applications, which is a stated goal for most of the research carried out at SIMLab.

The SIMLab model is in its current state able to represent the effects from most of the apparent mechanisms that compose the mechanical response of polymers [17, 18]. Specifically, it captures the response of a viscoplastic material where yielding is dependent on hydrostatic stress, the flow stress varies with strain rate, it can undergo plastic volume change, and it has a secondary rubber elastic stiffness. The accuracy for describing these mechanisms from small to large strains is however something that needs further investigation. In particular, it is suspected that the current flow rule, controlling the change of plastic volume, might be too simple for a sufficiently accurate representation of material behavior when it comes to implementation of a failure criterion in conjunction with the constitutive model. Reliable predictions of failure assume that the model captures the stress and strain fields during the subsequent deformation process in an adequate way. There are also unresolved questions pertaining to the separation of the material response into elastic, viscous, plastic and entropic elastic parts. These mechanisms may all be active at the same time in a single experimental test, which complicates the task of quantifying the contribution of the individual material properties.

4

1.2 Objectives

The goal of the PhD is to improve the knowledge of the mechanisms that constitute the mechanical behavior of ductile thermoplastics. This will be done by studying HDPE and PVC. The primary focus is on strain rate effects, volumetric change and hardening at large strains. In order to investigate these areas, it is also necessary to develop a framework for experimental testing and data treatment. The objectives of this thesis are:

- To develop a systematic approach for measuring the mechanical response of the materials in uniaxial tension and compression, with an emphasis on accurately capturing local strain behavior in uniaxial tension post necking.
- To measure mechanical behavior at large strains.
- To quantify the local change in volume when the materials are subjected to uniaxial tension.
- To measure adiabatic heating and its effects.
- To quantify the effects of changes in strain rate.
- To correlate mechanical behavior with, strain, strain rate and temperature.
- To develop a finite element material model that is able to capture the measured response of the materials.

1.3 Scope

The scope of this PhD project is limited by the specific materials investigated, the choice of measuring techniques and the choice of which boundary conditions are enforced.

The materials investigated are a semi-crystalline high-density polyethylene (HDPE) and an amorphous poly-vinyl chloride (PVC). Thus, both main classes of ductile thermoplastics are covered. The materials were acquired as off-the-shelf extruded plates from a whole-saler. They are hence not tailored for research projects. Indeed, the specific blend of these polymers is in accordance with typical commercial products, which means they have particle inclusions and filler material. The exact amount and type of these additives are not provided by the producers. This further restricts the scope towards an investigation of typical industrial blends

of these classes of polymers. The mechanical response of these two materials is only investigated in uniaxial tension and compression. This limits the range of hydrostatic stress in which data is recovered from.

Strain measurements are done using a DIC technique. Since this technique utilizes standard digital photography it is limited to measuring strains on visible surfaces, and so it provides no direct information about the deformation inside a volume. This technique is further limited to the use of a single camera, resulting in that only one surface of a test sample is monitored. This implies that assumptions have to be made for the surfaces not facing the camera. One important assumption in this thesis is that the materials are taken to behave isotropic.

In addition to DIC, some tests are also monitored with a thermal camera to log additional data. A thermal camera provides a thermal history, where the change of temperature may be assumed to be closely correlated with the dissipation and storage of energy. This is useful for evaluating the plastic work in the sample. It is thus an appropriate addition to the large strain measurements of DIC, and further narrows the research scope towards an investigation of energy retention and dissipation.

1.4 Organization of the Thesis

The thesis can be broken down into three main parts. Chapters 2 through 4 address the techniques used for measuring and calculating material response from experimental data. These techniques are then applied to uniaxial tension and compression tests, and the results are presented in Chapter 5 and 6. The final main part is presented in Chapter 7, where the experimental results are incorporated into a FEM material model, which is then compared to the observations in the tests.

Chapter 2 describes a custom made 2D DIC algorithm that has been designed and implemented to analyze the experimental data presented in this thesis. This DIC algorithm is supplemented by the edge tracing algorithm presented in Chapter 3. The edge tracing algorithm works in conjunction with the DIC algorithm to both validate DIC results as well as providing additional information required for an accurate determination of the volumetric

strain. The assumptions and models that are used to translate DIC and edge tracing data into material data from the uniaxial tension tests are then presented in Chapter 4.

The material data obtained with the methodology presented in Chapters 2 through 4 are presented in Chapter 5 and 6, were Chapter 5 concerns uniaxial tension test data from the two material HDPE and PVC where each material has been tested with two different sample geometries. Data from uniaxial compression tests of both materials is presented in Chapter 7.

The presented tests data is then used to improve a finite element method (FEM) material model in Chapter 7. This model is used to simulate both the uniaxial tension and compression tests in order to validate the obtained data and further analyze it.

Finally, conclusion and suggestions for further work are provided in Chapter 8.

2 Digital Image Correlation

The experimental results in this thesis are obtained with a purpose-made implementation of a 2D digital image correlation (DIC) code. The code is written in MatLab and it is a finite element-based formulation of DIC, as proposed by Sun et al. [19] and Besnard et al. [20]. The finite element-based DIC formulation is less known than the original subset-based Newton-Raphson formulation [21], but it is chosen for its inherent field continuity properties. In contrast to most of the work done on finite element-based DIC, the present code uses a higher order element with 16 nodes, whereas the norm elsewhere is to apply linear 4-node elements [6, 19, 20].

The choice to write a custom code for this thesis was motivated by the observations made during material tests on ductile thermoplastics. When performing uniaxial tension tests of polymers until failure, large strains are observed. The deformation localizes in a neck at approximately the same time as the onset of yielding. The large local strains then create a highly non-linear strain field in the length direction of the specimen. This nonlinearity is important for identifying the center of the neck where the maximum strain occurs. The nonlinearity of this strain field is not possible to capture with linear DIC elements, which for this purpose can be considered as constant strain elements.

The identification of the location of the neck can be done in one of two ways with DIC, either interpolating the close-to-constant strain values from linear elements in order to estimate the maximum strain and its location, or using the strain field from higher order elements directly. The latter option is chosen here. The order of the selected element should then reflect the order of the expected strain field. In the case of a uniaxial tension test with a neck, it is reasonable to assume that the longitudinal strain field is bell shaped when traversing the length of the specimen. Since it is the section of maximum strain that is of interest, it then follows that the element used should be able to describe a parabolic strain field (i.e., exhibit a maximum value). It might also be noted that in contrast to finite element simulations, an element in a DIC analysis has a minimum allowable element size. The limiting factor is the amount of pixels required inside an element for an analysis to be stable. For linear elements this limit is around $20 \times 20 \, \text{pix}^2$, where pix is applied as an abbreviation for pixels. This

inability in DIC for continued mesh refinement might also give some merit to the use of higher order elements.

2.1 Theoretical Formulation of DIC

The theoretical formulation for DIC in 2D using elements with only translational degrees of freedom is presented in the following. The aim of a DIC code is to locate the same points in two or more pictures, where a point is defined by its associated grayscale value (color) in a picture. For a single point that has moved from a position $\mathbf{X}$ in a reference configuration to a position $\mathbf{x} = \boldsymbol{\varphi}(\mathbf{X}, t)$ in the current configuration, where $\boldsymbol{\varphi}$ is a bijective mapping and t is time, the fundamental equation used is then

$$I_C(\mathbf{x}) = I_R(\mathbf{X}) \tag{2.1}$$

where $I_C(\mathbf{x})$ is the grayscale value at position $\mathbf{x}$ in a current image and $I_R(\mathbf{X})$ is the grayscale value at position $\mathbf{X}$ in a reference image. Both positions are given in a fixed coordinate system defined by the pixel grid of the images. Equation (2.1) states the principle of "conservation of optical flow". The vectors $\mathbf{x}$ and $\mathbf{X}$ are interpolated within an element defined by the positions of the n nodes of the element. The position vector $\mathbf{x}$ can then be defined as

$$\mathbf{x} = \begin{bmatrix} x \\ y \end{bmatrix} = \begin{bmatrix} \mathbf{N}(\xi,\eta) & \mathbf{0} \\ \mathbf{0} & \mathbf{N}(\xi,\eta) \end{bmatrix} \begin{bmatrix} \mathbf{n}_x \\ \mathbf{n}_y \end{bmatrix} = \mathbf{A}(\xi,\eta)\,\mathbf{n} \tag{2.2}$$

where $\mathbf{N}(\xi,\eta)$ is a row vector containing n isoparametric shape functions, and ξ and η are local element coordinates. The vectors $\mathbf{n}_x$ and $\mathbf{n}_y$ contain the x and y coordinates of the n nodes of the element. Similarly $\mathbf{X}$ can be defined as

$$\mathbf{X} = \begin{bmatrix} X \\ Y \end{bmatrix} = \begin{bmatrix} \mathbf{N}(\xi,\eta) & \mathbf{0} \\ \mathbf{0} & \mathbf{N}(\xi,\eta) \end{bmatrix} \begin{bmatrix} \mathbf{n}_X \\ \mathbf{n}_Y \end{bmatrix} = \mathbf{A}(\xi,\eta)\,\mathbf{n}_0 \tag{2.3}$$

where $\mathbf{n}_0 = \begin{bmatrix} \mathbf{n}_X & \mathbf{n}_Y \end{bmatrix}^T$ contains the initial coordinates of the nodes of the element.

10

A first-order Taylor expansion of $I_C(\mathbf{x})$ around $\mathbf{x}$ is given by

$$I_C(\mathbf{x}+\Delta\mathbf{x}) = I_C(\mathbf{x}) + \frac{\partial I_C}{\partial \mathbf{x}}\Delta\mathbf{x} \qquad (2.4)$$

where $\partial I_C / \partial \mathbf{x}$ is the grayscale value gradient expressed as

$$\frac{\partial I_C}{\partial \mathbf{x}} = \left[\frac{\partial I_C}{\partial x} \quad \frac{\partial I_C}{\partial y} \right] \qquad (2.5)$$

By taking $\mathbf{n}$ as the free variable, Equation (2.2) gives

$$\Delta\mathbf{x} = \frac{\partial \mathbf{x}}{\partial \mathbf{n}}\Delta\mathbf{n} = \mathbf{A}\Delta\mathbf{n} \qquad (2.6)$$

so that Equation (2.4) can be rewritten to

$$I_C(\mathbf{n}+\Delta\mathbf{n}) = I_C(\mathbf{n}) + \frac{\partial I_C}{\partial \mathbf{x}}\mathbf{A}\Delta\mathbf{n} \qquad (2.7)$$

If we then assume that we have a position $\mathbf{x}_0$ that is close to a position $\mathbf{x}$, where Equation (2.1) is satisfied, we can find $\mathbf{x}$ with the iterative equation

$$\mathbf{b}_k\Delta\mathbf{n}_k = I_R - I_{C,k} \qquad (2.8)$$

where k is the iteration counter and the row vector $\mathbf{b}_k$ is defined by

$$\mathbf{b}_k \equiv \left.\frac{\partial I_C}{\partial \mathbf{x}}\right|_k \mathbf{A} \qquad (2.9)$$

These equations are solved for the vector $\Delta\mathbf{n}$, namely the incremental change of the nodal positions. This is a system of equations with twice as many unknowns as element nodes, i.e., there are two degrees of freedom per node, and may hence not be solved for a single point. However, the system is solvable by taking several points within the element into account. Assuming there are m points within the element, we obtain a system of m equations in the form

11

$$\mathbf{b}_k^i \Delta \mathbf{n}_k = I_R^i - I_{C,k}^i, \quad i = 1, 2, ..., m \tag{2.10}$$

If the m row vectors $\mathbf{b}_k^i$ are collected into a matrix $\mathbf{B}_k$ and all the grayscale differences are gathered into a column vector $\Delta \mathbf{I}_k$, the result is a $2n \times m$ system that can be written as

$$\mathbf{B}_k \Delta \mathbf{n}_k = \Delta \mathbf{I}_k \tag{2.11}$$

Assuming that there are more points than twice the number of nodes, the system is solved as

$$\Delta \mathbf{n}_k = (\mathbf{B}_k^T \mathbf{B}_k)^{-1} \mathbf{B}_k^T \Delta \mathbf{I}_k \tag{2.12}$$

This solution is equivalent to a least squares solution of (2.11). The updated node coordinates of the element are then

$$\mathbf{n}_{k+1} = \mathbf{n}_k + (\mathbf{B}_k^T \mathbf{B}_k)^{-1} \mathbf{B}_k^T \Delta \mathbf{I}_k \tag{2.13}$$

The analysis can then be said to have converged to a local minimum when the absolute values of the components of $\Delta \mathbf{n}_k$ become smaller than a predefined limit.

2.2 DIC Implementation

The numerical implementation of a DIC code with a 16 node (Q16) element will now be outlined and discussed. A DIC code running an analysis can be broken down into six basic steps including post processing. The six steps are:

1. element definition,
2. pixel identification,
3. grayscale gradient calculation,
4. interpolation,
5. reference updating, and
6. post processing.

These steps will here be presented in the order they are performed. For this presentation, let us assume that we have a series of pictures showing the deformation, rotation and translation of a

12

plane surface positioned perpendicular to the camera. Let us further restrict our interest to tracking a region of the surface using only one DIC element.

2.2.1 Element Formulation

The first step is to define the element that is going to be used. The Q16 element is defined by its 16 shape functions $N_i(\xi,\eta)$, which should fulfil the interpolation conditions

$$N_i(\xi_j,\eta_j) = \delta_{ij}, \quad \sum_i N_i(\xi,\eta) = 1 \qquad (2.14)$$

where i, j are node numbers, ξ_i, η_i are the element coordinates for node i , and δ_{ij} is the Kronecker delta. These shape functions are established by first deciding the desired polynomial degree, which is here a bi-cubic polynomial. The individual components of the polynomial are then collected in a row vector $\mathbf{h}(\xi,\eta)$, which for this Q16 element is

$$\mathbf{h}(\xi,\eta) = \begin{bmatrix} 1 & \xi & \eta & \xi^2 & \xi\eta & \eta^2 & \xi^3 & \xi^2\eta & \xi\eta^2 & \eta^3 \\ & \xi^3\eta & \xi^2\eta^2 & \xi\eta^3 & \xi^3\eta^2 & \xi^2\eta^3 & \xi^3\eta^3 \end{bmatrix} \qquad (2.15)$$

This isoparametric element is given an internal node numbering as seen in Figure 2.1, with the origin of its local coordinate system (ξ,η) placed at node 1, and the coordinates of node 7 are equal to $(1,1)$.
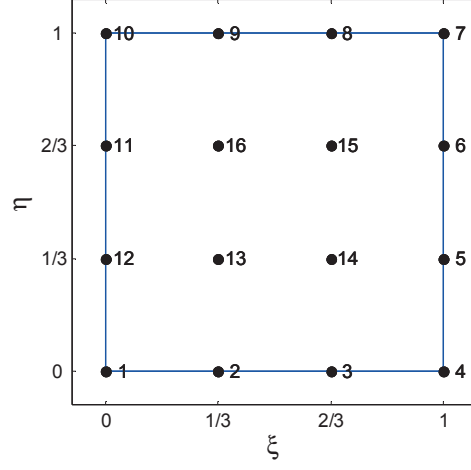
Figure 2.1: Internal node numbering of a 16 node isoparametric element used in a 2D DIC implementation.

The shape function $N_i(\xi, \eta)$ for node i is expressed as

$$N_i(\xi, \eta) = \mathbf{h}(\xi, \eta)\mathbf{c}_i \tag{2.16}$$

The 16 elements of the column vector $\mathbf{c}_i$ are then found by solving the equation system

$$\mathbf{Hc}_i = \mathbf{z}_i \tag{2.17}$$

where $\mathbf{z}_i$ has components $z_j = \delta_{ij}$ and the matrix $\mathbf{H}$ is defined by

$$\mathbf{H} = \begin{bmatrix} \mathbf{h}(\xi_1, \eta_1) \\ \mathbf{h}(\xi_2, \eta_2) \\ \vdots \\ \mathbf{h}(\xi_{16}, \eta_{16}) \end{bmatrix} \tag{2.18}$$

A compact representation of the shape functions can then be written as

$$\mathbf{N} = \mathbf{h}(\xi, \eta)\mathbf{C} \tag{2.19}$$

14

where $\mathbf{N} = \begin{bmatrix} N_1 & N_2 & \cdots & N_{16} \end{bmatrix}$ is a row vector containing the 16 shape functions and $\mathbf{C} = \begin{bmatrix} \mathbf{c}_1 & \mathbf{c}_2 & \cdots & \mathbf{c}_{16} \end{bmatrix}$ is a 16×16 matrix containing the column vectors $\mathbf{c}_i$. This compact formulation is useful, since differentiation of the shape functions is reduced to the differentiation of $\mathbf{h}(\xi, \eta)$. These derivatives are obtained as

$$\mathbf{N}_{,\xi} = \mathbf{h}_{,\xi}\mathbf{C}, \quad \mathbf{N}_{,\eta} = \mathbf{h}_{,\eta}\mathbf{C} \tag{2.20}$$

where $\mathbf{h}_{,\xi}$ and $\mathbf{h}_{,\eta}$ denote the differentiation of $\mathbf{h}$ with respect to ξ and η, respectively. These row vectors are given as

$$\begin{aligned} \mathbf{h}_{,\xi}(\xi,\eta) &= \begin{bmatrix} 0 & 1 & 0 & 2\xi & \eta & 0 & 3\xi^2 & 2\xi\eta & \eta^2 & 0 \\ & 3\xi^2\eta & 2\xi\eta^2 & \eta^3 & 3\xi^2\eta^2 & 2\xi\eta^3 & 3\xi^2\eta^3 \end{bmatrix} \\ \mathbf{h}_{,\eta}(\xi,\eta) &= \begin{bmatrix} 0 & 0 & 1 & 0 & \xi & 2\eta & 0 & \xi^2 & 2\xi\eta & 3\eta^2 \\ & \xi^3 & 2\xi^2\eta & 3\xi\eta^2 & 2\xi^3\eta & 3\xi^2\eta^2 & 3\xi^3\eta^2 \end{bmatrix} \end{aligned} \tag{2.21}$$

2.2.2 Element Coordinates

The second step is to choose the region of interest. This is done by defining $\mathbf{n}_X$ and $\mathbf{n}_Y$, which are the initial positions X and Y of the nodes. Figure 2.2 shows an undeformed test sample and the piecewise linear outline of an element with 16 nodes. It should be noted that the actual outline of the element is non-linear. All nodes and the internal node numbering are included in the figure. It can be seen that the nodes of the element are not arranged in a perfect rectangular grid in this undeformed reference image. This will usually be the case, but doing so also reduces the order of the shape functions resulting in a less general example.

15
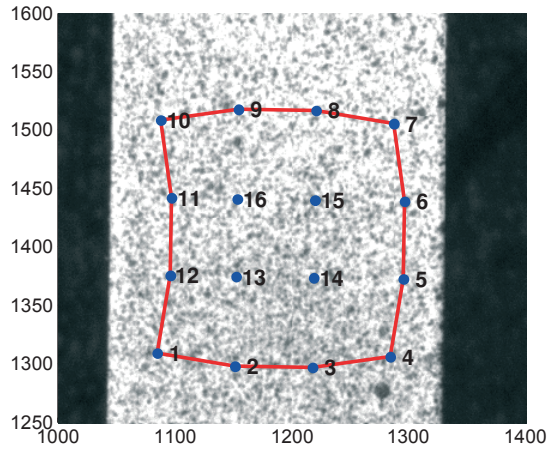
Figure 2.2: Outline of a 16 node DIC element with internal node numbering drawn on the surface of a uniaxial tension sample.

The element in Figure 2.2 has a size of about 200×200 pixels. It is now necessary to locate the pixels that are inside the element boundaries, and to determine their element coordinates ξ and η. This is approximated by first finding the smallest rectangle, having boundaries parallel with the image coordinate axes, which contains all nodes of the element, as shown with the blue lines in Figure 2.3. The four corners of the blue rectangle have coordinates $\left(\min n_{Xi}, \min n_{Yi} \right)$, $\left(\max n_{Xi}, \min n_{Yi} \right)$, $\left(\max n_{Xi}, \max n_{Yi} \right)$ and $\left(\min n_{Xi}, \max n_{Yi} \right)$, where n_{Xi} and n_{Yi} are the components of $\mathbf{n}_X$ and $\mathbf{n}_Y$, respectively. It is then trivial to find all the pixels in this region. Figure 2.3 shows all the pixels inside the limiting blue rectangle in a darker gray color. It should be noted that the pixels contained in the blue rectangle do not necessarily contain the whole set of pixels inside the actual element, but rather within the piecewise linear border of the element. This can be seen from Figure 2.2, where it is obvious that there exists a point on the non-linear element boundary between node 8 and node 9 that has a larger Y-coordinate than both nodes. Hence, this bounding box approach does not include pixels in areas like this. This is assumed to be negligible.

16
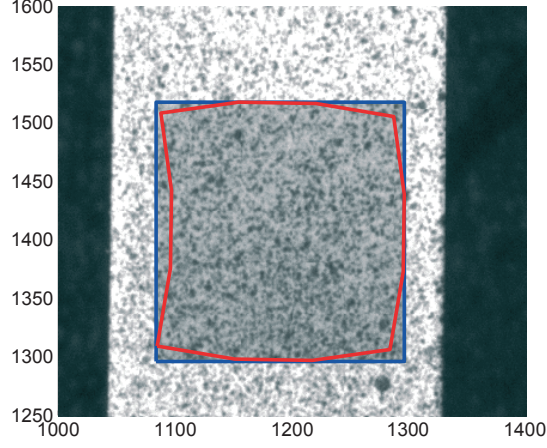
Figure 2.3: Search area for pixels inside Q16 DIC element. The red curve defines the piecewise linear element bound, and the blue rectangle defines the search area.

To find the subset of pixels that are inside the red element, it is sufficient to calculate the element coordinates of the entire set of pixels, and then keep only the pixels that satisfy $0 \le \xi \le 1$ and $0 \le \eta \le 1$ simultaneously. Calculating the element coordinates of the pixels is, however, not trivial since it involves an inversion of Equation (2.3). The initial coordinates X and Y of every pixel are known and so are the initial node positions defined by $\mathbf{n}_X$ and $\mathbf{n}_Y$. Applying Equations (2.3) and (2.19) then yields two equations with two unknowns ξ and η for each pixel, namely

$$X = \mathbf{h}(\xi,\eta)\mathbf{Cn}_X, \quad Y = \mathbf{h}(\xi,\eta)\mathbf{Cn}_Y \tag{2.22}$$

There is no explicit solution to this problem, and an iterative method is used to solve for the pixel coordinates. Re-writing Equation (2.22) in residual form, we get

$$R_X = X - \mathbf{h}(\xi,\eta)\mathbf{Cn}_X, \quad R_Y = Y - \mathbf{h}(\xi,\eta)\mathbf{Cn}_Y \tag{2.23}$$

where the correct solution for (ξ,η) implies that $R_X = R_Y = 0$. If we now use a first order Taylor approximation for the vector $\begin{bmatrix} R_X & R_Y \end{bmatrix}^T$ around the element coordinate (ξ,η), we get

17

$$\begin{bmatrix} R_X\left(\xi+\Delta\xi,\eta+\Delta\eta\right) \\ R_Y\left(\xi+\Delta\xi,\eta+\Delta\eta\right) \end{bmatrix} = \begin{bmatrix} X-\mathbf{h}\left(\xi,\eta\right)\mathbf{Cn}_X \\ Y-\mathbf{h}\left(\xi,\eta\right)\mathbf{Cn}_Y \end{bmatrix} - \begin{bmatrix} \mathbf{h},_\xi\left(\xi,\eta\right)\mathbf{Cn}_X & \mathbf{h},_\eta\left(\xi,\eta\right)\mathbf{Cn}_X \\ \mathbf{h},_\xi\left(\xi,\eta\right)\mathbf{Cn}_Y & \mathbf{h},_\eta\left(\xi,\eta\right)\mathbf{Cn}_Y \end{bmatrix}\begin{bmatrix} \Delta\xi \\ \Delta\eta \end{bmatrix} \tag{2.24}$$

Solving these equations for zero residuals, we get

$$\begin{bmatrix} \mathbf{h},_\xi(\xi,\eta)\mathbf{Cn}_X & \mathbf{h},_\eta(\xi,\eta)\mathbf{Cn}_X \\ \mathbf{h},_\xi(\xi,\eta)\mathbf{Cn}_Y & \mathbf{h},_\eta(\xi,\eta)\mathbf{Cn}_Y \end{bmatrix}\begin{bmatrix} \Delta\xi \\ \Delta\eta \end{bmatrix} = \begin{bmatrix} X-\mathbf{h}(\xi,\eta)\mathbf{Cn}_X \\ Y-\mathbf{h}(\xi,\eta)\mathbf{Cn}_Y \end{bmatrix} \tag{2.25}$$

The element coordinates for a pixel are found by solving this system of equations iteratively and updating the element coordinates. The solution will then converge if the initial values of ξ and η are sufficiently close to the correct values. A good choice of the initial values is obtained by placing the four nodes of a Q4 element at the positions of corner nodes of the Q16 element, as shown in Figure 2.4. Equations (2.22) are invertible for the Q4 element, and may be explicitly solved for the element coordinates ξ and η. This makes a Q4 element well suited for providing the initial element coordinates for the iteration procedure needed for the Q16 element. The shape functions for a Q4 element can be found and expressed in the same way as for the Q16 element, and are defined by

$$\mathbf{h}(\xi,\eta) = \begin{bmatrix} 1 & \xi & \eta & \xi\eta \end{bmatrix} \tag{2.26}$$

The mapping from element coordinates (ξ,η) to reference coordinates (X,Y) is given by Equation (2.22). The inverse mapping is then the solution of two second-order equations in ξ and η.

18
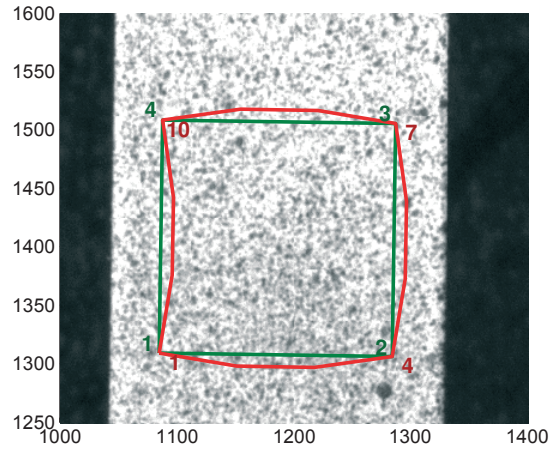
Figure 2.4: Outline of a Q16 (red) and Q4 (green) element with internal node numbering shown for the both elements.

With good initial values for ξ and η, the convergence is fast, and after four iterations the absolute values of $\Delta\xi$ and $\Delta\eta$ is smaller than 10^{-10} for this element, which is the convergence criterion used for finding the element coordinates. When all the element coordinates are found for the darker region in Figure 2.3 and all pixels outside the region $0 \leq \xi \leq 1 \cap 0 \leq \eta \leq 1$ are removed, the resulting region is within the element as shown in Figure 2.5.

19
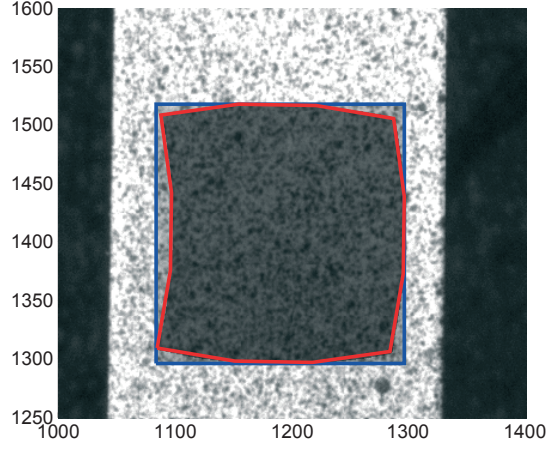
Figure 2.5: Pixels region inside a Q16 DIC element (red) shown with initial pixel search area (blue).

2.2.3 Grayscale gradient

When the region of interest is defined, it is necessary to determine the grayscale gradient given in Equation (2.5). However, since this gradient is defined with respect to the changing current position $\mathbf{x}$, the gradient has to be recalculated for each image. This would slow down the algorithm significantly, and a different approach is adopted herein. First, Equation (2.1) is reformulated as

$$I_C\left(\mathbf{x}\right) = I_C\left(\boldsymbol{\varphi}\left(\mathbf{X}\right)\right) = \overline{I}_C(\mathbf{X}) = I_R(\mathbf{X}) \tag{2.27}$$

where $\mathbf{x}$ is considered a function of $\mathbf{X}$ via the bijective mapping $\mathbf{x} = \boldsymbol{\varphi}\left(\mathbf{X}\right)$, which leads to the new function $\overline{I}_C(\mathbf{X})$. We can then define a function g with only the position vector $\mathbf{X}$ as a variable

$$g\left(\mathbf{X}\right) = I_C\left(\boldsymbol{\varphi}\left(\mathbf{X}\right)\right) - I_R(\mathbf{X}) = 0 \tag{2.28}$$

20

This function is equal to zero for all initial position vectors $\mathbf{X}$, and may be thought of as a plane in 3D space, with its third coordinate g equal to zero at all points. The gradient of this plane with respect to $\mathbf{X}$ must then also be equal to zero, and we can write

$$\frac{\partial g(\mathbf{X})}{\partial \mathbf{X}} = \frac{\partial I_C(\boldsymbol{\varphi})}{\partial \boldsymbol{\varphi}} \frac{\partial \boldsymbol{\varphi}}{\partial \mathbf{X}} - \frac{\partial I_R(\mathbf{X})}{\partial \mathbf{X}} = \mathbf{0} \tag{2.29}$$

We can then substitute $\boldsymbol{\varphi}$ with $\mathbf{x}$ to obtain the relation

$$\frac{\partial I_C(\mathbf{x})}{\partial \mathbf{x}} \frac{\partial \mathbf{x}}{\partial \mathbf{X}} = \frac{\partial I_C(\mathbf{x})}{\partial \mathbf{x}} \mathbf{F} = \frac{\partial I_R(\mathbf{X})}{\partial \mathbf{X}} \tag{2.30}$$

where $\mathbf{F} = \partial \mathbf{x} / \partial \mathbf{X}$ is the deformation gradient. The current grayscale gradient at a position $\mathbf{x}$ is then obtained as

$$\frac{\partial I_C}{\partial \mathbf{x}}(\mathbf{x}) = \frac{\partial I_R}{\partial \mathbf{X}}\left(\boldsymbol{\varphi}^{-1}(\mathbf{x})\right)\mathbf{F}^{-1}(\mathbf{x}) \tag{2.31}$$

where $\mathbf{X} = \boldsymbol{\varphi}^{-1}(\mathbf{x})$. This is helpful since $\partial I_R / \partial \mathbf{X}$ only needs to be calculated for the reference image. Equation (2.9) can then be rewritten as

$$\mathbf{b}_k \equiv \frac{\partial I_C}{\partial \mathbf{x}}\left(\mathbf{x}(\mathbf{n}_k)\right)\mathbf{A} = \frac{\partial I_R}{\partial \mathbf{X}}\left(\boldsymbol{\varphi}^{-1}\left(\mathbf{x}(\mathbf{n}_k)\right)\right)\mathbf{F}^{-1}\left(\mathbf{x}(\mathbf{n}_k)\right)\mathbf{A} \tag{2.32}$$

or more compact as

$$\mathbf{b}_k \equiv \left.\frac{\partial I_C}{\partial \mathbf{x}}\right|_k \mathbf{A} = \left.\frac{\partial I_R}{\partial \mathbf{X}}\right|_k \mathbf{F}_k^{-1}\mathbf{A} \tag{2.33}$$

The final result is that the grayscale gradient does not have to be recalculated for every image. Instead, the grayscale gradient in the reference image is mapped to the current image via the inverse of the deformation gradient. If we now choose to use only the gradient at the point where we want the iteration to converge, we can get rid of the iteration counter on the grayscale gradient from the reference gradient and approximate $\mathbf{b}_k$ as

$$\mathbf{b}_k \approx \frac{\partial I_R}{\partial \mathbf{X}} \mathbf{F}_k^{-1} \mathbf{A} \qquad (2.34)$$

This is equivalent to assuming a local constant grayscale gradient in the reference image. Alternatively, it could be considered as a form of the quasi-Newton method. The deformation gradient $\mathbf{F}$ still has to be calculated in each iteration, but as will be discussed later, this DIC implementation updates its reference frame. This means that at adequately small intervals the current configuration is taken as the new reference configuration. The deformation gradient $\mathbf{F}$ will then be close to the identity mapping $\mathbf{1}$. Thus, instead of calculating $\mathbf{F}$ for each iteration the reference image is updated with sufficient high frequency, so that $\mathbf{F} \approx \mathbf{1}$ always holds. Thus, Equation (2.12) can be written as

$$\Delta \mathbf{n} = (\mathbf{B}_R^T \mathbf{B}_R)^{-1} \mathbf{B}_R^T \mathbf{I}_k \qquad (2.35)$$

where $\mathbf{B}_R$ is a constant matrix containing the row vectors $\mathbf{b}^i$, $i = 1, 2, ..., 16$ and is defined in the reference configuration, so that only $\mathbf{I}_k$ has to be updated. The whole iteration can then be written as

$$\mathbf{n}_{k+1} = \mathbf{n}_k + (\mathbf{B}_R^T \mathbf{B}_R)^{-1} \mathbf{B}_R^T \mathbf{I}_k \qquad (2.36)$$

It is now only required to calculate the grayscale gradient in the reference configuration at the natural coordinates of the pixels within the element. These coordinates are defined by the pixel position in the image table. The calculation is done via the central difference formula using the closest pixel values around the pixel of interest

$$\begin{aligned}
\frac{\partial I_R(X,Y)}{\partial X} &\approx \frac{1}{2h} \left(I_R(X+h,Y) - I_R(X-h,Y) \right) \\
\frac{\partial I_R(X,Y)}{\partial Y} &\approx \frac{1}{2h} \left(I_R(X,Y+h) - I_R(X,Y-h) \right)
\end{aligned} \qquad (2.37)$$

where $h = 1$, corresponding to the spacing between neighbor pixels.

2.2.4 Grayscale value Interpolation

With $\mathbf{B}$ in Equation (2.13) defined, the iteration is reduced to a sequence of operations already presented in previous sections, with the exception of interpolating grayscale values. The necessity of interpolation originates from the fact that an image is discrete while the algorithm assumes a continuous field. A pixel in the reference image will have a coordinate $\mathbf{X}$, where $\mathbf{X}$ is represented by two integers. The location of the point $\mathbf{X}$ after deformation, denoted $\mathbf{x}$, is however represented by two real numbers. It is hence necessary to estimate $I_C(\mathbf{x})$ by interpolation. This is done with a standard bi-cubic interpolation based on the 16 closes pixels to the point $\mathbf{x}$. A bi-cubic interpolation is chosen as it has been shown to be vastly superior to a bi-linear interpolation [22] while still being relatively cost effective in terms of computational time. This operation is performed for every point referred to by $\mathbf{I}_k$ for every iteration k, and hence constitutes the largest computational cost.

All the quantities in the iteration shown in Equation (2.36) are now defined, so that the only task left is to define a criterion to stop the iteration. This algorithm uses a simple but strict convergence criterion given as

$$\max\left(\left|\Delta n_i\right|\right) < 10^{-7}\,\mathrm{pix} \tag{2.38}$$

where Δn_i are the components of the vector $\Delta\mathbf{n}$.

2.2.5 Update of reference frame

Since the grayscale gradient is not updated, it is necessary to update the reference frame during an analysis if there is significant strain or rotation. An obvious cause for updating the reference is in the case of rotation. As an example, consider a rotation of the region of interest of 90° counter-clockwise relative to the reference frame. In this case, $\partial I_C/\partial\mathbf{x}$ should, according to Equation (2.31), be equal to

$$\frac{\partial I_C}{\partial\mathbf{x}} = \frac{\partial I_R}{\partial\mathbf{X}}\mathbf{F}^{-1} = \begin{bmatrix}\dfrac{\partial I_C}{\partial X} & \dfrac{\partial I_C}{\partial Y}\end{bmatrix}\begin{bmatrix}0 & 1\\-1 & 0\end{bmatrix} = \begin{bmatrix}-\dfrac{\partial I_C}{\partial Y} & \dfrac{\partial I_C}{\partial X}\end{bmatrix}$$

while the assumption of $\mathbf{F} = \mathbf{1}$, i.e. no rotation, would give

$$\frac{\partial I_C}{\partial \mathbf{x}} = \begin{bmatrix} \dfrac{\partial I_C}{\partial X} & \dfrac{\partial I_C}{\partial Y} \end{bmatrix}$$

This would obviously not converge to a correct result. The algorithm presented here updates the reference frame by doing all the steps already presented with the exception of defining the position of the element. This means that an update is treated like starting a new analysis. The reference grayscale values are hence also updated, which has some important advantages when measuring large deformation, translation or rotation. The effect of rotation on the algorithm was illustrated by the simple example above. Large deformation and translation can on the other hand change the color of a point. This can happen as the sample moves relative to the light sources, or by stretching the paint resulting in a change in paint color. Stretching of the sample can change all the terms in the deformation gradient, and hence make the assumption that $\mathbf{F}$ is close to $\mathbf{I}$ invalid. The reference update interval in terms of number of pictures should hence vary from test to test, primarily depending on picture frequency and deformation speed. A good indication of when to update the reference frame can be found from the number of iterations required to fulfill the convergence criterion. This number will slowly rise as the sample deforms, and then return to a base level when the reference is updated. The update frequency is in this thesis selected manually on a basis of test characteristics, where deformation speed relative to picture frequency is the dominant factor.

2.2.6 Post processing

The key information from a DIC analysis is the positions of the nodes for all images of interest. The deformation gradient $\mathbf{F}$, describing the deformation from the initial, undeformed configuration to a deformed configuration at time t can then be expressed as

$$\mathbf{F} = \frac{\partial \mathbf{x}}{\partial \mathbf{X}} = \frac{\partial \mathbf{x}}{\partial \boldsymbol{\xi}} \left(\frac{\partial \mathbf{X}}{\partial \boldsymbol{\xi}} \right)^{-1} = \begin{bmatrix} \mathbf{N}_{,\xi}\mathbf{n}_x & \mathbf{N}_{,\eta}\mathbf{n}_x \\ \mathbf{N}_{,\xi}\mathbf{n}_y & \mathbf{N}_{,\eta}\mathbf{n}_y \end{bmatrix} \begin{bmatrix} \mathbf{N}_{,\xi}\mathbf{n}_X & \mathbf{N}_{,\eta}\mathbf{n}_X \\ \mathbf{N}_{,\xi}\mathbf{n}_Y & \mathbf{N}_{,\eta}\mathbf{n}_Y \end{bmatrix}^{-1} \qquad (2.39)$$

where $\mathbf{N}_{,\xi}$ and $\mathbf{N}_{,\eta}$ are defined in Equation (2.20) and $\boldsymbol{\xi}$ is the element coordinate vector equal to $\boldsymbol{\xi} = \begin{bmatrix} \xi & \eta \end{bmatrix}^T$. It is important to note that $\mathbf{X}$ now refers to the image where deformation is

assumed zero, and that it is not directly related to the reference images in the DIC algorithm. Applying polar decomposition, $\mathbf{F}$ can be written as

$$\mathbf{F} = \mathbf{R}\mathbf{U} \tag{2.40}$$

where $\mathbf{R}$ is an orthogonal rotation tensor (i.e., it describes local rigid rotation) and $\mathbf{U}$ is the right stretch tensor. The rotation tensor is found by a simple iteration scheme [23]

$$\mathbf{R}^{k+1} = \frac{\left(\mathbf{R}^k + \left(\mathbf{R}^k\right)^{-T}\right)}{2} \quad \text{with} \quad \mathbf{R}^0 = \mathbf{F} \tag{2.41}$$

With $\mathbf{R}$ given, the stretch tensor is obtained as

$$\mathbf{U} = \mathbf{R}^T \mathbf{F} \tag{2.42}$$

Logarithmic strain tensor $\boldsymbol{\varepsilon}$ can now be calculated as the logarithm of $\mathbf{U}$, so we have

$$\boldsymbol{\varepsilon} = \ln\left(\mathbf{U}\right) \tag{2.43}$$

2.3 Evaluation and verification of the DIC code

2.3.1 Verification

The presented DIC implementation will here be evaluated and verified by comparing the performance of the Q16 and a Q4 element when applied to the digital pictures of an HDPE sample in tension. This case is chosen because it has the largest deformations of the tests reported in this thesis. The specimen also exhibits significant strain localization. Further validation of the code will be presented in Section 4.1.

Figure 2.6 shows a HDPE uniaxial tension test at five different stages of deformation, indicated by picture number, starting with an undeformed state. A coarse Q16 DIC mesh consisting of 5×1 elements is shown in red, with initial element dimensions of $h \times w = 70 \times 300 \text{ pix}^2$, roughly corresponding to $0.45 \times 2 \text{ mm}^2$.

25

| Reference | 200 | 300 | 400 | 500 |
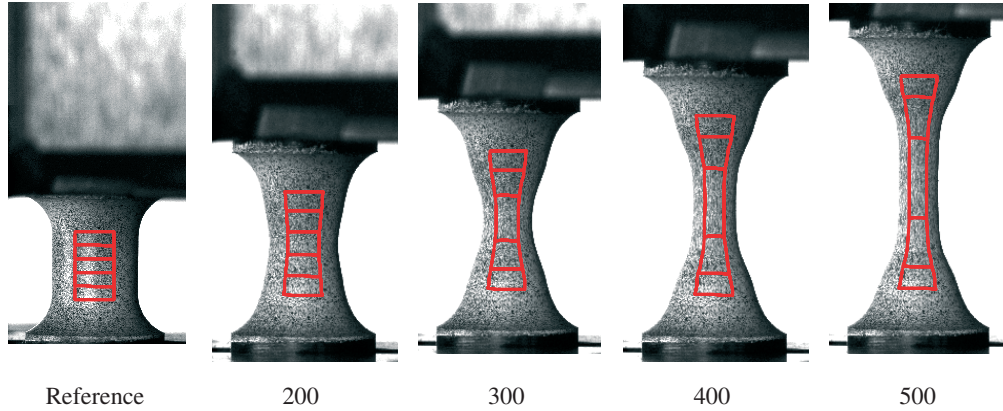
Figure 2.6: Element mesh for DIC analysis of HDPE at reference configuration and four subsequent stages of deformation specified with picture numbers.

A line approximately in the longitudinal *Y* and *y*-direction of the specimen is then defined through the center of the elements with a local coordinate $\xi = 0.5$, as shown in blue in Figure 2.7. The evaluation will pay attention to the longitudinal logarithmic strain as a function of current *y*-coordinate for the pictures shown in Figure 2.6. The mesh for the Q16 element is as shown in Figure 2.6 and Figure 2.7, while four different meshes are applied for the Q4 element. The coarsest mesh has Q4 elements with the same size as the Q16 elements, and the mesh is successively refined by dividing the Q4 element in two. Thus, the four meshes with Q4 elements have 5, 10, 20 and 40 elements over the height corresponding to the total height of the Q16 elements, and the dimension of the Q4 elements is, respectively, $h \times w = 70 \times 300 \text{ pix}^2$, $35 \times 300 \text{ pix}^2$, $17.5 \times 300 \text{ pix}^2$ and $8.75 \times 300 \text{ pix}^2$.
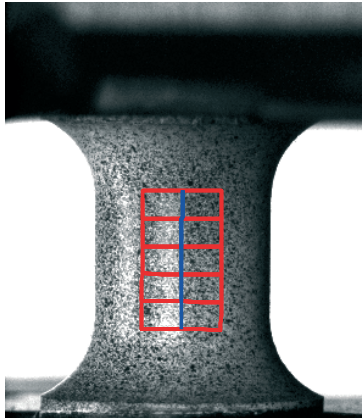
Figure 2.7: Path (blue line) for strain calculation on circular HDPE uniaxial tension sample with 5 Q16 elements (red).

Figure 2.8 shows the longitudinal logarithmic strain along the blue line on the specimen in Figure 2.7 at the four stages of deformation depicted in Figure 2.6 (excluding the reference frame). The four different meshes for the Q4 elements are addressed in sub-figures (a) to (d). There are several noteworthy observations in these plots. Firstly, the strains obtained with the Q4 elements converge to those obtained with the Q16 elements when the mesh is refined. This serves as a validation of the DIC implementation of the Q16 element. Secondly, based on the modest strain discontinuities when moving from one element to the next, the Q16 element seems well suited to describe the strain localization in the specimen. It is also a trend that the two element types predict the same strain at the center of the Q4 elements, and are furthest apart at the edges of the Q4 elements. Finally, it is worth noting the irregular strain profile of the Q4 analysis with the smallest elements, suggesting that the optimal element height for the Q4 elements is somewhere in-between 17.5 and 8.75 pixels for this analysis.

(a) Q4 1/1 height

(b) Q4 1/2 height

(c) Q4 1/4 height

(d) Q4 1/8 height
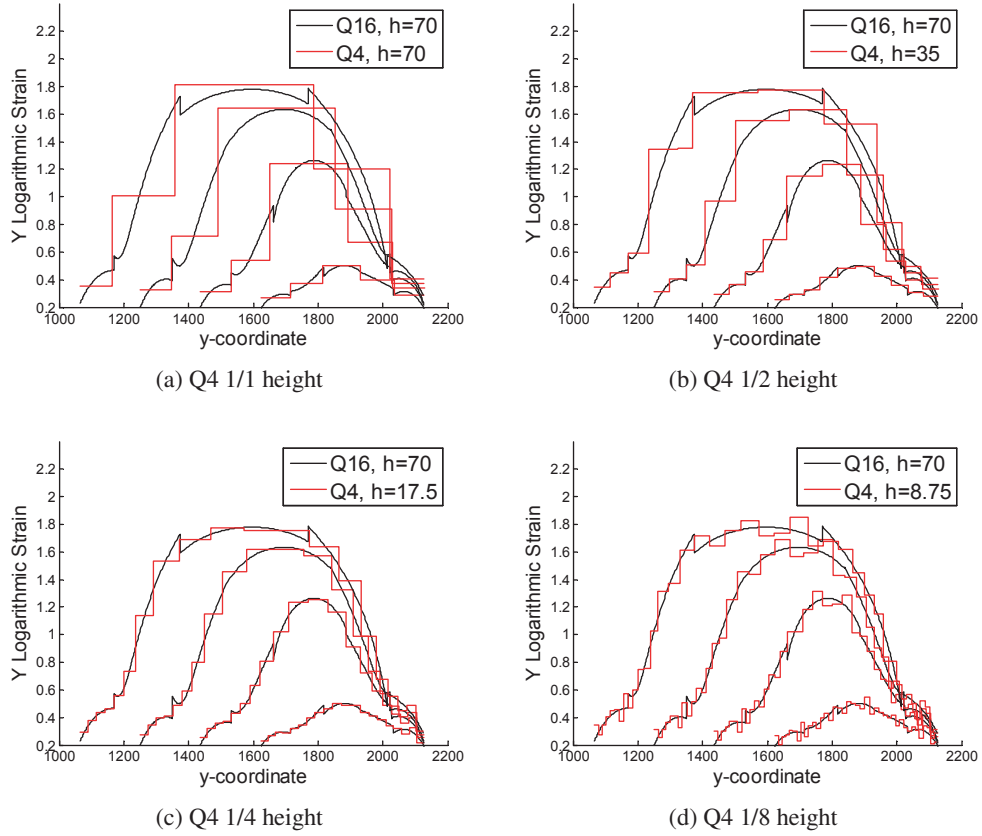
Figure 2.8: Profiles of longitudinal strain from a uniaxial tension test on HDPE as measured by use of a Q4 and a Q16 element at pictures 200, 300, 400 and 500. Increasing strains corresponds to higher picture numbers.

A second comparison between the performance of the element sizes and types is concerned with the ability to detect the correct grayscale values of the pixels compared to the reference image. The difference in grayscale values between the reference and current image in the region of interest can be expressed as $I_R^i - I_{C,k}^i$ for a point i at iteration k. This difference is the driving force of the DIC algorithm, and it is a measurement of the algorithm's ability to track an area. The average absolute error at the end of an iteration can then be calculated as

$$\frac{\sum_{i=1}^{N} \left| I_R^i - I_{C,end}^i \right|}{N} \tag{2.44}$$

28

where N is the numbers of points used in the analysis and the subscript *end* signifies that Equation (2.44) employs the final interpolated grayscale values found when the convergence criterion in Equation (2.38) has been met. This is shown for the four Q4 analyses and the one Q16 analysis in Figure 2.9 as a function of image number. The results here are more or less as expected, where the coarse Q4 mesh is seen to struggle when the neck starts to form after image 200. A finer Q4 mesh reduces the error, even in the case of the finest Q4 mesh. This can be seen as contradictory to what was seen in Figure 2.8, where this mesh had trouble reproducing a smooth strain field. This underpins the importance of not using grayscale error as the sole performance criterion. The Q16 element mesh has the smallest error by a slight margin, but the difference is minor. It should be noted that the error is here calculated with respect to image 1, while the actual analyses updated the reference frame. The large average difference above 10 in 8-bit grayscale value is a result of the paint changing color from being stretched as well as a change in light glare.
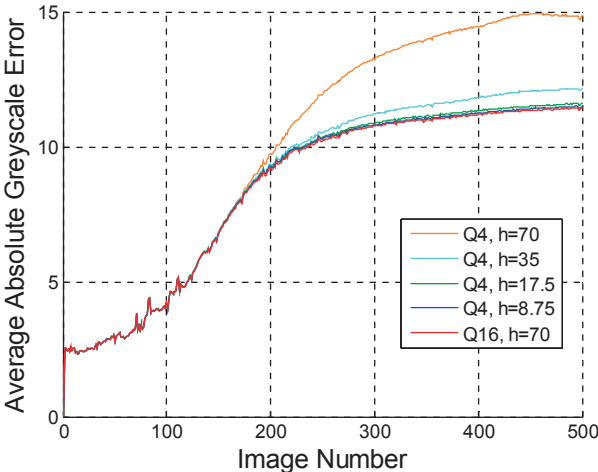
Figure 2.9: Average absolute grayscale error comparison between different sized Q4 elements and constant sized Q16 elements. Values are relative to a 8-bit grayscale ranging from 0-255.

With the result presented in Figure 2.8 and Figure 2.9, the Q4 and Q16 elements seem to perform at the same level, when run at their individual optimal mesh size. Defining the point of maximum strain is however an easier task with the Q16 element, since the strain field has a maximum within an element, and the coarser mesh ensures that the neck is contained within a

single element. This can be illustrated by plotting the strain along the same path as above, but now presented as a function of the reference Y-coordinate. Figure 2.10 shows where the point of maximum strain is in the reference configuration for the picture interval 200 to 400. The maximum variation of this position is equal to 0.83 pixels, which is considered acceptable.

(a) Longitudinal strain vs. Initial Y-position   (b) Y-position of maximum strain
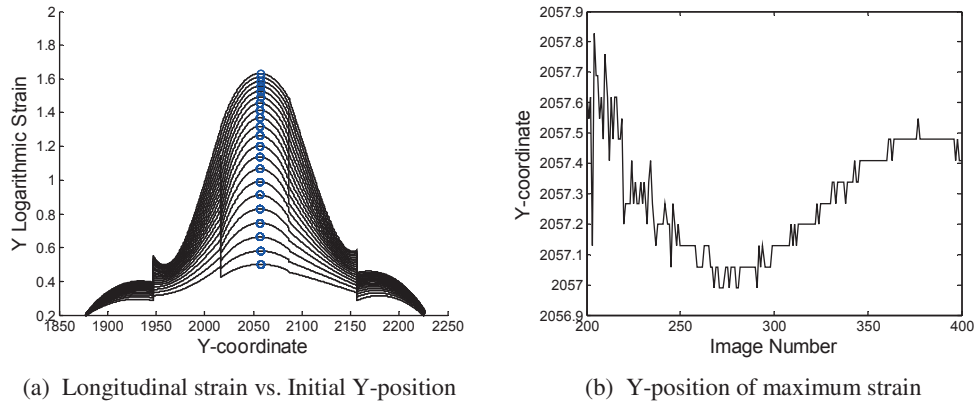
Figure 2.10: Point of localization in an HDPE uniaxial tension test as defined by the point of maximum longitudinal strain.

2.3.2 Mesh sensitivity

Another attractive property of the Q16 element is its low mesh sensitivity. This is here illustrated by comparing the analysis shown above with an analysis where the entire mesh has been moved 10 pixels in the Y-direction. Each element has a height $h = 70 \, pix$. These two analyses then result in the strain profiles and positions of maximum strain shown in Figure 2.11.

30

Longitudinal strain vs. Initial Y-position   Y-position of maximum strain
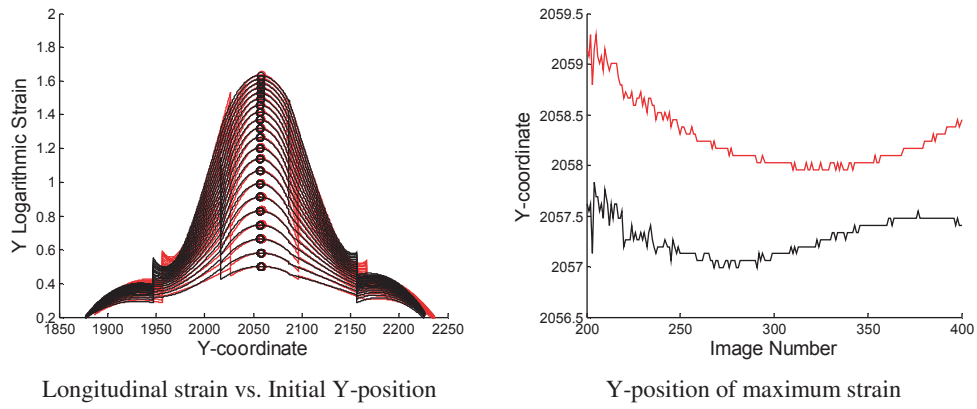
Figure 2.11: Mesh sensitivity for Q16 element, where location of point of localization is compared for two different mesh placements.

As seen in the figures above, the maximum strain seems to be preserved. The Y-positions of these points has shifted in the same direction as the mesh translation, but only by an average of about 1 pixel. The maximum strain in the two analyses is shown as a function of image number in Figure 2.12, where they can be seen to be in good agreement, with a maximum deviation of 3%.

31
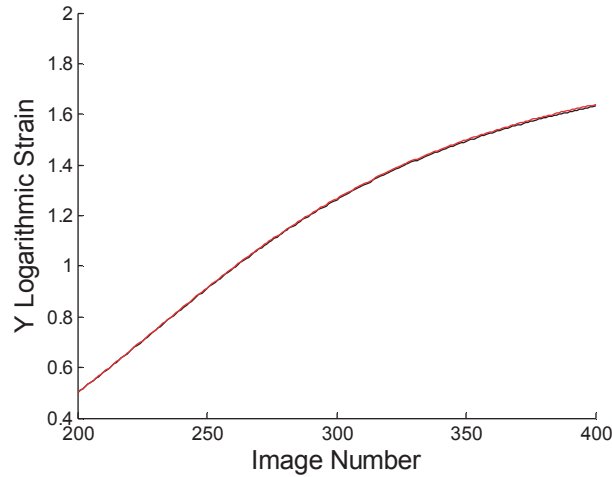
**Figure 2.12: Mesh sensitivity of maximum strain, where maximum longitudinal strain is found from two DIC analyzes where the mesh has a 10 pixels difference in vertical placement between the two analyzes.**

2.3.3 2D DIC analysis on non-plane surfaces

As half of the experimental data presented in this thesis involves tension samples with a circular cross-section, it is worth commenting on the implication of using 2D DIC on a non-planar surface.

An ideal surface for performing 2D DIC is a surface that resides on a plane with its normal vector pointing towards the camera, and where this plane does not move in its normal direction during deformation. A case where an object which is to be measured moves towards or away from the camera is the easiest concept to investigate first. Figure 2.13 shows a basic pinhole camera model with a field of view described by the angle α. This camera is pointed towards two objects, both with lengths L, located at distances u and $u + \Delta u$ from the camera. Intuitively, it seems reasonable that the object furthest away would be perceived as smaller by the camera. This relation can be formalized by realizing that perceived size of an object at a distance u is relative to the diameter or height H of the cone defining the camera view at the same distance.

32
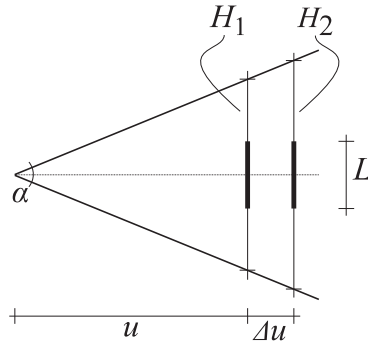
Figure 2.13: Pinhole camera model for calculation of camera perceived length.

It is now possible to calculate the perceived lengths $\tilde{L}_1$ and $\tilde{L}_2$ of the two objects in Figure 2.13, using this simple model. The cone will have two different heights at the two distances u and $u + \Delta u$, and they will be equal to

$$
\begin{aligned}
H_1 &= 2u\tan(\alpha/2) \\
H_2 &= 2(u+\Delta u)\tan(\alpha/2)
\end{aligned}
\tag{2.45}
$$

The perceived length can now be calculated as the ratio between actual length and the height of the view cone at the distance of the object. We can then express the two perceived lengths as

$$
\begin{aligned}
\tilde{L}_1 &= \frac{L}{H_1} = \frac{L}{2u\tan(\alpha/2)} \\
\tilde{L}_2 &= \frac{L}{H_2} = \frac{L}{2(u+\Delta u)\tan(\alpha/2)}
\end{aligned}
\tag{2.46}
$$

The ratio between these two lengths can now be calculated as

$$
\frac{\tilde{L}_1}{\tilde{L}_2} = \frac{u+\Delta u}{u} = 1 + \frac{\Delta u}{u}
\tag{2.47}
$$

From Equation (2.47) it can now be seen that the closest object will appear to be a factor $1 + \Delta u/u$ larger than the object furthest away. This equation can now be applied for the real world case where a neck forms in a uniaxial tension test. The initial distance between the

33

camera and the surface of the sample is then equal to u. If the neck now is conservatively assumed to reduce the cross sectional area towards zero, the surface will then move a distance of up to half the thickness of the sample further away from the camera. Assuming a circular cross section with radius r we can then from Equation (2.47) estimate the relative error in perceived length as $1+r/u$. Since large deformation of polymers is of interest, it is in a tension test necessary to place the camera around one meter from the samples in order to keep the sample within the frame of the image throughout the deformation. Assuming a radius equal to 3 mm, which is the radius of the samples used in the experimental work in this thesis, the perceived length factor is then equal to

$$1+\frac{3\,mm}{1000\,mm}=1.003 \qquad\qquad (2.48)$$

This effect is hence considered as only a minor source of inaccuracy.

A similar complication comes when a plane with its normal vector pointing towards the camera rotates about an axis within the plane. This will result in points moving towards or away from the camera. This results in the same type of change in perceived length, but given the limited distances a point on the sample can move towards or away from the camera, this is not investigated further. It might also be noted that in the analysis of uniaxial tension data, it is the point of initial necking that is of interest in this thesis. This area can be assumed to not rotate during deformation, which also makes a further analysis of the effects of rotation superfluous. A thorough investigation of the effects of out-of-plane motion on 2D and 3D DIC results has been done by Sutton et al. [24].

Measuring average radial stretch on a circular sample with a 2D DIC algorithm will not result in any significant inaccuracy if the mesh is applied to the whole visible width of the sample. This follows from the fact that the measured average radial stretch over the entire diameter can be expressed as D/D_0, where D and D_0 is the current and initial diameter of the sample. This will be demonstrated in the Section 4.1 by comparing the results from DIC and an edge tracing algorithm.

34

3 Edge Tracing

Edge tracing is used as a tool to quantify the parameters describing the geometry of the neck of a tension sample with a circular cross section. The characteristics of interest are the current minimum radius of the sample and the curvature of the neck. The method for establishing these parameters will be shown in this chapter.

3.1 Edge Identification

Identifying an edge is done by searching through the derivative of the grayscale value for a horizontal line of pixels parallel with the x-axis, where the grayscale value is numerically differentiated with respect to x. The location of an edge corresponds with a relatively large change in the absolute value of the derivative compared to the background noise. Figure 3.1 (a) shows the position of such a horizontal line, while Figure 3.1 (b) shows the corresponding grayscale values along the line. A grayscale value of 255 is equal to pure white, and 0 corresponds to black. It can be seen that even though the background appears to be white, some small level of gray is present together with some noise. It can also be seen that there is a trend of slight darkening from left to right.

| (a) Horizontal pixel line | (b) Grayscale value along line |
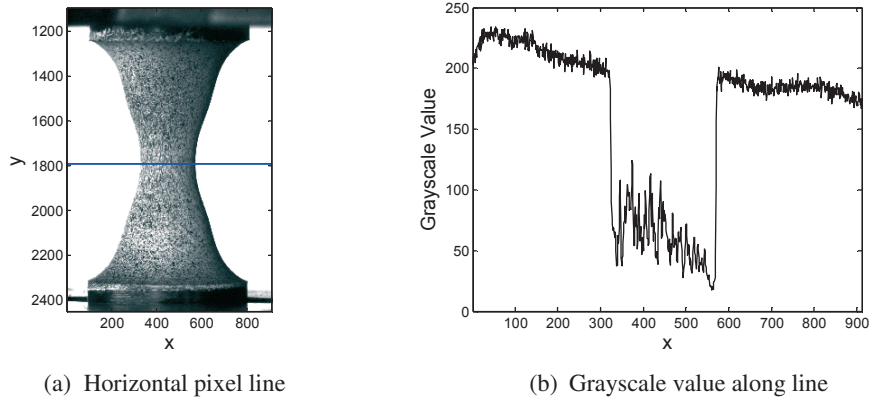
Figure 3.1: Grayscale value curve (b) along a horizontal line of a picture (a).

To reduce the noise seen in Figure 3.1 (b), the image is filtered with a 2D moving average algorithm, substituting each grayscale value with the average value of itself and the closest 25 pixels, creating a pixel square of 5×5 pixels. The filtered grayscale value curve is shown in Figure 3.2 (a), while Figure 3.2 (b) shows a comparison between the differentiated grayscale value for the raw and filtered data given in Figure 3.1 (b) and Figure 3.2 (a), respectively. The differentiation is done numerically with the central difference method.

The goal of the algorithm is to identify the two large peaks seen in the derivative plot. A good quantification of the success of the moving average filter is then the ratio of the values of the large peaks divided by the maximum noise level, which in this case is equal to 4.38 before filtering and 14.7 after the filter has been applied.

36

(a) Filtered row of pixels   (b) Raw and filtered absolute derivative of line
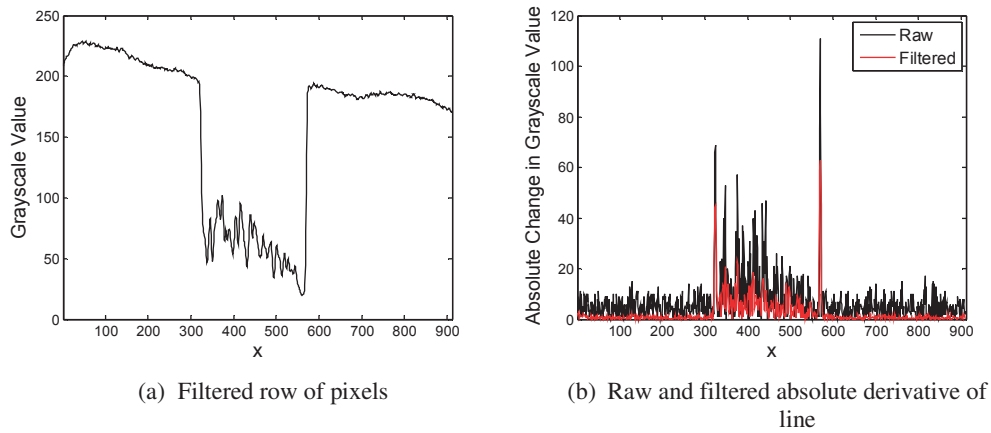
Figure 3.2: Effect of filtering an image with a moving average.

Identifying the peaks is done separately for the left and the right peak. The left peak is found by moving from left to right and identifying the first significant peak, while the right peak is found by moving right to left. This is necessary since the paint on the sample surface can create higher peaks than the edges do. The algorithm starts by moving from one of the sides towards the center, and searches for the first point above a set threshold which in this case is set to 5. This first point is now assumed to be a start point of the peak. The algorithm then climbs further up the peak until the value of the differentiated grayscale values is no longer increasing. This is equivalent with the second derivative changing sign, and marks the maximum value of the peak.

The result of doing this for all the horizontal lines of interest is shown in Figure 3.3. The lines or area of interest is found from the DIC results, where the positions of the DIC nodes with the highest and lowest y-coordinate define the search area. The tracing process is then automated and performed on all the pictures from the test at hand.

37
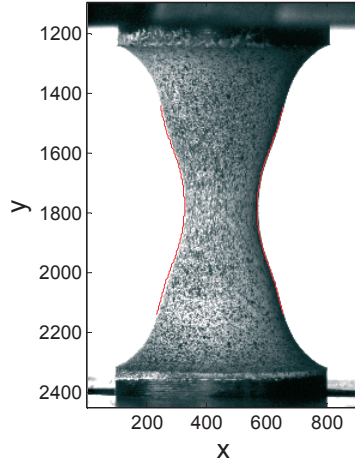
Figure 3.3: Traced edges of uniaxial tension test after necking.

3.2 Edge Mirroring

In order to find the radius, slope and curvature at a given point of the sample from the edge detection data, it is useful to know the current longitudinal axis of the sample. This axis might have a small deviation from the vertical y-axis in Figure 3.3 due to a combination of inaccurate mounting of the sample, non-level camera or eccentricity occurring during the stretching of the sample. The longitudinal axis is identified by assuming that the axis is a symmetry line for the two edges found from the edge identification procedure.

Let a vector $\mathbf{p}$ define a point that has been located on the edge of the sample. This vector can now be decomposed into three vectors as $\mathbf{p} = \mathbf{x}_0 + \mathbf{h} + \mathbf{r}$. The first term $\mathbf{x}_0$ defines an offset in the x direction of sample symmetry axis, while $\mathbf{h}$ has the same angle as the symmetry axis, with a length defining the position of the point $\mathbf{p}$ along the symmetry axis. The radius of the sample at this point is now described by $\mathbf{r}$, which is a perpendicular to the vector $\mathbf{h}$. This decomposition is shown in Figure 3.4.

38
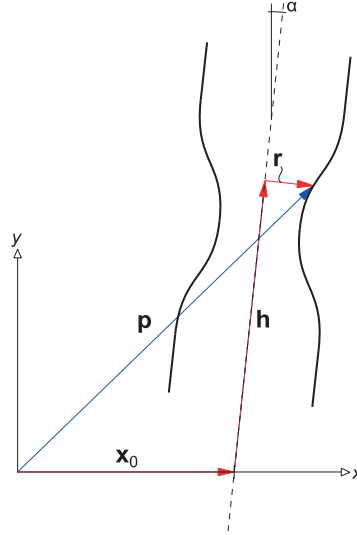
Figure 3.4: Edge point decomposition for symmetry calculation.

As stated, **p** is decomposed as

$$\mathbf{p} = \begin{bmatrix} p_x \\ p_y \end{bmatrix} = \mathbf{x_0} + \mathbf{h} + \mathbf{r} = \begin{bmatrix} x_0 \\ 0 \end{bmatrix} + \mathbf{h} + \mathbf{r} \qquad (3.1)$$

Further let the vector **h** be defined by a length H and an angle α, where α describes the angle between the symmetry axis and the y-axis with positive clockwise rotation. The vector **h** can then be written as

$$\mathbf{h} = \begin{bmatrix} a \\ 1 \end{bmatrix} \frac{H}{\sqrt{a^2 + 1}} \qquad (3.2)$$

where $a = \tan(\alpha)$. Let the vector **r** have a length R. Since **r** is defined as being normal to **h**, **r** can now be written as

$$\mathbf{r} = \begin{bmatrix} 1 \\ -a \end{bmatrix} \frac{R}{\sqrt{a^2 + 1}} \qquad (3.3)$$

Equation (3.1) is solved for H and R, giving

39

$$R = \frac{p_x - ap_y - x_0}{\sqrt{a^2 + 1}}$$

$$H = \frac{p_y + ap_x - ax_0}{\sqrt{a^2 + 1}}$$

(3.4)

The decomposition of $\mathbf{p}$ can then be written as

$$\mathbf{p} = \mathbf{x_0}(x_0) + \mathbf{h}(a, x_0, \mathbf{p}) + \mathbf{r}(a, x_0, \mathbf{p})$$

(3.5)

Assuming symmetry, there should for each point on the edge $\mathbf{p} = \mathbf{x_0} + \mathbf{h} + \mathbf{r}$ be a mirror point $\tilde{\mathbf{p}} = \mathbf{x_0} + \mathbf{h} - \mathbf{r}$ with $\mathbf{r}$ in the negative direction. If a and x_0 represent the true symmetry axis, two symmetrical points $\mathbf{p}$ and $\tilde{\mathbf{p}}$ should then satisfy the two equations

$$\mathbf{g}(a, x_0) = \mathbf{h}(a, x_0, \mathbf{p}) + \mathbf{r}(a, x_0, \mathbf{p}) - \mathbf{h}(a, x_0, \tilde{\mathbf{p}}) + \mathbf{r}(a, x_0, \tilde{\mathbf{p}}) = \mathbf{0}$$

(3.6)

If a and x_0 are not known, the scalar error from an assumed symmetry axis can then be found as

$$f(\alpha, x_0) = \sqrt{\mathbf{g}^T \mathbf{g}}$$

(3.7)

describing the absolute distance between two points, when one of them is mirrored about an axis given by α and x_0. This function is then linearized with a first order Taylor expansion to give

$$f_{k+1} = f_k + \left[\left. \frac{\partial f}{\partial \alpha} \right|_k \quad \left. \frac{\partial f}{\partial x_0} \right|_k \right] \begin{bmatrix} \Delta a \\ \Delta x_0 \end{bmatrix}$$

(3.8)

This equation can be optimized for $n > 2$ points with a least square fit algorithm by first writing it in vector form

$$
\begin{bmatrix} f_{k+1}^1 \\ f_{k+1}^2 \\ \vdots \\ f_{k+1}^n \end{bmatrix} = \begin{bmatrix} f_k^1 \\ f_k^2 \\ \vdots \\ f_k^n \end{bmatrix} + \begin{bmatrix} \left.\dfrac{\partial f}{\partial \alpha}\right|_k^1 & \left.\dfrac{\partial f}{\partial x_0}\right|_k^1 \\[2mm] \left.\dfrac{\partial f}{\partial \alpha}\right|_k^2 & \left.\dfrac{\partial f}{\partial x_0}\right|_k^2 \\[2mm] \vdots & \vdots \\[2mm] \left.\dfrac{\partial f}{\partial \alpha}\right|_k^n & \left.\dfrac{\partial f}{\partial x_0}\right|_k^n \end{bmatrix} \begin{bmatrix} \Delta a \\ \Delta x_0 \end{bmatrix} = \mathbf{f}_k + \partial \mathbf{F}_k \begin{bmatrix} \Delta a \\ \Delta x_0 \end{bmatrix} \qquad (3.9)
$$

where $\mathbf{f}_k$ is a vector containing n values of f_k, and the gradients are collected in the $(n \times 2)$ matrix $\partial \mathbf{F}_k$. The least square zero solution to Equation (3.9) yields

$$
\begin{bmatrix} \Delta a \\ \Delta x_0 \end{bmatrix} = (\partial \mathbf{F}^T \partial \mathbf{F})^{-1} \partial \mathbf{F}^T \mathbf{f}_k \qquad (3.10)
$$

Equation (3.10) provides updated values of a and x_0, and the iteration continues until a convergence criterion is met. In this implementation, convergence is assumed when $\max\left(\left\|[\Delta a \quad \Delta x_0]\right\|\right) < 10^{-5}\ \text{pixels}$.

When a and x_0 are known for a given picture, it is possible to convert the coordinates of both the left and right edge from picture coordinates to the coordinate system $H\text{-}R$, defined by Equation (3.4). Figure 3.5 shows the edges found in Figure 3.3 in $H\text{-}R$ coordinates, where in subfigure (a) it is assumed that $\alpha = 0$, while in subfigure (b) the algorithm has been applied resulting in $\alpha = -0.0079$, equal to $-0.45°$. The red line is the left edge plotted with the absolute value of R and the blue line is the right edge. It is seen from the difference in the two subfigures that even a small angle has a significant impact.
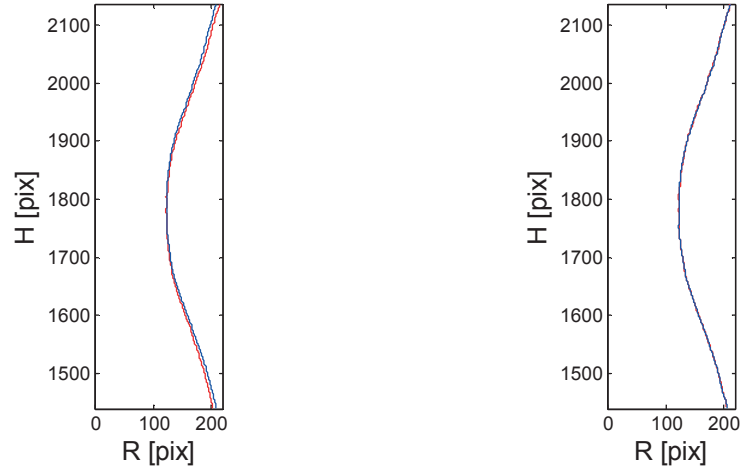
(a) Overlap with non-rotated symmetry axis   (b) Overlap with rotated symmetry axis

Figure 3.5: Sample edges in H-R coordinates. The red curve is the left edge plotted with the absolute value of R while the blue curve is the right edge.

The good agreement found in Figure 3.5(b) implies that the symmetry is well preserved for the sample during deformation. It also means that the edge data may be smoothed by averaging the data from both the left and the right edge in H - R space. This is useful since the accuracy of the original edge data is of the order of one pixel.

By applying the algorithm to all the pictures of a test it is possible to look at the angle α of the symmetry axis as a function of picture number. The shape of the curve describing this angle can also be found from DIC via $\mathbf{R}$ from the polar decomposition defined in Equation (2.40). Figure 3.6 shows the symmetry line angle found from the algorithm and from $\mathbf{R}$, where the initial angle from $\mathbf{R}$ is set equal to the initial angle found from the mirror algorithm. $\mathbf{R}$ is here calculated for the point of necking of the sample.

42
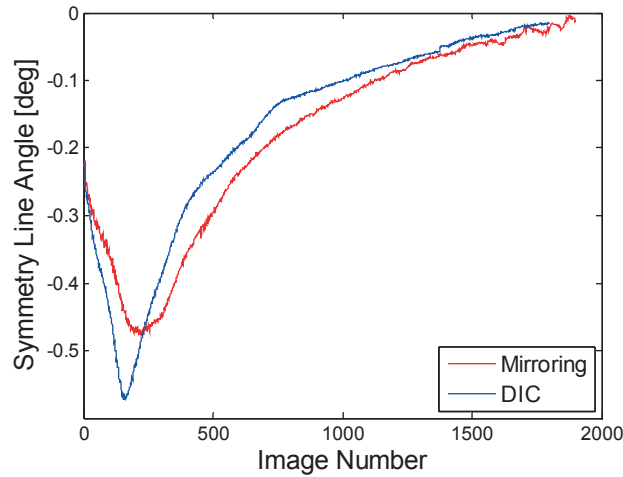
Figure 3.6: Angle of symmetry axis as a function of image number, found from edge mirroring (red) and DIC (blue).

As seen in Figure 3.6, the trends are quite similar for the two different calculations, which suggests that the measured rotations are not an artefact of the algorithm. The shape of the curve might indicate that the sample was slightly misaligned in the machine. It seems that the sample first sets by uneven slipping at the machine grips (image 0-250), before establishing a final misalignment that is slowly corrected as the sample gauge length increases. The angle found from the presented mirroring algorithm is preferred over the angle found from DIC since it represents the orientation of the sample as a whole, as well as providing an initial angle.

3.3 Curvature of Neck

The curvature of the neck can be found from the H - R data shown in Figure 3.5 (b). The first step is to find the H coordinate of the center of the neck, denoted H_C. The picture coordinates x_C and y_C for this point can be found from the DIC results by identifying the element coordinates of the point with the largest longitudinal strain when necking occurs. H_C can then be calculated from Equation (3.4)$_{\mathrm{II}}$ by substituting p_x and p_y with x_C and y_C, and using the established values for a and x_0. It is now possible to calculate the first derivative dR/dH of

43

the data in Figure 3.5 (b) by numerical differentiation and then performing a linear fit around H_C. Figure 3.7 shows the first derivative of the edge data shown in Figure 3.5 along with a linear fit of a sub-region around H_C. This sub region is here colored red and has the range $H = H_C \pm 75\,pix$. The figure also illustrates the linearity of the slope in the area of the neck, which is a general trend for any point in time during a test.
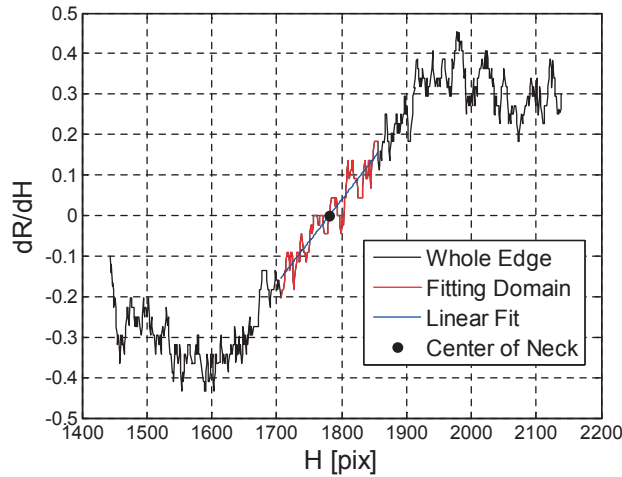

Figure 3.7: Angle of neck region as a function of sample length position shown with a linear fit around the center neck position.

The general expression for signed curvature κ of a function $y(x)$ is

$$\kappa = \frac{y''}{\left(1+\left(y'\right)^2\right)^{3/2}} \tag{3.11}$$

but since the slope of the center of the neck is zero we get $\kappa = y''$, which means that the slope of the linear fit of dR/dH can be assumed to represent the curvature of the center of the neck. When this method is applied to a series of pictures representing the deformation of a test sample, it is possible to plot curvature as a function of picture number as shown in Figure 3.8. It is seen from the figure that the curvature has the shape one would expect, with an initial value close to zero, then exhibiting a peak as the neck starts to form, before returning to zero as the neck propagates away from the initial point of localization.

44
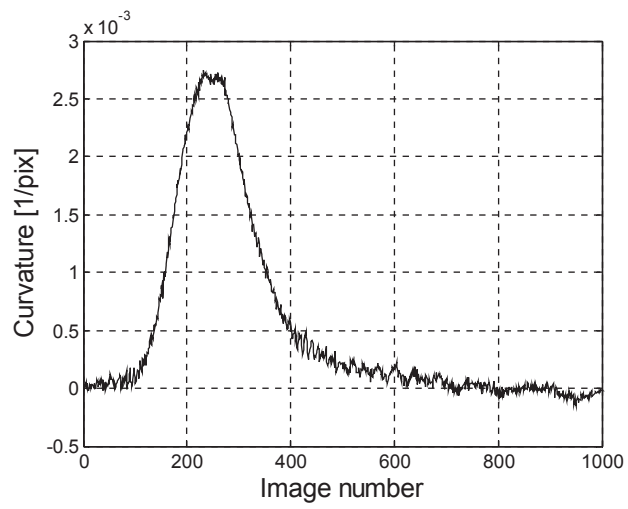
Figure 3.8: Neck curvature of a uniaxial tension test as a function of image number.

4 Analysis of Samples Subjected to Uniaxial Tension

This chapter presents the methodology used to determine the response the investigated polymers has to uniaxial tension. This response includes true stress and strain, Bridgman-correction of the stress, change of volume, and treatment of data from a thermal camera. Results from the individual tension tests follow in the next chapter, while Chapter 6 presents the compression data.

Each test is analyzed in two main steps. First the DIC algorithm described in Chapter 2 is used. Thereafter, the edge tracing algorithm presented in Chapter 3 is applied. This order is preferred since the edge tracing method uses the coordinates of the DIC element nodes to limit its trace area.

Before running the DIC analysis, it is necessary to define a mesh on the undeformed sample. Applying the higher-order DIC element presented in Section 2.2.1, the mesh consists of a single element in the width direction of the sample and an odd number of elements in the length direction. The mesh is centered and rotated to align with the initial orientation of the sample. Rotating the mesh to the sample orientation has the benefit that the element coordinate system has the same rotation as the sample coordinate system $R - H$, where $R - H$ is discussed in Section 3.2. A single run of the edge tracing algorithm provides a good estimate of the sample symmetry axis vector. Afterward, it is easy to rotate and center the mesh along the transverse axis of the sample. It is however also desirable that the centroid of the center element is located at the section where necking first occurs along the longitudinal axis of the sample. This choice of center point for the mesh best exploits the element shape functions, which are chosen so as to describe a parabolic strain field. The reference coordinates of this point are however unknown, hence it is necessary to run an initial DIC analysis up to necking to determine this coordinate. With an initial DIC analysis, it is possible to plot longitudinal strain as a function of the image coordinates in the first image, as shown in Figure 2.10, facilitating the final placement of the mesh. Figure 4.1 shows an image of an undeformed sample with a 1×3 mesh which has been aligned with the vertical symmetry-axis of the sample and the position of the neck. In the reference image in Figure 4.1, the symmetry-axis is found to be rotated clockwise with an angle $\alpha_0 = 0.514°$.

47
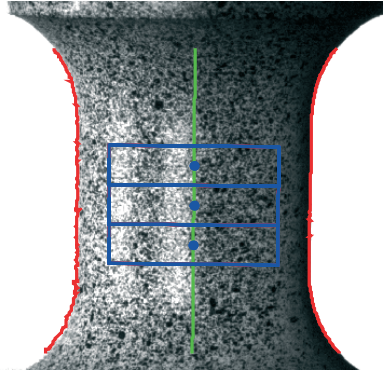
Figure 4.1: Mesh alignment on uniaxial tension test with edge tracing in red, mesh in blue and sample symmetry axis in green.

With the mesh established, a full DIC analysis is performed. Subsequently, the edges of the sample are traced in all the images, using the full DIC analysis to limit the region of interest. This provides sample edge data for all the images expressed in a current $R - H$ system, as well as providing the curvature of the neck.

4.1 Strain Measurements

With a complete DIC and edge analysis, it is possible to calculate the strains at the critical section of the sample, i.e. the section first experiencing yielding. This is defined as the section of initial necking. It is found by identifying the point of maximum longitudinal strain along the length axis of the sample around the time when the sample shows visible necking. Since the mesh is centered with respect to the location of the neck and rotated with the initial sample orientation, the critical section of the sample is defined by the local element coordinates $(\xi,\eta)=(\xi,0.5)$ for the center element.

A representative description of local deformation in the neck is then found from the average of the deformation gradient along the line ξ . The average deformation gradient $\overline{\mathbf{F}}$ is expressed as

$$\overline{\mathbf{F}} = \int_{0}^{1} \mathbf{F}(\xi,0.5)d\xi \tag{4.1}$$

where it is observed that the element dimension is unity in the local (ξ, η) coordinate system. This expression is approximated numerically as

$$\overline{\mathbf{F}} \approx \frac{\sum_{i=0}^{N} \mathbf{F}(i/N, 0.5)}{N+1} \qquad (4.2)$$

where N defines the number of points in the averaging process. Consistent results are obtained for values of N larger than 5, but since the operation is computationally cheap, $N = 10$ is used in the further work.

With $\overline{\mathbf{F}}$ defined, the average rotational tensor $\overline{\mathbf{R}}$ is found with the iteration described by Equations (2.41), and the average right stretch tensor $\overline{\mathbf{U}}$ is calculated as $\overline{\mathbf{U}} = \overline{\mathbf{R}}^T \overline{\mathbf{F}}$.

The matrix representation of $\overline{\mathbf{U}}$ denoted $\overline{U}$ is defined in the picture coordinate system, while what is of interest here is a matrix representation $\tilde{U}$ that refers to a coordinate system that has been rotated to the orientation of the sample in the reference picture. This coordinate transform is then expressed as

$$\tilde{U} = Q\overline{U}Q^T \qquad (4.3)$$

where Q is the transformation matrix defined as

$$Q = \begin{bmatrix} \cos(\alpha_0) & \sin(\alpha_0) \\ -\sin(\alpha_0) & \cos(\alpha_0) \end{bmatrix} \qquad (4.4)$$

Here, α_0 is the initial angle of the sample relative to the picture frame, with positive rotational axis counterclockwise. With $\tilde{U}$ defined, the longitudinal and radial stretch λ_L and λ_R are given as

$$\lambda_L = \tilde{U}_{22} \qquad (4.5)$$

and

$$\lambda_R = \tilde{U}_{11} \tag{4.6}$$

Next, the matrix representation of the true strain tensor $\tilde{\varepsilon}$, defined in the same coordinate system as $\tilde{U}$, is calculated from

$$\tilde{\varepsilon} = \ln\left(\tilde{U}\right) \tag{4.7}$$

The first and second diagonal element of $\tilde{\varepsilon}$ are then defined as the average radial and longitudinal true strain ε_R and ε_L, respectively, in the section experiencing the first onset of necking.

After λ_R has been calculated it is possible to evaluate the DIC results by comparing λ_R with R/R_0 found from edge tracing. The ratio R/R_0 is evaluated at a point H which is given in Equation (3.4) as a function of current coordinates (x, y) and the symmetry axis parameters α and x_0. Considering the center of the element, the coordinates (x, y) are calculated from the shape functions, current node positions and local element coordinates $(\xi, \eta) = (0.5, 0.5)$ with Equation (2.2). A comparison between λ_R and R/R_0 is shown in Figure 4.2, where it can be seen that the maximum difference between the measurements is around 1%. This comparison between radial stretch calculated from the edge tracing and DIC algorithm is done for all tests, and serves as an indication of the quality of a DIC analysis.

(a) Radial stretch   (b) Deviation of DIC from Edge Tracing
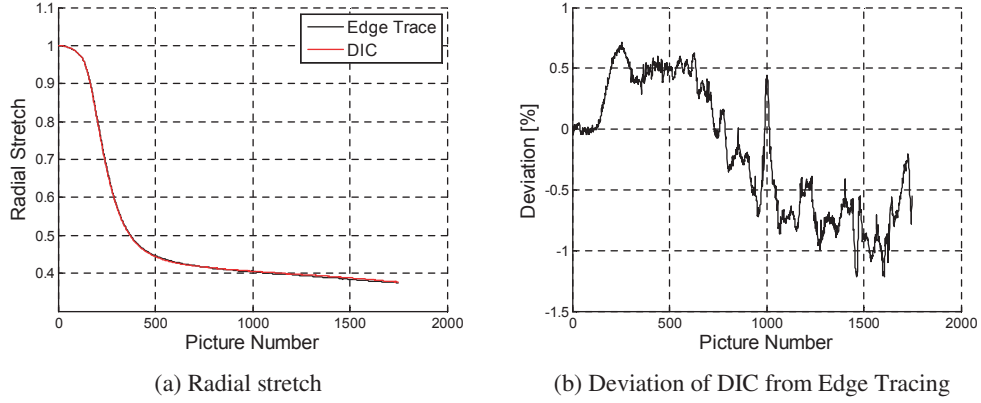
Figure 4.2: Comparison of radial stretch calculated with DIC and Edge Tracing.

Equivalent plastic strain and equivalent plastic strain rate, p and $\dot{p}$ respectively, are also of interest. Equivalent plastic strain is defined as

$$p = \varepsilon_L - \varepsilon_L^{el} = \varepsilon_L - \frac{\sigma}{E} \tag{4.8}$$

where E is the Young's modulus of the material in question, and σ is the average true stress in the longitudinal direction, as defined in Section 4.4. Similarly, longitudinal plastic strain rate is defined as

$$\dot{p} = \dot{\varepsilon}_L - \dot{\varepsilon}_L^{el} = \dot{\varepsilon}_L - \frac{\dot{\sigma}}{E} \tag{4.9}$$

Since the Young's modulus is not necessarily constant for polymers, it is assumed that the use of an effective modulus up to a stress level defined as yield stress is an adequate approximation.

4.2 Elastic Parameters

It is rather straightforward to find Young's modulus E and Poisson's ratio ν when the stress and strain have been determined. Both parameters are calculated in the elastic domain,

defined as the strain domain from zero to the onset of yielding. Poisson's ratio is simply calculated as

$$\nu = -\frac{\varepsilon_R}{\varepsilon_L} \qquad (4.10)$$

For a varying Poisson's ratio, the equation will then describe the mean value from zero up to a given point of strain. Young's modulus is similarly defined as an effective elastic stiffness, rather than a true tangent, and is defined as

$$E = \frac{\sigma}{\varepsilon_L} \qquad (4.11)$$

The elastic modulus is however sensitive to strain rate, so in order to quantify the observed viscoelastic response, a model is assumed for the strain rate dependency of the modulus, viz.

$$E = E_0\left(\varepsilon_L\right) + \eta\left(\varepsilon_L\right)\log\left(\frac{\dot{\varepsilon}_L}{\dot{\varepsilon}_0}\right) \qquad (4.12)$$

where E_0 is Young's modulus at a constant strain rate $\dot{\varepsilon}_0$ and η is the viscosity of the material in the elastic domain. The factor η then gives the additive increase of the modulus for a ten times increase in strain rate, compared to $\dot{\varepsilon}_0$. The viscosity can then be found by looking at the difference in Young's modulus of two tests performed at different speeds. Considering two tests k and l, the difference in stiffness $E^k - E^l$ is then, according to the model, equal to

$$E^k - E^l = \eta\left(\varepsilon_L\right)\left(\log\left(\frac{\dot{\varepsilon}_L^k}{\dot{\varepsilon}_0}\right) - \log\left(\frac{\dot{\varepsilon}_L^l}{\dot{\varepsilon}_0}\right)\right) \qquad (4.13)$$

which solved for η gives

$$\eta^{kl}\left(\varepsilon_L\right) = \frac{E^k - E^l}{\log\left(\dot{\varepsilon}_L^k / \dot{\varepsilon}_L^l\right)} \qquad (4.14)$$

If several pairs of tests performed at different speeds produce similar curves for η as a function of strain, the mean curve will describe the elastic viscosity of the material.

4.3 Calculation of Volumetric Strain

Average volumetric strain in the neck can easily be calculated if it is assumed that there exists a material volume with cylindrical shape that remains a cylinder throughout the deformation, yet with an evolving height and radius. Considering the section which necks first, the cylinder has an initial radius R_0, equal to the initial radius of the sample, and a small height h_0. It is then straightforward to find the volume ratio λ_V as

$$\lambda_v = \frac{V}{V_0} = \frac{\pi h R^2}{\pi h_0 R_0^{\;2}} = \frac{\lambda_L h_0 (\lambda_R R_0)^2}{h_0 R_0^{\;2}} = \lambda_L \lambda_R^2 \qquad (4.15)$$

where λ_L and λ_R were determined in Equations (4.5) and (4.6), respectively. This method is hereafter referred to as the "cylinder method".

The assumption of conserving the cylindrical shape throughout the entire deformation process is however not correct for a uniaxial tension test that exhibits necking. The problem with the assumption is illustrated in Figure 4.3, showing a schematic representation of the neck of a circular uniaxial tension test sample with a coordinate system (r, h) placed at the volumetric center of the sample. Any initially square infinitesimal element located at a point $\mathbf{X} = (R(h), h)$ at the surface of the sample, has to remain both parallel to the surface, now rotated with an angle β, and square. The conservation of the square shape comes as a result of the absence of shear stresses on the free surface of the sample. This means that any initially straight line, stretching from $r = 0$ to $r = R$ with $h \neq 0$, will not remain straight when necking occurs, hence a cylinder does not remain a cylinder.
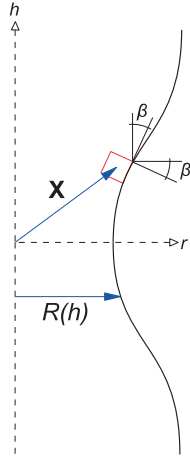
Figure 4.3: Schematic description of deformation in a neck of a tension sample with circular cross section.

What seems more reasonable is to assume that a cylinder in the reference gauge section without any neck deforms into a cylinder with parabolic-shaped end caps, as seen in Figure 4.4. Thus, it is assumed that the height $h(r)$ of the deformed cylinder, centered at the neck, is dependent on the radius r as well as the current angle β of the surface, viz.

$$h(r) = \frac{\beta}{2R}(R^2 - r^2) + H/2 \qquad (4.16)$$

where H is the current height of the cylinder inside the parabolic caps. The curve described by the equation is shown in Figure 4.4.
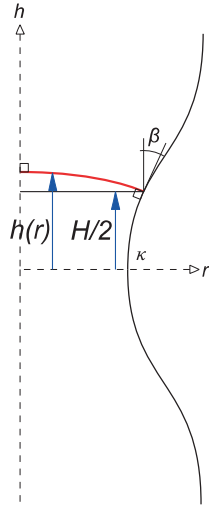
Figure 4.4: Principal for volumetric strain correction of tension sample with a circular cross section when a neck is formed.

If we now consider the local change of volume in the neck, i.e. H is small, we can assume that the radius R of the necked section is constant, and equal to the minimum radius of the neck. We can further estimate the angle β as $\beta \approx \kappa H / 2$, where κ is the curvature of the neck, see Equation (3.11). Assuming axi-symmetric conditions, the total volume V of this deformed cylinder with parabolic end-caps and height $2 \cdot h(r)$ is then

$$V = 2\left(2\pi \int_0^R r h(r) dr \right) = 4\pi \int_0^R \left(\frac{\kappa H}{4R}(R^2 - r^2)r + r\frac{H}{2} \right) dr \qquad (4.17)$$

where Equation (4.16) and the estimate $\beta \approx \kappa H / 2$ were employed in the last equality. Performing the integration, the volume reads

$$V = 4\pi\left(\frac{H\kappa R^3}{16} + \frac{HR^2}{4} \right) = \pi R^2 H\left(\frac{\kappa R}{4} + 1 \right) \qquad (4.18)$$

Setting $H = H_0\lambda_L$ and $R = R_0\lambda_R$, where H_0 and R_0 are respectively the initial height and radius of the cylinder, we can express the volume as

$$V = \pi R_0^2 H_0 \lambda_L \lambda_R^2 \left(\frac{\kappa R}{4} + 1 \right)$$ (4.19)

Dividing this expression by the initial volume V_0 gives

$$\lambda_V = \frac{V}{V_0} = \frac{\pi R_0^2 H_0 \lambda_L \lambda_R^2 (\kappa R / 4 + 1)}{\pi R_0^2 H_0} = \lambda_L \lambda_R^2 \left(\frac{\kappa R}{4} + 1 \right)$$ (4.20)

It is seen that a curvature κ equal to zero, which corresponds to a cylindrical shape of the sample, gives the same expression as that of Equation (4.15). A further observation is that the final expression is independent of a length scale. This method is hereafter referred to as the "parabolic method".

The performance of this method is illustrated by applying it to a uniaxial tension test of a M16 steel bolt of grade 8.8. Since steel and other metals normally are assumed to be isochoric during plastic deformation, the bolt is well suited as a benchmark for the correction. A snapshot of the bolt with data gathered by DIC and edge tracing is shown in Figure 4.5, where the bolt is depicted in its ultimate state. Clearly, a pronounced neck is present. The DIC algorithm described in Chapter 2 gives λ_L and λ_R while the edge tracing algorithm described in Chapter 3 gives κ and R. It is now possible to compute the local volumetric strain with both the cylinder and the parabolic method, as given by Equations (4.15) and (4.20) respectively.
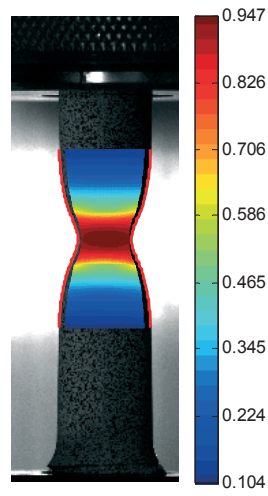
Figure 4.5: DIC and edge tracing data from a uniaxial tension test of a steel bolt, shown with a color map of longitudinal true strain.

The evolution of the neck is well captured by plotting the curvature of the neck versus local longitudinal strain, as shown in Figure 4.6. The curvature can be seen to be practically zero up to a strain of about 0.1, after which it increases almost linearly with the longitudinal strain.
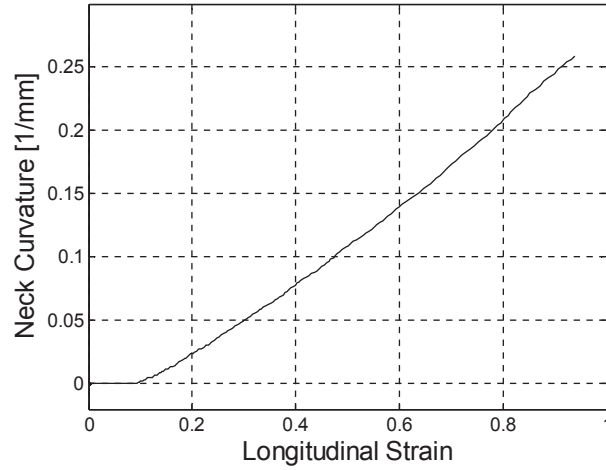
Figure 4.6: Neck curvature vs. longitudinal strain for uniaxial tension test of a steel bolt.

The volumetric strain calculated with the two methods is shown in Figure 4.7, where volumetric strain is taken as the logarithm of the volumetric stretch, i.e. $\varepsilon_V = \ln(\lambda_V)$. As expected, the methods produce identical results before necking occurs at $\varepsilon_L \approx 0.1$, but then rapidly diverge. It is clearly seen that the results obtained with the parabolic method is much closer to what one would expect for a steel sample in tension, never resulting in negative volumetric strain and ending on a positive, yet moderate, volumetric strain of 0.021. The measured positive volumetric strain could be related to void growth in the material. On the other hand, it is highly unlikely that the steel has a negative volumetric strain while subjected to positive hydrostatic stress, as suggested by the cylinder method. Assuming there is zero change in volume, the volumetric stretch from the parabolic method has a maximum absolute error of 2.1%, while the standard cylinder method has a maximum absolute error of 16%.
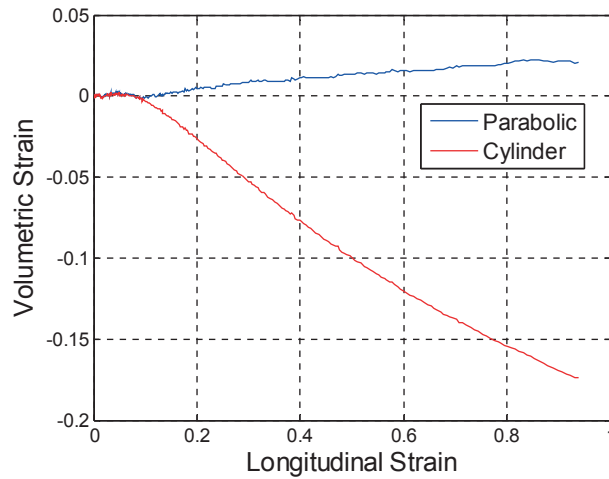
Figure 4.7: Volumetric strain vs. longitudinal strain for uniaxial tension test of steel bolt, calculated with the parabolic (blue) and cylinder (red) method.

This model for the variation in longitudinal strain through the cross section then predicts that a general straight section method, as with the cylinder method, will always under-predict volumetric strain in a neck. Furthermore it can be extrapolated that this effect will vary with the geometrical measurements of the cross section, where a wide and thin rectangular cross section will produce smaller error compared to a square cross section. This might indicate that the negative volumetric strain reported for glassy polymers in tension by some authors [25-28] might be an artifact.

4.4 Representative Stress

In principle, there are two fundamentally different strategies for extracting stress response from a uniaxial tension test. The first would be to not correct the stress for any varying parameters such as stress triaxiality, strain rate and temperature. In this case, the reported stress measurement from a test could be simple engineering stress or true stress. The problem with this approach is that the reported stress is ill-suited for comparison with other tests if the parameters affecting stress differ. The other strategy is then to try to calculate a stress that is independent of varying affecting parameters. In this section the effects of triaxiality, strain rate and temperature will be discussed.

The average true stress in the longitudinal direction is easily calculated as

$$\sigma_L = \frac{F}{A} = \frac{F}{\pi R^2}$$ (4.21)

where F is the force measured by the test machine. This stress will however not necessarily represent the equivalent stress in a uniaxial loading scenario when necking occurs because two transverse normal stress components also are present. The stress triaxiality correction of Bridgman defines the equivalent Mises stress σ_M as

$$\sigma_M = \frac{\sigma_L}{\left(1 + \dfrac{2}{\kappa R}\right)\ln\left(1 + \dfrac{R\kappa}{2}\right)}$$ (4.22)

where R is the current radius of the sample and κ is the curvature of the neck. The Bridgman correction assumes a material that yields according to the Mises yield criterion, and hence that yielding in the material is independent of hydrostatic pressure. Further, it presumes that all elements in the center section deform uniformly, resulting in the same yield stress across the center section [29]. Neither of these assumptions are necessarily correct for polymers, but the correction does give some indication of the difference between equivalent and longitudinal stress. As an example and a reference, Figure 4.8 shows the Bridgman correction factor, defined as the ratio σ_M / σ_L, as function of curvature for three different constant radii R. The selected range of radii and curvature covers the cases occurring in the tests, indicating that the uniaxial stress σ_L overestimates the equivalent stress σ_M with a factor not larger than about 1.1. For comparison, the overestimation factor is equal to 1.4 for the steel bolt shown in the previous section. The Bridgman correction is hence of less importance for polymers than for ductile steel materials, and can be selectively applied when the geometry of the neck calls for it. The true stress in the longitudinal direction may then be assumed to be equal to the Mises stress within a relatively small margin of error.
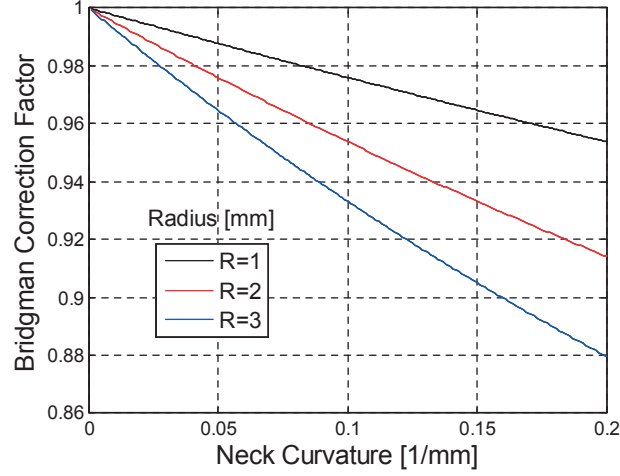
Figure 4.8: Bridgman reduction of longitudinal stress vs. curvature for three different, constant radii.

The second modification to the stress comes from the fact that the tests have been performed with a constant cross-head velocity, which in general does not produce a constant local strain rate. This can be accounted for by assuming how the material reacts to a change in strain rate. An additive formulation is adopted, decomposing the Mises stress into one rate-insensitive and one rate-sensitive term as

$$\sigma_M = \sigma_0(p) + \sigma_v(\dot{p}) = \sigma_0(p) + C \ln \frac{\dot{p}}{\dot{p}_0} \qquad (4.23)$$

where C is the plastic viscosity modulus and $\dot{p}_0$ is a reference plastic strain rate. The difference in Mises stress at a certain plastic strain for two tests k and l performed with different plastic strain rates $\dot{p}^k$ and $\dot{p}^l$, can be written as

$$\sigma_M^k - \sigma_M^l = \sigma_0 + \sigma_v(\dot{p}^k) - \left(\sigma_0 + \sigma_v(\dot{p}^l)\right) = \sigma_v(\dot{p}^k) - \sigma_v(\dot{p}^l) \qquad (4.24)$$

Inserting the expression for σ_v from Equation (4.23) into Equation (4.24) gives

$$\sigma_M^k - \sigma_M^l = C_{kl}\left(\ln \frac{\dot{p}^k}{\dot{p}_0} - \ln \frac{\dot{p}^l}{\dot{p}_0}\right) = C_{kl} \ln \frac{\dot{p}^k}{\dot{p}^l} \qquad (4.25)$$

Equation (4.25) can be solved for C_{kl}, giving

$$C_{kl} = \frac{\sigma_M^k - \sigma_M^l}{\ln(\dot{p}^k / \dot{p}^l)} \qquad (4.26)$$

where C_{kl} is identical to C_{lk}, i.e. $C_{kl} = C_{lk} = C$. With C established, the strain-rate insensitive part $\sigma_0(p)$ at a constant strain rate $\dot{p}_0$ can be expressed as

$$\sigma_0(p, \dot{p}_0) = \sigma_M(p, \dot{p}) - C \ln \frac{\dot{p}}{\dot{p}_0} \qquad (4.27)$$

This methodology may further be extended to include the effect of temperature change. Equation (4.23) is expanded to account for temperature sensitivity as follows

$$\sigma_M = \sigma_0(p)\theta(T) + \sigma_v(\dot{p}) = \sigma_0(p)\left(1 - \left(\frac{T - T_R}{T_M - T_R}\right)^m\right) + C \ln \frac{\dot{p}}{\dot{p}_0} \quad (4.28)$$

where $\theta(T)$ is a factor that modifies the rate-insensitive stress σ_0 as a function of current temperature T. T_R is the reference temperature, T_M is the melting temperature of the material and m is a material parameter governing the temperature sensitivity of the material. It should be noted that the viscous stress σ_v is then assumed to be independent of temperature. This is a simplification since it is normally assumed that viscosity increases with temperature [30-32]. With this expression it is then possible to express the stress at the reference temperature T_R as

$$\sigma_{T_R}(p, \dot{p}) = \sigma_0(p) + \sigma_v(\dot{p}) = \frac{\sigma_M(p, \dot{p})}{\theta(T)} + \sigma_v(\dot{p})\left(1 - \frac{1}{\theta(T)}\right) \quad (4.29)$$

The stress σ_0 at a prescribed and constant strain rate and temperature is then expressed as

$$\sigma_0(p, \dot{p}_0, T_R) = \frac{\sigma_M - C \ln \dfrac{\dot{p}}{\dot{p}_0}}{\left(1 - \left(\dfrac{T - T_R}{T_M - T_R}\right)^m\right)} \qquad (4.30)$$

It might also be of interest to calculate the effective stress in a cross-section with voids. This can be done if it is assumed that the increase in volume is caused by the formation of uniformly distributed cavities in the material. Supposing that the material is isochoric, i.e. the macroscopic change of volume is solely related to void growth, it follows that

$$\frac{\hat{A}}{A} = \frac{\hat{V}}{V} = \frac{1}{\lambda_V} \tag{4.31}$$

where A and V represent local cross sectional area and volume, and $\hat{A}$ and $\hat{V}$ represent effective material area and effective material volume [33]. The effective stress $\hat{\sigma}$ can then be calculated as

$$\hat{\sigma} = \sigma_M \lambda_V \tag{4.32}$$

where σ_M represents stress based on total cross sectional area. Effective stress should however be used with caution, as can be illustrated by calculating the effective stress from the true stress. The effective true stress $\hat{\sigma}$ is then equal to

$$\hat{\sigma} = \sigma \lambda_V = \frac{F}{A} \lambda_V = \frac{F}{A_0 \lambda_R^2} \lambda_L \lambda_R^2 = s \lambda_L \tag{4.33}$$

where s is the engineering stress. Effective stress may hence contribute to conceal bad radial deformation measurements, since they are not involved in the calculation.

4.5 Thermal data

In order for the thermal data to be used in conjunction with the DIC data, the images from the thermal camera have to be related to the images from the digital camera. This is necessary since the two cameras are pointed towards opposite faces, have different aspect ratios and resolution, are centered differently and have different amounts of zoom. The first step is then to left/right mirror the thermal images. It is then assumed that the difference in the images can be corrected by translating, rotating and stretching all the thermal images taken for a test by the same amounts. This can be expressed as the vector transformation

$$\mathbf{Q}(\theta)\tilde{\mathbf{v}}\alpha + \mathbf{b} = \mathbf{v} \qquad (4.34)$$

where $\mathbf{Q}(\theta)$ is the rotation matrix given in Equation (4.4), $\tilde{\mathbf{v}}$ and $\mathbf{v}$ are position vectors in the thermal and the digital images, respectively, addressing the same physical points, α is the stretch factor and $\mathbf{b}$ denotes the translation of the rotated and stretched thermal image. Equation (4.34) has four unknowns, i.e. θ, α, b_x and b_y. Applying a nonlinear least square fit procedure, an optimized solution is available for three or more sets of vectors $\tilde{\mathbf{v}}^i$ and $\mathbf{v}^i$, where the superscript i refers to a physical point in the images. The first step is to re-define the left-hand side of Equation (4.34) in component form as

$$f^i = \cos(\theta)\tilde{v}^i_x\alpha + \sin(\theta)\tilde{v}^i_y\alpha + b_x \qquad (4.35)$$

and

$$g^i = -\sin(\theta)\tilde{v}^i_x\alpha + \cos(\theta)\tilde{v}^i_y\alpha + b_y \qquad (4.36)$$

where f^i and g^i are two scalar functions of the four unknowns θ, α, b_x and b_y. A first order Taylor expansion of f^i and g^i gives

$$f^i_{k+1} \approx f^i_k + \begin{bmatrix} \dfrac{\partial f^i_k}{\partial \theta} & \dfrac{\partial f^i_k}{\partial \alpha} & \dfrac{\partial f^i_k}{\partial b_x} & \dfrac{\partial f^i_k}{\partial b_y} \end{bmatrix} \begin{bmatrix} \Delta\theta \\ \Delta\alpha \\ \Delta b_x \\ \Delta b_y \end{bmatrix} = f^i_k + \partial\hat{\mathbf{f}}^i_k\Delta\mathbf{\gamma} \qquad (4.37)$$

and

$$g^i_{k+1} \approx g^i_k + \begin{bmatrix} \dfrac{\partial g^i_k}{\partial \theta} & \dfrac{\partial g^i_k}{\partial \alpha} & \dfrac{\partial g^i_k}{\partial b_x} & \dfrac{\partial g^i_k}{\partial b_y} \end{bmatrix} \begin{bmatrix} \Delta\theta \\ \Delta\alpha \\ \Delta b_x \\ \Delta b_y \end{bmatrix} = g^i_k + \partial\hat{\mathbf{g}}^i_k\Delta\mathbf{\gamma} \qquad (4.38)$$

where the increments of the unknown quantities θ, α, b_x and b_y are gathered in the vector $\Delta\mathbf{\gamma}$. The subscripts k and $(k+1)$ refer respectively to the present and next increment. It is

then possible to write Equations (4.37) and (4.38) as one system of equations for $i = [1, N]$, where the number N of vectors $\tilde{\mathbf{v}}$ and $\mathbf{v}$ is larger than two

$$\begin{bmatrix} \mathbf{f}_{k+1} \\ \mathbf{g}_{k+1} \end{bmatrix} \approx \begin{bmatrix} \mathbf{f}_k \\ \mathbf{g}_k \end{bmatrix} + \begin{bmatrix} \partial \mathbf{F}_k \\ \partial \mathbf{G}_k \end{bmatrix} \Delta \gamma = \begin{bmatrix} \mathbf{v}_x \\ \mathbf{v}_y \end{bmatrix} \qquad (4.39)$$

where $\mathbf{f}$ and $\mathbf{g}$ represent vectors, each with N elements consisting of respectively f^i and g^i, and $\partial \mathbf{F}_k$ and $\partial \mathbf{G}_k$ are matrixes with N rows, each comprised of $\partial \hat{\mathbf{f}}_k^i$ and $\partial \hat{\mathbf{g}}_k^i$ respectively. The vectors $\mathbf{v}_x$ and $\mathbf{v}_y$ contain the x and y components of the N vectors $\mathbf{v}$. The system is now iteratively optimized by solving the equation

$$\Delta \gamma = \left(\begin{bmatrix} \partial \mathbf{F}_k \\ \partial \mathbf{G}_k \end{bmatrix}^T \begin{bmatrix} \partial \mathbf{F}_k \\ \partial \mathbf{G}_k \end{bmatrix} \right)^{-1} \begin{bmatrix} \partial \mathbf{F}_k \\ \partial \mathbf{G}_k \end{bmatrix}^T \left(\begin{bmatrix} \mathbf{v}_x \\ \mathbf{v}_y \end{bmatrix} - \begin{bmatrix} \mathbf{f}_k \\ \mathbf{g}_k \end{bmatrix} \right) \qquad (4.40)$$

and updating the values of γ.

The manual process of defining similar points is shown in Figure 4.9, where six corresponding points have been chosen in the DIC and a left/right mirrored thermal image. As can be seen from the thermal image, it is not trivial to identify features of the sample, which is why more points than strictly necessary are selected.

DIC image   Thermal image
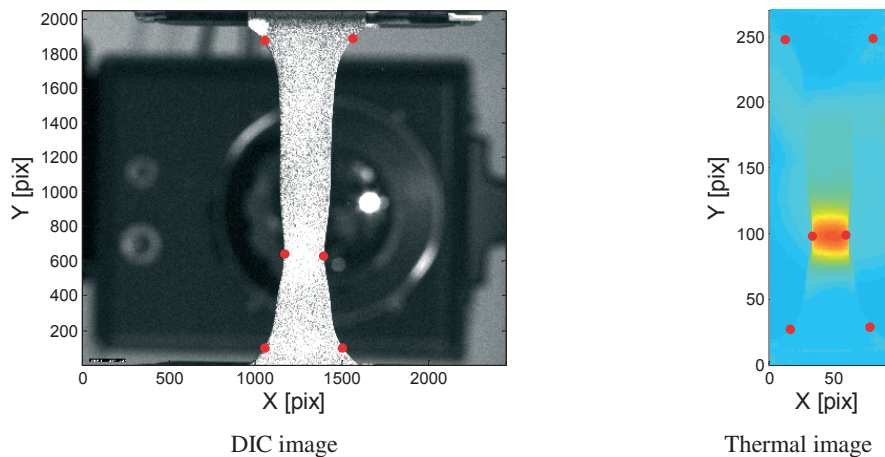
Figure 4.9: DIC and thermal image correlation by manual point identification.

For the sample shown in Figure 4.9, the iteration process of Equation (4.40) gives the correlation values of Table 4.1.

Table 4.1: Correlation values for test in Figure 4.9

θ [rad]	α	b_x [pix]	b_y [pix]
–0.0195	8.1065	892.86	–132.19

It can be seen from the table that the images are rotated about 1 degree relative to each other, and the α factor tells us that the DIC image has approximately an 8 times higher resolution in each direction compared to the thermal camera.

By applying Equation (4.34) with the parameters in Table 4.1, it is then possible to superimpose the thermal image onto the DIC image. This is shown in Figure 4.10, where two semitransparent thermal images are placed over two black and white DIC images. As can be seen, the correlation model and solution seems to work well, matching up images taken at different points of the deformation history using the same set of parameters.

| Reference pictures | Necked specimen |
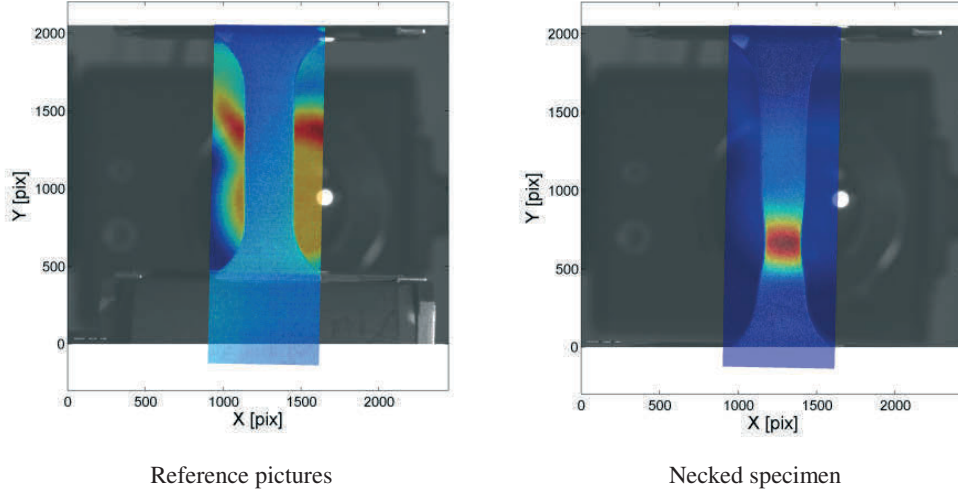
Figure 4.10: Merged DIC and thermal image, where a semi-transparent colored thermal image is superimposed on a gray scale digital image.

In order to correlate the temperature measured with digital image thermography (DIT) with the stress and strain obtained with DIC, it is necessary to have a model for adiabatic heat generation. For a material point undergoing plastic deformation it is assumed that a fraction of the plastic work is converted to heat. This fraction is referred to as the Taylor-Quinney coefficient χ [34]. For a simple case where there is no heat transfer, i.e. adiabatic conditions, the increase in temperature T at a material point can be expressed as

$$dT = \frac{\chi}{\rho C_p} \sigma_{eq} dp \qquad (4.41)$$

where ρ_M is the material density and C_p is the specific heat capacity of the material. The Taylor-Quinney coefficient is in general not constant. In order to estimate χ as a function of equivalent plastic strain, a rate form of Equation (4.41) is adopted

$$\chi(p) = \frac{\rho C_p \dot{T}(p)}{\sigma_{eq}(p) \dot{p}(p)} \qquad (4.42)$$

67

where it is assumed that ρ and C_p are constant. A change in the Taylor-Quinney coefficient can then signify that the ratio between stored and dissipated energy has changed.

5 Uniaxial Tension Tests

This chapter presents four series of tests involving two materials a semicrystalline HDPE and an amorphous PVC and two designs of the tension test sample. It also includes an analysis of the test results in accordance with the methodology outlined in the previous chapter. The first set that was tested used a traditional dog-bone geometry, while the second set took advantage of a new and improved geometry. This improved sample geometry was designed for more accurate DIC measurements at large strains. The time difference between the two series was about two years. The material was acquired about one year before the first test series.

5.1 Experimental Setup and Material Test Samples

5.1.1 Rectangular Test Samples with Thermal Monitoring

HDPE and PVC were tested in uniaxial tension at room temperature (23 °C). For each material a total of six samples were tested at six different yet constant crosshead velocities. The velocities were equivalent to the six nominal strain rates $10^{-3.5}\,\text{s}^{-1}$, $10^{-3.0}\,\text{s}^{-1}$, $10^{-2.5}\,\text{s}^{-1}$, $10^{-2.0}\,\text{s}^{-1}$, $10^{-1.5}\,\text{s}^{-1}$ and $10^{-1.0}\,\text{s}^{-1}$, calculated from the initial gauge length of the samples (33 mm). The strain rates were chosen so as to span the range from isothermal conditions up to close to adiabatic conditions. The tests were monitored by both an optical and a thermal camera.

The sample geometry is shown in Figure 5.1. This dog-bone shaped specimen was used for both materials, cut from 10 mm thick extruded plates and machined down to a constant thickness of 5 mm by removing 2.5 mm of thickness at both surfaces.
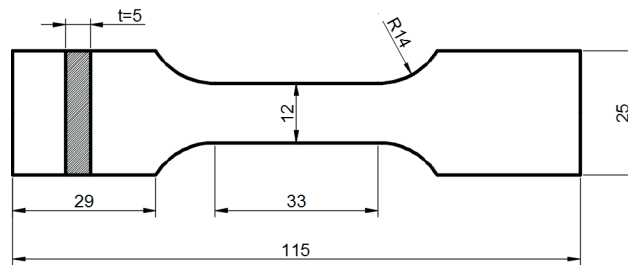
Figure 5.1: Rectangular uniaxial tension test sample for HDPE and PVC [mm].

The tension tests were carried out in an electronic screw-driven Zwick Z030 universal test machine. Data collection consisted of force and displacement measurements from the machine, images taken with a single 5 Mpix, 8 bit, CCD Nikon digital camera, and thermal images taken with a FLIR SC7500MB high-speed thermal camera. The sampling frequency was adapted to the velocity of the test at hand. The number of images taken per test varied between 100 and 300, where the faster tests had fewer images due to capturing speed limitations of the CCD camera system. The samples were airbrushed on one side to create a speckled pattern for DIC, with the digital camera facing this side. The thermal camera was facing the opposite, unpainted side.

5.1.2 Circular Test Samples

The second set of tests was performed on samples with circular cross section for the HDPE and PVC materials as shown in Figure 5.2 and Figure 5.3, respectively. The geometrical measures of the samples were custom defined to enable DIC measurements while the whole gauge length of the sample undergoes cold drawing. The short gauge length serves to maximize the resolution from the stationary monitoring camera while keeping the sample within the camera frame throughout the test. The shoulders have a small diameter of 6 mm to facilitate a quick increase of area when the neck reaches the shoulders. This rapid growth in cross sectional area at the shoulders increases the total force applied to the sample, resulting in strains and stresses in the gauge section that exceed those observed during cold drawing. The short gauge length does however increase the stress triaxiality, which is why the PVC sample has a longer gauge part. This is reasonable since PVC is less ductile that HDPE, so the deformed HDPE geometry will be longer than the deformed PVC geometry. The PVC

70

material is also assumed to be more sensitive to triaxiality [17], compared to the HDPE material.
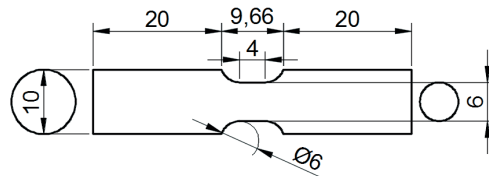
Figure 5.2: Circular uniaxial tension test sample for HDPE [mm].
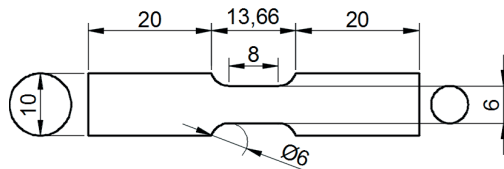

Figure 5.3: Circular uniaxial tension test sample for PVC [mm].

HDPE and PVC were tested in uniaxial tension at room temperature (23 °C). For each material a total of six samples were tested at three different crosshead velocities, i.e., there were two replicates at each velocity. The three speeds were chosen so as to be equivalent to the three nominal strain rates $10^{-2.5}\,\mathrm{s}^{-1}$, $10^{-2.0}\,\mathrm{s}^{-1}$ and $10^{-1.5}\,\mathrm{s}^{-1}$, calculated from the initial gauge length of the samples (4 and 8 mm).

These tests were also performed in the electronic screw-driven Zwick Z030 universal test machine. Data collection consisted of force and displacement measurements from the machine and images taken with a single 5 Mpix, 8 bit, CCD digital camera, equipped with a macro lens. The camera was placed approximately 1m from the specimen, and took a minimum of 500 images per test. The experimental setup is shown in Figure 5.4. These tests were not instrumented with the thermal camera.
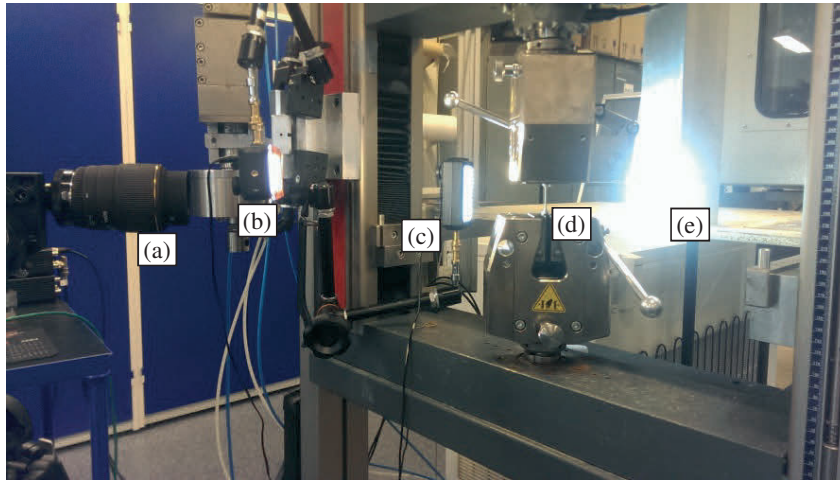
Figure 5.4: Test setup: (a) camera with macro lens, (b) sample lighting, (c) background lighting, (d) sample, (e) diffuse reflective background.

Lighting was set up so as to create a homogenous colored background. This was done in order to facilitate the identification of the boundaries of the specimens in the pictures by using the edge tracing algorithm described in Chapter 3. The background color was created by placing a piece of roughly polished metal about 30 cm behind the sample (Figure 5.4 (e)), and using a dedicated lamp to illuminate the metal (Figure 5.4 (c)). This resulted in a white-saturated background which is out of focus, creating excellent conditions for edge tracing, as demonstrated by the picture in Figure 5.5.

Figure 5.5: Representative image from tension test performed on a circular HDPE sample.

Undeformed samples and samples tested to failure were studied with a scanning electron microscope (SEM) after the test. The area of interest was a plane oriented along the length of the sample, dividing the sample in two, as seen in Figure 5.6. It was hence necessary to split the samples. This was done by cooling the samples in liquid nitrogen for 5 minutes, and then immediately cleaving the samples using a sharp knife blade and a hammer. The idea is to trigger a controlled brittle fracture, and hence avoiding tool marks. A similar method was described and used by Ognedal et al. [35]. As SEM requires conductive surfaces, the samples were coated with gold via a vaporization process. The intention with the SEM investigation was to see whether a macroscopic change of volume was related to void growth at the microscale.
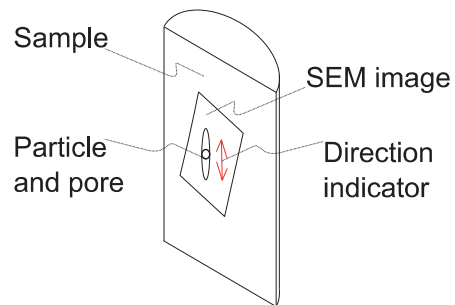
Figure 5.6: Cutting and image plane for SEM images from circular tensions samples.

5.2 Thermally Monitored rectangular HDPE samples

5.2.1 Raw Data

Figure 5.7 shows the force-displacement curves for the rectangular HDPE samples tested at five different nominal strain rates. These curves are based on the force and displacement data collected by the test machine during each test. Considering the two curves obtained at the lowest strain rates of $10^{-3.5}\,\mathrm{s}^{-1}$ and $10^{-3.0}\,\mathrm{s}^{-1}$, the difference in force is almost constant during the entire deformation process. This observation suggests that an isothermal state is retained at these low speeds. At higher strain rates, the curves tend to cross each other, possibly indicating that adiabatic heating plays a significant role at these loading velocities.

74
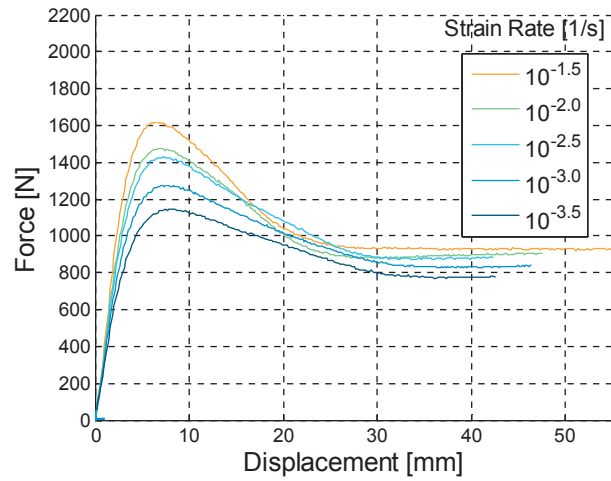
Figure 5.7: Force vs. displacement curves for rectangular HDPE samples tested at five different nominal strain rates.

Figure 5.8 shows an excerpt of the image data recorded of the test at the highest strain rate, i.e. $10^{-1.5}$ s^{-1}, where a partially transparent thermal image is superimposed on the digital pictures used for DIC, as described in Section 4.5. Since the normal photos define the coordinate system for the DIC analysis, it is possible to relate thermal and DIC data when the transformation between the two sets of pictures, see Section 4.5, is established. The right image in Figure 5.8, addressing the sample when the displacement is 30 mm, shows that there is a significant temperature increase of almost 30 °C in the gauge part.
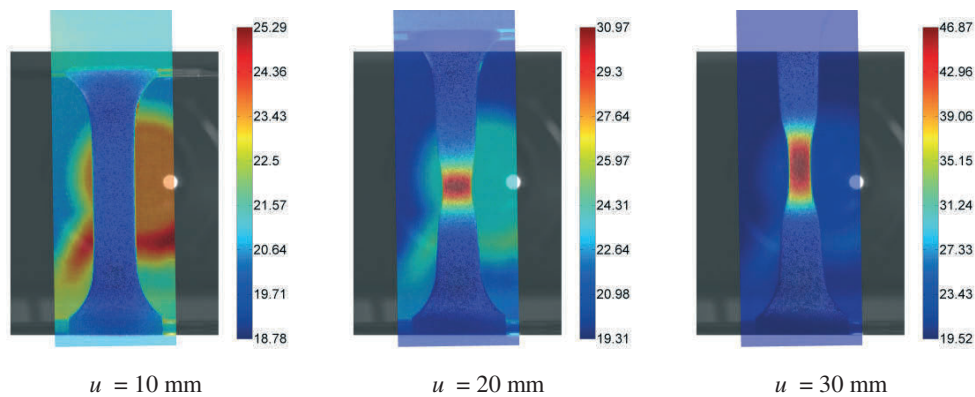
Figure 5.8: Merged photographic and thermal images for a rectangular HDPE sample stretched at a nominal strain rate of $10^{-1.5}$ s^{-1} shown at three different stages of displacement u. The color bars show temperature in degrees Celsius.

5.2.2 Stress-Strain and Thermal Response

Figure 5.9 shows the true stress vs. longitudinal logarithmic strain for the five tension tests, applying Equation (4.7) for the strain and Equation (4.21) for the calculation of the true stress. Stress and strain are calculated for the section of initial necking, as described in Sections 4.4 and 4.1. As suggested by the force-displacement curves, it can here be seen that the curves for the two lowest strain rates remain parallel to each other throughout the entire deformation process. This indicates that the speed of deformation is slow enough for the heat generated by plastic work to dissipate to the surroundings without producing any significant increase of temperature in the plastically deformed material. The faster tests do not follow this pattern, and it can be seen that the stress-strain curves for speeds from $10^{-2.0}$ s^{-1} and upwards cross the curves of lower speeds at a strain around 1.5. This again suggests that adiabatic heating is playing a role.

76
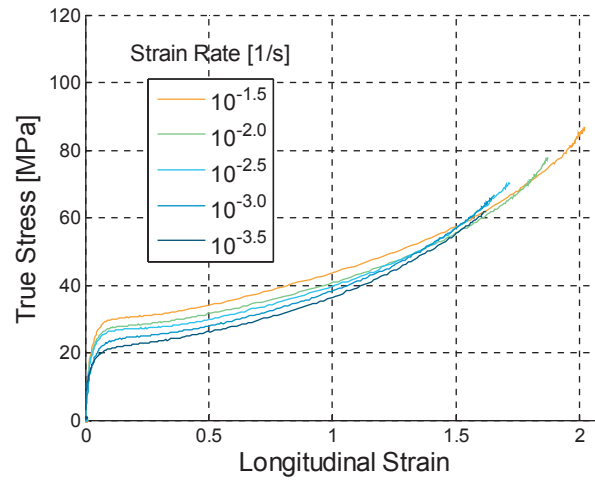
Figure 5.9: True stress vs. longitudinal strain curves for rectangular HDPE tension samples stretched at five different nominal strain rates.

With stress and the strains established, it is possible to calculate the elastic parameters of the material. Poisson's ratio and Young's modulus are calculated with Equations (4.10) and (4.11) respectively for a longitudinal strain level between 0.005 and 0.07. The evolution of the two parameters is shown in Figure 5.10. As can be seen, Poisson's ratio seems to be close to 0.5, with no apparent variation with strain rate. Young's modulus, on the other hand, clearly varies with both strain and strain rate.

Poisson's Ratio	Young's Modulus
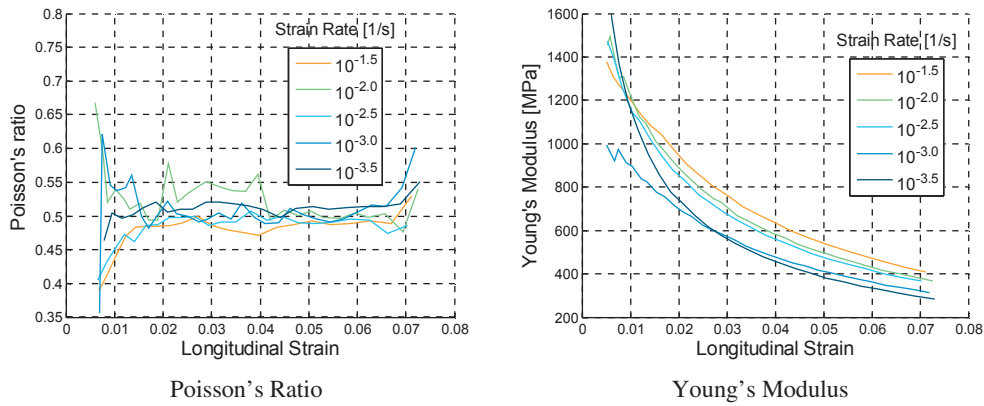
Figure 5.10: Elastic parameters for rectangular HDPE samples stretched at five different nominal strain rates.

The strain rate dependency of the measured Young's modulus can be quantified with Equation (4.14), giving elastic viscosity η as a relation involving the stiffness and strain rate in two tests with different velocity. The elastic viscosity as function of strain for the four fastest tests is shown in Figure 5.11. In all four cases, the slow test at a strain rate of $10^{-3.5}$ s^{-1} is selected as reference when using Equation (4.14). The data shows some spread, but in general it can be seen that a 10 times increase in strain rate increases the stiffness in the elastic domain with about 80 MPa.
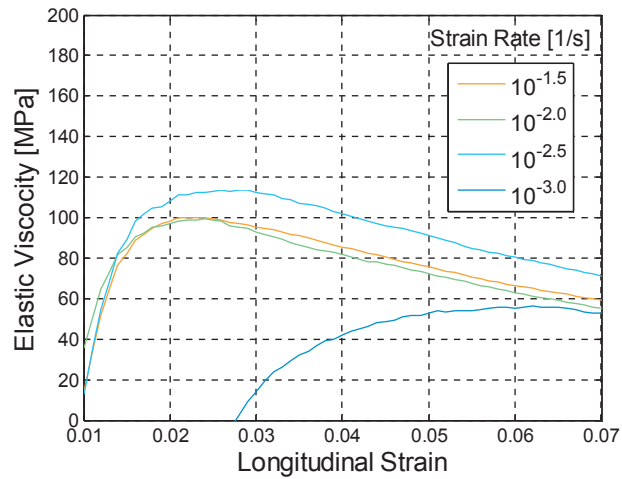
Figure 5.11: Elastic viscosity vs. longitudinal strain curves for rectangular HDPE tension samples stretched at four different nominal strain rates. Elastic viscosity is calculated relative to a fifth test stretched at a nominal strain rate equal to $10^{-3.5}\,\mathrm{s}^{-1}$.

The suspicion of heating in the two highest strain rates is further supported by the curves in Figure 5.12, showing temperature versus longitudinal strain for all tests. The temperature as well as the strain are measured in the neck. Here it can be seen that the temperature at the two fastest strain rates is significantly higher after a strain of approximately 1, compared to the three slowest tests. The maximum temperature of the fastest test is 47 °C. Indeed, Figure 5.12 shows that there also is a minor temperature increase of about 2 °C in the two slowest tests, but this does not seem to influence the stress-strain response. Another interesting feature, although not clearly visible in all five tests, is that there is a small decrease of approx. 1 °C in temperature during the initial elastic deformation, i.e. for strains below 0.05.
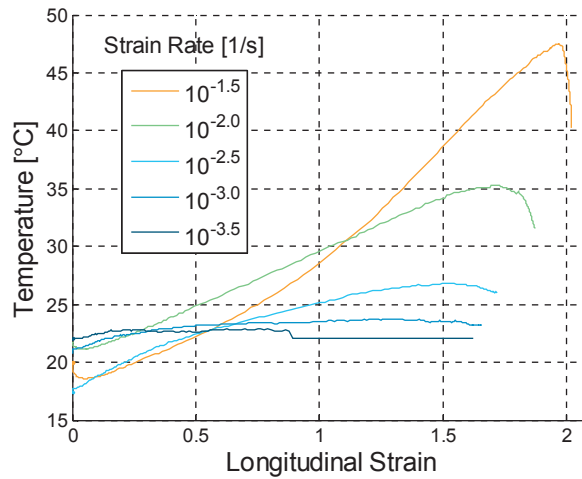
Figure 5.12: Temperature vs. strain response for rectangular HDPE tension samples stretched at five different nominal strain rates measured at the point of initial localization.

The local strain rate in the necked section can also be found for the tests, and will vary with respect to time and strain since the test machine operates at a constant cross head velocity. Figure 5.13 shows the curves describing plastic strain rate vs. plastic strain for the five tests. Plastic strain and plastic strain rate is calculated from Equations (4.8) and (4.9) with an assumed elastic modulus E=650 MPa. As seen from the figure, the strain rates vary within approximately half of a decade of their nominal values. A more surprising feature is that the shift observed between the tests is close to constant, as an intuitive expectation might be that thermal softening would increase the local strain rate relative to slower tests.
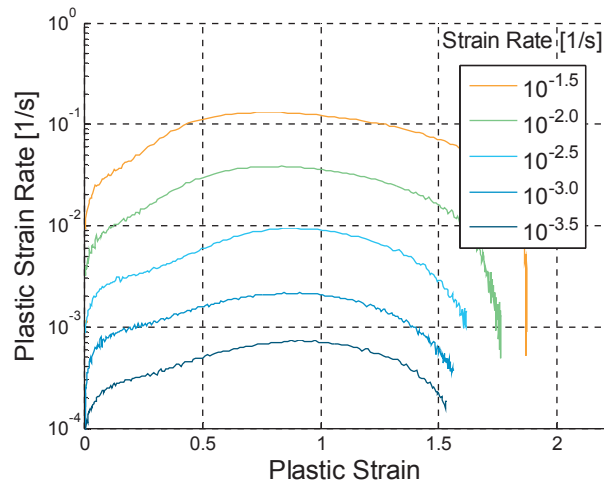
Figure 5.13: Plastic strain rate vs. plastic strain for rectangular HDPE tension samples stretched at five different nominal strain rates measured at the point of initial localization.

By combining the data from Figure 5.9 and Figure 5.13, the plastic viscosity parameter C can be found as a function of plastic strain from Equation (4.26). This is shown in Figure 5.14, where the slowest test with a nominal strain rate of $10^{-3.5}\,\text{s}^{-1}$ is used as a reference. Plastic viscosity is calculated for plastic strain between 0.03 and 0.6 to minimize uncertainties related to the choice of Young's modulus and heat influence. As can be seen from the figure, there is a clear trend of reduction in the parameter with larger strains, for further use however, C is assumed constant and equal to 1.8 MPa.
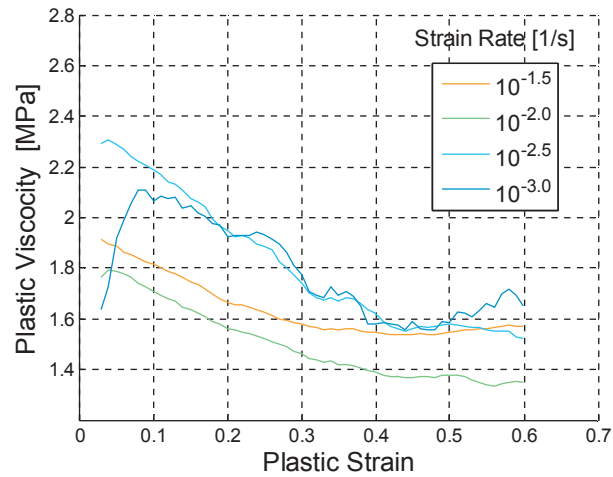
Figure 5.14: Plastic viscosity vs. plastic strain for rectangular HDPE tension samples stretched at four different nominal strain rates. Plastic viscosity is calculated relative to a fifth test stretched at a nominal strain rate equal to $10^{-3.5}\,\text{s}^{-1}$.

With C established, it is possible to normalize the stress-strain curves from Figure 5.9 to a constant strain rate by applying Equation (4.27). This is shown in Figure 5.15 where the response is normalized to a constant strain rate of $10^{-2.5}\,\text{s}^{-1}$. As seen from the figure, the curves collapse nicely up to a strain of about 1, after which the faster tests show less hardening. It will be shown subsequently that this scatter between the curves is likely to be caused by temperature softening.

82
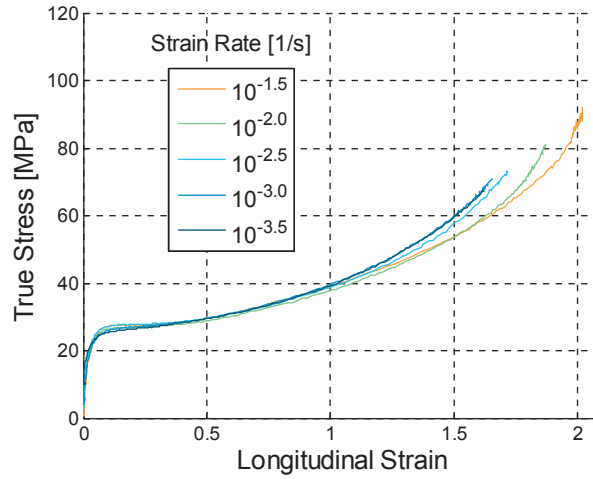
Figure 5.15: Strain rate normalized Stress vs. strain response for rectangular HDPE tension samples stretched at five different nominal strain rates, normalized to a constant strain rate of $10^{-2.5}$ s^{-1}.

Finally, the stress-strain data are normalized with respect to temperature by applying Equation (4.29). For this calculation, the room temperature was T_R = 22 °C, the melting temperature was set to T_M = 130 °C, which is within the normal limits for HDPE, and the value m = 1.1 was found to give good results for the temperature sensitivity. The resulting stress-strain curves after this normalization process are shown in Figure 5.16. It can now be seen that the curves do not intersect each other, and they are close to parallel.
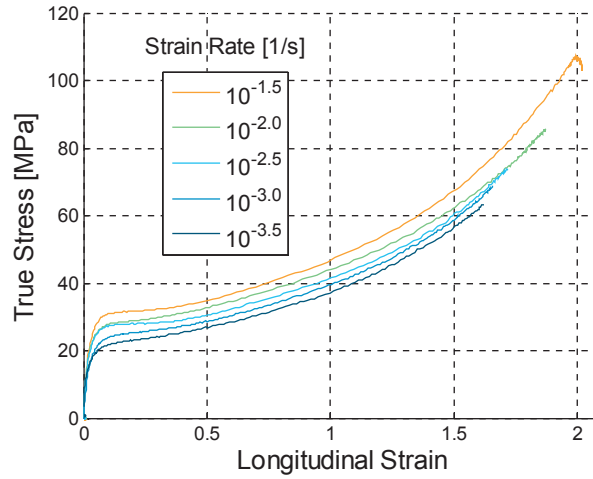
Figure 5.16: Temperature-normalized stress vs. strain response for rectangular HDPE tension samples stretched at five different nominal strain rates, normalized to a constant temperature of 22 °C.

With the parameters established for both strain rate sensitivity and temperature softening, it is possible to normalize the stress-strain curves with respect to both strain rate and temperature by applying Equation (4.30). This is shown in Figure 5.17, where the stress-strain curves are normalized to a constant strain rate of $10^{-2.5}$ s^{-1} and a constant temperature of 22 °C. As can be seen from the figure, the curves collapse pretty well into one master curve, indicating that the applied material model, see Equation (4.28) and parameters are well suited.
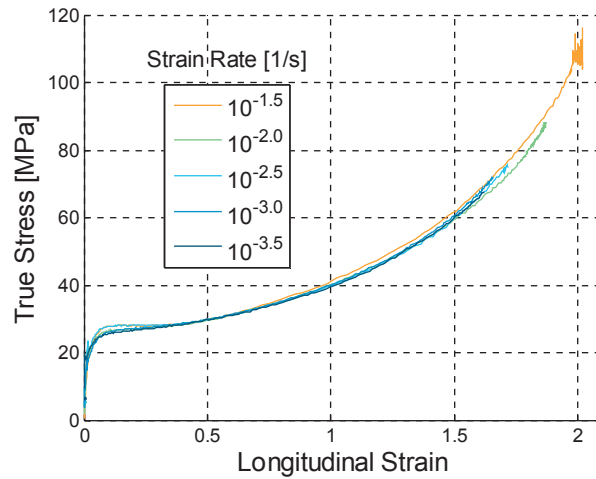
Figure 5.17: Temperature and strain rate normalized stress-strain response for rectangular HDPE tension tests stretched at five different nominal strain rates, normalized to a constant strain rate of $10^{-2.5}$ s^{-1} and a constant temperature of 22 °C.

It is also of interest to examine the relationship between the generated heat and plastic work with use of Equation (4.42). This is done for the fastest test with a nominal strain rate of $10^{-1.5}$ s^{-1}, where an assumption of no heat dissipation will be most correct. Figure 5.18 shows both the stress versus plastic strain curve and the evolution of the Taylor-Quinney coefficient versus plastic strain for this test. The material is assumed to have a constant density $\rho_M = 970$ kg/m^3 and a constant specific heat capacity $C_p = 2200$ J/kg K . The Taylor-Quinney coefficient starts at around 1 for small plastic strains. The coefficient then stabilizes at a level of 0.8 before decreasing rapidly when the plastic strain exceeds 1. The interesting part of this curve is the last half, which suggests that the part of the work converted to heat decreases significantly. This might be explained by the theory of network stretching, which assumes that the late stage exponential type hardening observed in uniaxial tension is an elastic process, and hence does not dissipate energy.
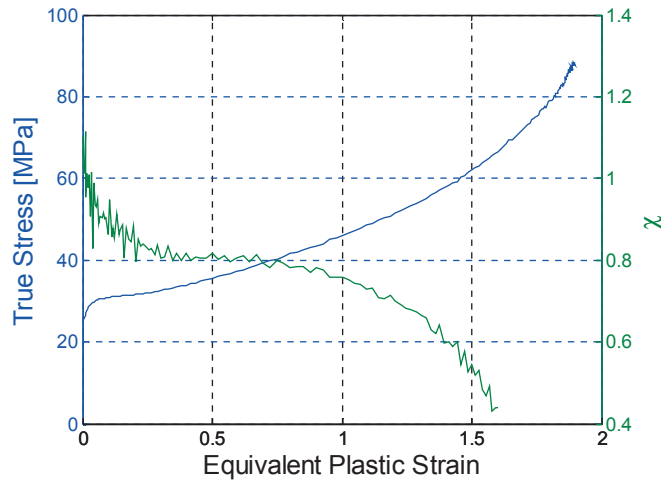
Figure 5.18: Stress vs. plastic strain and Taylor-Quinney coefficient vs. plastic strain for a rectangular HDPE tension test stretched at a nominal strain rate of $10^{-1.5}$ s^{-1}.

5.2.3 Volumetric Strain

Volumetric strain is calculated for the tests by using the somewhat simplified Equation (4.15). As the tests were instrumented with only one digital camera for subsequent DIC analyses, it is assumed that the width stretch is equal to the thickness stretch. This assumption relies on the material being isotropic as well as an absence of geometrical effects related to the dimensions of the cross section. As will be shown by the numerical simulations, see Chapter 7, the assumption seems to be correct, and the measured volumetric strain is representative for the considered section. The volume correction presented in Section 4.2 is not relevant, since it requires a circular cross section. Speculation by the same logic would however indicate that the combination of a small thickness of the sample relative to the width, and the small curvature of the main surface would produce only minor variations in length stretch through the thickness. A volumetric correction is hence of less importance.

The calculated volumetric strain is shown in Figure 5.19. The most striking feature is the apparent increase in volumetric strain with an increase in strain rate. It is also seen that volume growth does not set inn before a strain level of 0.5. It is worth remembering that the variation in volumetric strain between tests could also be related to temperature. This is

difficult to assess with this data set, but it is can be seen that the two lowest tests still exhibit a clear difference in volumetric strain level despite having similar temperatures, indicating that strain rate might be the primary variable. The proportionality of local strain rate between tests is also more consistent compared to the variation in temperature, as seen from Figure 5.13 and Figure 5.12. It might hence be speculated that the smooth and gradually increasing difference in volumetric strain reflects the proportionality in the strain rates.
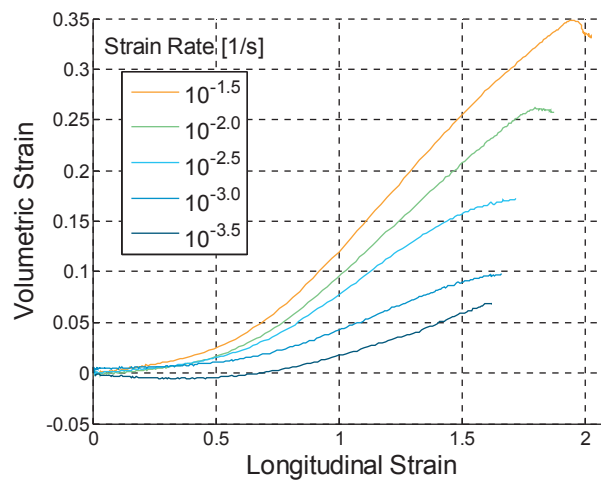

Figure 5.19: Volumetric strain vs. longitudinal strain for rectangular HDPE tension samples stretched at five different nominal strain rates.

5.3 Thermally Monitored Rectangular PVC Samples

5.3.1 Raw Data

Figure 5.20 shows the force-displacement curves for the rectangular PVC samples tested at six different nominal strain rates. Some of the trends are similar to the HDPE tests presented in the previous section, where a constant initial shift of the curves is followed by a relative decrease in strength for tests performed at higher strain rates compared to the slower tests. The softening is more pronounced for the PVC samples than in the case of HDPE. On the other hand, the initial elastic stiffness seems to be less rate dependent than for HDPE. Moreover, it can be seen that the two samples at the highest rate fail at a displacement of only

20 and 25 mm, which might indicate significant thermal softening. It should be noted that the test with a strain rate equal to $10^{-2.0}$ s^{-1} failed at a displacement of 48 mm. It is also here observed that the force-displacement curves of the two slowest tests only differ with a constant shift of stress level from the onset of yielding, indicating isothermal conditions. The two fastest tests also behave similarly, which suggests a similar amount of adiabatic heating in these two cases.
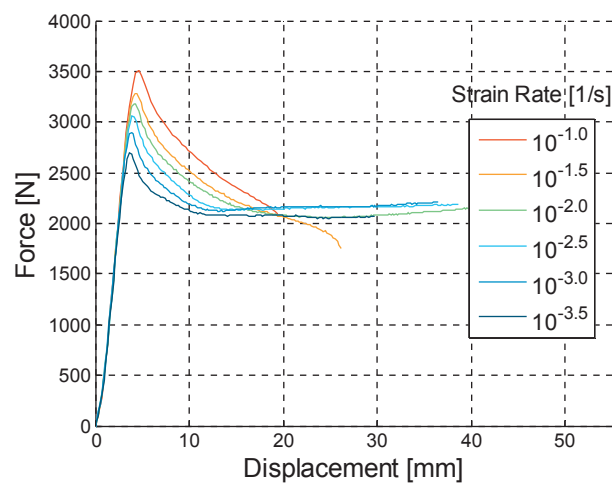
Figure 5.20: Force vs. displacement curves for rectangular PVC tension samples tested at six different nominal strain rates.

Figure 5.21 shows the merging of the DIC pictures and thermal data, where the thermal images have been adjusted to align with the images using the method described in Section 4.5. It can be seen that the temperature has increased with approximately 20 °C in the neck at a displacement of 16 mm. These hybrid images also give an indication of the temperature localization.

| $u = 8$ mm | $u = 12$ mm | $u = 16$ mm |
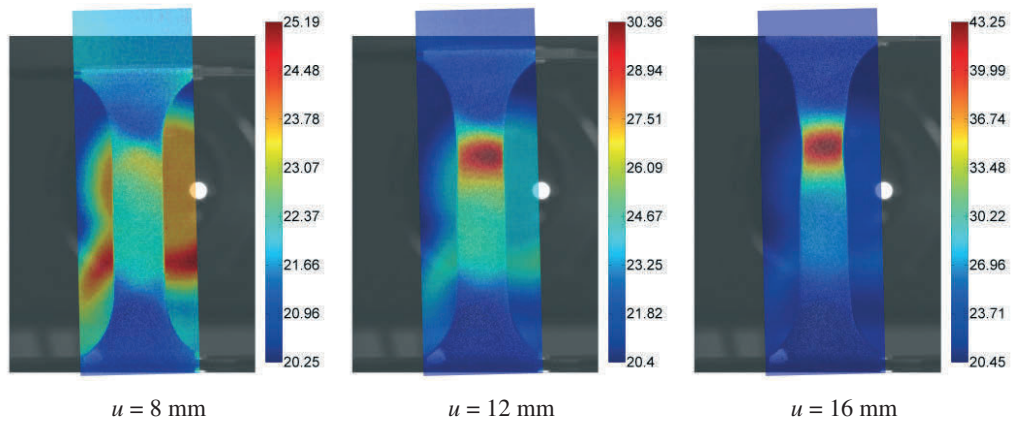
Figure 5.21: Merged photographic and thermal images for a rectangular PVC sample stretched at a nominal strain rate of $10^{-1.0}$ s^{-1} at three different stages of displacement u. The legend shows temperature in degrees Celsius.

5.3.2 Stress-Strain and Thermal Response

The stress-strain response, calculated with the force data shown in Figure 5.20 and DIC, is shown in Figure 5.22. As suggested by the force-displacement curves, the stress-strain data confirm that the response is isothermal at the two lowest rates as there is a constant shift between these two curves over the entire range of plastic deformation. The same type of constant shift is also seen for the two fastest tests up to a strain of approximately 0.6, indicating that these tests are fast enough to result in a similar temperature-strain profile. The curves for the two intermediate strain rates are then reasonable to characterize as transitional in terms of temperature.
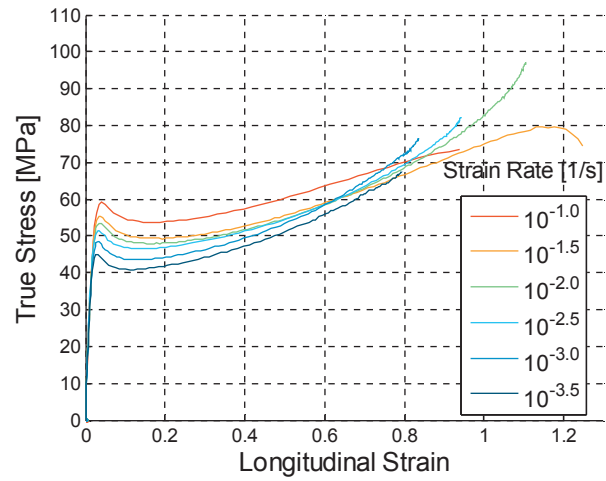
**Figure 5.22: Stress vs. strain response for rectangular PVC tension samples stretched at six different nominal strain rates.**

The elastic parameters ν and E can now be identified from Equations (4.10) and (4.11), and are shown in Figure 5.23. As for HDPE, Poisson's ratio of PVC does not seem to be dependent on strain rate, while the elastic stiffness has a more pronounced strain rate dependency.

(a) Poisson's Ratio   (b) Young's Modulus
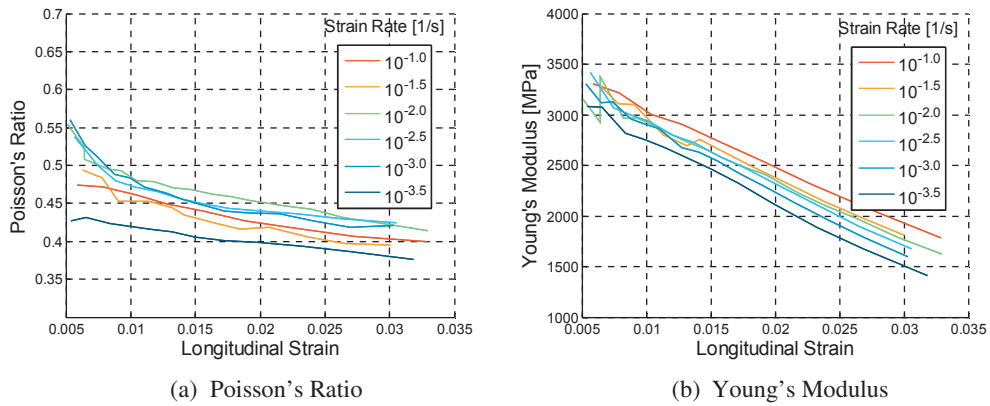
Figure 5.23: Elastic parameters of rectangular PVC tension samples stretched at six different nominal strain rates.

Again, the viscous effect on the elastic stiffness can be characterized by use of Equation (4.14). The viscosities of the samples tested at the five highest speeds are calculated from their stiffness and strain-rate relations to the slow test at $10^{-3.5}$ s^{-1}, and is shown in Figure 5.24. It can then be seen from the figure that a ten times increase in strain rate results in an increase in elastic stiffness of about 100 - 300 MPa.
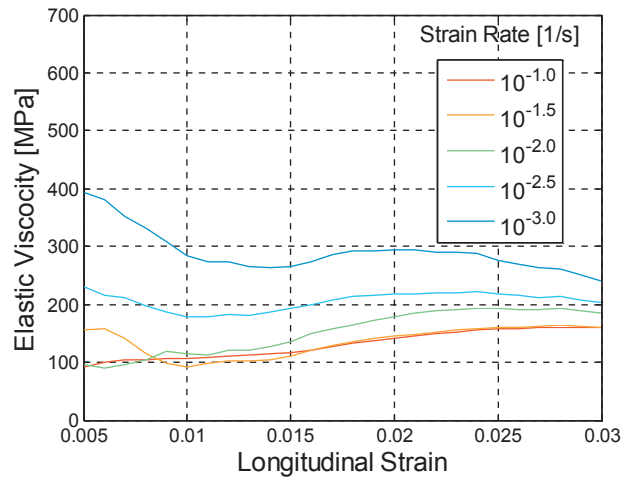
Figure 5.24: Elastic viscosity of rectangular PVC tension samples stretched at five different nominal strain rates. Elastic viscosity is calculated relative to a sixth test stretched at a nominal strain rate equal to $10^{-3.5}$ s^{-1}.

The suspicion of thermal involvement suggested by the stress-strain curves is further confirmed by looking at the temperature-strain curves, shown in Figure 5.25. Here it can be seen that the rise in temperature with strain is equal for the two fastest tests, while the temperature does not exceed 28°C in the two slowest tests. Again it can be seen that the temperature for the tests performed at the intermediate speeds has a transitional temperature profile, placing them somewhere in-between room temperature and maximum adiabatic temperature.
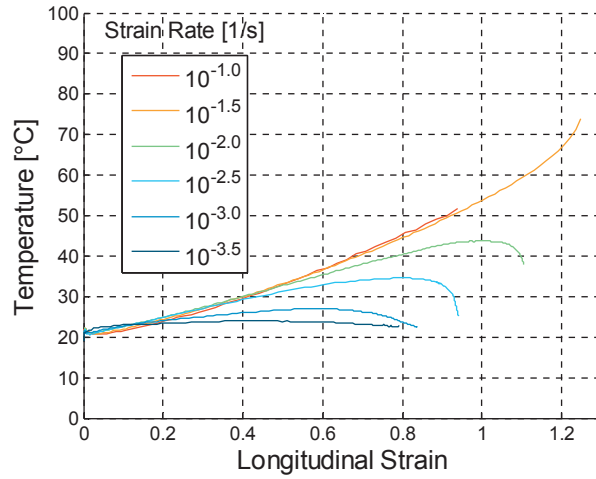
Figure 5.25: Temperature vs. strain response for rectangular PVC tension samples stretched at six different nominal strain rates.

The local plastic strain rate in the neck is shown as a function of plastic strain in Figure 5.26. The calculations were done by assuming an elastic stiffness of E=1700 MPa. It might be noted that the strain rate stabilizes at a certain level for the two faster tests, while for the tests performed at lower speeds, the strain rate reaches a peak and then decreases. This is a result of the temperature softening in the two fastest tests, which leads to a continued localization rather than a neck propagation, resulting in an accelerated failure process in the section of initial localization.
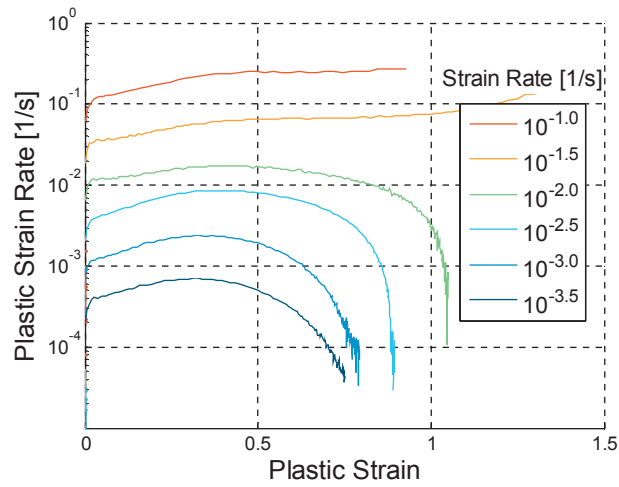
Figure 5.26: Plastic strain rate vs. longitudinal plastic strain response for rectangular PVC tension samples stretched at six different nominal strain rates.

As with the HDPE tests, the plastic strain rate sensitivity is investigated by calculating the plastic viscosity parameter C from Equation (4.26) and plotting it as a function of plastic strain. This is done for the five fastest tests with the slowest sixth test as a reference, with the result shown in Figure 5.27. The parameter is calculated for a plastic strain between 0.03 and 0.2 to minimize the effects of the generated heat. As with the rectangular HDPE tests a trend of a decrease in plastic viscosity is seen as a function of plastic strain, even when looking at the second slowest test. For the following work, the plastic viscosity parameter C is assumed constant and equal to 2.3 MPa.

94
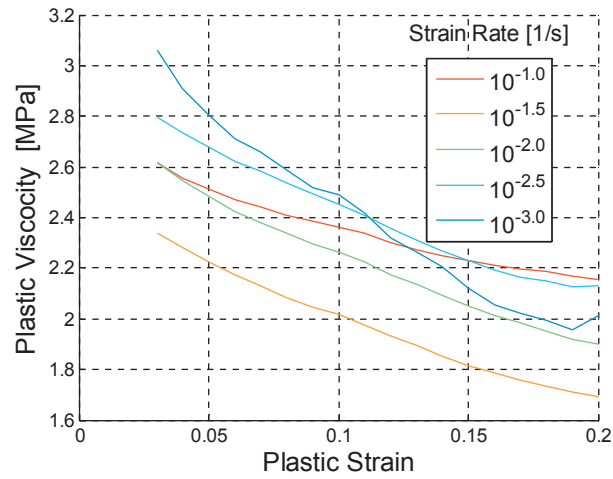
Figure 5.27: Plastic viscosity vs. plastic strain for rectangular PVC tension samples stretched at six different nominal strain rates. Plastic viscosity is calculated relatively to a sixth test performed at a nominal strain rate equal to $10^{-3.5}\,s^{-1}$

It is possible to look at the strain-rate normalized behavior of the material by using Equation (4.27) when the viscoplastic constant C has been found. These normalized stress-strain curves are shown in Figure 5.28. As expected, the curves collapse nicely at small and moderate deformation, but vary significantly towards the end, again owing to temperature softening.
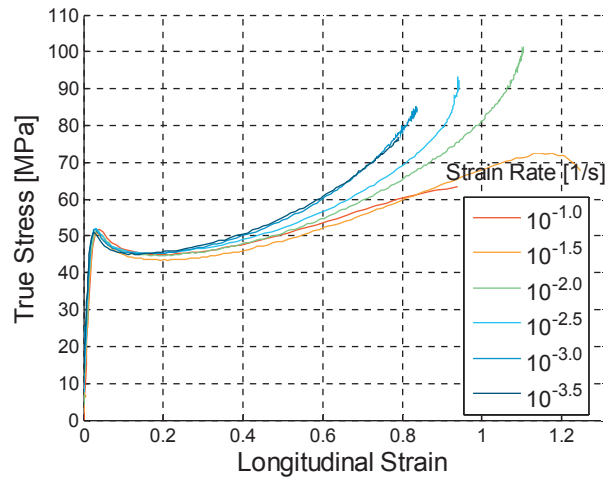
Figure 5.28: Strain rate normalized stress-strain response for rectangular PVC tension samples stretched at six different nominal strain rates, normalized to a constant strain rate of $10^{-2.5}\text{s}^{-1}$.

The stress-strain response is further normalized to a constant temperature by means of Equation (4.29). Figure 5.29 shows the temperature-normalized stress strain response, where the curves are normalized to a temperature of 22 °C, which corresponds to the room temperature T_R. Further, the melting temperature T_M is set to 100 °C, and a temperature sensitivity parameter $m = 1.3$ is adopted. With this normalization, it is seen that the curves do not intersect, and the difference in stress between the curves is more or less constant. The significant hardening of the second fastest test might also be noted, where the maximum stress has changed from 80 MPa in the original data to above 190 MPa in the normalized data.
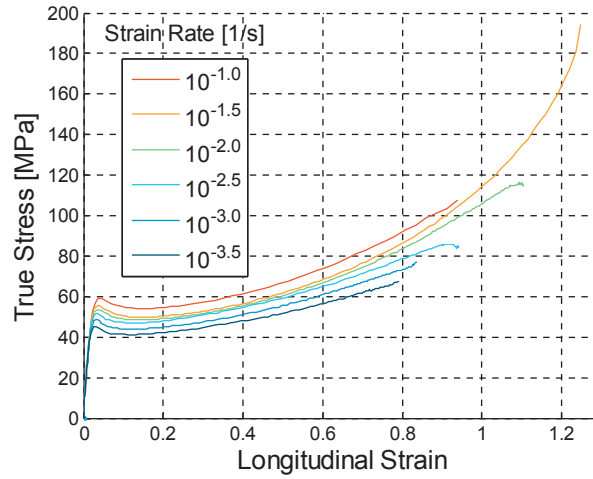
Figure 5.29: Temperature normalized stress-strain response rectangular PVC tension samples stretched at six different nominal strain rates, normalized to a constant temperature of 22 °C.

Finally, the stress-strain curves are normalized with respect to both temperature and strain rate, as shown in Figure 5.30. The normalized stress-strain response in this figure is plotted with a vertical axis covering the entire data range. In order to compare the normalized data with the raw data, Figure 5.31 shows the same curves together with the original stress strain curves with the same limits of the vertical axis. As can be seen from the figures, the data collapse nicely into a single master curve, illustrating the applicability of the material model outlined in Section 4.4 also for PVC.
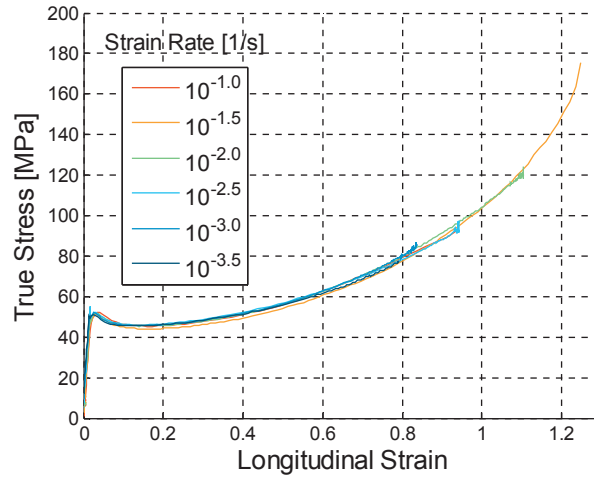
Figure 5.30: Temperature and strain rate normalized stress-strain response for rectangular PVC tension samples stretched at six different nominal strain rates, normalized to a constant strain rate of $10^{-2.5}$ and a constant temperature of 22 °C.

(a) Original data

(b) Normalized data
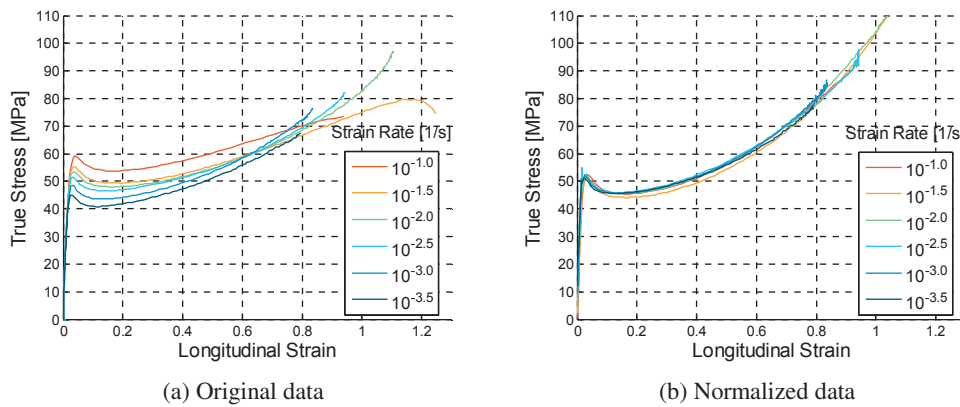
**Figure 5.31: Comparison of non-normalized (a) and temperature and strain rate normalized (b) stress-strain response for rectangular PVC tension samples stretched at six different nominal strain rates, normalized to a constant strain rate of $10^{-2.5}$ and a constant temperature of 22 °C.**

For subsequent use it is also of interest to look at how the heat is generated and dissipated. The generation of heat can be examined by using Equation (4.42) on the test performed at $10^{-1.5}\,\text{s}^{-1}$. The material is assumed to have a constant density ρ and a constant specific heat

capacity $C_p = 1000\,\text{J/kgK}$. The resulting Taylor-Quinney coefficient is shown in Figure 5.32, where it is plotted against plastic strain. A nonlinear least square fit is also included. The nonlinear fit uses a Voce type formulation

$$\chi(\varepsilon_{pl}) = a_1\left(1 - \exp(-b_1\varepsilon_{pl})\right) + a_2\left(1 - \exp(-b_2\varepsilon_{pl})\right) \qquad (5.1)$$

with the parameters shown in Table 5.1.

Table 5.1: Fit of parameters for Equation (5.1) representing the Taylor-Quinney coefficient for PVC.

a_1	b_1	a_2	b_2
0.3421	5.0807	0.4974	47.4509

The chosen fitting model, represented by Equation (5.1), seems reasonable for the evolution of the Taylor-Quinney coefficient. It is seen in Figure 5.32 that χ rises from a value close to zero, and then stabilizes as it gets closer to one. The initially low value is believed to reflect the gradual transition from pure elastic to elasto-plastic deformation. It is observed that the evolution of χ is completely different for HDPE and PVC, see Figure 5.18.
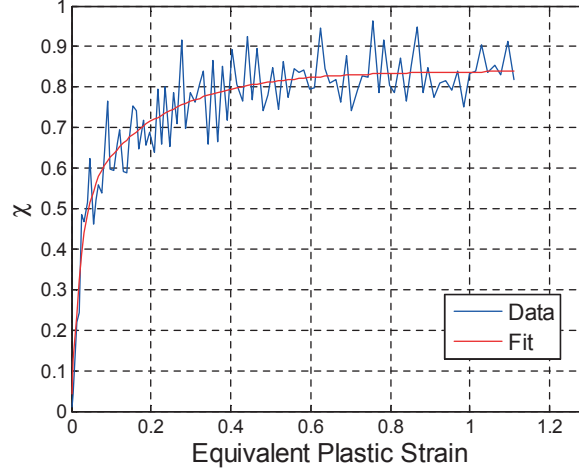
Figure 5.32: Taylor-Quinney coefficient vs. plastic strain for rectangular PVC tension sample performed at a nominal strain rate of $10^{-1.5}\text{s}^{-1}$.

By use of Equation (5.1), it is now possible to accurately model the adiabatic temperature rise in the two fastest tests. For future use it is however also of interest to look at the temperature in the slower tests, and it is hence necessary to include some form of heat transfer. It is here assumed that heat only transfers to air through convection, i.e. it is assumed that heat radiation and conduction is negligible. These assumptions might be reasonable since the difference in temperature between the room and the material is small in a radiation perspective, while the low conductivity of polymers in general might justify the assumption of no conduction. Energy dissipation by convection is assumed to be linear with the difference in temperature between the air and the material [36]. The increase of the local surface area that is exposed to air in the neck of the sample is incorporated. The equation for the temperature T in the neck at a time $t + \Delta t$ is then given as

$$T_{t+\Delta t} = T_t + \left(\chi\left(\varepsilon_{pl} \right) \sigma \dot{\varepsilon}_{pl} + h\left(T_R - T_t \right) \frac{A_{int}}{V} \right) \frac{\Delta t}{\rho C_p} \qquad (5.2)$$

where h is the heat transfer coefficient between PVC and air, A_{int} represents the surface area in the neck, V is the volume, and T_R is the room temperature.

The ratio between interface area and volume, is then approximated as

100

$$\frac{A_{int}}{V} = \frac{2(lw + lt)}{lwt} = \frac{2(w_0\lambda_w + t_0\lambda_w)}{w_0 t_0 \lambda_w^2} = \frac{2(w_0 + t_0)}{w_0 t_0 \lambda_w} \qquad (5.3)$$

where w_0 and t_0 is the initial width and thickness of the sample and λ_w is the stretch in the width direction. Having established a complete model for generation and transfer of heat, it is now possible to simulate the temperatures observed in the tests. This is shown in Figure 5.33, where both the measured and modeled temperatures are plotted against equivalent plastic strain. It was found that a heat transfer coefficient h equal to 20 W/Km^2 gave the best result. This value should serve as an upper limit, since it in principle is used to model several mechanisms for heat transfer. As can be seen, the agreement for all tests is quite good considering the simple model defined by Equation (5.2). In particular, the model captures the decrease of temperature in the last phase of the slow and medium rate tests. This decrease occurs when the neck starts to propagate, resulting in less local deformation per time, while the convection to the surrounding air increases due to the increased surface area in the necked section.
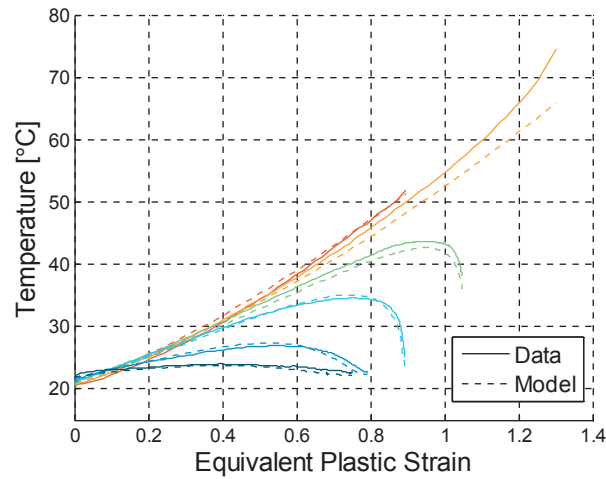
Figure 5.33: Temperature vs. equivalent plastic strain, measured and modeled, for rectangular PVC tension samples stretched at six different nominal strain rates.

5.3.3 Volumetric Strain

Volumetric strain is calculated with the same simplified assumption as for the rectangular HDPE samples, i.e. with use of Equation (4.15) and taking the natural logarithm of the volumetric stretch. Figure 5.34 shows volumetric strain vs. longitudinal strain for the six tests. As can be seen from the curves for the four lowest strain rates, there are some variations in the data with no obvious relation to strain rate. A general trend seen in the four slowest tests is however a rapid increase of volume in the initial phase of the tests, followed by a decrease of the gradient and finally a constant volumetric strain around 0.1. The two fastest tests, which also experienced significant heating, do however not stabilize in volume, but rather exhibit an exponential growth after 0.4 in strain. The data then suggests that strain rate does not affect the volumetric strain, while temperature might be a governing parameter.
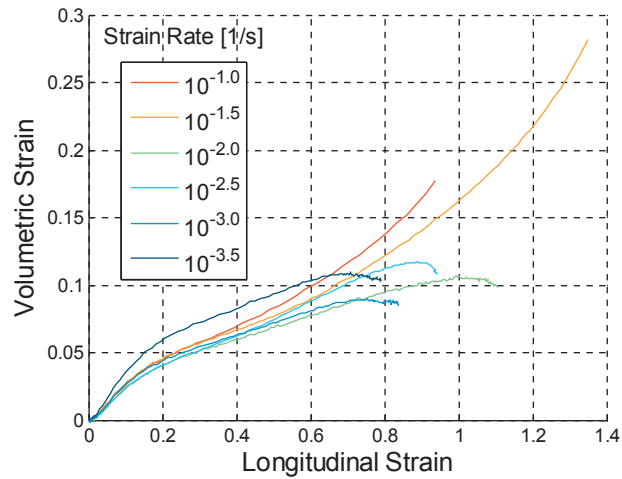
Figure 5.34: Volumetric strain vs. longitudinal strain for rectangular PVC tension samples stretched at six different nominal strain rates.

5.4 HDPE samples with Circular Cross-Section

This part of the experimental program contains six uniaxial tension tests on the HDPE material, this time applying the custom-designed sample with a rather short gauge length and also shoulders with limited length, see Figure 5.2. The circular cross section combined with the instrumentation with a digital camera facilitates a Bridgman-correction of the calculated stress. The tests were carried out at three different nominal strain rates of $10^{-2.5}$, $10^{-2.0}$ and $10^{-1.5}$ s^{-1}, and there were two replicate tests at each rate. All the HDPE test specimens behaved well in the sense that they exhibited repeatable force-displacement response, necking initialized at the center of the test samples, and the final fracture occurred at the shoulders of the samples after the neck had propagated through the entire gauge length of the samples. This test series was not monitored with the thermal camera. The calculation of the elastic parameters is not addressed in this section as the results are similar to those of the rectangular tension tests, see Section 5.2.2.

5.4.1 Raw Data

Figure 5.35 shows the force-displacement response for six tension tests of HDPE carried out at the three different nominal strain rates of $10^{-2.5}$, $10^{-2.0}$ and $10^{-1.5}$ s^{-1}. It can be seen from the figure that the replicate tests performed at the same nominal strain rate have strong similarities, indicating a good repeatability for the tests. The effect of the custom sample geometry is also visible, and is seen by the increase in force-displacement slope when the displacement exceeds approximately 30 mm. This is the point where the neck has propagated through the whole gauge length and reached the shoulders of the sample. The neck then starts to propagate into the shoulders of the sample where the larger dimensions of the cross section increases the force.

It might also be noted that three of the tests were unloaded, while the others were stretched to failure. The controlled unloading was done when the measured force started to decrease, and hence all tests may be considered as being stretched up to failure.
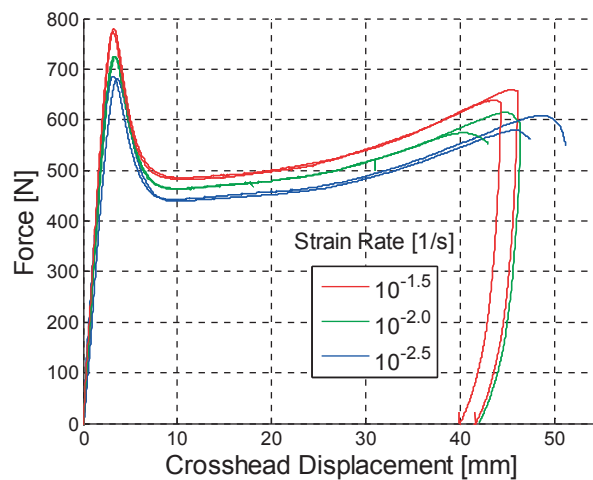
Figure 5.35: Force vs. crosshead displacement curves for six circular HDPE tension samples subjected to uniaxial tension at three different nominal strain rates.

Figure 5.36 shows images of the deformation of a sample at different cross head displacements u. A pronounced neck is visible at $u = 5\,\text{mm}$, and cold drawing of the sample is easily recognizable from $u > 10\,\text{mm}$. The deformation of the middle region of the sample is

104

again homogeneous when the deformation exceeds about 20 mm. From this stage onwards, the central region is for the second time in a pure uniaxial tension state, with little to no interference from triaxiality.

| $u = 0$ mm | $u = 5$ mm | $u = 10$ mm | $u = 20$ mm | $u = 30$ mm |
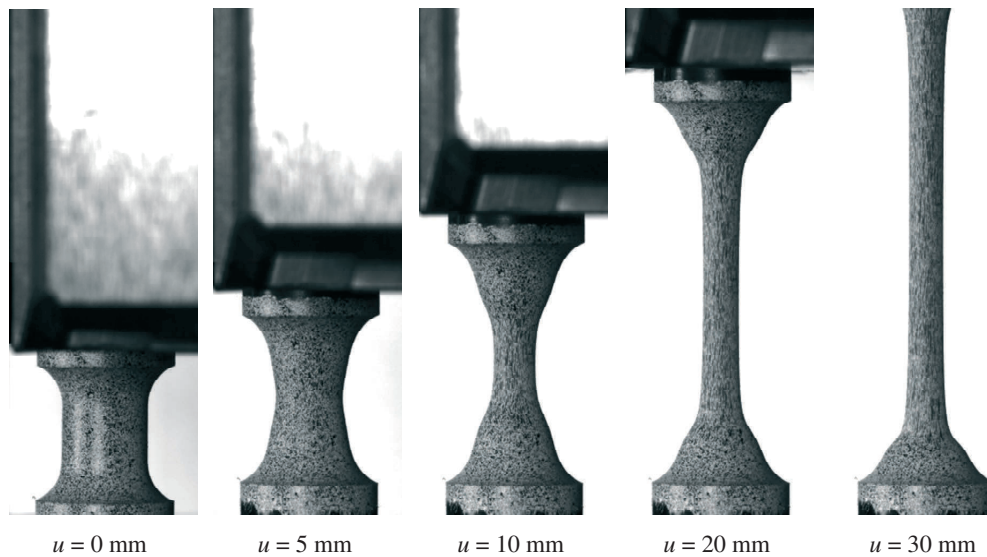
Figure 5.36: Deformation of circular HDPE sample in uniaxial tension at different cross head displacements u, stretched at a nominal strain rate of $10^{-2.5}$ s^{-1}.

5.4.2 Stress-Strain Response

Figure 5.37 shows the average true stress as defined in Equation (4.21) versus the local logarithmic longitudinal strain in the section that experiences the onset of necking. As seen from the figure, both the local strain and in particular the stress reach significantly higher values than observed for the conventional sample, see Figure 5.9. The maximum logarithmic strain, occurring in one of the tests at the highest strain rate, is 2.11, and the accompanying true stress is 162.3 MPa. A logarithmic strain of 2.11 is equivalent to a stretch of 8.24, while the maximum stress is about 5.4 times higher than the yield stress. The effects of strain rate are more apparent in Figure 5.38, which addresses only the first part of the stress-strain curve and therefore has an improved resolution at the ordinate axis. Figure 5.38 also serves to illustrate the good consistency between tests performed at the same nominal strain rate.
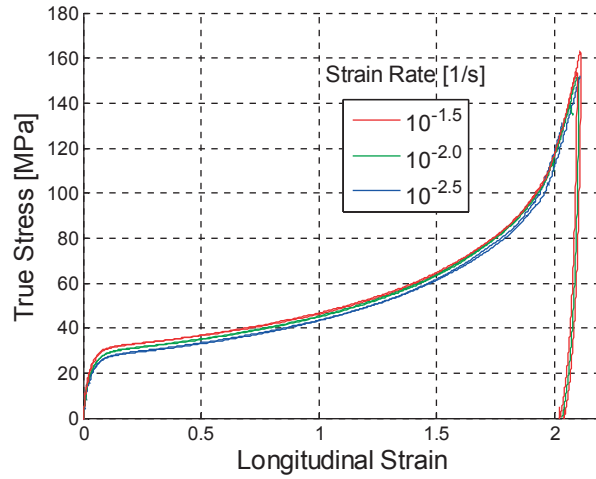
Figure 5.37: True stress vs. logarithmic longitudinal strain curves for six circular HDPE tension samples stretched at three different nominal strain rates.
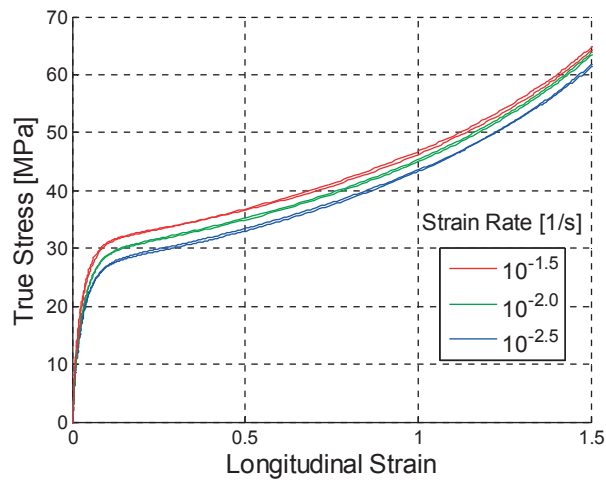
Figure 5.38: Excerpt of stress-strain curves for six circular HDPE tension samples stretched at three different nominal strain rates.

The radius and curvature of the neck can be found from the edge tracing algorithm described in Chapter 3, and are shown in Figure 5.39. As can be seen from the curvature plot, the neck is most pronounced at a strain of about 0.75, this is a bit after the neck radius changes slope.

This could indicate a transition from deformation dominated byplasticly to deformation governed by network stretching.

(a) Neck radius   (b) Neck curvature
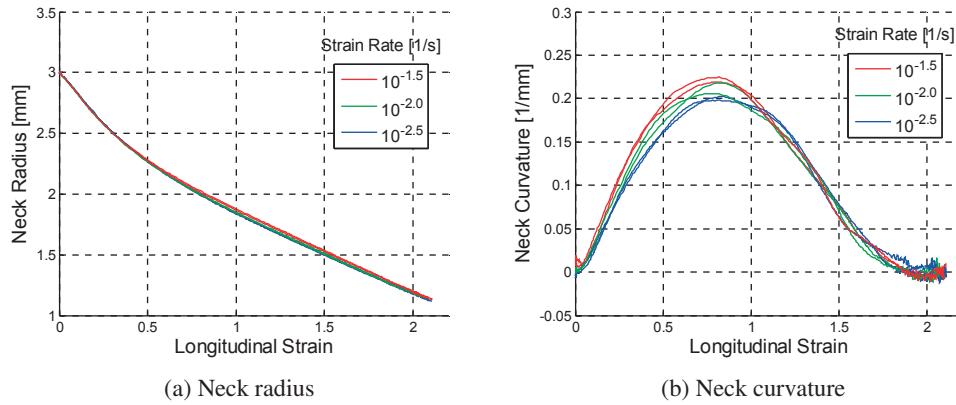
Figure 5.39: Geometrical measures at neck as a function of local logarithmic strain for six circular HDPE tension samples stretched at three different nominal strain rates. (a) Neck radius and (b) neck curvature.

Having found the local radius and curvature of the neck during the test, it possible to calculate the uniaxial Mises stress with the help of the Bridgman correction given in Equation (4.22). The effect of the Bridgman correction for one of the tests carried out at a nominal strain rate of $10^{-2.5} \, \mathrm{s}^{-1}$ is illustrated in Figure 5.40 (a), showing a maximum reduction in stress of about 4 MPa. In accordance with the neck curvature shown in Figure 5.39 (b), it appears that the Bridgman correction is relevant for longitudinal strains between approx. 0.2 and 1.5. For larger strains, the curvature in the section is close to zero, as already shown in the two photos to the right in Figure 5.36, and the correction is therefore superfluous. Figure 5.40 (b) shows all six curves with the applied correction. The effect of the Bridgman correction is almost identical for all six tests, as is expected from the strong similarities between the curves at different rates in Figure 5.39. The Bridgman corrected curves are used in the further work.

(a) Effect of Bridgman correction (b) Bridgman corrected curves
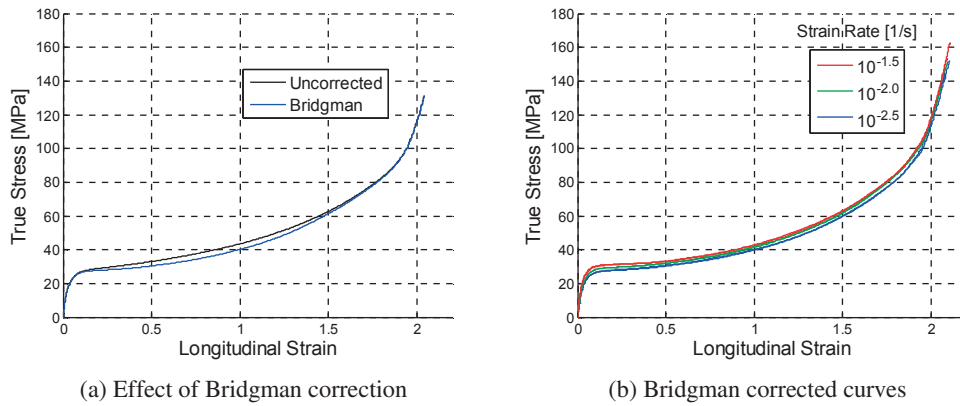
Figure 5.40: Difference between uncorrected and Bridgman corrected stress(a), and Bridgman correction of stress for six circular HDPE tension samples stretched at three different nominal strain rates (b).

Strain rate correction to the calculated stress, see Equation (4.27), is possible by first establishing the local strain rate versus strain for the tests, as shown in Figure 5.41.
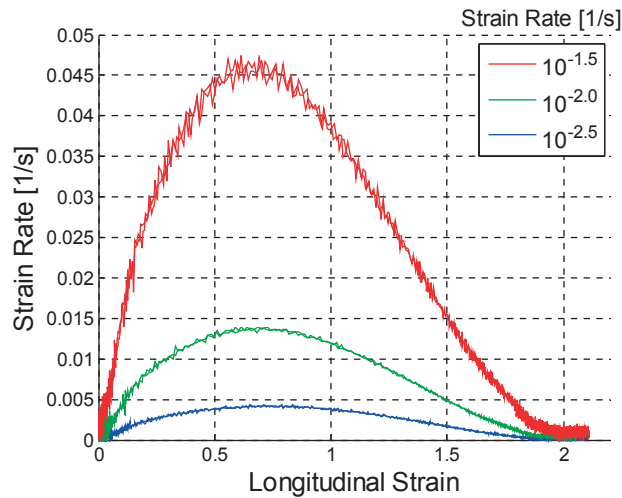
Figure 5.41: Strain rate in section first experiencing necking as a function of logarithmic strain for six circular HDPE tension samples stretched at three different nominal strain rates.

By assuming the additive split of the stress into a plastic and an viscoplastic part, as shown in Equation (4.23), it is possible to investigate the validity of the viscoplastic coefficient C. Equation (4.26) states that

108

$$C_{kl} = \frac{\sigma_M^k - \sigma_M^l}{\ln(\dot{p}^k / \dot{p}^l)}$$

In order to calculate plastic strain and strain rate, a constant Young's modulus of 650 MPa is assumed. It is then possible to calculate the plastic viscosity parameter C for the tests as a function of plastic strain. This is shown in Figure 5.42 where C is calculated from the relations between the tests performed at the two fastest speeds and one of the tests performed at a nominal strain rate of $10^{-2.5}\,\text{s}^{-1}$. As seen from the figure, C shows some initial decrease, but then seems to stabilize at around 1.4 MPa for plastic strains between 0.2 to 0.8 for three of the tests. In the further work these tests are assumed to have a constant C equal to 1.42 MPa.
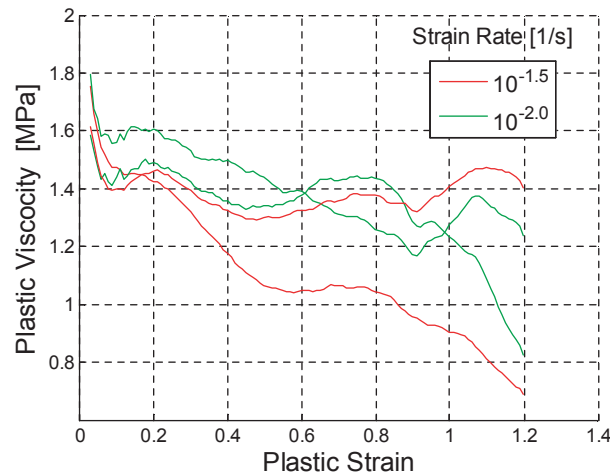
Figure 5.42: Plastic viscosity vs. plastic strain for circular HDPE tension samples stretched at two different nominal strain rates. Plastic viscosity is calculated relatively to a third test stretched at a nominal strain rate equal to $10^{-2.5}\,\text{s}^{-1}$

Applying Equation (4.27), Figure 5.43 shows the strain-rate independent stress σ_0 as function of total strain for all six tests. The reference plastic strain rate is selected as $\dot{p}_0 = 10^{-2.5}\,\text{s}^{-1}$. All six curves collapse into more or less the same curve. Again, this good agreement validates that the viscoplastic model, defined in Equation (4.23), with an additive decomposition of the equivalent stress is well suited as a model. The average of the six curves in Figure 5.43 can be viewed as the master curve for this material.
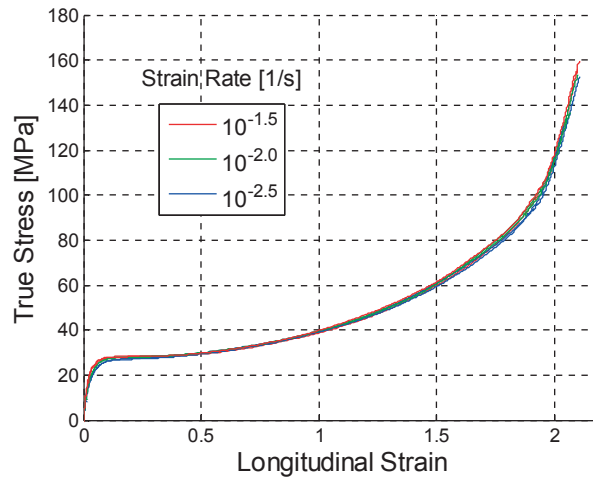
Figure 5.43: Strain-rate corrected stress vs. logarithmic longitudinal strain for six circular HDPE tension samples stretched at three different constant loading velocities.

Figure 5.44 shows the comparison between a strain rate corrected and uncorrected stress-strain curve for a test with a nominal strain rate equal to $10^{-2.0}\,\text{s}^{-1}$. The corrected curve represents the stress-strain response at a constant local strain rate equal to the nominal strain rate. As expected from looking at the strain rate history in Figure 5.41, the uncorrected curve in Figure 5.44 underestimates the yield stress, gives a fair representation of the intermediate stress, and again underestimates the last third of the stress-strain response. It is in other words important to take the local strain rate into account when determining an accurate representative value of the stress.

110
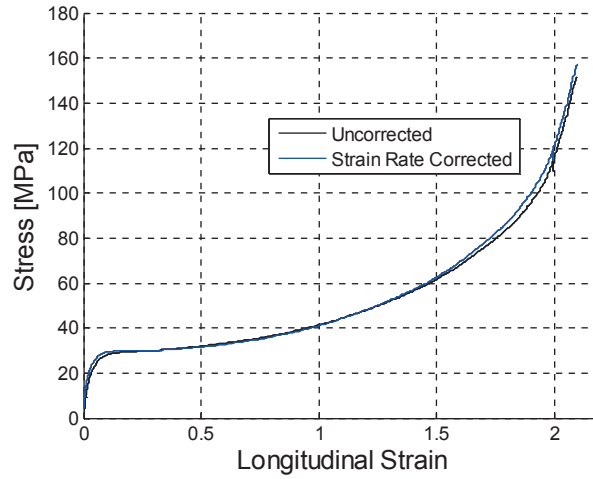
Figure 5.44: Comparison between strain-rate corrected and uncorrected stress vs. logarithmic strain for a test stretched at a nominal strain rate of 10^{-2} s^{-1}.

5.4.3 Volumetric Strain

A straightforward calculation of the average volumetric strain with the "cylinder method", see Equation (4.15), yields the six curves shown in Figure 5.45. Clearly, this method for calculating volumetric strain results in a significant amount of negative volumetric strain as the neck initializes, before the volumetric strain attains a positive value as the neck stabilizes and propagates. As argued for in Section 4.2, this negative volumetric strain is a fictive measurement stemming from an incorrect assumption of the deformation of a finite volume in the neck.
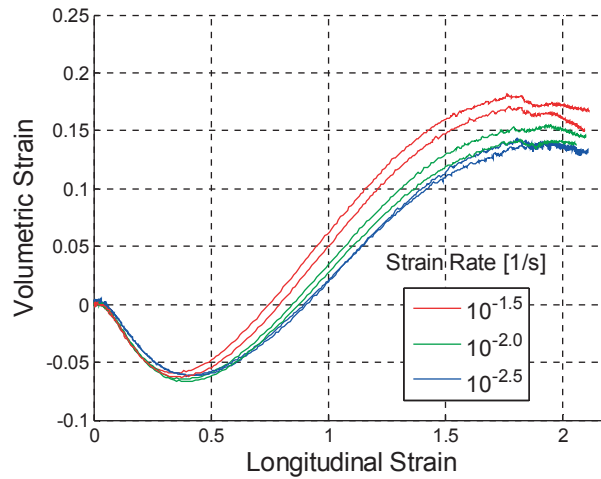
Figure 5.45: Logarithmic volumetric strain vs. logarithmic longitudinal strain calculated with the "cylinder method" for six circular HDPE tension samples stretched at three different nominal strain rates.

On the other hand, applying the correction defined by the "parabolic method" in Equation (4.20) gives the plots shown in Figure 5.46. It is seen that the negative volumetric strain in the initial phase of the test has disappeared. The volumetric strain seems to be close to zero for strains below 0.25. Thereafter, the volumetric strain increases almost linearly until it saturates at a strain value around 1.25. The deformation at high strains is in other words isochoric, i.e. volume preserving. Recalling the observations in Figure 5.19, also these data indicate that volumetric strain in HDPE is dependent on strain rate, as higher strain rates seem to produce larger volumetric strains.

112
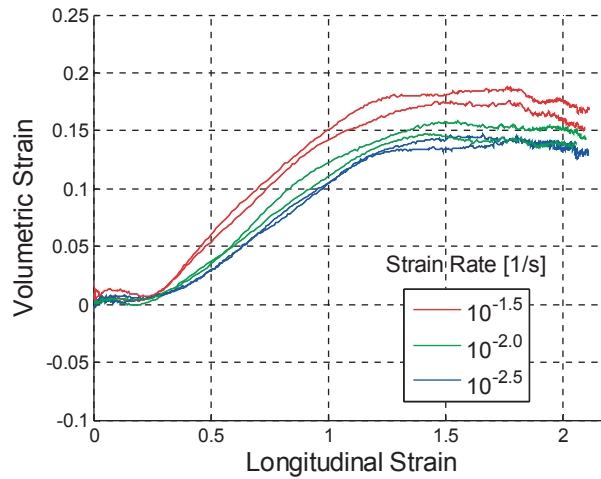
Figure 5.46: Logarithmic volumetric strain vs. logarithmic longitudinal strain calculated with the "parabolic method" for six circular HDPE tension samples stretched at three different nominal strain rates.

5.4.4 SEM Study

Virgin and deformed HDPE material samples were investigated using a scanning electron microscope (SEM). The purpose was to try to identify the mechanism behind the measured increase in volume. Figure 5.47 and Figure 5.48 show micrographs of an undeformed HDPE sample at two different magnifications. It is not clear if the observed porous web-like structure is representative of the material or is an artifact of the method used to split the sample, see Section 5.1.2. What is clear is that small spherical particles are present in the material. These particles have a size of about 0.5 μm.
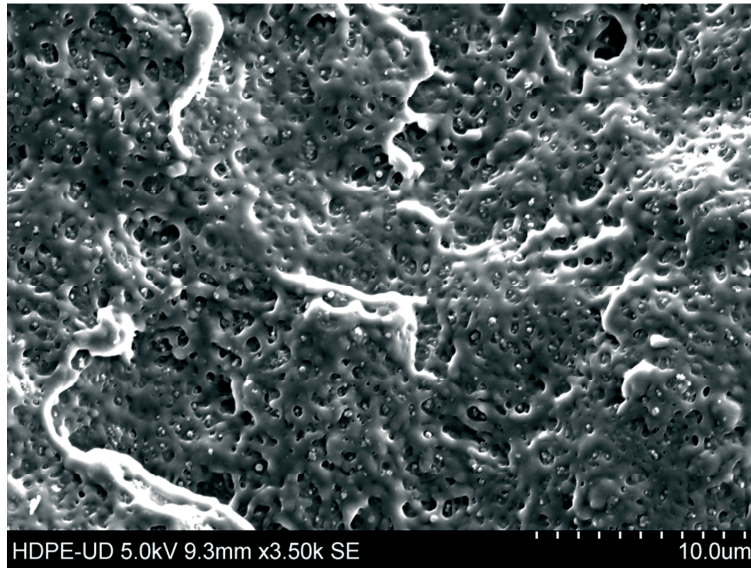
Figure 5.47: SEM micrograph of the interior of an undeformed HDPE sample, magnified 3500 times.
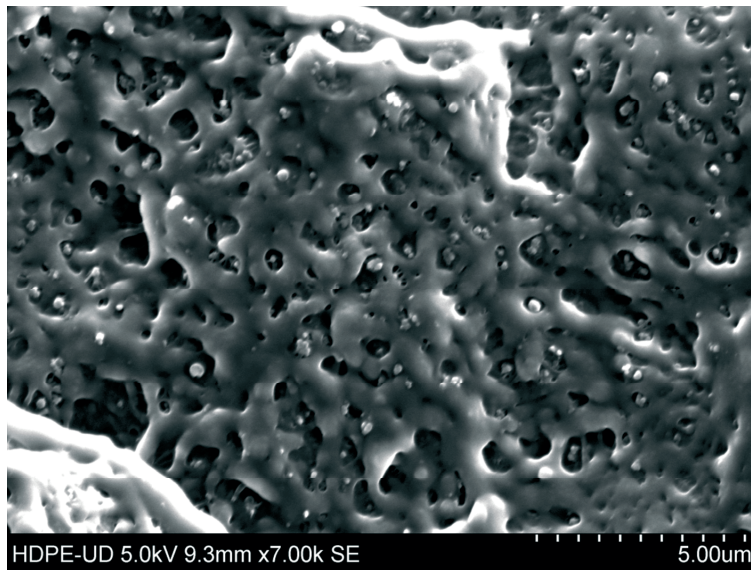
Figure 5.48: SEM micrograph of the interior of an undeformed HDPE sample, magnified 7000 times.

Micrographs of samples deformed at a nominal strain rate of $10^{-2.5}$ s^{-1} are shown in Figure 5.49, Figure 5.50 and Figure 5.51. The SEM images are taken from a surface inside the sample, as shown in Figure 5.6 in the area of initial necking. This means that the plane has been elongated by a factor of about 8 in one direction marked by the red arrows, and compressed to a factor of 0.14 in the normal direction to the arrows. The image in Figure 5.49 does not show many interesting features, and it is suspected that the method of splitting the sample combined with the high ductility of the material has created a smeared surface. The direction of deformation is however easily identified, and some elongated cavities can be seen. The particles observed in the undeformed material are not found, and no apparent effect can be linked to them from the image. The micrographs in Figure 5.50 and Figure 5.51 are from a sample split with a different method, where the sample was cooled with liquid nitrogen and then ripped in two along the length axis of the sample. The fact that it is possible to easily split a deformed sample in the radial direction is by itself interesting in that it gives a qualitative idea of the anisotropy in a deformed sample. According to the micrographs, this anisotropy seems to be caused by a material structure resembling a collection of filaments oriented along the stretching direction of the sample. The filaments appear to be loosely connected in their radial direction, explaining the weak radial strength.
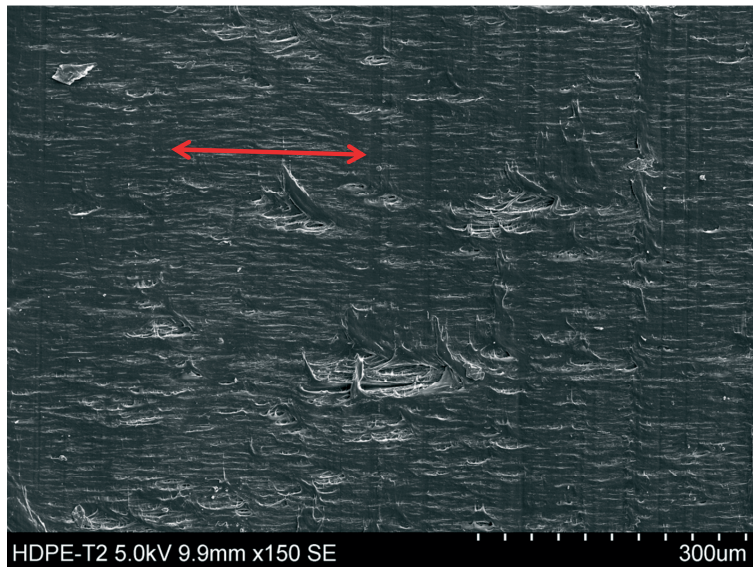
Figure 5.49: SEM micrograph of the interior of a circular HDPE sample stretched in uniaxial tension along the horizontal axis, sample split by cleaving, magnified 150 times. The red arrow indicates the tension direction.
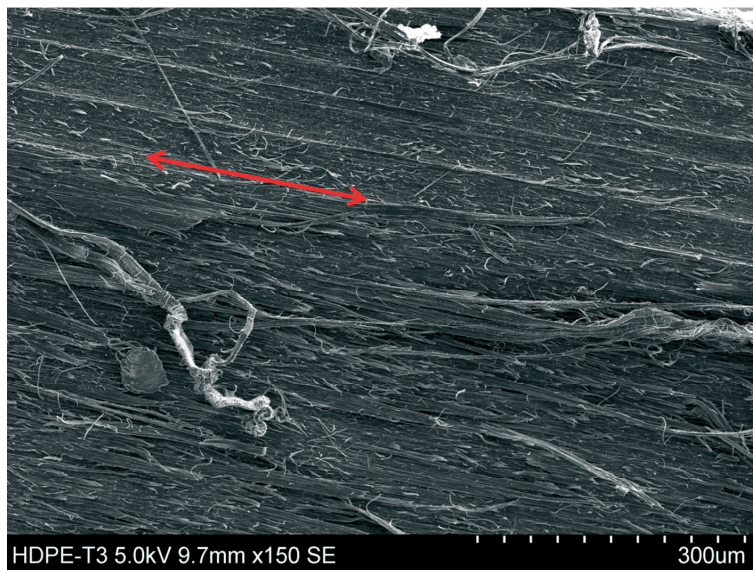
Figure 5.50: SEM micrograph of the interior of a HDPE sample stretched in uniaxial tension along the horizontal axis, sample split by ripping, magnified 150 times. The red arrow indicates the tension direction.
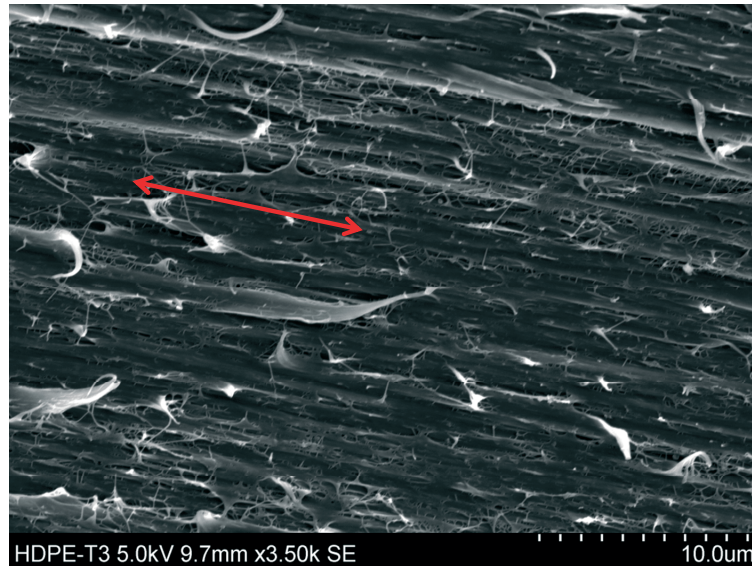
Figure 5.51: SEM micrograph of the interior of a HDPE sample stretched in uniaxial tension along the horizontal axis, sample split by ripping, magnified 3500 times. The red arrow indicates the tension direction.

5.5 PVC samples with Circular Cross-Section

The experimental program of the PVC samples with circular cross section was similar to the one described for HDPE in the previous section: Six tests were carried out at nominal strain rates of $10^{-2.5}$, $10^{-2.0}$ and $10^{-1.5}$ s^{-1}; two samples at each rate. In contrast with the HDPE tests, the neck did not initiate at the center length of the PVC samples in all the tests, and fracture occurred at different parts of the test samples. The calculation of the elastic parameters is not addressed in this section as the results are similar to those of the rectangular tension tests, see Section 5.3.2.

5.5.1 Raw Data

Figure 5.52 shows the force-displacement curve for six PVC samples tested at the same three crosshead velocities as HDPE, i.e. $10^{-2.5}$, $10^{-2.0}$ and $10^{-1.5}$ s^{-1}. As is obvious from the curves, the repeatability of the tests was good with respect to force-displacement measurements. It is

117

noted that curves representing tests at higher nominal strain rates cross the curves of tests at lower nominal strain rates. It will be demonstrated in the next section that this is an effect of material softening caused by adiabatic heating.
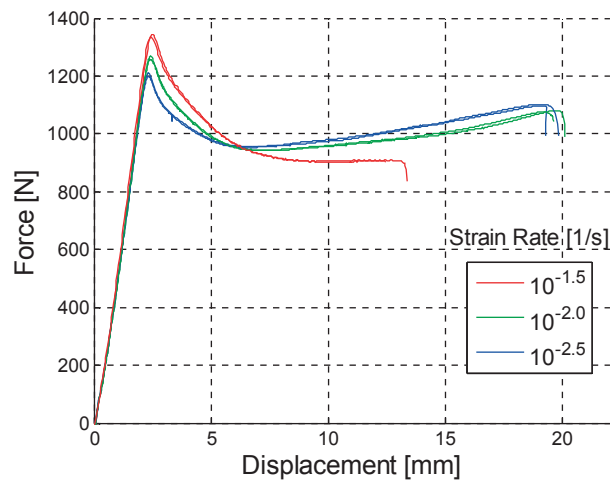
Figure 5.52: Force vs. crosshead displacement curves for six circular PVC tension samples stretched at three different nominal strain rates.

Figure 5.53 shows the DIC pictures for one of the two slowest PVC tests, taken at five different stages during the test. The pictures illustrate that this PVC material produces a less pronounced neck than what was observed for HDPE. This seems contradictory in that the material initially has a negative hardening slope after necking, which intuitively should lead to a highly localized neck. The explanation is that relatively small plastic strains are required to reach a high positive hardening. The deformation in the section of initial localization is hence limited, as the neck propagates early compared to HDPE. The rapid increase in volume exhibited by PVC in tension, as was seen in Figure 5.34, should also contribute to hide the neck since the sample does not contract as much compared to a plastically incompressible material. Despite the rather diffuse neck, it is still possible to find the section with the local maximum of the strain from the digital images and the DIC analysis. The stress-strain data presented in the subsequent figures are taken from this section.

118

u = 0 mm   u = 5 mm   u = 10 mm   u = 15 mm   u = 19 mm
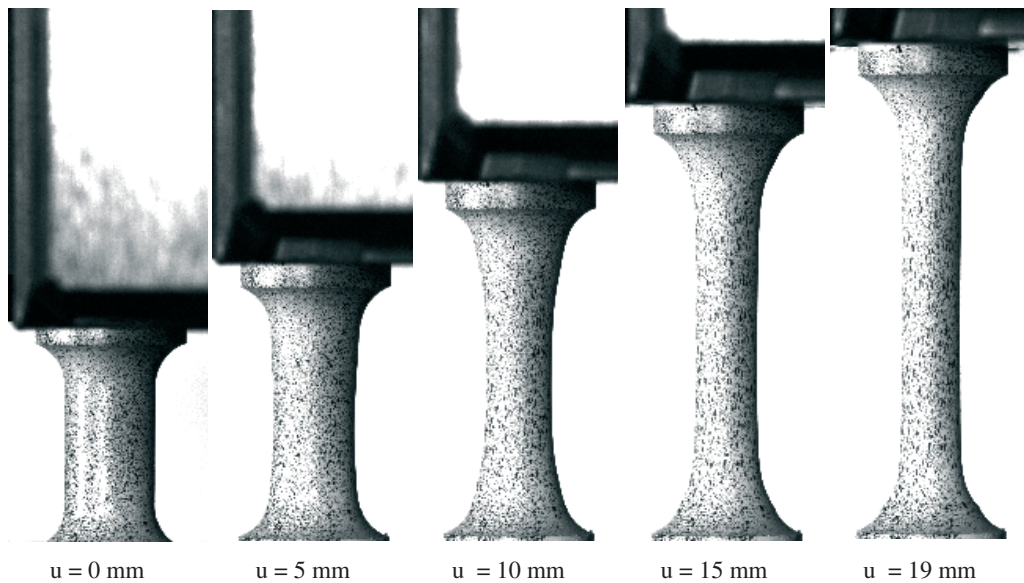
Figure 5.53: Deformation of PVC in uniaxial tension at different cross head displacements u. Stretched at a nominal strain rate of $10^{-2.5}$ s^{-1}.

5.5.2 Stress-Strain Response

Figure 5.54 shows the true average stress versus logarithmic longitudinal strain for the six PVC tests. Again, it is observed that the curves from the higher strain rate tests cross the curves from the tests with lower strain rates. This means that the crossing of the force-displacement curves in Figure 5.52 is not a pure result of differences in cross sectional area, but a de facto change of strain hardening with increasing rate. This variation in strain hardening is a result of adiabatic heating in the material. The reason why this temperature softening is much more prevalent in the PVC tests compared to the HDPE tests is that the yield stress in PVC is about twice as high as it is for HDPE, further, PVC has a much lower specific heat capacity. This results in more dissipated energy per unit of strain, hence more heat. Indeed, Figure 5.12 and Figure 5.25, show that PVC experiences a larger increase in temperature than HDPE does. The crosshead velocity was also twice as high for the PVC samples because these samples had a longer gauge section, see Figure 5.3. The generated heat therefore had less time to diffuse. A secondary effect of the temperature softening is that the tests performed at the highest strain rates reach higher local strains. This comes as a

consequence of the material in the neck requiring more straining to reach a high enough hardening slope to stabilize the neck. For higher strain rates it would be expected that failure would always take place in the neck, as the slope of hardening would not get large enough to stabilize the neck before failure occurs. There is also an obvious visco-plastic component to the stress response of the material, as can be seen from the stress values at yielding.
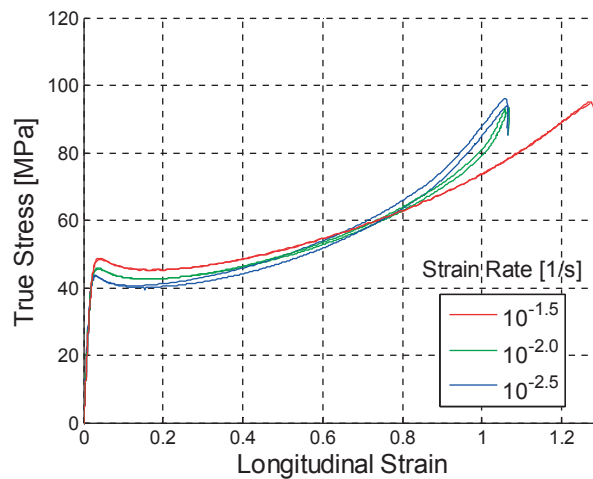
Figure 5.54: True stress vs. logarithmic longitudinal strain curves for six circular PVC tension samples stretched at three different nominal strain rates.

Effective stress calculated from Equation (4.32) is shown against logarithmic longitudinal strain in Figure 5.55. Since PVC exhibits a significant change of volume, it is especially interesting to look at the effective stress, where two differences might be noted compared to the results in Figure 5.54. Firstly, most of the strain softening after yielding has now disappeared, and the initial plastic slope is close to zero. This could indicate that a major part of the strain softening observed in PVC is a direct result of rapid void growth. The second interesting feature is that the curves representing tests performed at the same strain rate are more similar when effective stress is used. This could indicate that volumetric growth has varied between the tests stretched at the same speed. Another possible explanation for the observed variation in the response of identical tests could be material anisotropy in the radial direction. The result of this would be that an initialy circular cross-section would change into a eliptical cross section when stretched, rendering the assumtions used for calculating the

120

cross sectional area invalid. This could affect the samples differently since they were tested with an arbitrary radial orientation, resulting in differences in calculated stress.
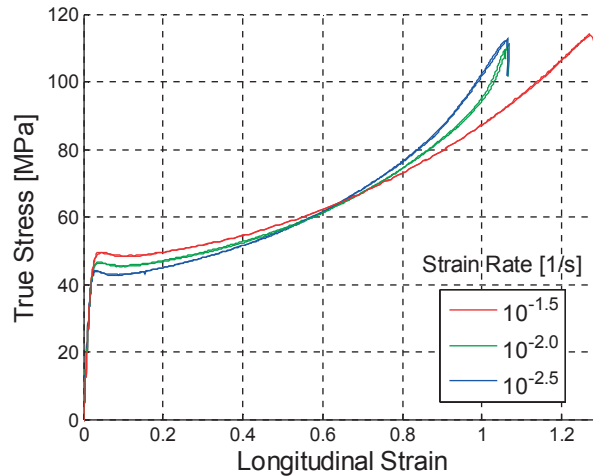
Figure 5.55: True effective stress vs. logarithmic longitudinal strain curves for six circular PVC tension samples stretched at three different nominal strain rates.

Figure 5.56 (a) shows the change of neck radius as a function of longitudinal strain, where it can be seen that there is some variation between samples tested at the same speed. Figure 5.56 (b) shows neck curvature as a function of longitudinal strain. Firstly it is observed that the curvature of the neck is quite small, about 40% of that observed for HDPE. Secondly it seems to depend on strain rate, but the actual cause is most likely heat. The faster tests achieve a higher temperature, resulting in more softening and hence more localization before the neck propagates. It can also be seen that at these speeds, the neck is still able to propagate, as evident from the eventual decrease of curvature. The small curvature of the neck makes the use of the Bridgman correction less relevant compared to the HDPE tests. From Figure 4.8 it can be estimated that the largest error from assuming that the longitudinal stress is equal to the Mises stress is around 5%.

<div style="text-align: center;">(a) Neck radius   (b) Neck curvature</div>
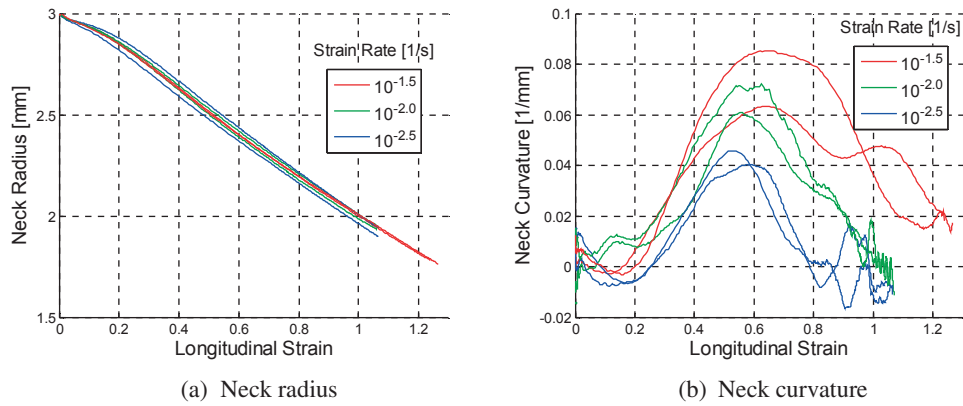
Figure 5.56: Geometrical measures at neck as a function of local logarithmic strain for six circular PVC tension samples stretched at three different nominal strain rates.

Figure 5.57 shows the strain rate vs. logarithmic longitudinal strain for the three PVC tests. It can be seen that necking occurs quite suddenly compared to HDPE, as evident by the fast change of slope before the strain approaches 0.1. Secondly the end of localization can be characterized as the point of maximum strain rate, occurring at about 0.5 in strain. These observations support the earlier hypotheses concerning the evolution of the neck.

122
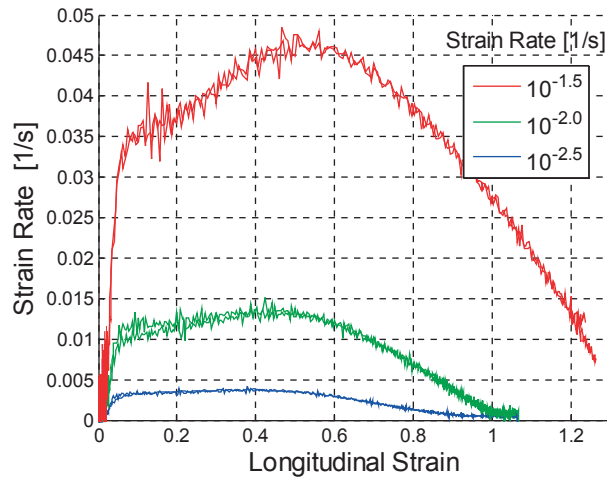
Figure 5.57: Strain rate vs. logarithmic longitudinal strain curves for six circular PVC tension samples stretched at three different nominal strain rates.

With the local strain rate established, it is possible to look at the plastic strain rate sensitivity of the material. Since the material shows temperature softening, it is again reasonable to only look at plastic viscosity for small plastic strains. A constant Young's modulus of 1700 MPa is again assumed, and C is calculated for plastic strain form 0.03 to 0.2. This is shown in Figure 5.58, where one of the tests performed at a nominal strain rate of $10^{-2.5} s^{-1}$ is used as the reference. The evolution of C is similar to what was seen for the rectangular PVC tension samples, see Figure 5.27, and as for the rectangular samples, a constant C equal to 2.3 MPa is assumed in the following calculations.
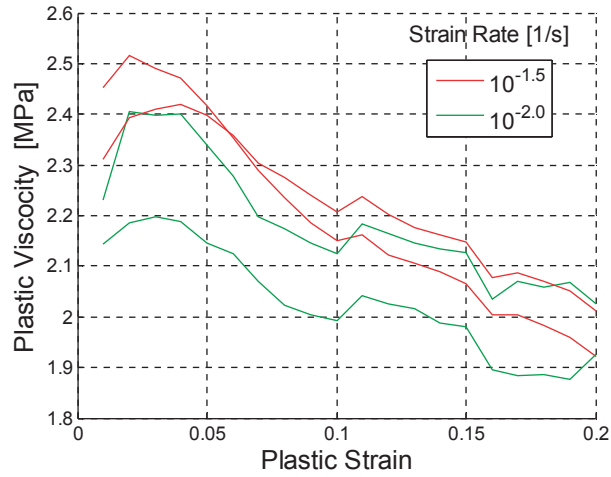
Figure 5.58: Plastic viscosity vs. longitudinal plastic strain for four circular PVC tension samples loaded at two different nominal strain rates. Plastic viscosity is calculated relatively to a fifth test stretched at a nominal strain rate equal to $10^{-2.5}\,\text{s}^{-1}$.

It is now possible to normalize the stress-strain curves with respect to plastic strain rate. This is done by applying Equation (4.27) to the stress-strain data, using the established value for *C*. This is shown in Figure 5.59, where the curves are normalized to a constant strain rate of $10^{-2.5}\,\text{s}^{-1}$. As would be expected, the curves collapse nicely at yield but start to deviate significantly after a strain of about 0.4, which is a similar trend to that of the rectangular PVC tests. This is a result of temperature softening.
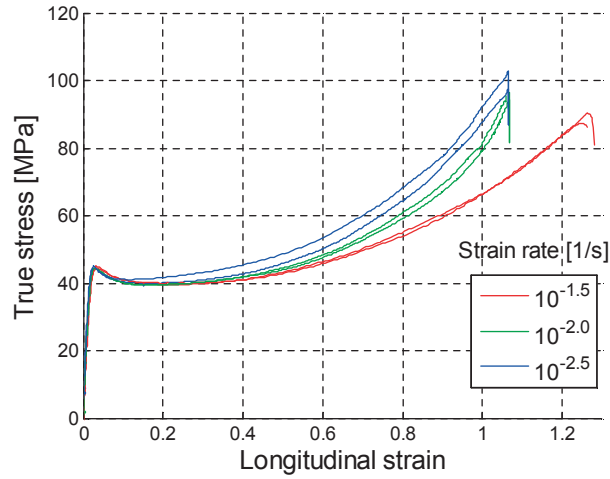
Figure 5.59: Strain-rate normalized stress-strain response for six circular PVC tension samples stretched at three different nominal strain rates, normalized to a constant strain rate of $10^{-2.5}$ s^{-1}.

In order to investigate the effect of temperature, temperature change is modeled for these tests by using Equation (5.2) and the temperature parameters found for the rectangular PVC tension tests. The ratio of interface area to volume for a circular specimen is then equal to

$$\frac{A_{int}}{V} = \frac{2\pi r l}{\pi r^2 l} = \frac{2}{r_0 \lambda_R} \tag{5.4}$$

where r_0 represents the initial radius and λ_R is the local radial stretch. The initial temperature is assumed to be equal to room temperature, assume to be 21 °C. It is now possible to simulate the temperature in the specimens, as shown in Figure 5.60, where simulated temperature is plotted versus equivalent plastic strain. The predicted temperatures seem reasonable compared to those found for the rectangular samples. The tests performed at nominal strain rates of $10^{-2.0} s^{-1}$ and $10^{-2.5} s^{-1}$ show significant heat transfer towards the end of the deformation process, while the temperature of the test performed at $10^{-1.5} s^{-1}$ has a close to linear increase with plastic strain.

125
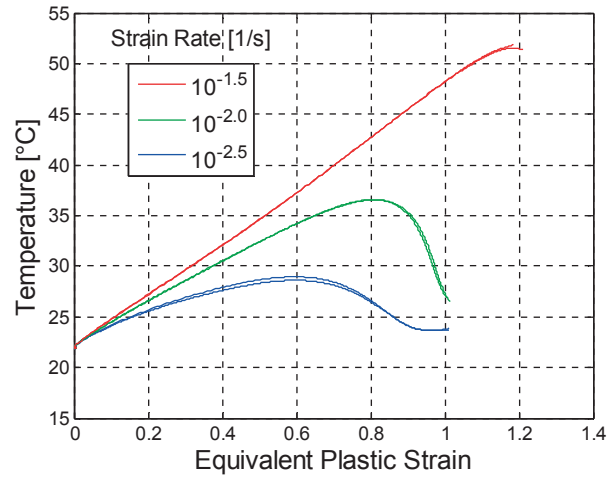
Figure 5.60: Simulated temperature versus equivalent plastic strain for six circular PVC tension samples stretched at three different nominal strain rates.

The validity of these simulated local temperatures can be somewhat confirmed by trying to normalize the stress-strain curves with respect to these temperatures. Temperature normalization is done by using Equation (4.29), and is shown in Figure 5.61. As can be seen, the curves are now stacked according to nominal strain rate, and have a more or less constant shift of stress. The major outlier is one of the tests performed at the nominal strain rate of $10^{-2.5} \mathrm{s}^{-1}$.
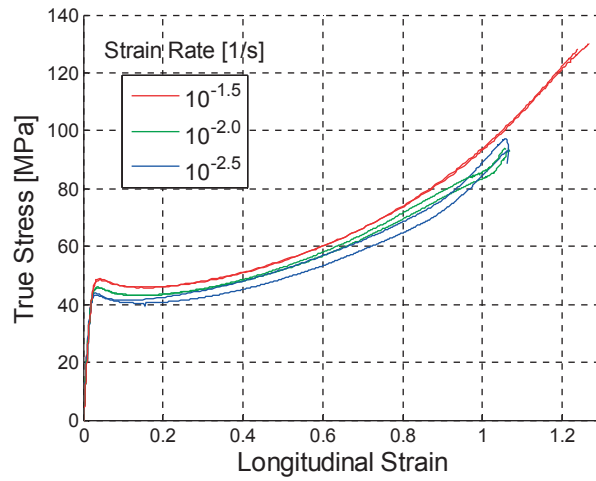
Figure 5.61: Temperature normalized stress-strain response six circular PVC tension samples stretched at three different nominal strain rates, normalized to a constant temperature of 22 °C.

Removing the one outlier test and normalizing the stress-strain data with respect to both strain rate and temperature results in the curves shown in Figure 5.62 and Figure 5.63 (b). As can be seen, the curves collapse nicely, indicating that both temperature and strain rate sensitivity have been characterized to a satisfactory level of accuracy. The mean of the curves in Figure 5.62 can now be considered a master curve for this PVC material.
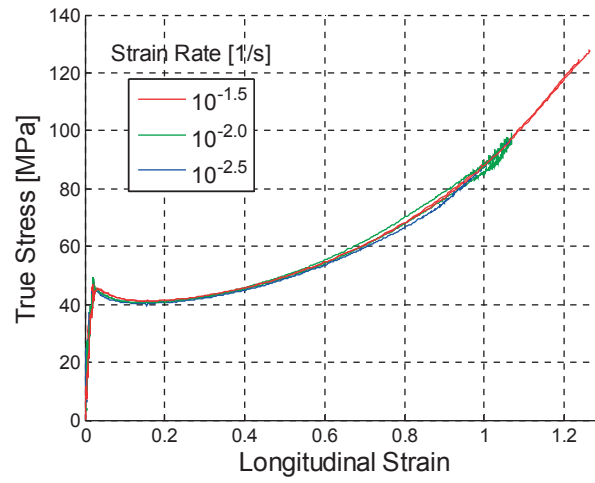
Figure 5.62: Plastic strain rate and temperature normalized stress-strain response for six circular PVC tension samples stretched at three different nominal strain rates, normalized to a constant strain rate of $10^{-2.5}$ s^{-1} and a constant temperature of 22 °C.

(a) Original data	(b) Normalized data
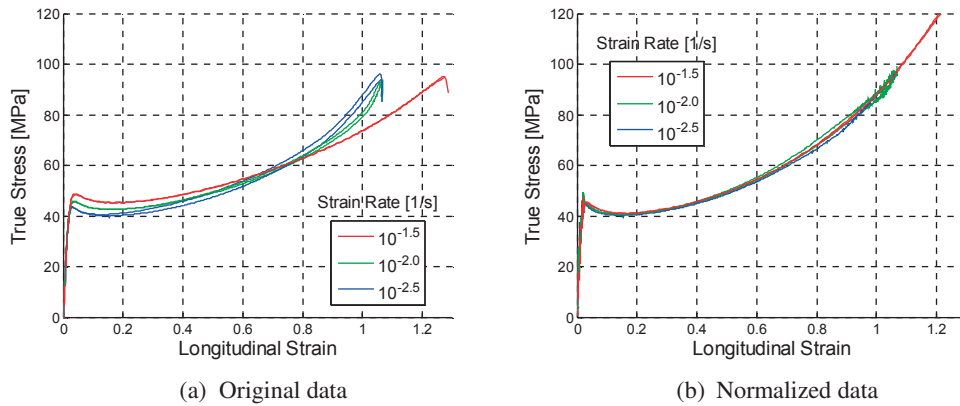
Figure 5.63: Comparison between stress-strain response for non-normalized and normalized stress. Calculated for six circular PVC tension samples stretched at three different nominal strain rates. Normalized stress is calculated for a constant strain rate of $10^{-2.5}$ s^{-1} and a constant temperature of 22 °C.

5.5.3 Volumetric Strain

The average volumetric strain calculated by the somewhat inaccurate "cylinder method", see Equation (4.15), is shown for the six tests in Figure 5.64 as a function of strain. The general response seems reasonable, with an initial rapid increase in volume followed by a less pronounced growth. It is also worth mentioning that the two outlying curves are the same two curves that show the least degree of conformity when the stress-strain curves are normalized. This could indicate that a difference in volumetric growth is the reason for the differences seen in stress-strain behavior. The reason for this variation might be a stochastic variation in the volumetric growth mechanism or anisotropy. As will be shown, SEM micrographs suggest that the major mechanism is debonding between matrix material and stiff particles, which is similar to what was found by other authors [37]. It might also be noted that the volumetric growth gets a steeper slope at about 0.02 in strain, coinciding with yield in the material. This could imply a correlation between yielding and void growth.
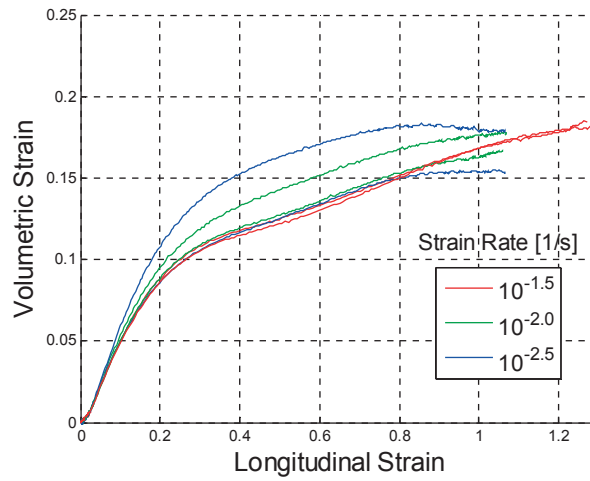
Figure 5.64: Volumetric strain vs. longitudinal strain curves for six circular PVC tension samples stretched at three different nominal strain rates. Volumetric strain is calculated with the "cylinder method".

Calculating the volume with the "parabolic method" is done by applying Equation (4.20). The resulting logarithmic volumetric strain is shown as a function of longitudinal strain in Figure 5.65. The difference between the two methods is less significant for PVC compared to HDPE, and this observation is expected because HDPE experienced much more pronounced necking than PVC. Nevertheless, the volumetric strain approaches a saturation level when calculated with the "parabolic method", and this trend was much less apparent in Figure 5.64.
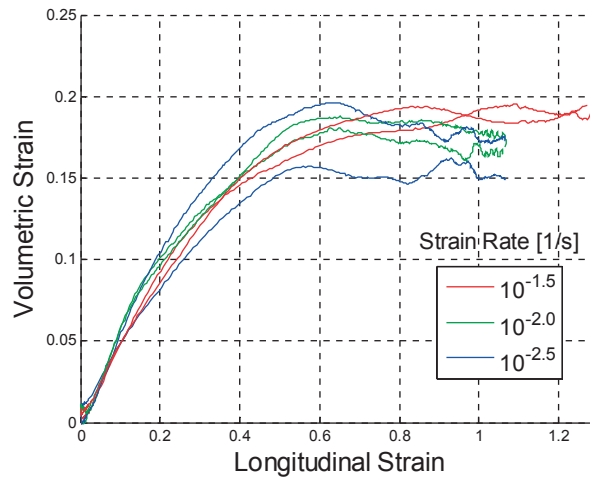
Figure 5.65: Volumetric strain vs. longitudinal strain curves for six circular PVC tension samples stretched at three different nominal strain rates. Volumetric strain is calculated with the "parabolic method".

5.5.4 SEM Study

The PVC material was also investigated by SEM. The purpose was to explore the mechanism behind the measured increase in volume. Figure 5.66 shows undeformed PVC and Figure 5.67 and Figure 5.68 show stretched PVC, where the deformed sample corresponds to one of the PVC tests stretched at a strain rate of $10^{-2.5}\,\mathrm{s}^{-1}$. The SEM images are taken from a surface inside the sample, as shown in Figure 5.6 in the area of initial necking. The plane has then been elongated by a factor of about 2.7 in the one direction, and compressed to a factor of 0.14 in the other direction. Particles are present in the undeformed material but there are no apparent visible voids. The images of the deformed PVC on the other hand show around 100 ellipsoidal shaped pores with rigid particles at the center. The ellipsoidal pores are oriented along the stretching direction, shown with the red arrows. This seems to indicate that the mechanism of volume growth is the debonding of the material matrix from particles, creating a small void that continues to stretch with the material. The particle also seems to prevent the void from collapsing in the transverse direction. These observations agree with what was seen by Ognedal et al. [17], who also showed that the total volume of the voids corresponded with the macroscopically measured volumetric strain.

131
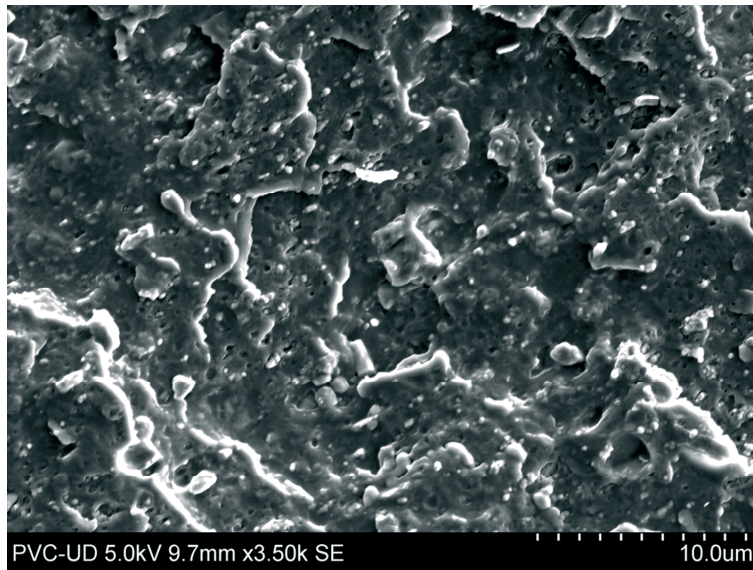
Figure 5.66: SEM micrograph of undeformed PVC, magnified 3500 times.
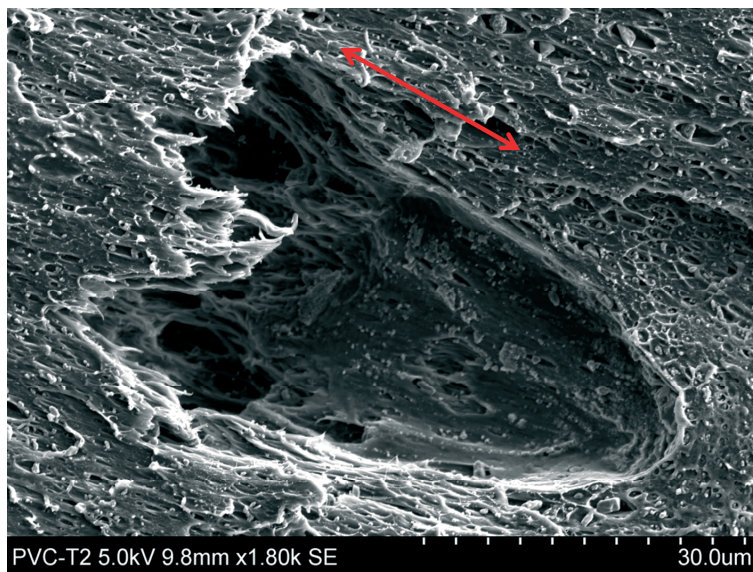
Figure 5.67: SEM micrograph of deformed PVC, magnified 1800 times. The red arrow indicates the tension direction.
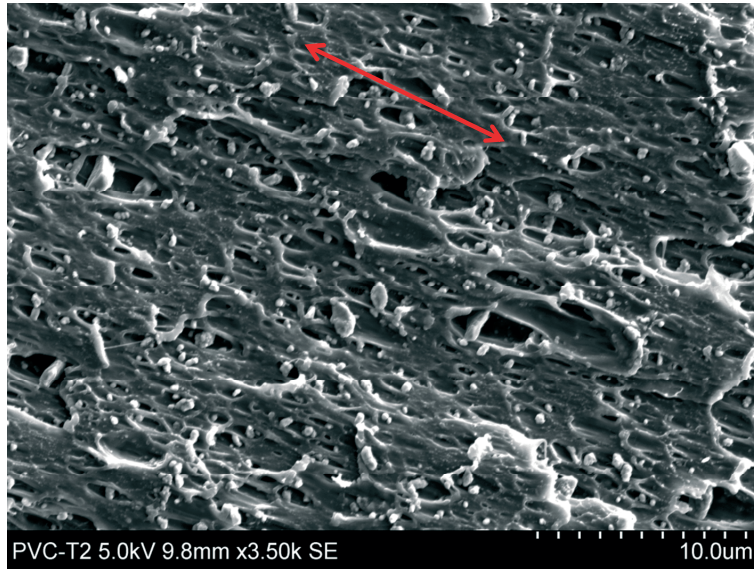
Figure 5.68: SEM micrograph of deformed PVC, magnified 3500 times. The red arrow indicates the tension direction

6 Compression tests

Two compression tests at a nominal strain rate of $10^{-2.5}\,\mathrm{s}^{-1}$ were performed for each of the two materials. Only one test per material was suited for edge tracing, meaning that curvature is only calculated for these two tests. The test samples were machined from extruded plates into cylinders with a height of 10 mm and a diameter of 8 mm, with the height of the cylinders along the extrusion direction of the plates. The samples were compressed between two smooth steel cylinders. To minimize friction at these contact surfaces a piece of teflon tape was applied to each side of the samples, and also lubricated with a small amount of oil. The tape was applied to the samples rather than the steel cylinders to avoid the problem of the sample carving in to the teflon. By applying the tape to the samples, it is deformed with the samples, providing a decrease in friction throughout the tests. The pieces of tape were neatly cut to fit the top of the samples, so as not to obstruct the view of the monitoring DIC camera. The samples were deformed past the point where DIC was feasible. Data is hence only presented for the ranges of deformation were DIC is applicable. Force and images were logged with a frequency of 5 Hz, resulting in approximately 700 data points per test.

6.1 Treatment of experimental data

The compression tests are also analyzed with the DIC algorithm presented in Chapter 2, but more elements are used to analyze the compression tests compared to the tension tests. The samples are meshed with 5×5 elements, with element height and width respectively of 210 and 180 pix. The mesh is shown in Figure 6.1, where it can be seen that the location of the mesh ensures that as much of the visible surface as possible is covered. The mesh is rotated to match the initial orientation of the sample.

6.1.1 Strain Measurements and Stress

Strains are calculated from a mean deformation gradient, as described in Section 4.1. Two approaches are used, where either the mean deformation gradient is calculated along a radial line, as shown in Figure 6.1, or it is calculated from all the elements in the analysis.

Longitudinal and radial strain is then defined in the same way as for tension tests, given by Equation (4.7).

<div style="text-align:center">Undeformed   Deformed</div>
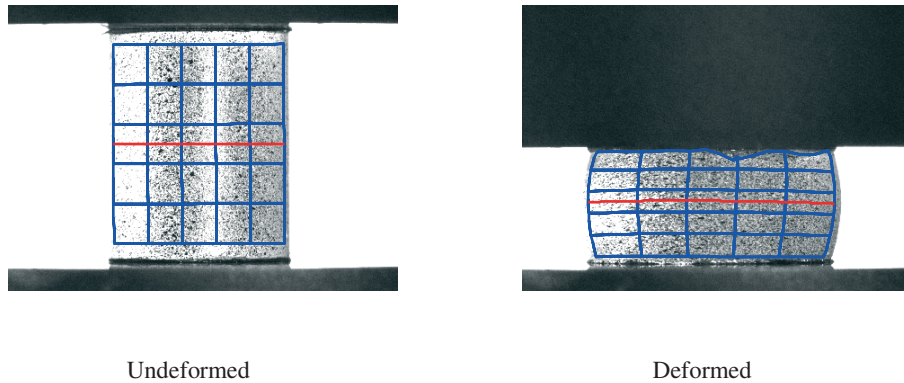
Figure 6.1: DIC mesh on a PVC compression test in undeformed and deformed states.

The volumetric strain is calculated as the natural logarithm of the volumetric stretch, defined in Equation (4.15), and true stress is calculated using Equation (4.21) .

The stress response is not corrected for strain rate. The reason for this is that strain rate does not vary significantly through the test (from $10^{-2.6}$ to $10^{-2.4} \mathrm{s}^{-1}$), compared to the tension tests. This comes as a result of less stress localization in the compression tests compared to the tension tests.

6.2 Results

The as-measured force-displacement data are shown in Figure 6.2. The response of PVC has a striking feature: there is a drop in force level right after yield. This is interesting since there is no local neck in compression, which suggests that the force reduction after yielding is related to material and not geometrical instabilities for PVC. It can also be seen that the test setup provides a good repeatability for both materials.
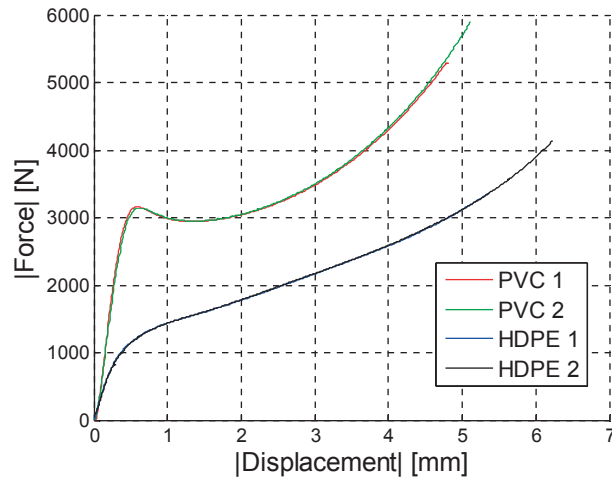
Figure 6.2: Force vs. displacement curves for PVC and HDPE in uniaxial compression deformed at a nominal strain rate of $10^{-2.5}$ s^{-1}.

Absolute true stress-strain curves for the four tests are shown in Figure 6.3. Stress and strain are here calculated locally for the center sections of the samples. The stress-strain response of PVC does still exhibit a drop in resistance, as would be expected from the force-displacement curves, followed by some hardening. From the HDPE curves it can be seen that there in no strain hardening after a strain levels of 0.4. As can be seen, the stress and strain behavior is also consistent between the two replicate tests for each material. In the remaining part of this section on the compression tests, only the samples PVC 1 and HDPE 1 will be considered.

137
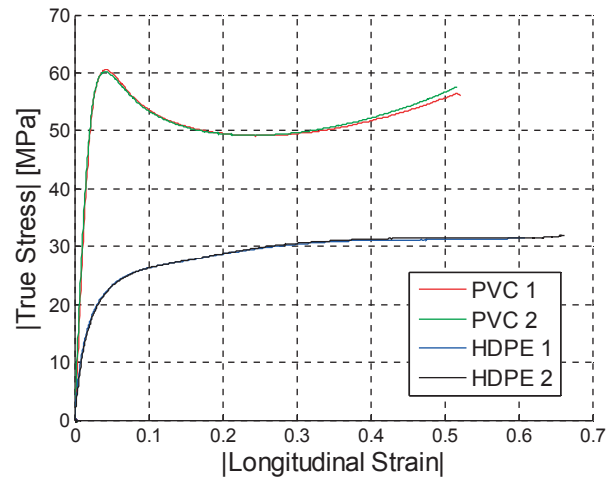
Figure 6.3: Stress vs. strain curves for HDPE and PVC in compression deformed at a nominal strain rate of $10^{-2.5}$ s^{-1}.

To investigate the difference between calculating stress and strain for the center section and calculating it from all the elements over the entire height of the specimen, the two approaches are compared in Figure 6.4. The response calculated from strains found from the center section of the sample is labelled "Local", while the curves labeled "Global" are found from the mean strains for the entire sample. As can be seen, the response is close to identical in the two cases, with the exception that larger longitudinal strains are present when the global mean strain is used. This is a result of the strain localizing at the top and/or the bottom of the sample when the sample starts to barrel, generating larger longitudinal strains in this region, compared to at the center of the sample.

138
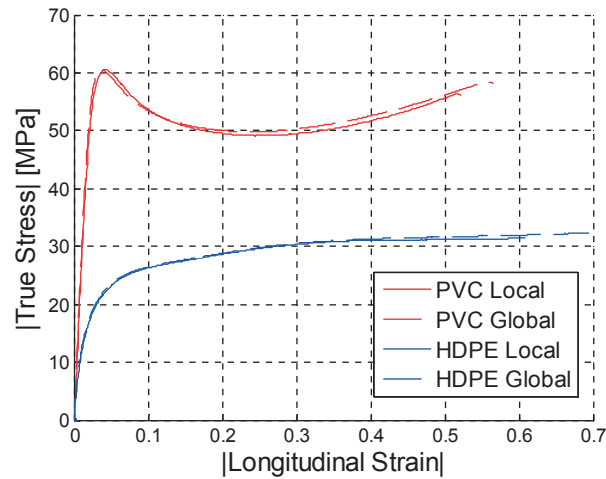
Figure 6.4: Stress vs. strain curves for HDPE and PVC in compression deformed at a nominal strain rate of $10^{-2.5}$ s^{-1}. Calculated with the average strains across the sample (Global) and with the center section strains (Local).

The difference in stress-strain behavior in compression and tension is shown in Figure 6.5 for both materials. The tension curves are the uncorrected curves from the tests performed at the same speeds. HDPE appears to have a very similar behavior for the two load cases up to a strain of about 0.4. On the other hand, PVC shows significantly different response in compression and tension. Firstly, the yield stress is about 18 MPa higher in compression, but this difference is reduced to about 10 MPa at a strain of 0.2. This can be explained by assuming that particle-matrix debonding determines the onset of yielding, and that this process requires more force in compression, involving debonding in two transverse directions, compared to tension. It is then a comparatively larger stress that has to be released in compression than in tension. The difference in stress between the two tests on PVC in compression and tension is reduced to about 8 MPa at the end of the softening process, i.e. at a longitudinal strain around 0.3. This offset of 8 MPa between the curves seems to be retained for the remaining part of the test, and is likely to be related to some intrinsic behavior of the matrix material.
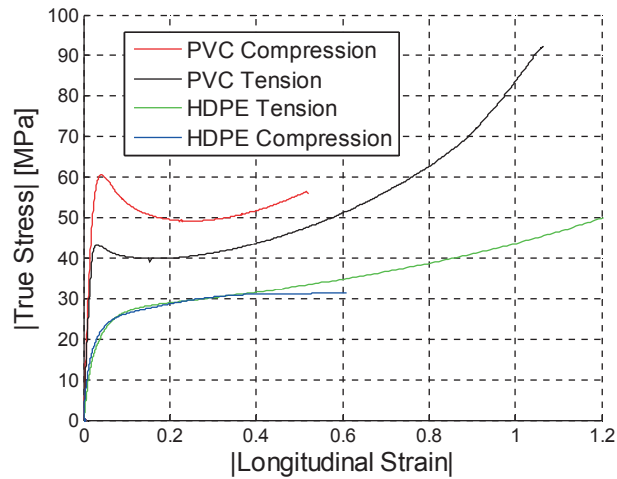
Figure 6.5: Comparison between stress-strain response in uniaxial compression and tension for PVC and HDPE stretched at a nominal strain rate of $10^{-2.5}$ s^{-1}.

The evolution of the curvature of the samples is interesting also in compression because this quantity gives an indication of the applicability of classical uniaxial loading assumptions and demonstrates the onset of barreling. The curvature was found with the algorithm described in Section 2.3.3, and is plotted against longitudinal strain for both samples in Figure 6.6. Curvature is found in a reoriented $H - R$ system as described in Section 3.2 where the H - axis is oriented along the length of the sample at a radius equal to zero and R is defined as positive. With this convention, a barreling compression test will have a negative signed curvature. As can be seen, there is a significant difference in longitudinal strain when the samples start to barrel. The onset of barreling in PVC occurs right after yielding, while the HDPE sample remains straight for a much longer time. The early onset of barreling for PVC can be seen as support for the involvement of particle debonding in yielding, as will be further discussed when the SEM images of the tested samples are studied.
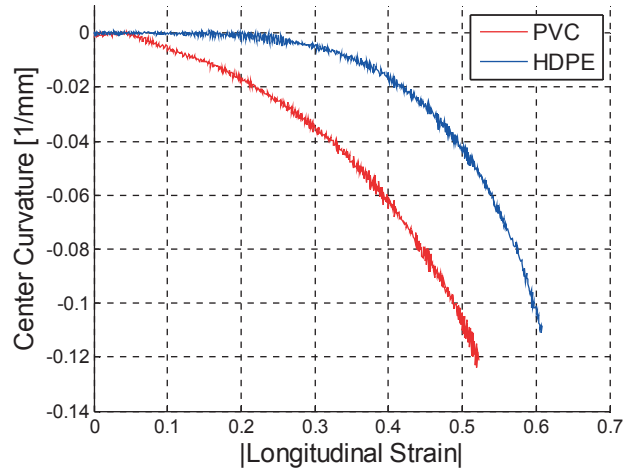
Figure 6.6: Center curvature vs. longitudinal strain response for PVC and HDPE in uniaxial compression deformed at a nominal strain rate of $10^{-2.5}$ s^{-1}. Negative curvature indicates barreling.

The volumetric strain is calculated in two ways. The local approach uses the strain measured locally at the center section, while the global volumetric strain is found for the entire sample. The volumetric strain is plotted against the absolute value of the longitudinal strain in Figure 6.7, where the first thing to note is the large discrepancy between the local and the global measurements. To try to explain this, it might be noted that the local measurement curve for HDPE changes tangent at about 0.3 in strain. Looking at the curvature-strain graph in Figure 6.6, it can be seen that HDPE starts to barrel around the same amount of strain. This is not believed to be a coincidence, since, according to the same argument as that used for the volume correction method presented in Section 4.2, barreling should lead to an overestimation of local volumetric strain. The same explanation can also be applied to the PVC test, where the divergence of the global and local volumetric strain happens earlier, as would be expected from the early barreling of the sample. The global response is hence assumed to best represent how the materials change volume in uniaxial compression. The global response then indicates that there is in fact an increase in volume for both materials when subjected to uniaxial compression. This is somewhat counterintuitive since hydrostatic stress in uniaxial compression is negative, but of importance for modelling the materials.

141
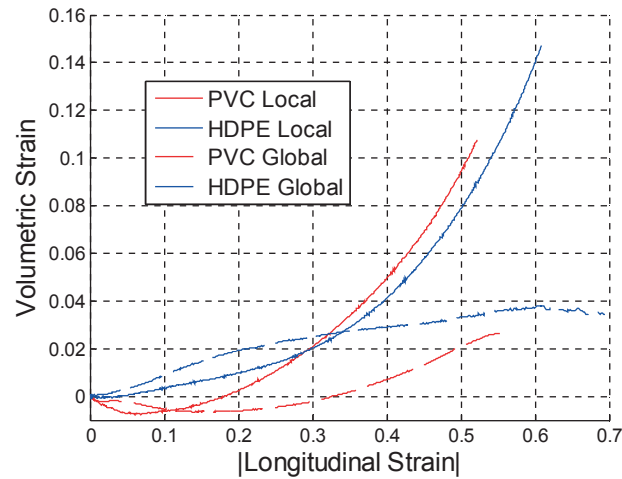
Figure 6.7: Volumetric strain vs. longitudinal strain for PVC and HDPE tested in uniaxial compression, calculated for the center section and the whole specimen.

6.3 SEM Investigation

The deformed samples were inspected with a SEM in order to study what occurs around the particles in the material. The deformed samples were cooled in liquid nitrogen before they were split in two. The splitting plane is the same as the cross section plane, so that the images represent a plane in the radial direction of the samples. The surfaces shown are from the center section of the sample, so they have undergone the deformation shown by the earlier figures.

The HDPE micrograph in Figure 6.8 does not exhibit many interesting features, and it is difficult to identify the particles seen in the undeformed material in Figure 5.47. Again this is believed to be related to the method of splitting the sample, where the fracture seems to have been more ductile than expected, creating a smeared surface.

The micrograph for the less ductile PVC is shown in Figure 6.9, where more features are visible. The particles are seen as white spheres, where the surrounding material is clearly not adhering to the particles. This seems to point to a mechanism where voids are created around particles in compression by debonding from the particles in the normal direction to the

142

applied force, while the particle keeps the void from collapsing. From the measured volumetric strain and curvature, debonding is believed to happen at yielding. This could serve as an explanation for relatively larger spike seen at yielding in compression compared to in tension, assuming debonding requires more force in compression than in tension.
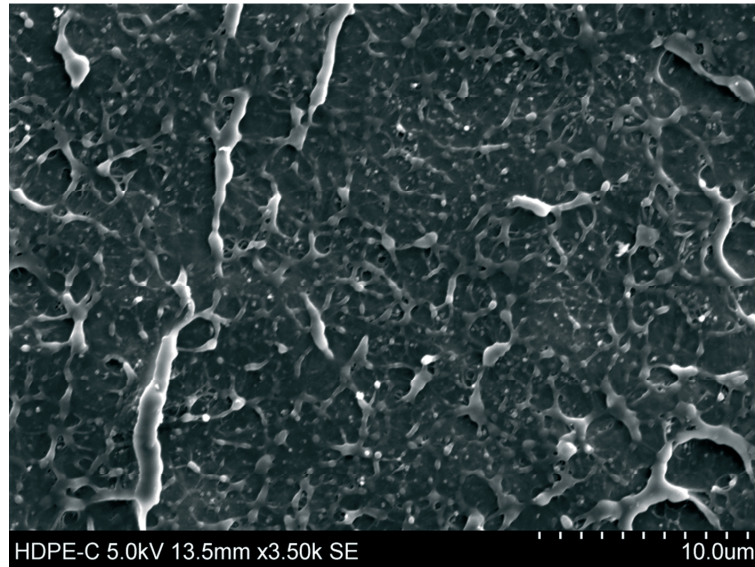
Figure 6.8: SEM micrograph of the interior of a HDPE sample deformed in uniaxial compression normal to the picture plane, sample split by cleaving, magnified 3500 times.
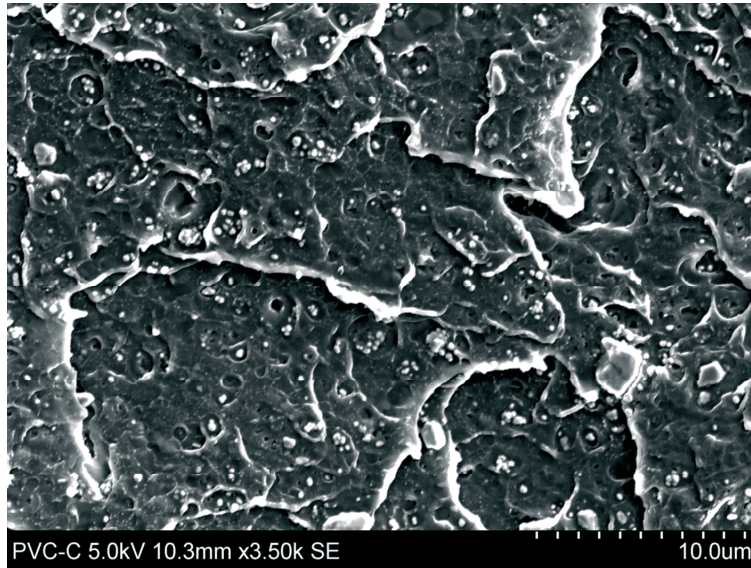
Figure 6.9: SEM micrograph of the interior of a PVC sample deformed in uniaxial compression normal to the picture plane, sample split by cleaving, magnified 3500 times.

7 Simulation

In order to validate and further analyze the experimental data, the performed tests are simulated with the finite element program Abaqus [38]. The simulations are performed with the explicit module of Abaqus, utilizing a user defined material model. A hyperelastic-viscoplastic constitutive relation previously presented by Polanco-Lorai et al. [7] was chosen as a base-line model. This model is reviewed in the next section. It appears that some of the features observed in the tests were not well captured by the model. Thus, the experimental observations are used to propose improvements of the model. This chapter presents numerical simulations of all tests and the implementation of a custom material model that allows for a more accurate investigation of the measured response.

7.1 Material model

The implemented material model is a modified version of the hyperelastic-viscoplastic model proposed by Polanco-Loria et al. [7]. As shown in Figure 7.1 (a), the model consists of two sub-models connected in parallel, designated Part A and Part B. The two parts are exposed to the same deformation gradient $\mathbf{F}$. Part A is classic elastic-viscoplastic model, yet it is expressed with the deformation gradient as the main kinematic variable. It uses a neo-Hookean elastic formulation with a Raghava [16] equivalent stress and a non-associated flow potential, also defined by the Raghava function, and an Arrhenius type of rate of flow [32]. The hyperelastic Part B represents the stretching of polymer chains, which is modeled with the non-linear entropic-elastic potential function proposed by Arruda and Boyce [39]. A fundamental assumption in the model is that the total deformation gradient $\mathbf{F}$ is equal to the deformation gradients $\mathbf{F}_A$ and $\mathbf{F}_B$ of Parts A and B, respectively, emphasizing the parallel nature of the model. The multiplicative decomposition of the deformation gradient of Part A, $\mathbf{F}_A = \mathbf{F}$, into a plastic and an elastic part, designated $\mathbf{F}_p$ and $\mathbf{F}_e$ respectively, is illustrated in Figure 7.1 (b).

(a) Rheological Model
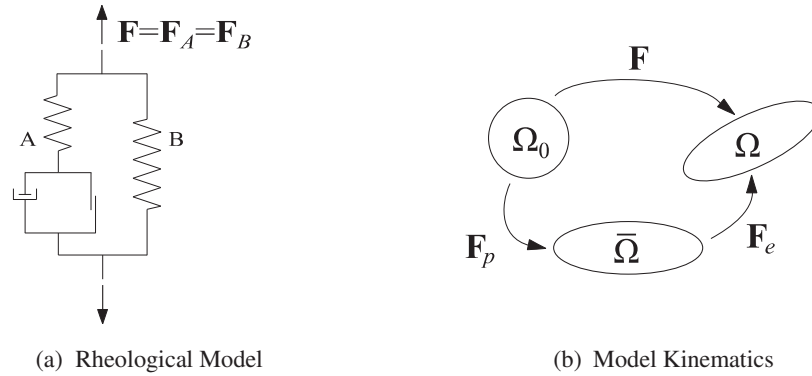
(b) Model Kinematics

Figure 7.1: Material model whit rheological model in subfigure (a), and the kinematics shown in subfigure (b).

7.1.1 Part A

A multiplicative split of the deformation gradient $\mathbf{F}_A = \mathbf{F}$ gives

$$\mathbf{F} = \mathbf{F}_e \mathbf{F}_p \tag{7.1}$$

The plastic deformation gradient $\mathbf{F}_p$ maps a material point from an undeformed configuration Ω_0 to an incompatible intermediate configuration $\overline{\Omega}$, while the elastic deformation gradient $\mathbf{F}_e$ maps the material point from the intermediate configuration $\overline{\Omega}$ to a current configuration Ω, as illustrated in Figure 7.1 (b). The velocity gradient $\mathbf{L} = \mathbf{L}_A$ is defined in the current configuration Ω as

$$\mathbf{L} = \dot{\mathbf{F}}\mathbf{F}^{-1} \tag{7.2}$$

Inserting Equation (7.1) into Equation (7.2), then gives

$$\mathbf{L} = \dot{\mathbf{F}}_e \mathbf{F}_e^{-1} + \mathbf{F}_e \dot{\mathbf{F}}_p \mathbf{F}_p^{-1} \mathbf{F}_e^{-1} = \mathbf{L}_e + \mathbf{L}_p \tag{7.3}$$

where $\mathbf{L}_e$ and $\mathbf{L}_p$ are the elastic and plastic velocity gradients, respectively, in the current configuration Ω. Plastic deformation power P_d of Part A is equal to

146

$$P_d = \int_V \boldsymbol{\sigma}_A : \mathbf{L}_p dV \tag{7.4}$$

where $\boldsymbol{\sigma}_A$ is the Cauchy stress tensor of Part A, and dV represents an infinitesimal current volume. Inserting the expression for the plastic velocity gradient into the equation for plastic power, we get

$$
\begin{aligned}
P_d &= \int_V \boldsymbol{\sigma}_A : \mathbf{F}_e \dot{\mathbf{F}}_p \mathbf{F}_p^{-1} \mathbf{F}_e^{-1} dV \\
&= \int_{\overline{V}} J_e \mathbf{F}_e^T \boldsymbol{\sigma}_A \mathbf{F}_e^{-T} : \dot{\mathbf{F}}_p \mathbf{F}_p^{-1} d\overline{V} = \int_{\overline{V}} \overline{\boldsymbol{\Sigma}}_A : \overline{\mathbf{L}}_p d\overline{V}
\end{aligned}
\tag{7.5}
$$

where $d\overline{V} = J_e dV$ is an infinitesimal volume in the intermediate configuration $\overline{\Omega}$, and $J_e = \det(\mathbf{F}_e)$ is the elastic change of volume. Further, the Mandel stress $\overline{\boldsymbol{\Sigma}}_A$ on the intermediate configuration is defined as

$$\overline{\boldsymbol{\Sigma}}_A = J_e \mathbf{F}_e^T \boldsymbol{\sigma}_A \mathbf{F}_e^{-T} \tag{7.6}$$

Equation (7.5) also introduces $\overline{\mathbf{L}}_p$ as the rate-of-plastic-deformation tensor conjugate to the Mandel stress, where $\overline{\mathbf{L}}_p$ is expressed in the intermediate configuration $\overline{\Omega}$ as

$$\overline{\mathbf{L}}_p = \dot{\mathbf{F}}_p \mathbf{F}_p^{-1} \tag{7.7}$$

The elastic Neo-Hookean potential function used in Part A is given as [40]

$$U(\mathbf{C}_e) = \frac{1}{2} \mu_e \left(\ln J_e \right)^2 - \lambda_e \ln J_e + \frac{1}{2} \lambda_e (\operatorname{tr} \mathbf{C}_e - 3) \tag{7.8}$$

where μ_e and λ_e are the Lamé constants and $\mathbf{C}_e$ is the elastic right Cauchy-Green deformation tensor, defined as $\mathbf{C}_e = \mathbf{F}_e^T \mathbf{F}_e$. The two Lamé constants may be exchanged with the more familiar elastic constants E and ν, corresponding respectively to Young's modulus and Poisson's ratio.

The Mandel stress tensor for Part A, $\overline{\boldsymbol{\Sigma}}_A$, may then be expressed in the $\overline{\Omega}$ configuration as [7]

$$\bar{\mathbf{\Sigma}}_A = 2\mathbf{C}_e \frac{\partial U}{\partial \mathbf{C}_e} = \lambda_e \ln(J_e)\mathbf{I} + \mu(\mathbf{C}_e - \mathbf{I}) \tag{7.9}$$

where $\mathbf{I}$ is the second-order unit tensor.

The equivalent stress proposed by Raghava et al. [16] reads

$$\bar{\sigma}_A = \frac{(\alpha-1)I_{1A} + \sqrt{(\alpha-1)^2 I_{1A}^2 + 12\alpha J_{2A}}}{2\alpha} \tag{7.10}$$

where $I_{1A} = \operatorname{tr}\bar{\mathbf{\Sigma}}_A$ and $J_{2A} = 1/2\,\bar{\mathbf{\Sigma}}_A^{\mathrm{dev}} : \bar{\mathbf{\Sigma}}_A^{\mathrm{dev}}$ are respectively the first invariant and the second deviatoric invariant of the Mandel stress tensor of Part A. The deviatoric part of the Mandel stress tensor in Part A is defined as $\bar{\mathbf{\Sigma}}_A^{\mathrm{dev}} = \bar{\mathbf{\Sigma}}_A - (1/3)\left(\operatorname{tr}\bar{\mathbf{\Sigma}}_A\right)\mathbf{I}$. The material parameter $\alpha \geq 1$ controls hydrostatic stress dependency, and is commonly defined as the ratio between the yield stresses $\sigma_{A,C}$ and $\sigma_{A,T}$ in compression and tension, respectively, i.e. $\alpha = \sigma_{A,C}/\sigma_{A,T}$. It may be noted that $\alpha = 1$ reduces the equivalent stress to $\bar{\sigma}_A = \sqrt{3J_{2A}}$, which is the Mises equivalent stress. The Raghava equivalent stress also corresponds to the applied stress in uniaxial tension, and α times the absolute value of the applied stress in uniaxial compression.

The flow potential function g is similarly expressed as

$$g = \frac{(\beta-1)I_{1A} + \sqrt{(\beta-1)^2 I_{1A}^2 + 12\beta J_{2A}}}{2\beta} \geq 0 \tag{7.11}$$

where $\beta \geq 1$ controls the plastic volumetric growth. The model is thus non-associated for $\alpha \neq \beta$, and this possibility allows for a more precise representation of plastic dilatation than an associated formulation does. The plastic velocity gradient tensor $\bar{\mathbf{L}}_p$ in the intermediate configuration is defined by the flow rule

$$\bar{\mathbf{L}}_p = \dot{\mathbf{F}}_p \mathbf{F}_p^{-1} = \dot{\lambda}_p \frac{\partial g}{\partial \bar{\mathbf{\Sigma}}_A} = \dot{\lambda}_p \left(g_1 \mathbf{I} + g_2 \bar{\mathbf{\Sigma}}_A^{\mathrm{dev}} \right) \tag{7.12}$$

148

where $\dot{\lambda}_p$ is the rate of the plastic multiplier and the gradients g_1 and g_2 of the flow potential function are defined as

$$g_1 = \frac{\partial g}{\partial I_{1A}} = \frac{\beta-1}{2\beta} + \frac{(\beta-1)^2 I_{1A}}{2\beta\sqrt{(\beta-1)^2 I_{1A}^2 + 12\beta J_{2A}}}$$
$$g_2 = \frac{\partial g}{\partial J_{2A}} = \frac{3}{\sqrt{(\beta-1)^2 I_{1A}^2 + 12\beta J_{2A}}} \qquad (7.13)$$

Inserting Equation (7.12) into the expression for the plastic deformation power, see Equation (7.5), gives

$$P_d = \int_V \bar{\Sigma}_A : \bar{L}_p d\bar{V} = \int_V \bar{\Sigma}_A : \dot{\lambda}_p \frac{\partial g}{\partial \bar{\Sigma}_A} d\bar{V} = \int_V \dot{\lambda}_p g d\bar{V} \qquad (7.14)$$

which is non-negative when $\dot{\lambda}_p \geq 0$. It is also of interest to look at the relationship between the plastic multiplier and the equivalent plastic strain rate $\dot{p}$, which can be found from the integrand of Equation (7.14) by enforcing the equality

$$\bar{\Sigma}_A : \bar{L}_p = \dot{\lambda}_p g = \bar{\sigma}_A \dot{p} \qquad (7.15)$$

which defines the relationship between the plastic multiplier and the equivalent plastic strain rate as

$$\dot{\lambda}_p = \dot{p} \frac{\bar{\sigma}_A}{g} \qquad (7.16)$$

The equivalent plastic strain rate is defined by the Arrhenius type relationship

$$\dot{p} = \begin{cases} 0 & \text{if } f \leq 0 \\ \dot{p}_0 \left[\exp\left(\frac{\bar{\sigma}_A - \sigma_{A0}}{C}\right) - 1 \right] & \text{if } f > 0 \end{cases} \qquad (7.17)$$

149

where $\dot{p}_0$ is a reference plastic strain rate, $\sigma_{A0} = \sigma_{A0}(p)$ is the stress response of Part A in uniaxial tension at the reference plastic strain rate, and C is a parameter controlling the plastic viscosity. The yield function f can then be written as

$$f = \bar{\sigma}_A - \sigma_{A0}(p) \tag{7.18}$$

For $f > 0$, Equation (7.17) defines the constitutive visco-plastic relation for Part A as

$$\bar{\sigma}_A = \sigma_{A0}(p) + C \ln\left(1 + \frac{\dot{p}}{\dot{p}_0}\right) \tag{7.19}$$

This equation differs from the constitutive visco-plastic relation proposed by Polanco-Loria et al. [7] in that the term containing the plastic viscosity now is added to the strain hardening term $\sigma_{A0}(p)$, whereas they used a multiplicative relation. The strain hardening response of Part A, $\sigma_{A0}(p)$, is assumed to be a Voce-type function of the equivalent plastic strain p, defined as

$$\sigma_{A0}(p) = \sigma_{y0} + \sum_{i=1}^{2} Q_i \left[1 - \exp(-C_i p)\right] \tag{7.20}$$

where σ_{y0} corresponds to the yield stress in uniaxial tension at the reference plastic strain rate $\dot{p}_0$, and the shape of the strain-hardening curve is described by the Voce parameters Q_i and C_i, where $i = 1, 2$.

7.1.2 Part B

Part B, representing chain resistance from orientation and stretching, is based on the Arruda-Boyce model [39]. The constitutive law can be written for Cauchy stress tensor as

$$\boldsymbol{\sigma}_B = \frac{1}{J} \frac{C_R \bar{\lambda}_L}{3\bar{\lambda}} \mathcal{L}^{-1}\left(\frac{\bar{\lambda}}{\bar{\lambda}_L}\right) \left(\mathbf{B}^* - \bar{\lambda}^2 \mathbf{I}\right) \tag{7.21}$$

150

The material parameters C_R and $\bar{\lambda}_L$ describe the initial stiffness and the locking stretch, respectively. The function $\mathcal{L}^{-1}$ is the inverse of the Langevin function $\mathcal{L}(x) = \coth(x) - 1/x$ and J is the determinant of the deformation gradient. The effective distortional stretch $\bar{\lambda}$ is calculated from the distortional left Cauchy-Green deformation tensor $\mathbf{B}^*$ as

$$\bar{\lambda} = \sqrt{\frac{1}{3} \operatorname{tr}\left(\mathbf{B}^*\right)} \tag{7.22}$$

where $\mathbf{B}^*$ is calculated as

$$\mathbf{B}^* = \left(\mathbf{F}^*\right)\left(\mathbf{F}^*\right)^T, \; \mathbf{F}^* = J^{-1/3}\mathbf{F} \tag{7.23}$$

There exists no analytical expression for the inverse function $\mathcal{L}^{-1}$ of the Langevin function. An approximation recently proposed by Jedynak [41] is used herein. The approximation reads

$$\mathcal{L}^{-1}(x) \approx x \frac{3 - 2.6x + 0.7x^2}{(1-x)(1+0.1x)} \tag{7.24}$$

An important aspect of the network stretching model is how its response differs depending on the type of deformation. It is of special interest in this thesis to look at the difference in response between uniaxial compression and tension. This can be done by looking at the first element of an assumed diagonal stress tensor $\boldsymbol{\sigma}_B$, denoted $\sigma_{B,1}$, in uniaxial tension and compression. The ratio s between these two stress components can then be defined as

$$s\left(\mathbf{F}^t, \mathbf{F}^c, \bar{\lambda}_L\right) = \frac{\sigma_{B,1}\left(\mathbf{F}^t, \bar{\lambda}_L\right)}{-\sigma_{B,1}\left(\mathbf{F}^c, \bar{\lambda}_L\right)} \tag{7.25}$$

where $\mathbf{F}^t$ and $\mathbf{F}^c$ are the resulting deformation gradients when a material point is loaded in uniaxial tension and compression respectively. Assuming that these two deformation gradients only have non-zero elements on the main diagonal and that the second and third diagonal elements are equal, they can be written as

$$\mathbf{F}^t\left(\lambda_1^t, J\right) = \begin{bmatrix} \lambda_1^t & 0 & 0 \\ 0 & \sqrt{\left(J / \lambda_1^t\right)} & 0 \\ 0 & 0 & \sqrt{\left(J / \lambda_1^t\right)} \end{bmatrix} \qquad (7.26)$$

and

$$\mathbf{F}^c\left(\lambda_1^c, J\right) = \begin{bmatrix} \lambda_1^c & 0 & 0 \\ 0 & \sqrt{\left(J / \lambda_1^c\right)} & 0 \\ 0 & 0 & \sqrt{\left(J / \lambda_1^c\right)} \end{bmatrix} \qquad (7.27)$$

where λ_1^t and λ_1^c are the stretches in the 1 direction, representing the loading direction. The determinant J of the deformation gradients is assumed to be equal in both deformation modes since the case of isochoric behavior is going to be investigated. We now want to evaluate the ratio s at comparable states of uniaxial tension and compression. It is here chosen to evaluate the ratio s when

$$\varepsilon_1^c = -\varepsilon_1^t \qquad (7.28)$$

where ε_1^c and ε_1^t is the logarithmic strain in the 1 direction in compression and tension, respectively. Recalling the relation $\varepsilon = \ln(\lambda)$ between logarithmic strain and stretch, this gives the relation

$$\lambda_1^c = \frac{1}{\lambda_1^t} \qquad (7.29)$$

Inserting this result into Equations (7.26) and (7.27), we can write both deformation gradients in terms of the stretch λ_1^t and the determinant J. The deformation gradients can again be inserted into Equation (7.25), and we get the ratio s as a function of the variables λ_1^t and J, and the constant $\bar{\lambda}_L$. This ratio is plotted in Figure 7.2 against the logarithmic longitudinal strain ε_1^t for the case of $\bar{\lambda}_L = 6$ and $J = 1$. As evident from the figure, the stress ratio s

152

increases rapidly from unity, and Part B has hence a significantly larger contribution to the stiffness in uniaxial tension compared to uniaxial compression. This ratio goes towards infinity when the effective distortional stretch approaches the locking stretch, i.e. when $\bar{\lambda} \to \bar{\lambda}_L$.
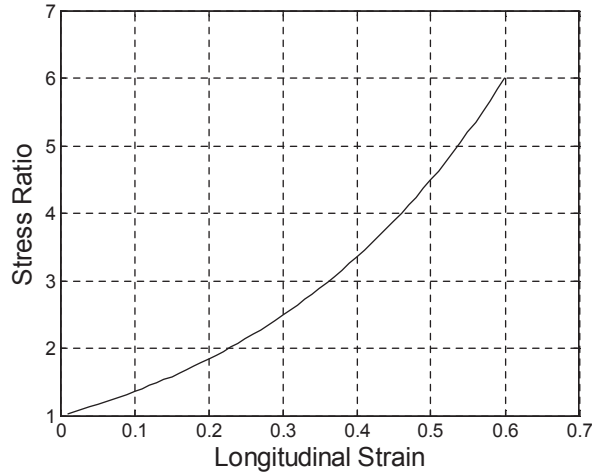
Figure 7.2: Part B stress response ratio from uniaxial tension and compression as a function of longitudinal strain calculated with no volume change and a locking stretch equal to 6.

The parameters of the entire model are summarized in Table 7.1 where the Lamé constants μ_e and λ_e of Equation (7.8) have been replaced by the classic elastic constants E and ν. As emphasized at the start of the chapter, the model relies on the framework described by Polanco-Loria et al. [7]. The main modifications so far are that an additive rather than multiplicative formulation of the strain-rate dependency is employed, see Equation (7.19), and strain-hardening described by the Voce law is introduced in Equation (7.20).

Table 7.1: Parameters for the base-line polymer model.

Elasticity		Yielding	Plastic hardening				Plastic rate dependency		Pressure sensitivity	Plastic dilatation	Elastic network	
E	ν	σ_{y0}	Q_1	C_1	Q_2	C_2	C	$\dot{p}_0$	α	β	C_R	$\bar{\lambda}_L$

7.1.3 Change of Volume During Plastic Deformation

The experimental tests have revealed that there is a significant increase of volume during plastic deformation in both materials. It is therefore of interest to look closer at the evolution of volumetric strain in the model. Equation (7.12) gives

$$\dot{\mathbf{F}}_p = \dot{\lambda}_p \frac{\partial g}{\partial \bar{\boldsymbol{\Sigma}}_A} \mathbf{F}_p = \dot{\lambda}_p \mathbf{r} \mathbf{F}_p \qquad (7.30)$$

where $\mathbf{r} = \partial g / \partial \bar{\boldsymbol{\Sigma}}_A$ is defined in Equation (7.13) as

$$\mathbf{r} = g_1 \mathbf{I} + g_2 \bar{\boldsymbol{\Sigma}}_A^{\mathrm{dev}} \qquad (7.31)$$

representing the gradient of the flow potential function g. We now assume that $\mathbf{F} = \mathbf{U} = \mathbf{F}_p$, i.e. that the deformation process is purely plastic and that stretching only occurs along the eigenvectors of $\mathbf{F}_p$. A further assumption is that that the second and third eigenvalue have the same values. The plastic deformation gradient can then be written as

$$\mathbf{F}_p = \begin{bmatrix} \lambda_1 & 0 & 0 \\ 0 & \lambda_2 & 0 \\ 0 & 0 & \lambda_2 \end{bmatrix} \qquad (7.32)$$

From Equation (7.12) it can also be seen that $\partial g / \partial \bar{\boldsymbol{\Sigma}}_A$, which is equal to $\mathbf{r}$, becomes a diagonal tensor for a diagonal stress tensor. Assuming that the second and third eigenvalues of $\mathbf{r}$ are equal, the diagonal elements of $\mathbf{r}$ can be written as r_1, r_2 and r_2. Equation (7.30) is now written as

$$\dot{\mathbf{F}}_p = \dot{\lambda}_p \begin{bmatrix} r_1 \lambda_1 & 0 & 0 \\ 0 & r_2 \lambda_2 & 0 \\ 0 & 0 & r_2 \lambda_2 \end{bmatrix} \qquad (7.33)$$

Let now λ_1 be equal to

$$\lambda_1 = 1 + \dot{\lambda}_1 t \qquad (7.34)$$

154

where $\dot{\lambda}_1$ represents a constant stretch rate and t represents time. This is equivalent to $\dot{F}_{p,11} = \dot{\lambda}_1$, and the plastic multiplier $\dot{\lambda}_p$ is then according to Equation (7.33) equal to

$$\dot{\lambda}_p = \frac{\dot{\lambda}_1}{r_1 \lambda_1} \tag{7.35}$$

Applying this expression for the plastic multiplier $\dot{\lambda}_p$ for the transverse component $\dot{F}_{p,22}$ yields

$$\dot{F}_{p,22} = \dot{\lambda}_2 = \dot{\lambda}_p r_2 \lambda_2 = \frac{\dot{\lambda}_1}{\lambda_1 r_1} r_2 \lambda_2 \tag{7.36}$$

A differential equation can then be defined for the unknown λ_2

$$\frac{1}{\lambda_2} d\lambda_2 = \frac{r_2}{r_1} \frac{1}{\lambda_1} d\lambda_1 \tag{7.37}$$

If the ratio r_2 / r_1 is assumed to be constant, the differential equation can be solved to give

$$\int_1^{\lambda_2} \frac{1}{\lambda_2} d\lambda_2 = \frac{r_2}{r_1} \int_1^{\lambda_1} \frac{1}{\lambda_1} d\lambda_1 \quad \Rightarrow \quad \ln(\lambda_2) = \frac{r_2}{r_1} \ln(\lambda_1) \tag{7.38}$$

Recalling that the relation between true strain and stretch reads $\varepsilon_i = \ln(\lambda_i)$, the transverse strain can be calculated from

$$\varepsilon_2 = \frac{r_2}{r_1} \varepsilon_1 \tag{7.39}$$

The volumetric strain ε_V is equal to $\varepsilon_V = \varepsilon_1 + 2\varepsilon_2$. The ratio γ between volumetric strain and longitudinal strain can then be expressed as

$$\frac{\varepsilon_V}{\varepsilon_1} = \gamma = 1 + 2\frac{r_2}{r_1} \tag{7.40}$$

155

The volumetric strain ratio γ can now be calculated for different stress states. For the special cases of uniaxial loading, we can write the deviatoric Mandel stress tensor as

$$\overline{\Sigma}_A^{dev} = \frac{1}{3}\sigma \begin{bmatrix} 2 & 0 & 0 \\ 0 & -1 & 0 \\ 0 & 0 & -1 \end{bmatrix} \tag{7.41}$$

where σ is the applied uniaxial stress. The first invariant of the Mandel stress tensor in the case of uniaxial tension and compression is respectively $I_{1A}^t = \sigma$ and $I_{1A}^c = -\sigma$, while the second deviatoric invariant is equal to $J_{2A} = \sigma^2/3$ for both loading modes. The functions g_1 and g_2 in Equation (7.13) can then be written as

$$\begin{aligned} g_1^t &= \frac{\beta-1}{\beta+1} & g_2^t &= \frac{3}{\sigma(\beta+1)} \\ g_1^c &= \frac{\beta-1}{\beta(\beta+1)} & g_2^c &= \frac{3}{|\sigma|(\beta+1)} \end{aligned} \tag{7.42}$$

where the superscripts t and c indicates $\sigma > 0$ and $\sigma < 0$, respectively, or simply tension or compression. The ratio r_2/r_1 can now be evaluated, and for tension and compression respectively we get from Equation (7.31)

$$\begin{aligned} \frac{r_2^t}{r_1^t} &= \frac{g_1^t - g_2^t\sigma/3}{g_1^t + 2g_2^t\sigma/3} = \frac{\beta-2}{\beta+1} \\ \frac{r_2^c}{r_1^c} &= \frac{g_1^c - g_2^c\sigma/3}{g_1^c + 2g_2^c\sigma/3} = -\frac{2\beta-1}{\beta+1} \end{aligned} \tag{7.43}$$

It is now possible to find the γ ratio for these two load cases, where for uniaxial tension we get

$$\gamma_{UT} = \frac{3(\beta-1)}{\beta+1} \tag{7.44}$$

and for uniaxial compression we get

$$\gamma_{UC} = -\frac{3(\beta - 1)}{\beta + 1} \qquad (7.45)$$

where γ_{UT} and γ_{UC} is the volume to length strain ratio in uniaxial tension and uniaxial compression, respectively. Considering the shape of the flow potential, which is defined by the Raghava function in Equation (7.11), it is a bit counter-intuitive that the absolute values of these two volumetric strain ratios are equal. The similarity between tension and compression arises from the fact that logarithmic strain is being used in the ratio, while the partial derivatives of the flow potential controls the plastic deformation gradient via the plastic velocity gradient. Nevertheless, if the ratio γ_{UT} is known from an experiment, it is then possible to calculate an appropriate β value for a simulation by solving Equation (7.44) for β and get

$$\beta = \frac{\gamma_{UT} + 3}{3 - \gamma_{UT}} \qquad (7.46)$$

This expression is useful for calibration of β from a uniaxial tension test.

It is also of interest to investigate the models response when β is assumed to vary with the strain component ε_1, which then implies a non-constant ratio r_2 / r_1. From Equation (7.37) we get the relation

$$d\lambda_2 = \frac{r_2}{r_1} \frac{\lambda_2}{\lambda_1} d\lambda_1 \qquad (7.47)$$

Volumetric stretch is calculated as $\lambda_V = \lambda_1 \lambda_2^2$. An infinitesimal change in volumetric stretch is then equal to

$$d\lambda_V = \lambda_2^2 d\lambda_1 + 2\lambda_1 \lambda_2 d\lambda_2 \qquad (7.48)$$

By inserting Equation (7.47) into Equation (7.48) we then get the relation

$$d\lambda_V = \left(1 + 2\frac{r_2}{r_1}\right)\lambda_2^2 d\lambda_1 \qquad (7.49)$$

157

Using the relations $\lambda_V = \exp(\varepsilon_V)$ and $\lambda_1 = \exp(\varepsilon_1)$, we can substitute $d\lambda_V$ and $d\lambda_1$ in Equation (7.49) and get the relation

$$\frac{d\varepsilon_V}{d\varepsilon_1} = \left(1 + 2\frac{r_2}{r_1}\right) \tag{7.50}$$

The ratio r_2 / r_1 is for uniaxial tension defined in Equation (7.43)$_\mathrm{I}$, and inserting it into Equation (7.50) we the final equation for the change in volumetric strain becomes

$$\frac{d\varepsilon_V}{d\varepsilon_1} = \frac{3(\beta(\varepsilon_1) - 1)}{\beta(\varepsilon_1) + 1} \tag{7.51}$$

or solved for β and assuming that $\varepsilon_1 = p$ and $\varepsilon_V = \varepsilon_V^p$

$$\beta(p) = \frac{\dfrac{d\varepsilon_V^p}{dp}(p) + 3}{3 - \dfrac{d\varepsilon_V^p}{dp}(p)} \tag{7.52}$$

This relation can now be used to find an evolution law for β as a function of equivalent plastic strain p from experimental data.

7.2 Simulation of Material Tests

Chapter 5 presented uniaxial tension tests on two polymeric materials; HDPE and PVC. Moreover, two different samples were used in the tension tests; one with circular and one with rectangular cross-section. The tests were carried out at different strain rates, and the increase of temperature during plastic deformation was measured for the test series with rectangular cross section. The uniaxial compression tests on both materials followed in Chapter 6.

Applying the material model outlined in Section 7.1, numerical simulations of the material tests presented in Chapters 5 and 6 will here be compared with the experimental results. To this end, all data reported from the simulations, if not stated otherwise, will be extracted from the surface of the simulated samples. This way of finding the strains etc. in the simulations

corresponds closely to how the strains were determined in the tests, and hence provides the best basis for comparison. The strains reported from the simulations are calculated from the coordinates of surface nodes in the cross-section first experiencing necking. These strains are further used to calculate the current area of the cross-section.

Throughout the subsequent sections, the experimental observations will be used to augment the baseline constitutive model presented in Section 7.1. In particular, an improved description of the dilatation will be included in the model in Sections 7.2.1 and 7.2.3. Both these sections address HDPE. Additionally, incorporation of the temperature-dependent flow stress curve proposed in Chapter 4 is presented in Section 7.2.3.

All the performed simulations are explicit simulations. Mass scaling is used in all simulations in order to keep the time steps at a reasonable level. This can lead to unwanted oscillations and unrealistic inertia forces. In order to avoid this, kinetic energy is monitored, and the ratio total kinetic energy divided by total strain energy is not allowed to exceed 2% at any point during the simulation. A second simulations parameter is the choice of element. The simulations of the tests of both HDPE and PVC using dog-bone samples use a reduced integrated 8-noded thermally coupled brick elements with the Abaqus designation C3D8RT. Simulations of the circular PVC tension samples as well as the cylindrical PVC compression tests both use reduced integrated 4-noded thermally coupled axisymmetric elements designated CAX4RT. The circular HDPE tension samples as well as the cylindrical HDPE compression tests are simulated without thermal coupling and use reduced 4-noded axisymmetric elements with the designation CAX4R. Hourglass control is used to minimize spurious modes, and as with kinetic energy, total hourglass energy is controlled against total strain energy. The accepted ratio of hourglass energy to strain energy is set to 5%.

7.2.1 HDPE Samples with Circular Cross-section

The circular HDPE tension tests are the first tests to be simulated since the effects of adiabatic heating on material behavior seemed to be negligible, as shown in Section 5.4. On the other hand, the determination of the volumetric strain is quite accurate for this sample geometry, and it also facilitated true strains exceeding 2. The experimental results were presented in Section 5.4. For the numerical simulations, it is assumed that an axisymmetric half-model is

able to represent the behavior of the test specimen. The mesh used in the simulations is shown in Figure 7.3. It is observed that the elements in the gauge part of the model are rectangular with a 4:1 ratio in width versus length. This is done in order to better preserve reasonable element dimension ratios as the mesh undergoes large deformations. It might also be noted that the grip of the simulated sample is shorter than the grip of the actual samples. The samples in the numerical model have a grip length of 10 mm, whereas the tested samples had a grip length of 20 mm, as seen in Figure 5.2.

In the same way as in the test, the simulations were performed under displacement control. A constant velocity corresponding to half of the nominal cross-head velocity of the testing machine was applied to the exterior grip nodes which are shown as red dots on the lower right horizontal edge of Figure 7.3. This loading length and location roughly corresponds to the size of the clamps that stretched the samples during the experiments. The remaining unloaded grip area closest to the sample shoulders in Figure 7.3 can also be seen in the experiments in Figure 5.36. Crosshead displacement is measured as the horizontal translation of the bottom right node. Any compliance of the test machine was disregarded.

In all simulations the neck initiated at the center of the sample, corresponding to the left vertical boundary of the mesh in Figure 7.3. All local data presented is hence calculated for this section.
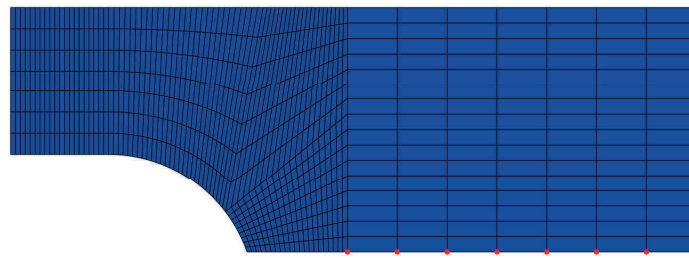
Figure 7.3: Mesh for simulations of circular HDPE samples in tension.

The material constants for the simulations are given in Table 7.2. The elastic parameters ν and E are found from Figure 5.10 (a) and (b) respectively. For numerical stability it is chosen to apply a value slightly lower than 0.5 for ν, while Young's modulus E was taken at a strain of approx. 0.025 for the slowest tests in Figure 5.10 (b). It should be kept in mind, however,

160

that the elastic response is not the central topic of this investigation, and it is anticipated that the elastic response of the samples with circular cross-section does not differ much from the observations in Figure 5.10, which addresses tests on rectangular-shaped samples. Plastic hardening is described using only one term of the Voce hardening described by Equation (7.20), where the two constants Q_1 and C_1 are fitted to the strain rate corrected stress seen in Figure 5.43. Concerning the viscous part of the model, the reference strain rate is selected as $\dot{p}_0 = 10^{-7} s^{-1}$. The plastic viscosity parameter C is found from Figure 5.42, and the yield stress parameter σ_{y0} at the defined reference strain rate $\dot{p}_0$ is calculated from Equation (4.27) . The α factor, representing the ratio between the yield stress in compression and tension, was seen to be close to unity in Figure 6.5. The value of the β parameter is found from Figure 5.45 , where it can be seen that the volumetric strain is equal to about 0.15 at a longitudinal strain of 2. The corresponding volumetric strain ratio is $\gamma_{UT} = \varepsilon_V / \varepsilon_1^t = 0.15/2 = 0.075$. The parameter β is then calculated with Equation (7.46). The calibration of the Part B parameters, i.e. C_R and $\overline{\lambda}_L$, is less straightforward, and they were found with an iterative approach involving several simulations.

Table 7.2: Material parameters for simulations of the circular HDPE tests.

E [MPa]	ν	σ_{y0} [MPa]	Q_1 [MPa]	C_1	C [MPa]	$\dot{p}_0$ [s^{-1}]	α	β	C_R [MPa]	$\overline{\lambda}_L$
650	0.48	5.27	6.57	40	1.421	$1 \cdot 10^{-7}$	1	1.051	1.65	6

The resulting stress-strain response with the given parameters is shown in Figure 7.4 together with the experimental results. The continuous lines, representing the test data, are taken from Figure 5.37, and correspond to one representative curve from each strain rate. It is recalled from Figure 5.38 that the scatter between the two replicate tests at each rate was negligible. The curves in Figure 7.4 and throughout this chapter have the same color coding as the curves throughout Chapter 4, indicating the same nominal strain rates. The true stress and longitudinal strain from the experimental tests are taken from the first section experiencing necking. The dashed curves are from the simulations, where stress and strain also have been calculated from the longitudinal and transverse strains occurring at the surface of the sample and the total force. Neither the test nor the simulation data in Figure 7.4 are Bridgman-

corrected. As can be seen, the overall similarity is quite good, but the simulation of the tests with the highest strain rate is slightly overestimating the hardening of the material for strains between 0.5 to 1.7. The small deviation could possibly be attributed to thermal softening, which is not captured by the present isothermal model.
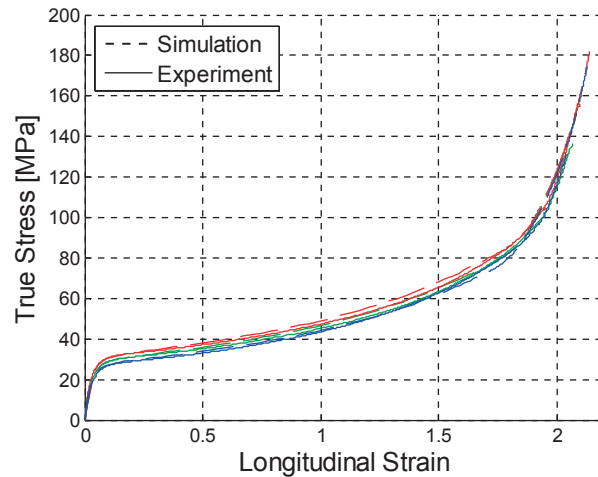
Figure 7.4: Comparison between simulations and experiments for uniaxial tension tests on HDPE with samples with circular cross-section, stretched at three different nominal strain rates. True stress versus longitudinal strain.

Volumetric strain vs. longitudinal strain curves from the simulations and the experiments are shown in Figure 7.5 (a). Volumetric strain is here calculated with the "cylinder method", as defined by Equation (4.15), for both experiments and simulations. This volumetric strain is referred to as apparent volumetric strain, since it is entirely based on the longitudinal and transverse strains measured at the surface. In the simulations, the volumetric strain was also found in a different way; by calculating the average determinant of the elements constituting the section of initial necking. This measure is in the following referred to as actual volumetric strain.

Figure 7.5 (a) addresses the so-called apparent volumetric strain from both experimental tests and simulations, i.e. ε_v as found with the "cylinder method" in Section 4.3. It is seen that the simulated apparent volumetric strain follows the general trend observed in the tests, but it is obvious that the model is not able to capture the exact details of the response. As can be seen,

162

the choice of $\beta = 1.051$ gives a volumetric strain that approaches a level of about 0.15, which corresponds well with the experimental data at the end of the tests. On the other hand, the numerical model initially overestimates, then underestimates, and again overestimates ε_v. It is also of interest that the model predicts slightly higher volumetric strains with decreasing rate, which is the opposite of what was measured in the tests, see Figure 5.45 (and Figure 5.46). The simulations also show that even though actual volumetric strain should increase linearly with longitudinal strain, as shown by Equation (7.44), the apparent volumetric strain is highly non-linear. It is also seen that apparent volumetric strain is negative for longitudinal strains between 0 and 1, even though the constitutive model as such does not allow for negative plastic volumetric strains. This further supports the hypothesis that negative volumetric strain comes as a consequence of an erroneous assumption, i.e. the "cylinder method". This issue will shortly be investigated more thoroughly.

The strain rate is plotted against longitudinal strain in Figure 7.5 (b). Again, the section experiencing the first onset of necking is addressed in the case of both test and numerical analysis, and the strain rates are in both cases determined from the longitudinal strains at the surface. Three deviations between simulations and experiments are worth pointing out. It can be seen that the initial strain rate in the simulations is too high. This was found to be a result of machine compliance. More interesting is the distinct change of slope for the dashed curves obtained from the simulations at a strain of about 0.15. This is an effect of the sudden transition from elastic to plastic deformation that results from the choice of applying a yield criterion in the constitutive model, see Equation (7.17). Thirdly, it is obvious that the strain rate in the simulations overestimates the strain rate in the experiments. This indicates that neck propagation initiates later in the simulation compared to the experiments. The delayed propagation comes as a result of too little hardening after a strain of around 1. This lack of hardening is related to the rigidity in the model, where Part B almost exclusively controls late stage hardening.
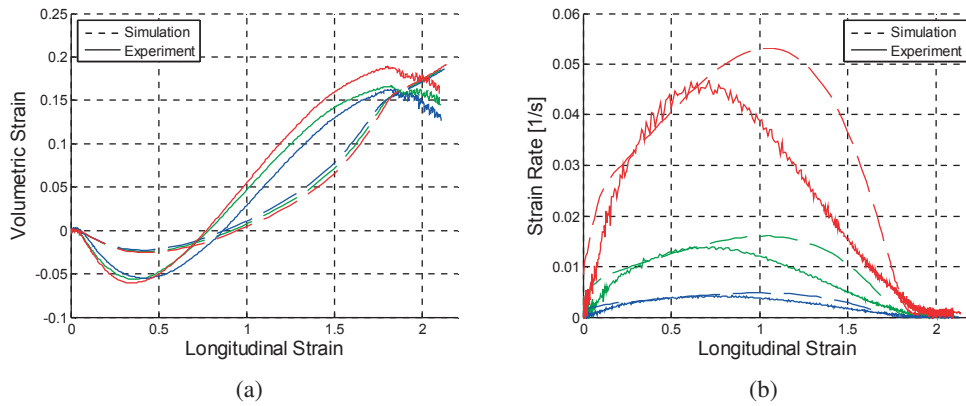
Figure 7.5: Comparison between simulation and experiments for uniaxial tension tests on HDPE with samples having circular cross-section. (a) Volumetric strain calculated with the "cylinder method" versus longitudinal strain, and (b) strain rate versus longitudinal strain.

So far, the comparison between tests and simulations has been concerned with local measures such as stress, strain and volumetric strain. It is also of great interest to look at global, or integrated quantities such as force, displacement and reduction of diameter at the neck. This information is provided in Figure 7.6. As would be expected from the good data agreement on the material scale as seen in Figure 7.4 and also to some extent in Figure 7.5 (a), the force-displacement curves from the simulations are close to the experimental curves, see Figure 7.6 (a). It should be noted that the origin of the force vs. displacement curves from the simulations in Figure 7.6 (a) have been shifted to the right so that the peak points of the curves from the simulations coincide with the peak points of the experimental curves. This was done to account for machine compliance, and was validated for these three tests by calculating the displacement using DIC and comparing it to the machine displacement shown in the figure. It was then observed that the deformation speed found from DIC was lower up to peak force compared to the velocity applied by the machine, while the two speeds quickly converge after peak force. It is hence assumed that machine compliance is negligible after peak force. A similar shift of the force vs. crosshead displacement curves has been done in all subsequent simulations.

It can be seen that the general agreement between the force-displacement curves is good. The simulations capture the peak force, the subsequent softening, the drawing force and finally the

164

force increase as the neck propagates into the sample shoulders. Such an agreement requires that the model is able to represent both the longitudinal stress-strain behavior of the material as well as the transverse deformations. It is however noted that the force level after 30 mm displacement is slightly underpredicted for the two fastest tests. The force level on this plateau is highly sensitive to the calibration of Part B. With the current model it is possible to capture this level exactly for only one of the three strain rates covered in this investigation. This observation suggests that Part B should include some rate sensitivity.

Figure 7.6 (b) shows the force as function of the minimum cross-section radius in the neck. Such a plot serves to display whether the transverse deformations and the subsequent cold-drawing process are captured. The general trend is that there is a good agreement between results from tests and simulations. Yet, a systematic overprediction of the force, followed by an underprediction, with decreasing radius can be observed. This is a result of the simplicity of the implemented plastic dilatation model, where the parameter β, and hence γ is constant. It can also be seen that the force in the simulations converge at the final radius around 1.2 mm, while it in the experiments increases from the slowest to the fastest one. Again, this suggests that plastic dilatation is dependent on viscosity.

(a) Force vs. Crosshead Displacement   (b) Force vs. Radius at Neck
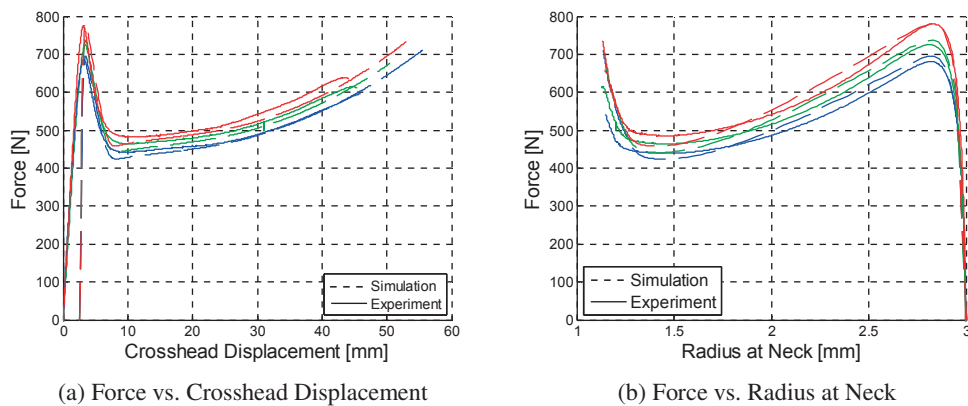
Figure 7.6: Force vs. displacement and force vs. neck radius comparison between simulation and experiments of tests performed with circular HDPE samples, stretched at three different nominal strain rates.

The simulation of the slowest test, which was performed at a nominal strain rate of $10^{-2.5}$ s^{-1}, is shown at three stages of localization and neck propagation in Figure 7.7. The non-

165

homogenous distribution of longitudinal strain through the radius of the sample seen in Figure 7.7 (a) illustrates the problem of calculating a representative strain based on exterior strain measurements. This in turn also leads to the difference in results obtained with the "cylinder" and "parabolic" method as discussed in Section 4.3. This strain inhomogeneity in the radial direction can be seen to follow the front of the neck propagation, leaving a homogenous strain field in its wake.

<table>
<tr><td>+5.40e-01
+4.95e-01
+4.50e-01
+4.05e-01
+3.60e-01
+3.15e-01
+2.70e-01
+2.25e-01
+1.80e-01
+1.35e-01
+9.04e-02
+4.55e-02
+5.12e-04</td></tr>
</table>

(a) Initial localization, u=3.6 mm   (b) Early stage neck propagation, u=5.8   (c) Late stage neck propagation, u=13.2
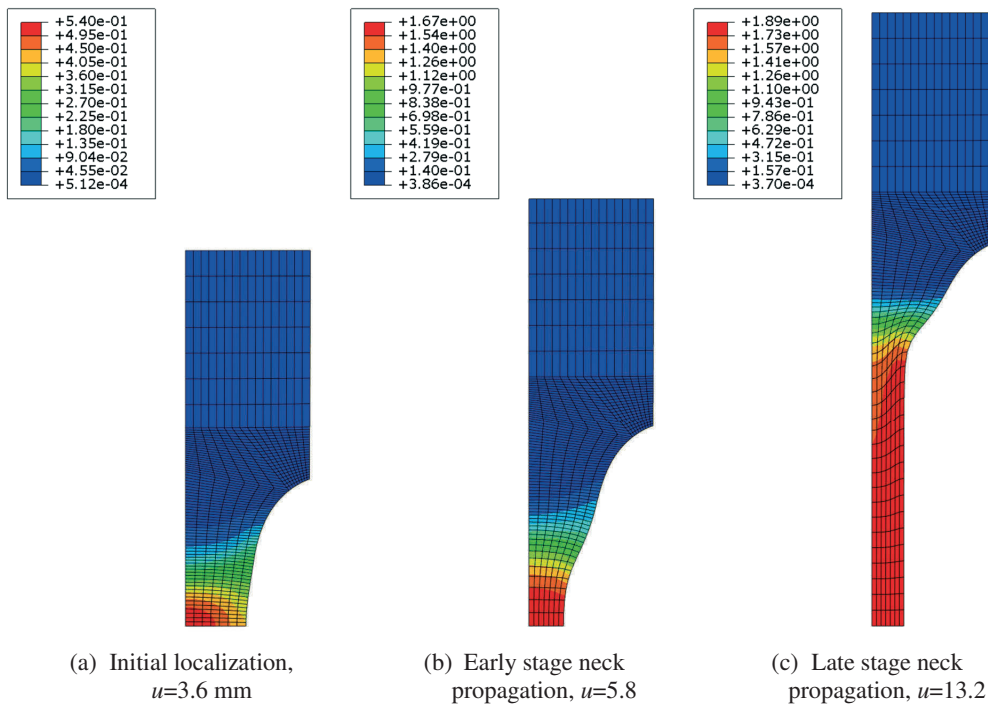
Figure 7.7: Simulation of circular HDPE sample stretched at a nominal strain rate of $10^{-2.5}$ s^{-1} shown at three different elongations. The colors map indicates level of principal logarithmic strain.

Assuming that the current model provides an overall good representation of the material, it is now possible to look more in depth on the plastic volume change. The dilatation is primarily governed by the parameter β. Applying three different values for β, the resulting volumetric strains from simulating the experiment with the intermediate loading speed of $10^{-2.0}$ s^{-1} are shown in Figure 7.8 along with the measured volumetric strain of the corresponding experiment. The figure shows apparent volumetric strain calculated with the "cylinder

method" as solid lines, while actual volumetric strain determined from the determinant of the deformation gradient is shown with dashed lines. As can be seen, there is a significant deviation between the two sets of numerical predictions up to a longitudinal strain of about 1.7. This is the point in the test where the neck starts to propagate, and the section of initial necking returns to a straight section. At this stage the two volumetric strain calculations start to give similar results in terms of shape and volumetric strain level. It can also be seen that the material initially appears to conserve its volume up to a strain of about 0.25, as the apparent volumetric strain in the experiment is close to the apparent volumetric strain of the volume preserving simulation with $\beta = 1.00$.
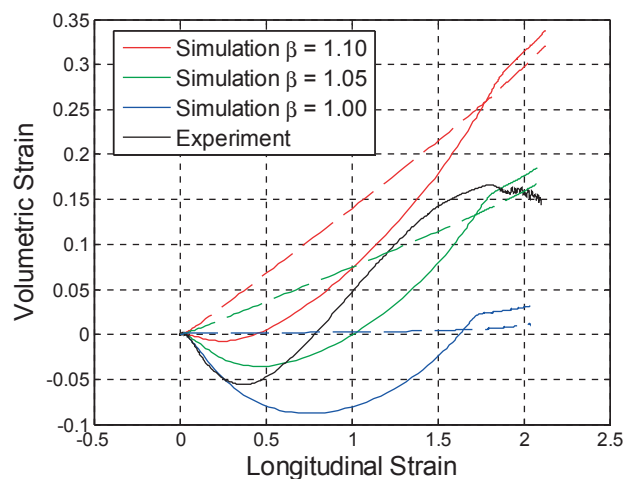
Figure 7.8: Apparent and actual volumetric strain in simulations for different values of β, shown with apparent measured volumetric strain from experiment (black). Solid lines are apparent and dashed lines are actual volumetric strain (red, green and blue).

With the data shown in Figure 7.8, it is now possible to estimate the shape of the actual volumetric vs. longitudinal strain curve from the experiment. This can be done by assuming that the level of apparent volumetric strain at a given point of longitudinal strain is only a function of the current level of actual strain. It is then possible through interpolation of the simulation data do determine what value of actual volumetric strain is required to produce an experimentally measured value of apparent volumetric strain. An example of this is show in Figure 7.9, where the blue, green and red circles represent the actual and apparent volumetric strain from the three simulations at a longitudinal strain level of 1. This data is then

167

interpolated to get an actual volumetric strain for an apparent volumetric strain equal to 0.045, which is what was measured in the experiment at the same longitudinal strain level.
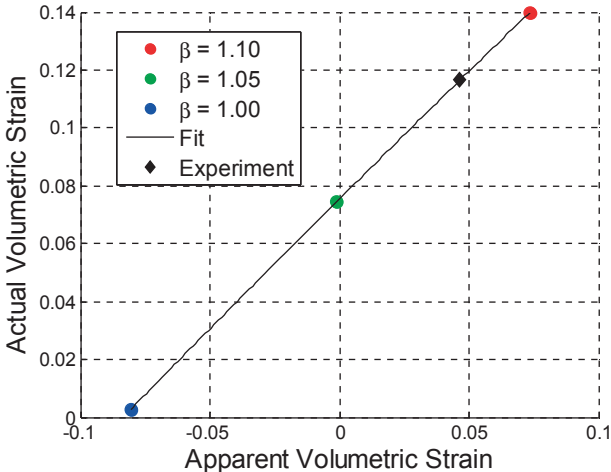
Figure 7.9: Interpolation of actual volumetric strain as a function of apparent volumetric strain at a longitudinal strain level of 1.

The process illustrated by Figure 7.9 can now be performed for the whole range of longitudinal strain, and an approximation of the actual volumetric strain in the experiment can be obtained. This interpolation approximation is shown in Figure 7.10 together with the original measurement ("apparent") as well as the corrected volumetric strain obtained with the "parabolic method" as defined by Equation (4.20). As can be seen, there is a good agreement between the correction suggested in this thesis and the volumetric strain found by interpolating the simulation results. This further validates the proposed volumetric correction. The largest deviation between the interpolated and corrected volumetric strain is at a longitudinal strain equal to 1.5. Interestingly, the interpolated volumetric strain here shows a tendency to reach a maximum, and then reduce with about 0.02.

168
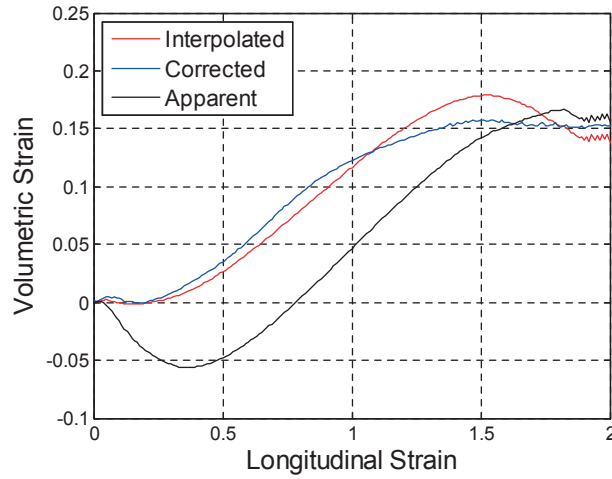
Figure 7.10: Volumetric strain for a test performed with circular HDPE sample stretched at a nominal strain rate equal to $10^{-2.5}$ s^{-1}. Comparison between apparent, corrected and interpolated volumetric strain.

When the actual behavior of volumetric strain is known, it is possible to refine the FEM material model. This can be done by first calculating $\beta(p)$ using Equation (7.52) and the experimental data. This is shown in Figure 7.11 along with a calibrated model for $\beta(p)$. The model for $\beta(p)$ used a simple Gaussian bell function. This function is defined as

$$\beta(p) = a \exp\left(\frac{-(p-b)^2}{2c^2}\right) + 1 \qquad (7.53)$$

where the fitted set of constants is $[a, b, c] = [0.14 \quad 0.78 \quad 0.30]$. As can be seen, $a+1$ is equal to the peak value of β, b defines at which value of p the maximum β occurs, while c defines how steep the peak of the function is.
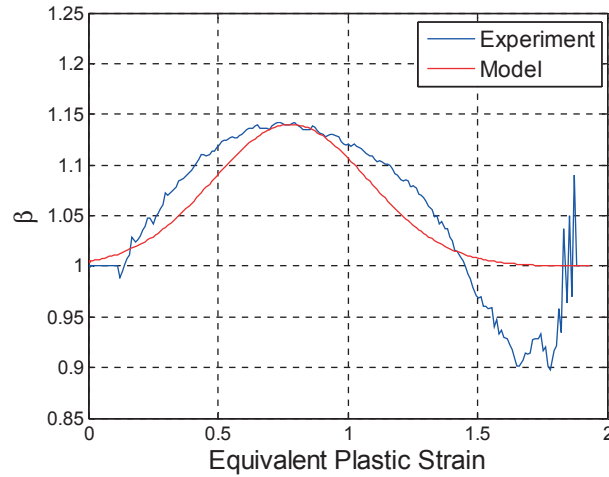
Figure 7.11: Plastic dilation parameter β plotted as a function of equivalent plastic strain for a tests performed on a circular HDPE sample (blue) shown with fitted model (red).

This function for β was implemented in the material model, and the resulting volumetric strain is shown in Figure 7.12. As evident from the comparison with the experiment, the refined dilatation model is a considerable improvement over the original constant β implementation. As a side note, this variation of β with equivalent plastic strain could potentially also be used for α, making the flow rule of Section 7.1.1 associated. Since yielding occurs at the same stress level in compression and tension, while there is clear volumetric growth in tension, it has earlier been assumed that the material model is non-associated. If α were to vary with β as described by Equation (7.53) and the given calibration, these experimental observations would still hold true since α initially would be equal to 1. It can further be see that an associated model like this would lead to an increase in yield strength in compression relative to tension with an increase in equivalent plastic strain. This is also something that seems to be supported by experiments. The drawback of such an assumption is however that it would impose a complicated plastic volumetric strain evolution in compression without the experimental data to validate it. This concept is hence not developed further in this thesis, and is left for further work.
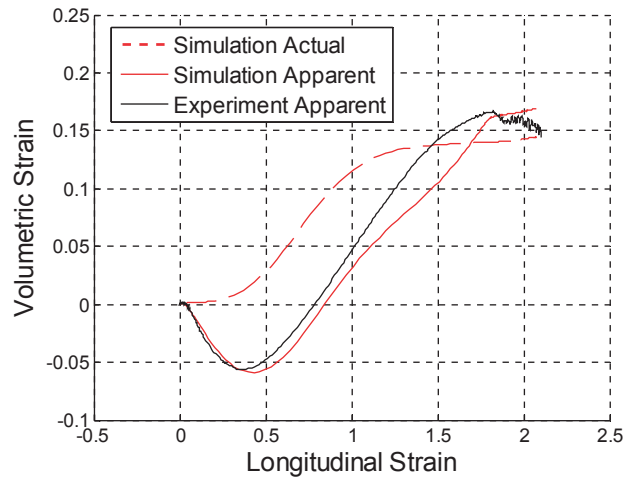
Figure 7.12: Volumetric vs. longitudinal strain for a circular HDPE sample in tension, experimental and simulation. Simulation with modified material model adding varying β with equivalent plastic strain.

7.2.2 HDPE in Compression

The same set of material parameters as used in tension (Table 7.2) is also employed for a simulation of the compression test, thus applying a constant value of β. The problem is assumed to be axisymmetric, where the sample is compressed between two rigid plates. The rigid plates are represented as two analytical, mesh free, rigid surfaces. Coulomb friction is assumed between the rigid surfaces and the sample with a constant friction coefficient equal to 0.03. The mesh is shown along with a representation of the rigid analytical surfaces in Figure 7.13.

171
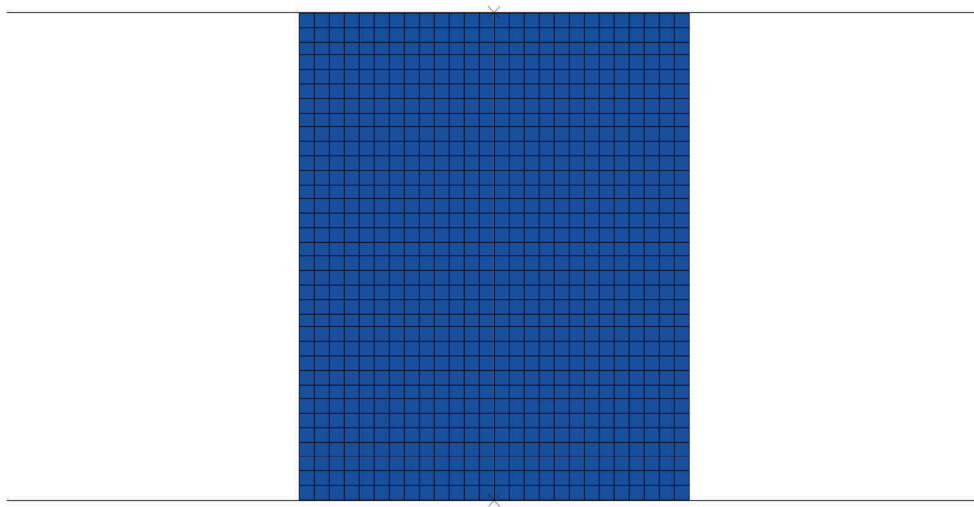
Figure 7.13: Axisymmetric mesh for simulations of cylindrical HDPE samples in compression.

A contour plot showing volumetric stretch λ_V at the end of the simulation is presented together with the initial geometry of the sample in Figure 7.14. Note that the largest volumetric stretch is equal to 1.055, which is equivalent to a volumetric strain of 0.053. The corresponding longitudinal strain is around –0.6. Again, all material response curves presented from the simulation are calculated from the strains occurring at the surface of the sample and the total compression force.
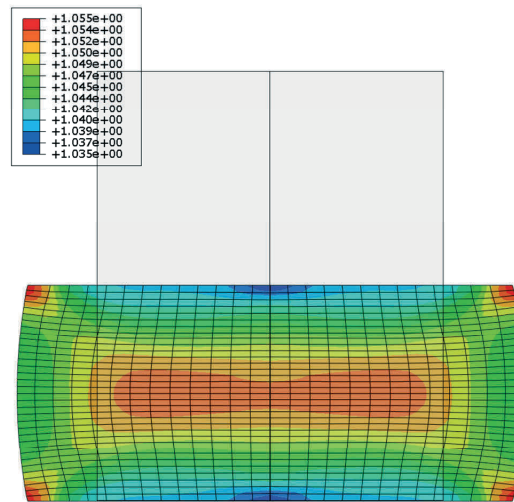
Figure 7.14: Contour plot from axisymmetric simulation of HDPE sample in compression at the end of the simulation superposed on the undeformed sample. The contours address volumetric stretch λ_V.

The true stress-strain curve obtained in the simulation is shown in Figure 7.15, which also includes the curve found from the experimental test. As evident from the figure, the simulation follows the test results well up to a strain of 0.15, after which there is a difference of 2-3 MPa. The choice of friction coefficient will affect the stress-strain curve from the numerical analysis. A detailed study of how the results are affected by different values of the friction coefficient is, however, not within the scope for this evaluation of the numerical model. Yet, some comments will be provided in the following, and the effect of changing the friction coefficient will be elaborated in Section 7.2.6 dealing with PVC in compression.
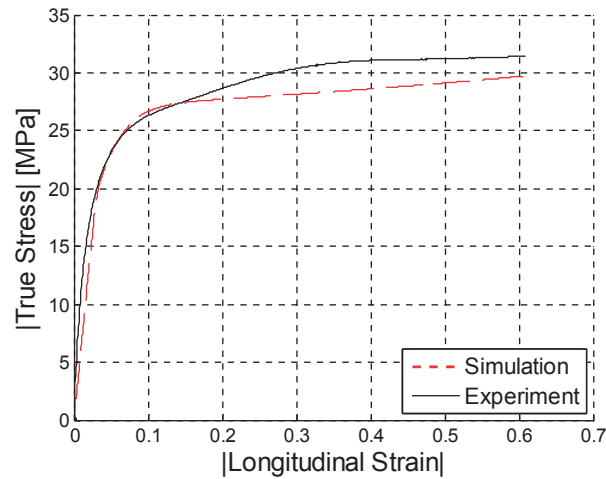
Figure 7.15: |True stress| vs. |longitudinal strain| for HDPE in compression, comparison between simulation and experiment.

As for the tension tests, a comparison of the deformed shape of the sample from the compression test and the corresponding simulation is of interest. The center section, located half-way between the two rigid plates, is chosen for this evaluation. The center radius and the curvature of the boundary at the center are compared between experiment and simulation in Figure 7.16 (a) and (b), respectively. In both cases, the longitudinal strain is taken as reference at the horizontal axis. Looking at the radius, it can be seen that the simulation slightly overpredicts the radius at intermediate strain levels. This observation suggests that the transverse strains and hence change of volume is reasonably captured by the numerical model.

On the other hand, it can be seen from Figure 7.16 (b) that the curvature in the simulation differs significantly from the curvature measured in the test. It was found that this curvature is extremely sensitive to the friction coefficient used in the simulations. Additionally it seems that it is not possible to recreate the shape of the curve from the test using a constant friction coefficient. This can be seen when comparing the two curves in Figure 7.16 (b) for center curvature. The sample in the simulation has an earlier onset of barreling, see also Figure 7.16 (a), and is overpredicting barreling up to a strain of 0.5. At a strain of 0.5, the curvatures are the same, whereas after, the simulation underpredicts curvature with a large slope difference between the two curves in Figure 7.16 (b). The reason for the rapid increase in barreling seen

174

in the experiment could possibly be attributed to a change in lubricant condition, but it could also be caused by a local and considerable volume expansion in the center section of the sample.

(a) Center radius vs. |longitudinal strain| (b) Center curvature vs. |longitudinal strain|
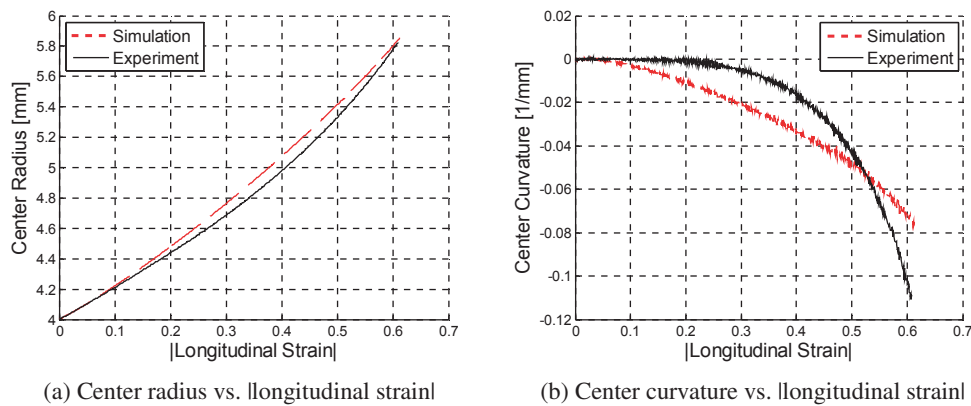
Figure 7.16: Radius and curvature at center section of the sample versus |longitudinal strain|. Comparison between simulation and experiment.

Figure 7.17 shows volumetric strain in the center section of the sample for test and simulation. The volumetric strain is in both cases calculated from the strains at the surface of the sample, applying the same assumptions as for the "cylinder method" described in Section 4.3. Figure 7.17 in other words presents an average volumetric strain in the center section. This figure is included to show the large error present when trying to measure volumetric strain locally in compression. This is apparent by comparing the maximum values in Figure 7.17 to those previously shown in the contour plot of the volumetric stretch in Figure 7.14. In the latter case, which represents the end of the simulation and hence a longitudinal strain of – 0.6, there is no element that ever experiences a volumetric strain larger than 0.053. Despite this, the local exterior calculation yields a maximum value of about 0.15. This large inaccuracy is a result of the sample barreling, resulting in non-homogeneous strains through the volume of the sample. This explains why the volumetric strain seems to start increasing at the onset of barreling, as well as the seemingly inverse relationship between curvature and local volumetric strain. Another observation is that the volumetric strains are larger in the interior of the center section than at the surface, see Figure 7.14.This means that the "cylinder method" for calculation of volumetric strains is strongly misleading after the onset of

barreling. Additionally it was found that this method of calculating volumetric strain was highly sensitive to a change in the friction coefficient, as will be shown for the PVC compression test in Section 7.2.6.
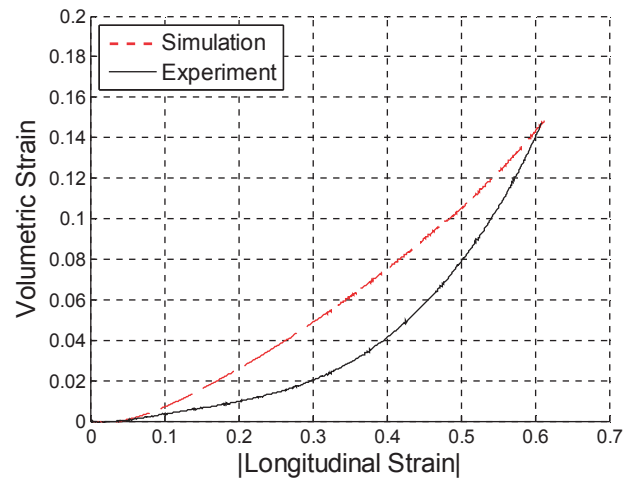
Figure 7.17: Volumetric strain vs. |longitudinal strain| for HDPE in compression, comparison between simulation and experiment. Volumetric strain calculated for the center section of the specimen with the "cylinder method".

Force versus displacement curves from tests and simulations are compared in Figure 7.18. Keeping the large deviations between tests and simulations in Figure 7.16 and Figure 7.17 in mind, the agreement of the curves in Figure 7.18 is surprisingly good. The reason for this is that stress was underpredicted in the simulations, see Figure 7.15, while the cross sectional area was overpredicted in Figure 7.16 (a). The net result is then that the deviations somewhat cancel each other out. The good agreement is thus not fully representative of the quality of the simulation. Hence, Figure 7.16 to Figure 7.18 demonstrate that even if the global response is well captured in a numerical simulation, it is also worthwhile to have a close look at the local deformation during an evaluation process of a numerical model.

176
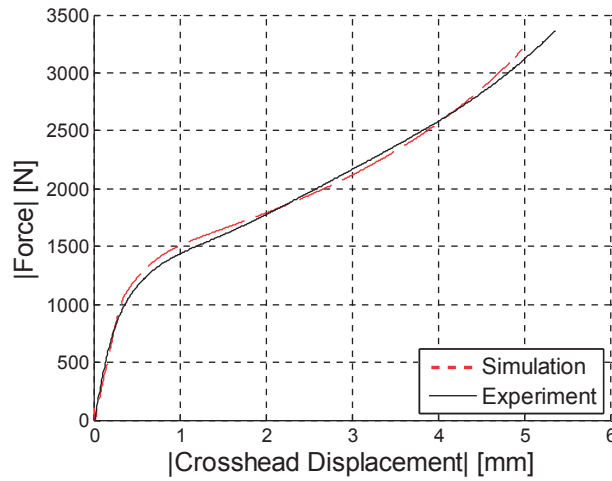
Figure 7.18: |Force| vs. |displacement| curves for HDPE in compression, comparison between simulation and experiment.

7.2.3 HDPE Samples with Rectangular Cross-section

The tests performed with the rectangular HDPE samples were simulated with the material parameters shown in Table 7.3. The improved model for change of volume, i.e. the relation for evolution of β as function of accumulated plastic strain p, see Equation (7.53), is now employed. The parameter β is therefore not given in Table 7.3.

An inspection of the parameters in Table 7.2 and Table 7.3 reveals that some of them differ, although both sets refer to the same HDPE material. The cause of this is believed to be that the tests with the rectangular samples were performed two and a half years before the series on the circular samples, respectively in 2012 and 2014. The minor changes of the mechanical properties of the material could be due to an aging effect. This hypothesis is however difficult to prove since different sample geometries were used. Hence, some or all of the difference between the material parameters in Table 7.2 and Table 7.3 could potentially come as a result of different design of the specimens.

Table 7.3: Material parameters for simulations of the rectangular HDPE tests

E [MPa]	ν	σ_{y0} [MPa]	Q_1 [MPa]	C_1	C [MPa]	$\dot{p}_0$ [s^{-1}]	α	β	C_R [MPa]	$\bar{\lambda}_L$
650	0.48	2.43	5.1	40	1.788	$1\cdot10^{-7}$	1	-	1.9	6

The two material calibrations are compared in Table 7.4. As can be seen, different values occur for the initial yield stress σ_{y0}, the plastic hardening parameter Q_1, the plastic viscosity parameter C and in the network stiffness coefficient C_R. The initial yield strength seems to have increased with time, which corresponds well with typical aging effects. On the other hand, the viscosity is reduced. The net effect of these two changes at the strain rates investigated here is that the circular tests have an increased yield stress of about 1.2 MPa. The decrease in network stiffness C_R might suggest some form of material deterioration with time. Given the lack of data on this subject it is not further investigated, and for practical purposes the two test series of rectangular and circular specimens are assumed to be of similar but not identical materials.

Table 7.4: Comparison of material calibration for rectangular and circular HDPE samples

	E [MPa]	ν	σ_{y0} [MPa]	Q_1 [MPa]	C_1	C [MPa]	$\dot{p}_0$ [s^{-1}]	α	β	C_R [MPa]	$\bar{\lambda}_L$
Rectangular (2012)	650	0.48	2.43	5.1	40	1.788	10^{-7}	1	-	1.9	6
Circular (2014)	650	0.48	5.27	6.57	40	1.421	10^{-7}	1	1.051	1.65	6
Difference	0	0	-2.84	-1.47	0	0.367	0	0	-	0.25	0

As was seen in Figure 5.19, there is a significant increase of the volumetric strain in the rectangular specimens during the tension test. Moreover, the figure also suggests that the evolution of the volumetric strain is dependent on the strain rate. Employing the same method as used for the circular samples in Section 7.2.1, it is possible to calculate β as a function of plastic strain for the tests using Equation (7.52). This is shown in Figure 7.19, where again it seems to be a strong strain-rate dependency. Additionally, β seems to evolve with plastic strain in a similar fashion as was seen for the circular samples. It then seems natural to extend

Equation (7.53) to incorporate strain rate sensitivity. To this end, the value of β at a plastic strain equal to 1.17 has been marked in the plot, and it can be seen that this is close to the maximum of β for all tests.
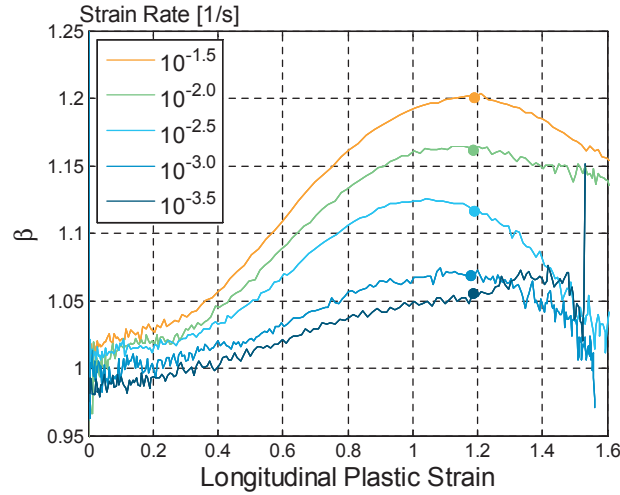
Figure 7.19: Plastic dilatation factor β as a function of longitudinal plastic strain for rectangular HDPE tests.

Equation (7.53), describing the model for $\beta(p)$, can now be extended to incorporate strain rate dependency. This is done by first assuming that the maximum value of β occurs at the same value of equivalent plastic strain $p = \tilde{p}$ for all tests. This implies that $b = \tilde{p}$, which reduces Equation (7.53) to $\beta(\tilde{p}) = a + 1$. It then seems reasonable to assume that the parameter a should depend on strain rate. We now propose that a is a logarithmic-linear function of strain rate

$$a(\dot{p}) = d + e \ln\left(\frac{\dot{p}}{\dot{p}_0} + 1 \right) \qquad (7.54)$$

where d and e are calibration parameters and $\dot{p}_0$ is a reference plastic strain rate. Recalling the $\beta(\tilde{p}) = a + 1$ at the strain level $p = \tilde{p}$ identified with circles in Figure 7.19, there are now two relations available for $a = a(\dot{p})$

$$a(\dot{p}) = d + e\ln\left(\frac{\dot{p}}{\dot{p}_0} + 1\right) = \beta(\tilde{p}) - 1 \qquad (7.55)$$

The parameters d and e can now be optimized by performing a linear fit to the values $\beta(\tilde{p}) - 1$ on the vertical axis and the values $\ln\left(\dot{p}/\dot{p}_0 + 1\right)$ on the horizontal axis. This is shown in Figure 7.20 where the β values found for $\tilde{p} = 1.17$ are denoted as "Beta Max" at the vertical axis. The reference strain rate $\dot{p}_0$ is set to $10^{-7}\ s^{-1}$ which is the same value as used in the visco-plastic model, see Table 7.3. As can be seen, the assumed logarithmic linear model provides a good fit to the experimental observations in Figure 7.20, and the parameters in Equation (7.54) are found to be $d = -0.193$ and $e = 0.0295$. It should be noted that having the parameter $d < 0$ can result in $\beta < 1$ for low strain rates. This is not allowed in the model, so it is hence necessary to specify that $a(\dot{p})$ should not be allowed to become negative.
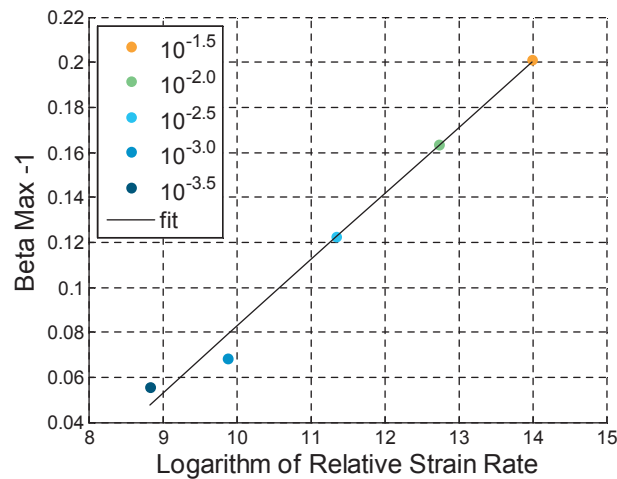
Figure 7.20: β-1 as a function of relative plastic strain rate for tests performed with rectangular HDPE samples.

It was found that a value of 0.5 for the last coefficient c in Equation (7.53) resulted in a good agreement. The extended function for β, which now also incorporates the strain rate, is then

$$\beta(p, \dot{p}) = \left(d + e\ \ln\left(\frac{\dot{p}}{\dot{p}_0} + 1\right)\right)\exp\left(\frac{-(p-b)^2}{2c^2}\right) + 1 \qquad (7.56)$$

where the value of the parameters are $\begin{bmatrix} b & c & d & e \end{bmatrix} = \begin{bmatrix} 1.17 & 0.5 & -0.193 & 0.295 \end{bmatrix}$. It may be noted that $b = 1.17$ and $c = 0.5$ in this case, while the values from the tests performed on the circular samples were found to be $b = 0.78$ and $c = 0.3$. This shows that volumetric strain stabilizes at an earlier stage of plastic deformation in the tests performed with the circular specimens compared to the rectangular ones. It was also seen in the data from the circular samples that there was little variation in volumetric growth between strain rates. This is consistent with the reduced plastic viscosity seen in the yield stress. These variations in volumetric growth are also assumed to be a result of the time difference between the two sets of tests. The complete model as described with Equation (7.56) is compared against the experiments in Figure 7.21. As can be seen, the model seems to describe the variation of β quite well.
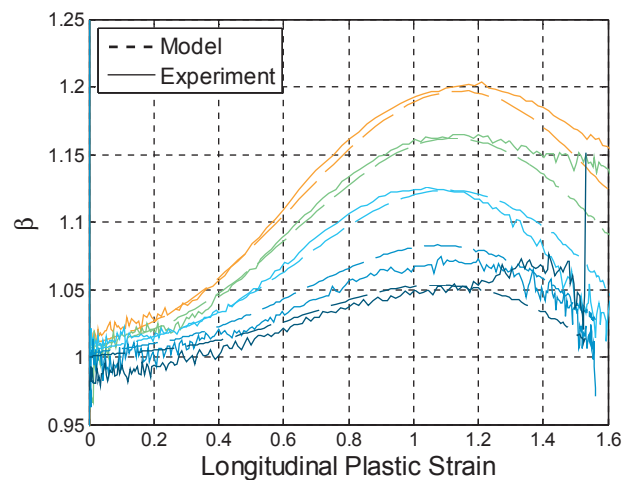
Figure 7.21: Variation in β as a function of longitudinal plastic strain in HDPE tests and model.

In addition to plastic strain and strain rate, temperature caused by adiabatic heating was also measured in the tests on the specimens with rectangular cross section. It should be noted that since strain rate and temperature have not been varied independently in the tests, it is difficult to evaluate their individual influence on volumetric growth. A pragmatic approach is to assume that β is only dependent on one of them. Strain rate was chosen since β increases with increased strain rates, as seen from Figure 7.20, even between the three slowest tests that

experienced modest to no increase in temperature, confer Figure 5.12. On the other hand, no such clear dependency was found for temperature. The validity of this assumption should however be evaluated by performing equivalent uniaxial tension tests at constant strain rate, but with varying temperature.

The test series with rectangular samples was monitored with an infrared camera and it was shown in Figure 5.12 that significant heat was generated for strain rates of $10^{-2.0}$ s^{-1} and higher. This adiabatic heating affects the behavior of the material, so in order to evaluate and simulate this problem, it is necessary to run a fully coupled explicit thermo-mechanical analysis. The thermal parameters used in the simulations are shown in Table 7.5. Specific heat C_p and thermal conductivity k was found from the online database MATBASE [42]. As was seen in Figure 5.18, there is significant variation in the Taylor-Quinney coefficient χ with plastic strain when calculated from the total stress. However, in the material model used in the simulations, it is only Part A that dissipates heat. This serves as an explanation for the high constant χ factor used when compared to the measured one. The thermal convection coefficient h between HDPE and air was estimated from a simple experiment. In the experiment, a thin square sheet of HDPE was first submerged in 50°C hot water for 5 minutes, before being removed from the bath, dried off and then left to air cool. While the sheet air cooled, the temperature was measured every 15 seconds for approximately 10 minutes. The change in material temperature $\dot{T}$ with respect to time can then be expressed from the last part of Equation (5.2). We then have

$$\dot{T} = h\left(T_R - T\right)\frac{A_{int}}{V\rho C_p} \tag{7.57}$$

which solved for the unknown convection coefficient h gives

$$h = \frac{V\rho C_p \dot{T}}{A_{int}\left(T_R - T\right)} \tag{7.58}$$

For a square sheet with widths W and a thickness t, the ratio V/A_{int}, describing the volume of the body divided by the external surface area, is

$$\frac{V}{A_{\text{int}}} = \frac{W^2 t}{\left(2W^2 + 4Wt\right)} = \frac{Wt}{\left(2W + 4t\right)} \qquad (7.59)$$

Equation (7.58) can then be solved when the temperature is measured, and the time derivative of the temperature $\dot{T}$ is calculated with numerical differentiation.

Table 7.5: Thermal parameters for simulating tests performed with rectangular HDPE samples.

ρ [kg/m^3]	χ	C_p [J/kgK]	k [W/mK]	h [W/m2K]
970	0.9	2200	0.5	8

In addition to the thermal parameters, a model for how temperature affects the stress is also required. A temperature scaling factor Ψ is defined as

$$\Psi(T) = 1 - sign(T - T_R)\left|\frac{T - T_R}{T_M - T_R}\right|^m \qquad (7.60)$$

where T is the temperature in the material point, T_R is the room temperature, T_M is the melting temperature of the material and m is a calibration parameter. The shape of the function for different values of m is shown in Figure 7.22 for $T_R \leq T \leq T_M$, with $T_R = 20°C$ and $T_M = 100°C$.
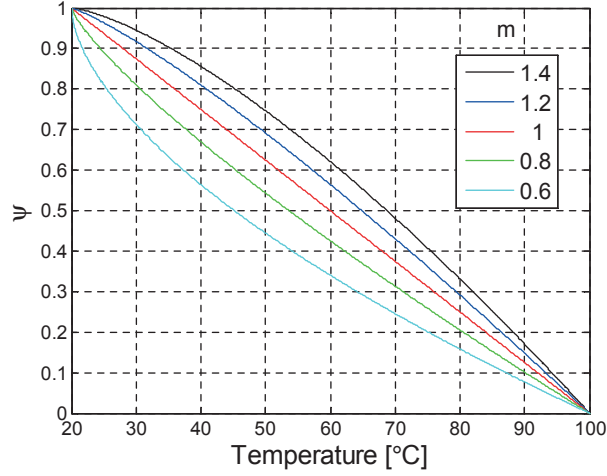
Figure 7.22: Temperature scaling factor ψ presented with different values of m, shown against temperature. Room and melting temperatures are set to 20°C and 100°C.

Equation (7.60) is simply a numerically more robust version of the temperature dependent stress scaling factor $\theta(T)$ in Equation (4.28). The use of the *sign* function and the absolute value ensures that $\Psi(T)$ is real number for $T < T_R$, i.e. at low temperatures, and arbitrary choices of m. This scaling factor is then multiplied with the flow stress $\sigma_{A0}(p)$ in the constitutive visco-plastic relation for Part A shown in Equation (7.19). We then get

$$\bar{\sigma}_A = \Psi(T)\sigma_{A0}(p) + C\ln\left(1 + \frac{\dot{p}}{\dot{p}_0}\right) \qquad (7.61)$$

where $\sigma_{A0}(p)$ is defined in Equation (7.20). In addition, the initial stiffness parameter C_R in Part B, see Equation (7.21), is also multiplied with the same factor $\Psi(T)$. As seen from Equation (7.61), the viscosity is assumed to be independent of the temperature in the material. Thermoelastic effects are neglected in this presented model and in all simulations in general.

As the model now is expanded to include strain rate sensitivity in the evolution of β, and also incorporates possible change of temperature due to adiabatic heating, it is now possible to simulate the tests. The simulations assume three planes of symmetry, reducing the 3D model of the entire specimen to a 1/8 model with half the length, thickness and width of the sample

184

dimensions given in Figure 5.1. The mesh used is shown in Figure 7.23. It consists of thermally coupled elements with 8 nodes, having the ABAQUS designation C3D8RT. All material curves reported from the simulations are taken from the surface of the center section since necking initiated at this point at all loading rates. All simulated samples were given initial homogenous temperatures equal to what was measured as initial temperatures in the experiments.
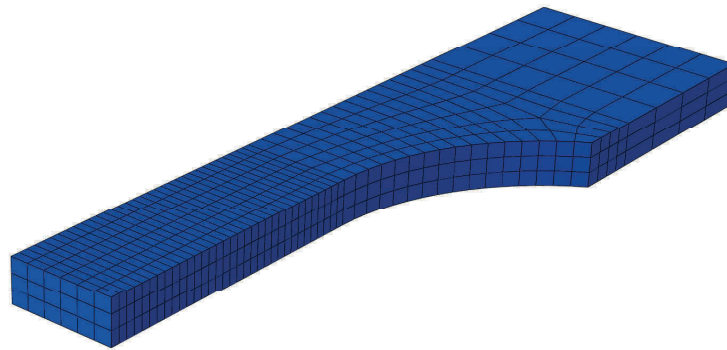
Figure 7.23: Mesh for simulations of rectangular HDPE samples in tension.

True stress vs. longitudinal strains curves for the five strain rates are compared between simulations and experiments in Figure 7.24. The general trends are well captured by the model. The largest deviation is observed in the test with the highest strain rate, where it is observed that the simulation predicts too much thermal softening. This is primarily a result of an excessively high temperature at strains up to 1.3 in the simulation of this test at $10^{-1.5}$ s^{-1} (as seen in Figure 7.25).
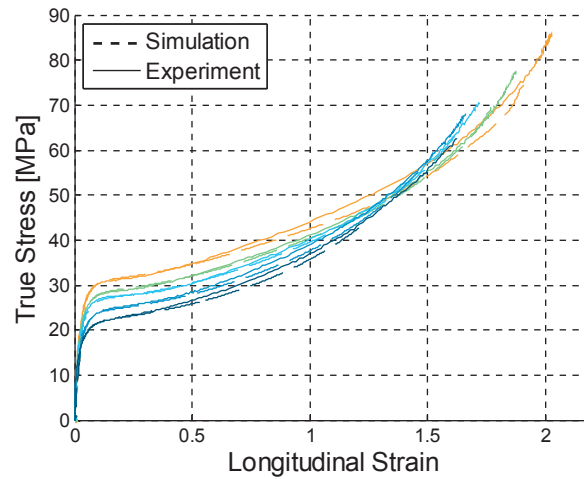
Figure 7.24: Stress vs. strain curves for experiments and simulations of uniaxial tension tests performed with rectangular HDPE tension samples, stretched at five different nominal strain rates.

Temperature versus strain for the simulations and experiments is shown in Figure 7.25. The simulations capture the measured temperatures well for the four slowest tests, whereas the simulation of the fastest test does not manage to follow the non-linear evolution of temperature as function of strain seen in the experiment. This is related to the use of a constant value of the Taylor-Quinney coefficient χ. According to Figure 7.25, there is an increase in slope of the fastest test when the strain exceeds 1. The model represents this stage of deformation as a non-linear elastic network, but the underestimation of the temperature suggests that an energy-dissipating mechanism is more likely to be correct.

186
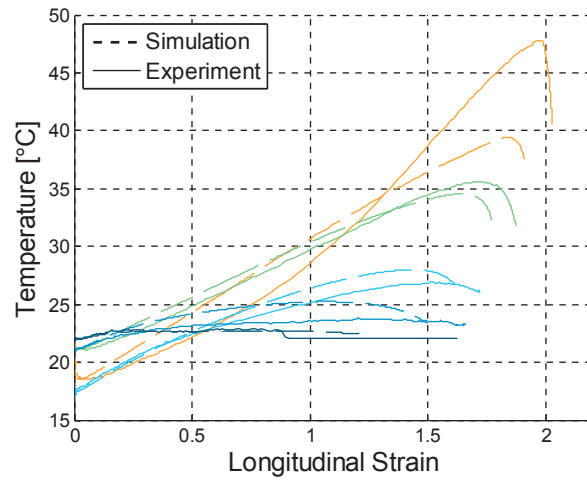
Figure 7.25: Temperature vs. strain curves for experiments and simulations of tests performed with rectangular HDPE tension samples stretched at five different nominal strain rates.

Figure 7.26 shows volumetric strain versus longitudinal strain curves. This figure hence highlights the ability of the implemented evolution function for the β parameter, see Equation (7.56), to capture the dilatation. As seen from the figure, the model is in good agreement with the experimental results. It is recalled that the response in Figure 7.26 addresses the section experiencing the first necking. There is a significant change in the strain rate in this section during the deformation process, yet the model represents the dilatation in an adequate way.
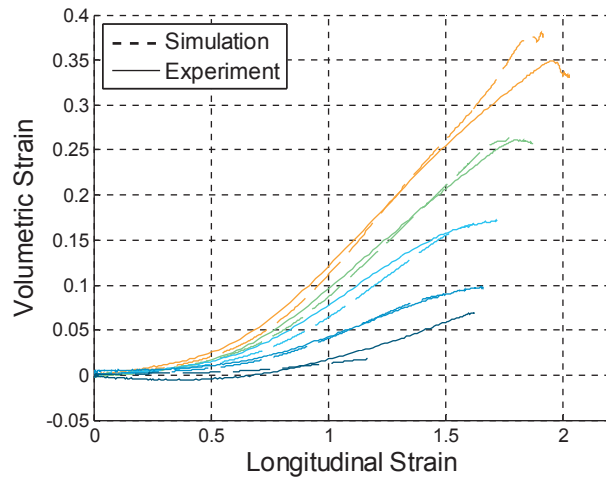
Figure 7.26: Volumetric strain vs. longitudinal strain curves for experiments and simulations of tests performed with rectangular HDPE tension samples stretched at five different nominal strain rates.

For the sake of completion, strain rate versus strain curves are shown in Figure 7.27. Again, the response in the neck is addressed. The simulations capture the general strain-rate levels and the overall shapes of the curves from the experimental tests quite well, but there is a trend of a delay in peak values in the simulations.
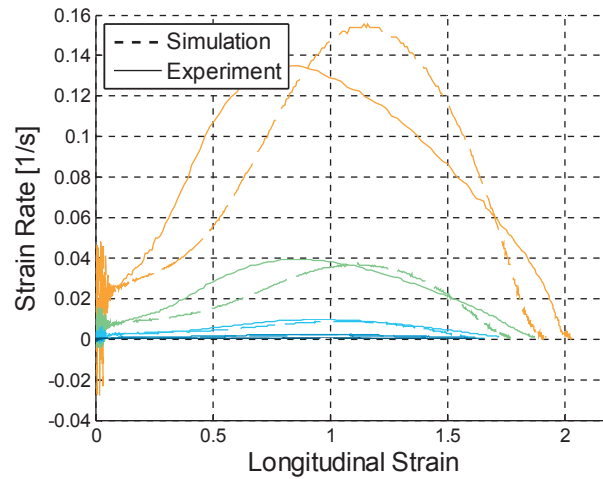
Figure 7.27: Strain rate vs. longitudinal strain for experiments and simulations of tests performed with rectangular HDPE tension samples stretched at five different nominal strain rates.

The last comparison involves force versus displacement curves obtained from experiments and simulations. Figure 7.28 pays attention to these global response parameters. In a similar way as in the previous Figure 7.6 (a), the origin of the force-displacement curve in the simulations is shifted in the right-hand direction to compensate for an inaccurate representation of the elastic stiffness in the experimental data. Again, this is due to compliance of the test machine and possibly also deformation of the gripping parts of the specimen. It is observed from Figure 7.28 that the peak force and the constant force levels corresponding to cold drawing are well captured in all the simulations, i.e. at all strain rates. Also the softening transition from peak force to the drawing force level is excellent in the three slowest cases. However, the level of force is overestimated in this softening region in the faster tests. This overestimation of force indicates that the stiffness in the simulations is too high at some point between yield and maximum obtained strain. Recalling from Figure 7.25 that the temperature was too high for moderate strains in the simulations, the mismatch for the fastest test could be related to temperature softening.
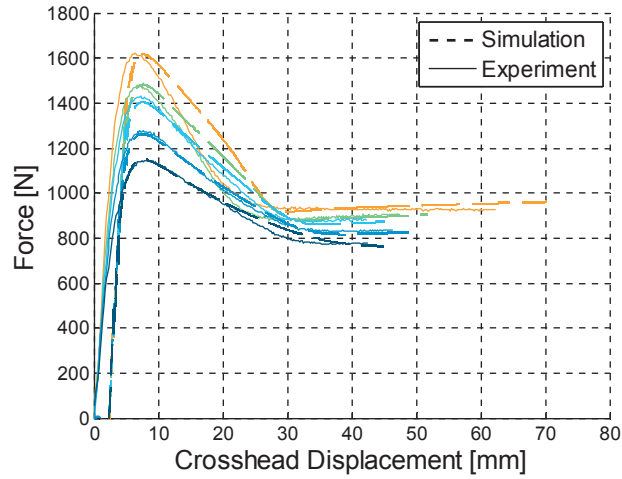
Figure 7.28: Force vs. displacement curves for experiments and simulations of tests performed with rectangular HDPE tension samples stretched at five different nominal strain rates.

7.2.4 Rectangular PVC Samples

Numerical simulations of the uniaxial tension and compression tests on the HDPE material were presented in the previous sections. All these simulations employed the hyperelastic-viscoplastic constitutive model outlined in Section 7.1. Based on observations in the experimental tests on HDPE, the model was extended with some features in order to improve the representation of the physical response. Firstly, the tests revealed that the evolution of the volumetric strain depends on both strain and strain rate. The volumetric strain is governed by the parameter β, and Equation (7.56) proposes an expression for $\beta = \beta(p, \dot{p})$. Further, the tension tests on HDPE samples with rectangular cross section were instrumented with a thermal camera, facilitating measurements of the significant temperature increase due to adiabatic heating in the tests at strain rates of $10^{-2.0}$ s^{-1} and higher. A factor allowing for thermal softening of the flow stress was introduced in Equation (7.60).

The material model, including the extensions proposed in the previous sections, will now be used in numerical simulations of the uniaxial tests on PVC. The rectangular PVC samples were instrumented with a thermal camera in the experimental tests. These tests are therefore used for identification of the parameters in the material model, including the thermal part.

190

Subsequently, the model will be applied in simulations of circular tests and compression tests in Sections 7.2.5 and 7.2.6, respectively.

The PVC samples are modeled without Part B, representing the network stiffness. All stiffness increase after yield is in other words assumed to be isotropic plastic hardening. This is done in order to better capture the dissipation of energy, resulting in temperatures closer to what was measured in the experiments. Within the context of large deformations, it is also recalled from Section 5.3 that the failure strain in the experimental tests on PVC is around 1, while the HDPE samples experienced twice as high logarithmic strain at failure.

The material parameters used to simulate the rectangular PVC samples are shown in Table 7.6. The elastic parameters ν and E are found from the results presented in Figure 5.23 (a) and (b) respectively, while the plastic viscosity parameter C is taken from the results shown in Figure 5.27. The initial yield stress σ_{y0} at the selected plastic reference plastic strain rate $\dot{p}_0$ can be found from the average of the strain-rate normalized curves shown in Figure 5.28, combined with Equation (4.27). Both the initial softening and the eventual hardening of the PVC material are modeled using a two-term Voce hardening law. By letting Q_i take on a negative value, it is possible to approximate plastic softening, while defining the values of both Q_i and C_i as negative results in an exponential type hardening. The Voce parameters are found by doing a fit to a stress vs. plastic strain curve corrected for both strain rate and temperature, as shown in Figure 5.30. In contrast to HDPE, it is seen from Table 7.6 that the parameter α, controlling yield sensitivity to hydrostatic stress, is not set to unity, but rather 1.3. This stress ratio is found directly from the yield stresses in compression and tension as seen in Figure 6.5. The shape of the volumetric strain vs. longitudinal strain curve was observed to be less non-linear compared to the HDPE tests, see Figure 5.34. The plastic dilatation parameter β is hence assumed to be constant for these simulations, and Equation (7.56) is therefore not employed for PVC. The value for β is found from Figure 5.34 where it can be seen that the volumetric strain is about 0.1 at a longitudinal strain of 0.8. The ratio of volumetric strain to longitudinal strain is then $\gamma_{UT} = 0.125$. Inserting this into Equation (7.46) then gives $\beta = 1.09$.

Table 7.6: Material parameters for simulation of rectangular PVC samples.

E [MPa]	ν	σ_{y0} [MPa]	Q_1 [MPa]	C_1	Q_2 [MPa]	C_2	C [MPa]	$\dot{p}_0$ [s^{-1}]	α	β
1700	0.41	23.21	-7	-2.5	-10	20	2.309	$1\cdot10^{-8}$	1.3	1.09

The parameters controlling heat generation, conductivity, convection and the effect on hardening are shown in Table 7.7, which also includes the density. Density ρ, specific heat C_p and thermal conduction k were all found from the database MATBASE [43]. The Taylor-Quinney coefficient χ was found from Figure 5.32, while the thermal film convection coefficient h between PVC and air was estimated in the same way as for HDPE, described in Section 7.2.3. The melting temperature T_M and the softening parameter m were both found through iterative simulations, where the best choice of parameters within reasonable limits was used. Room temperature T_R was set to 20°C for all simulations. Thermal softening is defined by Equation (7.61).

Table 7.7: Thermal parameters for simulation of rectangular PVC samples.

ρ [kg/m^3]	χ	C_p [J/kgK]	k [W/mK]	h [W/m^{2}K]	m	T_R [°C]	T_M [°C]
1414	0.8	1000	0.2	7	0.8	20	100

With the model parameters defined, it is now possible to perform the simulations. The tests are simulated using a 1/4 model, were the model has half the thickness and width of the physical samples. The element discretization can be seen in Figure 7.29. The full length of the sample was used in these simulations since, as will be shown, there was a tendency to localization close to the shoulder at higher rates. Using a half-length model would then imply that two necks formed rather than one. This problem was solved by introducing a small imperfection in the form of a thickness reduction of 0.005 mm. This imperfection was introduced approximately at the middle of the section with the finest mesh, seen as the right part of the gauge area of the sample in Figure 7.29. As with all simulations, strains were taken only from the surface of the section first necking. Since necking initiated at different areas of

the geometry dependent on the loading speed, the location of the section for data collection varies between the simulations.

Figure 7.29: Mesh for simulations of rectangular PVC samples in uniaxial tension.

The stress-strain curves from the simulations are shown with the curves from the experiments in Figure 7.30. The curves from the tests, addressed with solid lines, are previously shown in Figure 5.22. In general, there is a good agreement between the solid and corresponding dashed curves, yet with some overestimation of the stress for the three fastest tests. The differences can primarily be attributed to the thermal softening model and calibration. It should also be noted that the plot does not show the complete curves of the simulations of the two fastest strain rates. These curves continue to increase to unrealistically large strain values. It was found that at higher loading speeds, the thermal softening was so large that it prevented propagation of the neck from the section of initial necking. This section hence continued to localize and without a fracture criterion, their cross-section area was monotonically reduced towards zero. The same phenomenon is also responsible for the abrupt drop in stress seen in the simulation of the third fastest test (dashed blue graph). In this simulation the continued strain localization happens outside the point of initial localization, resulting in an unloading of the section addressed in the stress-strain curve in Figure 7.30.
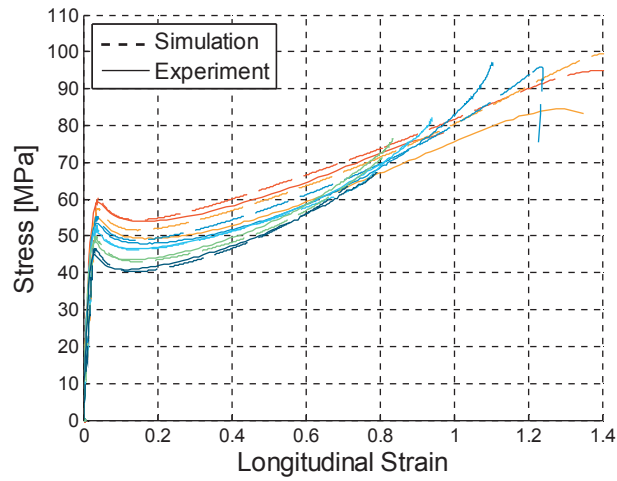
Figure 7.30: Stress vs. strain curves for experiments and simulations of rectangular PVC samples stretched at six different nominal strain rates.

The curves showing the relation between temperature and longitudinal strain for experiments and simulations are presented in Figure 7.31. The simulations capture the measured temperature well, and it can be seen that the use of a constant Taylor-Quinney coefficient results in a good agreement. It should be kept in mind that the entire exponential-type of hardening is now defined as plastic because Part B of the material model is omitted, and hence contributes to heat generation. Even with this conservative approach an underestimation of temperature is still observed in the simulation of the two fastest tests.
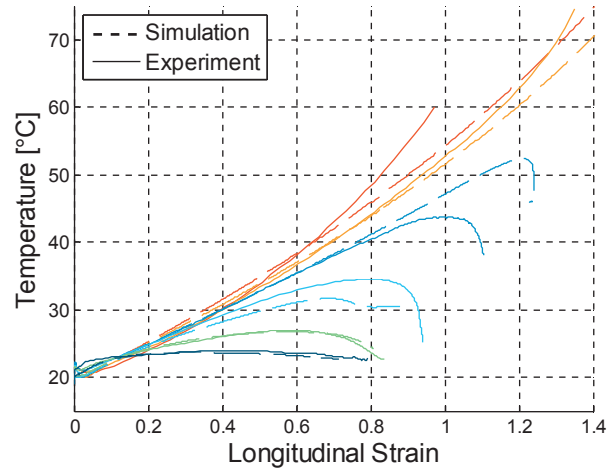
Figure 7.31: Temperature vs. strain curves for experiments and simulations of tension tests performed with rectangular PVC samples stretched at six different nominal strain rates.

Volumetric strain and strain rate are shown against longitudinal strain in Figure 7.32 (a) and (b), respectively. As can be seen from Figure 7.32 (a), the choice of a constant β results in a reasonable representation of the dilatation to what was measured from the tests. Looking at Figure 7.32 (b), it can be seen that the strain rate is well described up to a longitudinal strain of 0.4, while the simulations overestimate the strain rate at larger strains. This deviation from the experimental curves comes as a result of thermal softening and a slight difference in the propagation of the neck.

(a) Volumetric strain   (b) Strain rate
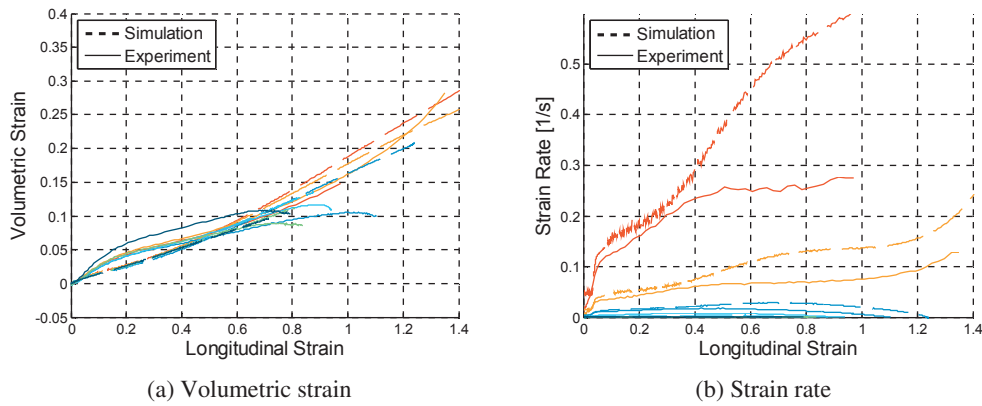
Figure 7.32: Volumetric strain versus longitudinal strain curves (a), and strain rate versus longitudinal strain (b). Comparison between simulation and tests performed with rectangular PVC samples stretched at six different nominal strain rates.

Figure 7.33 shows force vs. displacement curves for the simulations and the experiments. As seen, the curves from the simulations are quite close to the experimental curves for all strain rates. An interesting and somewhat unexpected feature is that the simulations predict failure through localization for all three tests where failure was observed, i.e. the fastest tests, although at less displacement than in the experiments. This numerical representation of the final localization and subsequent failure is made possible by omitting Part B, which at a limit level of strain predicts a stiffness approaching infinity for all positive values of C_R. This would hence halt localization in the simulation and rather promote neck propagation. The fact that the simulations are able to capture this localization behavior also underpins the importance of including thermal softening if material failure is of interest. Thus, Figure 7.33 demonstrates that constitutive model at hand seems to capture the distinctly different physical response of PVC at strain rates ranging from $10^{-3.5}$ to $10^{-1.0}$ s^{-1}.
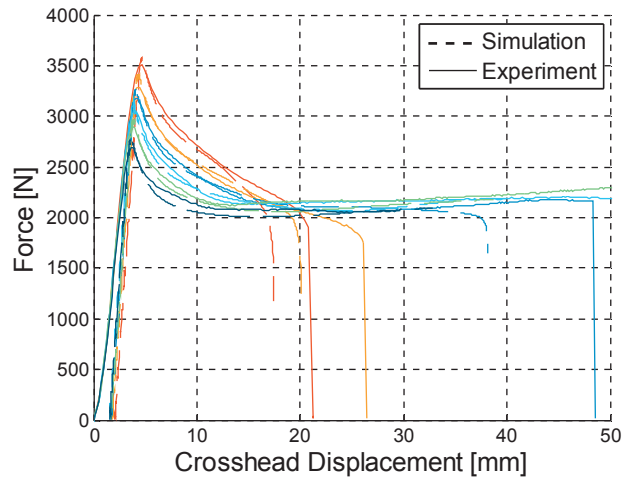
Figure 7.33: Force vs. displacement curves for experiments and simulations of rectangular PVC samples stretched at six different nominal strain rates.

The degree of localization as function of nominal strain rate is illustrated in Figure 7.34, showing the deformed shape as found from all six simulations at a crosshead displacement of 15 mm. The color map shows the distribution of longitudinal strain in the samples. The general trend is that all simulations initially localize close to both shoulders due to the slightly increased stress triaxiality at the end of the gauge part of the sample. At low loading rates, the thermal softening is negligible, and the strain hardening ensures that the two diffuse necks converge quickly to the center of the sample, creating a visually distinct neck. However, at higher loading speeds, the significant thermal softening prevents these diffuse necks from propagating to the center of the sample, and instead a distinct neck is formed at one or both locations. As mentioned, the homogeneity of the simulations initially resulted in two symmetric necks close to the shoulders, so a small local reduction in thickness was introduced in all simulations approximately where the neck is seen to form in the faster tests.

$10^{-1.0}$ s^{-1} $10^{-1.5}$ s^{-1} $10^{-2.0}$ s^{-1} $10^{-2.5}$ s^{-1} $10^{-3.0}$ s^{-1} $10^{-3.5}$ s^{-1}
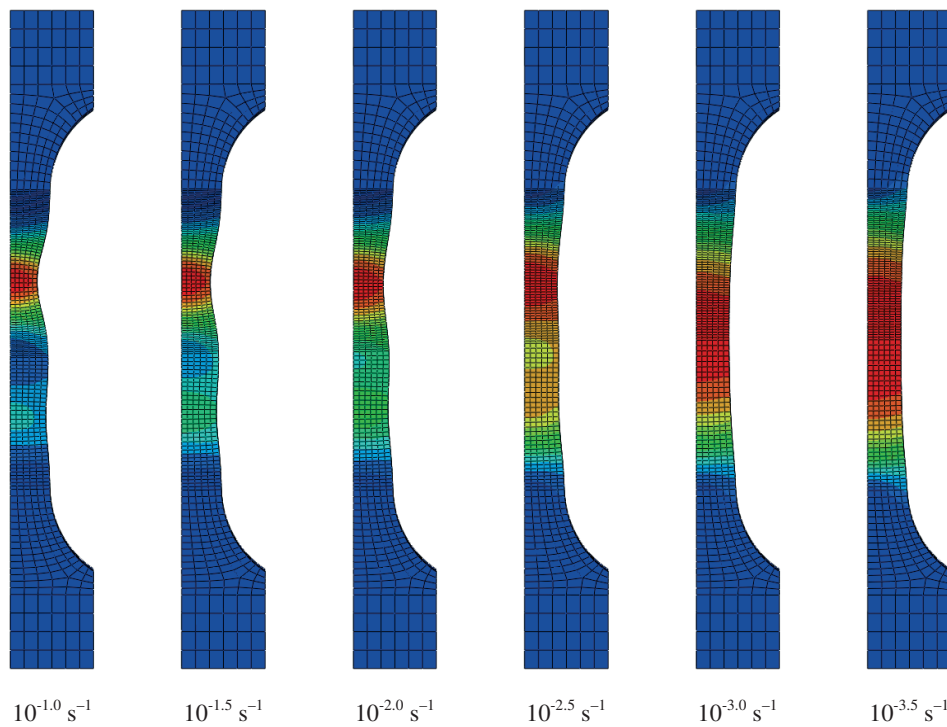
Figure 7.34: Contour plots of longitudinal strain from simulations of PVC performed at six different loading speeds, taken at a crosshead displacement of 15 mm.

7.2.5 Circular PVC Sample

The benefit of the circular cross-section is that this design of the sample facilitates larger deformations before failure, and also that the determination of volumetric strain is somewhat more reliable than it is for the rectangular specimens. The tests performed with the circular PVC samples were simulated with an explicit thermo-mechanical axisymmetric model with the mesh shown in Figure 7.35. All simulations localized at the center of the sample, hence, this mid-section defines the area where local data is recovered from.
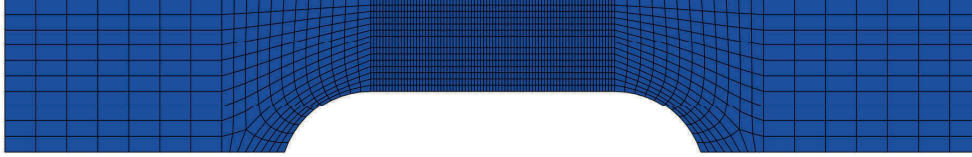
Figure 7.35: Mesh for simulations of circular PVC samples in tension.

The material parameters used to simulate the circular PVC tests are given in Table 7.8. The parameters have the same values as those applied for the rectangular PVC samples, with the exception of σ_{y0}, Q_1, C_1 and Q_2. As previously emphasized for the HDPE material, the tests on the specimens with circular cross section were carried out two years after the tests with the rectangular specimens also in the case of PVC, and the decreased level of the flow stress might be attributed to time-dependent degeneration of the material.

Table 7.8: Material parameters for simulation of circular PVC samples.

E [MPa]	v	σ_{y0} [MPa]	Q_1 [MPa]	C_1	Q_2 [MPa]	C_2	C [MPa]	$\dot{p}_0$ s^{-1}	α	β
1700	0.41	16.0	-3.2	-3	-8	20	2.309	$1 \cdot 10^{-8}$	1.3	-

The parameters describing the plastic strain hardening are compared in Table 7.9. As seen, the initial yield stress σ_{y0} is lower in the tests with the circular tension samples, but so is the parameter Q_2 controlling the softening occurring immediately after yielding. The net result is that the tests with the rectangular samples exhibit a larger peak stress value compared to the tests with circular samples, but this difference is reduced with softening. This can be seen by looking at the sum of σ_{y0} and Q_2, the results are then equal to 13.21 and 8 MPa for the model of the rectangular and circular tests respectively. They were also found to have a difference in hardening, as seen by the value of Q_1 and C_1.

Table 7.9: Comparison of material calibration for square and circular PVC samples.

	σ_{y0} [MPa]	Q_1 [MPa]	C_1	Q_2 [MPa]	C_2
Rectangular (2012)	23.21	-7	-2.5	-10	20
Circular (2014)	16	-3.2	-3	-8	20
Difference	7.21	-3.8	0.5	-2	0

The thermal parameters are equal to those found for the simulations of the rectangular samples, and were shown in Table 7.7.

As seen from the experimental test results in Figure 5.64 and Figure 5.65, volumetric growth was more or less the same at different strain rates. In order to replicate this behavior, β is assumed to vary only with equivalent plastic strain p, while the factor due to strain rate $\dot{p}$ in Equation (7.56) is discarded. The function shown in Equation (7.53) is used with the parameter set $[a,b,c]=[0.45 \quad 0 \quad 0.28]$. These parameters are calibrated from the corrected volumetric strain shown in Figure 5.65, calculated with the "parabolic method". Setting the parameter b equal to 0 is equivalent to assuming that the maximum slope of volumetric strain growth $\gamma_{UT} = d\varepsilon_V^p / dp$ occurs when $p = 0$, which corresponds well with Figure 5.65. The initial value for β is then equal to the value of $a+1=1.45$, and from Equation (7.51) it can be seen that this result in the initial volumetric growth $d\varepsilon_V^p / dp = 0.55$.

The stress-strain behavior in the simulations and tests are compared in Figure 7.36. As seen from the figure, the simulations do a fair job of replicating what was measured in the experiments. The model captures the local stress maximum at the onset of yielding and the trends of thermal softening, but overestimates the stress at higher strain levels. This could either be a result of an underestimation of temperature or an underestimation of thermal softening. This cannot be determined since thermal data was not recorded for this test series.
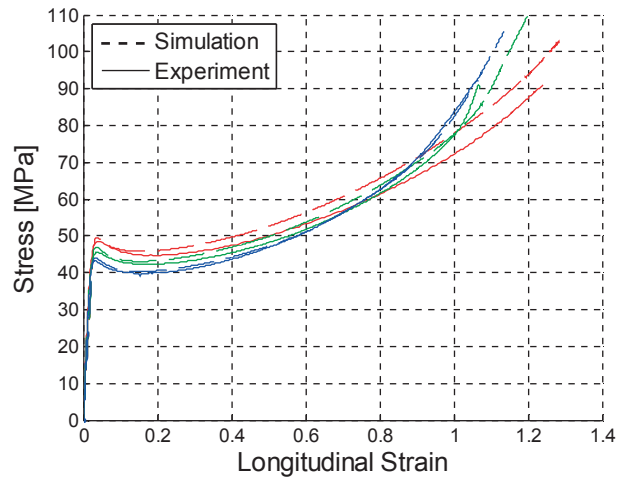
Figure 7.36: Stress vs. strain curves for experiments and simulations of circular PVC samples stretched at three different nominal strain rates.

On the other hand, the numerical model provides predictions of the temperature increase, and it is shown for the three strain rates in Figure 7.37. It is difficult to comment on the accuracy of these curves, but it was previously shown in Figure 7.31 that the agreement between the temperatures measured in the tests and calculated in the simulations was satisfactory for the PVC samples with rectangular cross-section. It can be seen from Figure 7.37 that the slowest of the tests has a modest temperature increase of 6°C. This test at $10^{-2.5}$ s^{-1} is hence assumed to represent conditions that are close to isothermal.
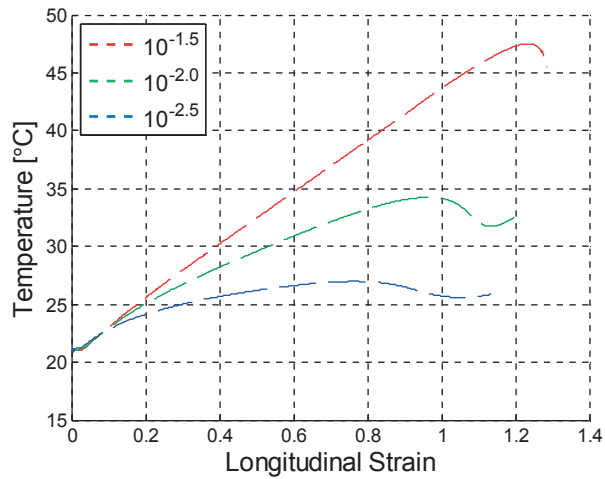
Figure 7.37: Temperature vs. strain curves for simulations of circular PVC samples stretched at three different nominal strain rates.

Strain rate is shown against strain in Figure 7.38 for the experiments and simulations. As can be seen, the simulations capture the general levels of strain rate well, with the exception of the distinct peaks predicted at a strain of 0.1. The peaks in the simulations are obviously related to plastic softening and hardening, where the strain rate increases as the material softens, and then decreases as it again hardens. The question is then; why is the peak not present in the experimental data? The answer seems to be that necking in the simulations is a more localized and rapid process.
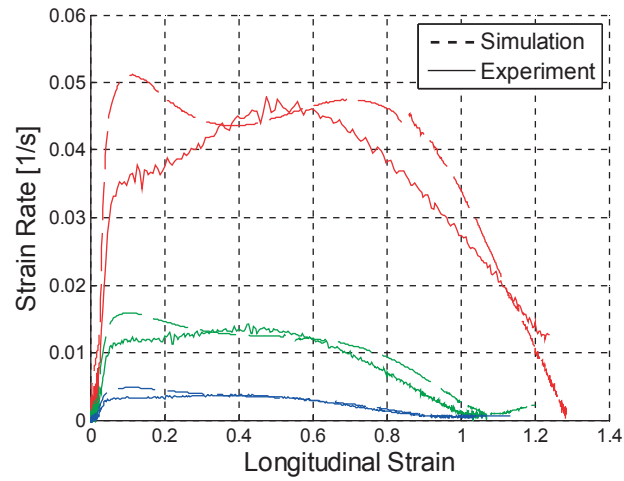
Figure 7.38: Strain rate vs. strain curves for experiments and simulations of circular PVC samples stretched at three different nominal strain rates.

The effects of employing a strain-dependent function for β, see Equation (7.53), can best be seen in Figure 7.39 where volumetric strain is shown against longitudinal strain. As evident from the figure, the simulations describe the apparent volumetric strain well, even capturing the difference in slope between the three tests. This shows that the proposed evolution law in Equation (7.53) for the β parameter is flexible enough to handle different materials and that there is a common trend for both tested materials that the volumetric strain converges to a limit level.
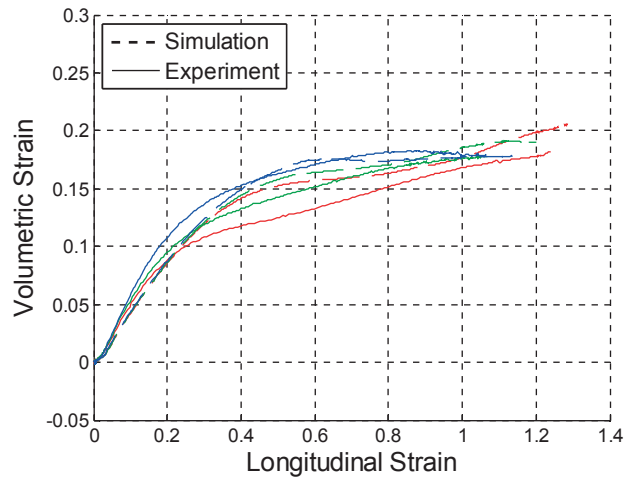
Figure 7.39: Volumetric strain vs. longitudinal strain curves for experiments and simulations of circular PVC samples stretched at three different nominal strain rates.

As the simulations capture the correct level of volumetric strain as function of longitudinal strain, but overpredicts the level of stress, it is natural that the simulations also overestimates the force level as a function of the radius of the section first experiencing necking. This is confirmed in Figure 7.40. Moreover, it appears from the figure that the force approaches a constant level for the fastest test, while there is some increase in force when the neck radius is around 2 for the two other cases. This difference is likely to be a result of thermal softening.
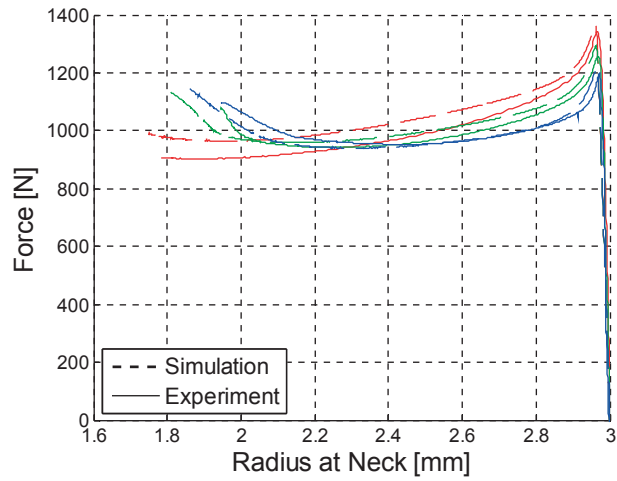
Figure 7.40: Force vs. radius curves for experiments and simulations of circular PVC samples stretched at three different nominal strain rates.

The final figure from the simulations of these tests shows the force-displacement curves. Again, the simulations in Figure 7.41 capture the trends from the tests well, and follow the curves from the experiments throughout the whole range of deformation for the two slowest tests. The simulation captures the slope immediately before failure of the fastest test, but overestimates the force level. This is again related to the overestimation of stress as seen in Figure 7.36.
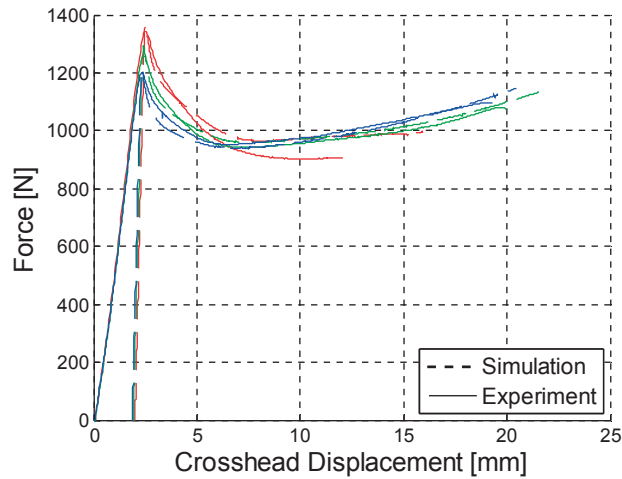
Figure 7.41: Force vs. displacement curves for experiments and simulations of circular PVC samples stretched at three different nominal strain rates.

7.2.6 PVC in Compression

The PVC compression test is simulated with a full length thermo-mechanical axisymmetric model. The simulation uses the same boundary conditions and mesh as the one used for the simulation of the HDPE compression test, as seen in Figure 7.13. The material parameters used in the simulations of the circular PVC tension samples are also used to simulate the PVC compression test, with the exception of assuming a constant value of $\beta = 1.09$ of the plastic dilatation parameter. It is assumed constant since volumetric growth data is considered unreliable. Any simulation result would hence have no solid basis of comparison.

As mentioned when the simulation of the HDPE compression test was discussed, it was found that it is challenging to capture friction correctly in the simulations. This can be seen in most response parameters, but is especially influential when it comes to apparent volumetric strain. It is recalled that this corresponds to the volumetric strain calculated with the "cylinder method", i.e. $\varepsilon_V = \ln(\lambda_V) = \ln(\lambda_L \lambda_R^2)$. The stretches are determined from the surface of the mid-section of the sample in the test as well as the simulations. Figure 7.42 shows apparent volumetric strain from an experimental test and three simulations where only the Coulomb friction coefficient is varied. The friction coefficient is set to 0.12, 0.06 and 0.04 for the black,

red and green curve respectively. It is an obvious problem that the volumetric strain, which normally is assumed to be independent of friction, is seen to be highly influenced by friction. This is a fundamental problem associated with compression test samples having a cylindrical shape with constant radius. In the following figures, the friction coefficient is assumed to be equal to 0.03.
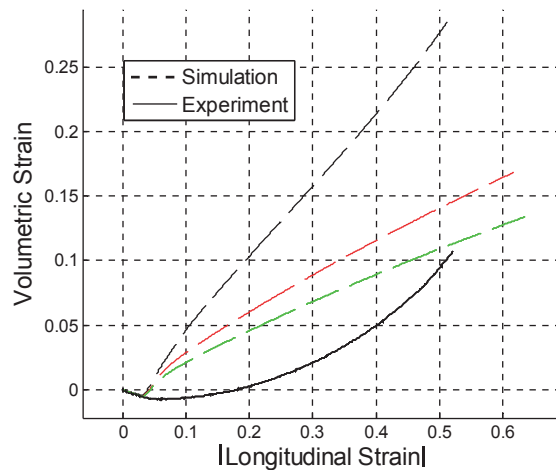
Figure 7.42: Volumetric strain vs. |longitudinal strain| curves for experiment and simulations of PVC compression test. Simulations shown apparent local volumetric strain, calculated with the "cylinder method" for simulations run with three different values of Coulomb friction equal to 0.12 (black curve), 0.06 (red curve) and 0.04 (green curve).

The absolute value of stress is plotted against the absolute value of strain in Figure 7.43. As seen from the figure, the simulation captures the yield stress level, and represents the softening in an adequate manner. The good agreement in yield stress shows that the α parameter is well calibrated. However, when it comes to the hardening, the simulation is vastly overestimating the stress. This comes as a result of the use of the isotropic plastic Voce hardening to model what is more likely to be the network stiffness of the material. As demonstrated in Figure 7.2, the contribution from Part B to the stiffness in uniaxial compression is much smaller than it is for uniaxial tension, but such a difference between tension and compression is not present for Voce's hardening law. Thus, the simulation predicts way too high hardening modulus.

Depending on whether Part B is employed to model network stiffness or not, it appears that the current model can only represent either tension or compression in a proper way. It can either omit Part B and capture the plastic work needed to create the adiabatic heating measured in the tension tests, providing the correct thermal softening, or provide an accurate hardening modulus in both tension and compression, but then only for isothermal conditions.
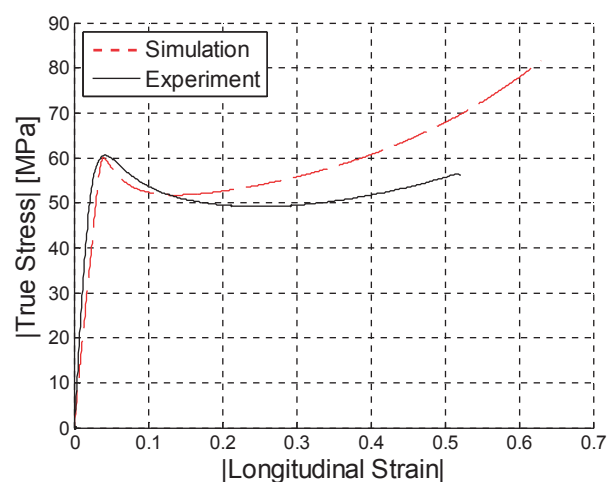
Figure 7.43: |True stress| vs. |longitudinal strain| curves for experiment and simulations of PVC compression test.

Center radius and volumetric strain is shown against the absolute value of longitudinal strain in Figure 7.44 (a) and (b). As seen, the simulation roughly captures the response at the end of the test, i.e. at a strain around 0.5, but is overestimating both radius and volumetric strain for most of the deformation process. The strong dependency on friction does however complicate the analysis of the data. The inability of the simulations to capture the non-linearity of the measured volumetric growth could be a result of the assumed friction model. As will be showed in the Figure 7.45 (a), it seems that Coulomb friction coefficient increases throughout the test. It can then be assumed that this would lead to an exponential type increase in apparent volumetric growth, from the results seen in Figure 7.42.

(a) Center radius   (b) Volumetric strain
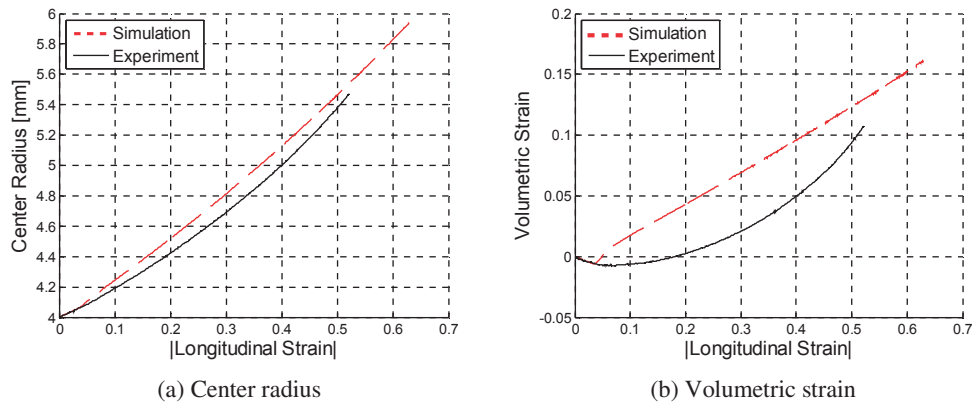
Figure 7.44: Radius vs. |longitudinal strain| (a) and volumetric strain vs. |longitudinal strain| (b) for a simulation and test of a PVC sample in compression.

It has already been demonstrated that the simulation of compression tests with the assumption of constant Coulomb friction does not seem to adequately represent the reality of the test. Another illustration is provided by looking at the evolution of the curvature of the sample, as compared between simulation and experiment in Figure 7.45 (a). The same trend seen for the simulation of HDPE in compression is also observed here, where the choice of friction parameter initially seems to be too high, while it is probably too low at larger strains.

Since the simulation is a coupled thermo-mechanical analysis, predicted temperature is also available. The temperature calculated at the surface of the center section of the sample is shown in Figure 7.45 (b). Since the stress is too high, the temperature is probably also overestimated, yet it is likely that the current choice of loading rate in the compression test creates a substantial increase in temperature. Further work should hence monitor the temperature, also in compression tests.

209
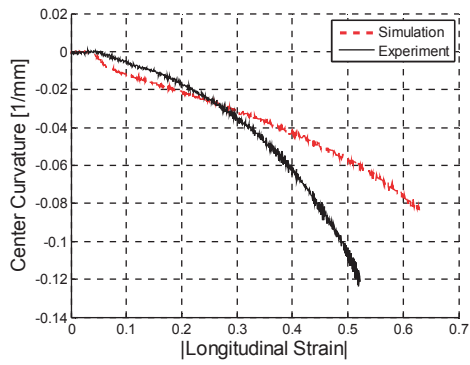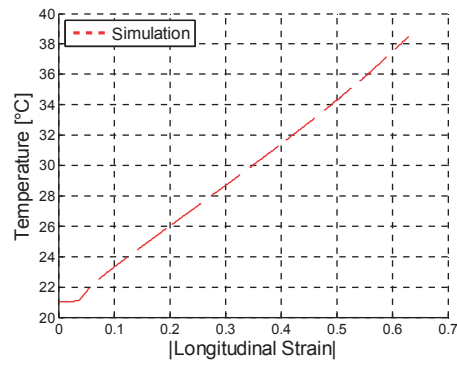
(a) Center curvature   (b) Temperature in simulation

Figure 7.45: Curvature vs. |longitudinal strain| (a), comparison between simulations and test of PVC in compression. Predicted temperature vs. |longitudinal strain| from simulation (b) for PVC in compression.

The final figure from the simulation of the compression test shows the force-displacement curves for the simulation and the experiment. As would be expected, the force is overestimated in a fashion similar to the difference in stress-strain response already reported in Figure 7.43. The deviation in the radius plot in Figure 7.44 (a) also contributes to the deviation between the force-displacement curves.
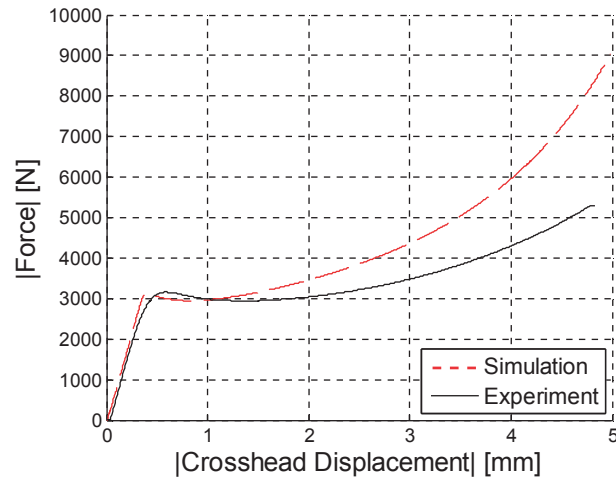
Figure 7.46: |Force| vs. |crosshead displacement| curves for test and simulations of cylindrical PVC compression sample.

7.2.7 Summary of Numerical Simulations

This chapter has been devoted to numerical analyses of the uniaxial tension and compression test presented in Chapters 5 and 6, respectively. Moreover, an incremental expansion of the baseline material model presented in Section 7.1 have been outlined, where extensions to the model have been added when the complexity of the experimental observations has demanded it.

A consistent method for characterizing and modeling the sensitivity of volumetric growth to plastic strain and strain rate in uniaxial tension has been presented through Equations (7.46), (7.52) and Section 7.2.3. The final equation for the plastic dilatation parameter β expressed as a function of equivalent plastic strain p and strain rate $\dot{p}$ was given in Equation (7.56).

A simple but effective temperature softening formulation was also included in the model in Section 7.2.3, with the formulation shown in Equation (7.60). The incorporation of this softening formulation as well as the use of a coupled thermo-mechanical analysis has

211

throughout this chapter been shown to be essential for simulating both HDPE and PVC over the range of strain rates covered in the laboratory tests.

Finally, it has been shown that there seems to be a problem unifying the use of the elastic eight-chain network stretching model [39] with the dissipated energy measured as an increase in temperature. It was shown in Section 7.2.4 that there is a significant dissipation in PVC which is not possible to capture with the assumption that late stage hardening is not dissipating energy. On the other hand, it was also shown that the assumption that hardening in PVC is a plastic and isotropic process most likely is incorrect, as this assumption leads to substantial overestimation of the stiffness in PVC in uniaxial compression, as was shown in Section 7.2.6. Thus the mechanisms for energy dissipation and subsequent temperature increase during deformation call for further investigation.

Nevertheless, the extended model has been shown to be highly capable in its ability to simulate the mechanical and thermal response of both HDPE and PVC in uniaxial tension up to large strains at several strain rates. Its predictive prowess outside this narrow range of triaxiality is uncertain, but it is believed that the presented model and model development methodology can be used and expanded on in order to create a more general model.

8 Conclusions and Suggestions for Further Work

8.1 Conclusions

Ductile thermoplastics is a class of materials that often experiences large deformations before the ultimate failure. Moreover, such materials typically localize rather early in the tensile deformation process, after which the neck cold-draws until the molecular chains start straightening out, giving an excess straining before the material fails. State-of-the-art today is to instrument uniaxial tension tests with a digital camera, and subsequently analyze the pictures with digital image correlation (DIC) to determine the strain field. A dog-bone shaped test sample is most frequently employed in such investigations.

It has been shown in this thesis that linear DIC elements have shortcomings in their representation of the strains during the necking process. To improve the accuracy of the strains found from a set of picture, a higher order DIC element with 16 nodes has been developed and implemented. Moreover, this new DIC element is complemented with an edge tracing technique serving to determine the radius of curvature at the neck. The use of higher order DIC elements simplifies the process of locating and recording the deformation of the material section first experiencing necking in a uniaxial tension test. The proposed method of locating and calculating the strains for this material section has been shown to give consistent results across repetitions of tests. The combination of DIC and edge tracing is advantageous in that the measurements both overlap and complement each other. They hence serve as validations of each other as well as providing additional information. The use of a custom-made DIC code has also proven beneficial for the process of combining thermal imagery with strain measurements. This measurement methodology has been validated through FEM simulations. As a part of the improvement of the test protocol, the uniaxial tension test sample has been re-designed. In order to explore the large post-necking strains occurring towards the end of a test, the new sample has a comparatively short gauge length to assure that the resolution of the digital pictures is maintained. Moreover, investigations on the failure process call for accurate measurements of the volumetric strains, and the new test sample therefore has a circular cross section.

It has been shown that the combination of a 1D material model and experimental data serves to separate and quantify the effects of strain rate and temperature on mechanical response found from experimental data, even when these quantities have large variations throughout a single test. It appears from the uniaxial tension tests that both HDPE and PVC, which were the materials investigated in this thesis, experience a significant increase in temperature even at strain rates of order 10^{-2} s^{-1} as a result of adiabatic heating. This temperature increase greatly affects the mechanical material response in both materials.

Great care should be taken when local deformation is quantified in the post-necking phase during a tension test. This is especially obvious when it comes to measuring volumetric strain. It has been demonstrated that using the traditional method for calculating the change of volume in uniaxial tension, assuming that the volumetric strain is the sum of the three normal strain components, can lead to severely inaccurate results. An alternative method for calculating volumetric strains, taking the radius of curvature of the neck into account, has been proposed in the form of an equation which has been validated through FEM simulations and an experiment. This improved equation is believed to be applicable to a wide range of materials, although it is limited to samples with circular cross section in its present form.

Applying the purpose-made higher-order DIC element and the edge tracing technique in combination with the improved formula for volumetric strain, new insight into the evolution of volumetric strain up to large deformation for the two materials was gained. Volumetric growth in PVC, when subjected to uniaxial tension, has through electron microscopy been linked to the debonding of rigid particles and the material matrix. It was further observed that volumetric growth in PVC is non-linear with longitudinal strain, and appears to saturate at large longitudinal strains. Volumetric strain in PVC was not much affected by strain rate. The volumetric increase in HDPE in uniaxial tension had a somewhat similar evolution to that of PVC, but with a delayed initiation and a slower rate of growth. In contrast to PVC, the volumetric growth in HDPE was seen to be dependent on strain rate. The mechanism behind dilatation in HDPE was not identified, but the absence of observable voids in an electron microscope might indicate that the mechanism operates on an inter-molecular level.

The material model proposed by Polanco-Loria et al. [7] has been modified and extended to account for the non-linear volumetric growth measured in tension and the material softening

214

that follows from adiabatic heating. FEM simulations with this new material model have revealed that the eight-chain entropic elastic network stretching model proposed by Arruda and Boyce [39] is well suited to capture the exponential type hardening observed in HDPE, even at strains past the natural draw ratio. It was however seen that the inclusion of this hyperelastic model at higher strain rates resulted in an underprediction of dissipated energy, as measured by the increase of material temperature. This was even more prominent in PVC. In the simulations, it was therefore necessary to assume that all hardening was plastic in order to achieve the material temperatures measured in the experiments. This indicates that the late stage hardening observed in the tests on both HDPE and PVC is not a pure elastic mechanism as it appears to dissipate energy.

The inclusion of temperature softening has been shown to be integral to the simulation of these materials, even at relatively low strain rates. The simple softening model proposed in this thesis was seen to give results that were in good agreement with the experimental results. The proposed model for plastic volumetric strain, where it is assumed that plastic volumetric strain can vary with equivalent plastic strain and equivalent plastic strain rate, was shown to give excellent results in the simulations of uniaxial tension tests.

Finally, the simulations of cylindrical material samples subjected to uniaxial compression highlighted several problems with this type of material test at strains past yielding. The main challenge is friction, and it was seen that the mechanical response measured in the tests was highly sensitive to a change in the coefficient of friction. The simulation of PVC cylinders in uniaxial compression also revealed that even though exponential hardening in tension was best modeled as a plastic process, this hardening cannot be isotropic, as it was seen that isotropic hardening resulted in a significant overestimation of the force in compression.

8.2 Suggestions for further work

Two main types of uniaxial tension test samples have been used in this thesis: samples with a circular cross section and samples with a rectangular cross section. These two sample geometries were seen to indicate different mechanical response for the same material. This has been assumed to be related to the storage time since the tests on the different sample types

were performed about two years apart. This assumption should however be verified by performing uniaxial tension tests using both geometries within a short span of time.

The volumetric growth in HDPE and PVC has been thoroughly documented and investigated in uniaxial tension. Further work is however required in order to answer some remaining research questions:

- How does volumetric growth respond to a change in triaxiality?
- What are the limits of the assumption that volumetric strain is independent of temperature?
- What is the mechanism or mechanisms behind volumetric growth in HDPE?
- How is volumetric growth connected to failure?
- What is the mechanism behind the saturation of volumetric strain?

Temperature effects have been analyzed and quantified, but material behavior has only been observed at elevated temperatures that came as a result of adiabatic heating. Temperature and strain rate has hence not been varied independently, and the materials have not been subjected to temperatures lower than room temperature. Further work should hence include equivalent uniaxial tension tests performed at a close-to isothermal strain rate, but with higher and lower constant temperatures relative to the room temperature applied in this thesis. Unanswered questions are:

- Is the presented temperature softening model valid at lower temperature?
- How does plastic viscosity change with temperature?
- How is mechanical response at low strains affected by temperature change?

The presented extended material model is likely to be limited in terms of larger changes in triaxiality. In addition, it was shown that it does not manage to represent both uniaxial tension and compression when temperature softening is relevant. Unanswered questions pertaining to modeling the two materials are:

- How should network stretching be modeled in order to both capture the reported temperature increase and also capture the difference in stiffness seen in tension and compression?

216

- Can the materials be modeled with an associated yield function and flow potential if they both are assumed to vary despite a constant triaxiality?
- How should failure be modeled?

9 References

1. Standard, N., *ISO 527-2:2012*, in *Plast - Bestemmelse av strekkegenskaper - Del 2: Prøvingsbetingelser for støpe- og ekstruderingsplast* 2012, Standard Norge: standard.no.

2. G'Sell, C., J.M. Hiver, A. Dahoun, and A. Souahi, *Vide-controlled tensile testing of polymers and metals beyond the necking point.* Journal of Materials Science, 1992. **27**: p. 5031-5039.

3. Rastogi, P.K., *Photomechanics*. 1 ed. Vol. 77. 2000: Springer.

4. Parsons, E., M.C. Boyce, and D.M. Parks, *An experimental investigation of the large-strain tensile behavior of neat and rubber-toughened polycarbonate.* Polymer, 2004. **45**(8): p. 2665-2684.

5. Jerabek, M., Z. Major, and R.W. Lang, *Strain determination of polymeric materials using digital image correlation.* Polymer Testing, 2010. **29**(3): p. 407-416.

6. Fagerholt, E., *Field Measurements in Mechanical Testing Using Close-Range Photogrammetry and Digital Image Analysis*. 2012: NTNU.

7. Polanco-Loria, M., A.H. Clausen, T. Berstad, and O.S. Hopperstad, *Constitutive model for thermoplastics with structual application.* 2010(37).

8. Haward, R.N. and G. Thackray, *The Use of a Mathematical Model to Describe Isothermal Stress-Strain Curves in Glassy Thermoplastics.* Proceedings of the Royal Society of London, 1968. **302**(1471): p. 453-472.

9. Boyce, M.C., D.M. Parks, and A.S. Argon, *Large Inelastic Deformation of Glassy Polymers, Part I: Rate-Dependent Constitutive Model.* Mechanics of Materials, 1988. **7**(1): p. 15-33.

10. Boyce, M.C. and E.M. Arruda, *Constitutive Model for the Finite Deformation Stress-Strain Behavior of PET above the Glass Transition.* Polymer, 2000. **41**(6): p. 2183-2201.

11. Tervoort, T.A., R.J.M. Smit, W.A.M. Brekelmans, and L.E. Govaert, *A constitutive equation for the elasto-viscoplastic deformation of glassy polymers.* Mechanics of Time-Dependent Materials, 1998. **1**(3): p. 269-291.

12. Wu, J.J. and C.P. Buckley, *Plastic deformation of glassy polystyrene: A unified model of yield and the role of chain length.* Journal of Polymer Science Part B: Polymer Physics, 2004. **42**(11): p. 2027–2040.

13.   Dupaix, R.B. and M.C. Boyce, *Constitutive modeling of the finite strain behavior of amorphous polymers in and above the glass transition.* Mechanics of Materials, 2007. **39**(1): p. 39-52.

14.   Richeton, J., S. Ahzi, K.S. Vecchio, F.C. Jiang, and A. Makradi, *Modeling and validation of the large deformation inelastic response of amorphous polymers over a wide range of temperatures and strain rates.* International Journal of Solids and Structures, 2007. **44**(24): p. 7938-7954.

15.   Anand, L., N.M. Ames, V. Srivastava, and S.A. Chester, *A thermo-mechanically coupled theory for large deformations of amorphous polymers. Part I: Formulation.* International Journal of Plasticity, 2009. **25**(8): p. 1474-1494.

16.   Raghava, R., R.M. Caddell, and G.S.Y. Yeh, *The macroscopic yield behaviour of polymers.* Journal of Materials Science, 1973. **8**(2): p. 225-232.

17.   Ognedal, A.S., A.H. Clausen, A. Dahlen, and O.S. Hopperstad, *Behavior of PVC and HDPE under highly triaxial stress states: An experimental and numerical study.* Mechanics of Materials, 2014. **72**(0): p. 94-108.

18.   Ognedal, A.S., A.H. Clausen, M. Polanco-Loria, A. Benallal, B. Raka, and O.S. Hopperstad, *Experimental and numerical study on the behaviour of PVC and HDPE in biaxial tension.* Mechanics of Materials, 2012. **54**(0): p. 18-31.

19.   Sun, Y., J.H.L. Pang, C.K. Wong, and F. Su, *Finite element formulation for a digital image correlation method.* Applied Optics, 2005. **44**(34): p. 7357-7363.

20.   Besnard, G., F. Hild, and S. Roux, *"Finite-Element" Displacement Fields Analysis from Digital Images: Application to Portevin–Le Châtelier Bands.* Experimental Mechanics, 2006. **46**(6): p. 789-803.

21.   Michael A. Sutton, S.R.M., Jeffrey D. Helm, Yuh J. Chao, *Advances in Two-Dimensional and Three-Dimensional Computer Vision*, in *Photomechanics*, D.P.K. Rastogi, Editor. 09.02.2000, Springer Berlin Heidelberg. p. 323-372.

22.   Schreier, H.W., J.R. Braasch, and M.A. Sutton, *Systematic errors in digital image correlation caused by intensity interpolation.* Optical Engineering, 2000. **39**(11): p. 2915-2921.

23.   Wikipedia. *Polar decomposition.*   [cited   2016   30.03];   Available   from: https://en.wikipedia.org/wiki/Polar_decomposition.

24.   Sutton, M.A., J.H. Yan, V. Tiwari, H.W. Schreier, and J.J. Orteu, *The effect of out-of-plane motion on 2D and 3D digital image correlation measurements.* Optics and Lasers in Engineering, 2008. **46**(10): p. 746-757.

25.   Addiego, F., A. Dahoun, C. G'Sell, and J. Hiver, M., *Processus de la variation volumique du polyéthylène à haute densité au cours d'essais de traction et de fluage.* Oil & Gas Science and Technology - Rev. IFP, 2006. **61**(6): p. 715-724.

26. Powers, J.M. and R.M. Caddell, *The macroscopic volume changes of selected polymers subjected to uniform tensile deformation.* Polymer Engineering & Science, 1972. **12**(6): p. 432-436.

27. Tang, H.I., A. Hiltner, and E. Baer, *Biaxial orientation of polypropylene by hydrostatic solid state extrusion. Part III: Mechanical properties and deformation mechanisms.* Polymer Engineering & Science, 1987. **27**(12): p. 876-886.

28. Gaucher–Miri, V., C. Depecker, and R. Séguéla, *Reversible strain-induced order in the amorphous phase of a low-density ethylene/butene copolymer.* Journal of Polymer Science Part B: Polymer Physics, 1997. **35**(13): p. 2151-2159.

29. Hill, R., *The mathematical theory of plasticity.* Oxford University Press, 1950.

30. Eyring, H., *Viscosity, Plasticity, and Diffusion as Examples of Absolute Reaction Rates.* The Journal of Chemical Physics, 1936. **4**(4): p. 283-291.

31. Ree, T. and H. Eyring, *Theory of Non‐Newtonian Flow. II. Solution System of High Polymers.* Journal of Applied Physics, 1955. **26**(7): p. 800-809.

32. Argon, A.S., *A theory for the low-temperature plastic deformation of glassy polymers.* Philosophical Magazine, 1973. **28**(4): p. 839-865.

33. Mohanraj, J., D.C. Barton, I.M. Ward, A. Dahoun, J.M. Hiver, and C. G'Sell, *Plastic deformation and damage of polyoxymethylene in the large strain range at elevated temperatures.* Polymer, 2006. **47**(16): p. 5852-5861.

34. Taylor, G.I. and H. Quinney, *The Latent Energy Remaining in a Metal after Cold Working.* Proceedings of the Royal Society of London, 1934. **143**(849): p. 307-326.

35. Ognedal, A.S., A.H. Clausen, T. Berstad, T. Seelig, and O.S. Hopperstad, *Void nucleation and growth in mineral-filled PVC – An experimental and numerical study.* International Journal of Solids and Structures, 2014. **51**(7–8): p. 1494-1506.

36. Wikipedia. *Convective heat transfer.* [cited 2016 24.02]; Available from: https://en.wikipedia.org/wiki/Convective_heat_transfer.

37. Addiego, F., J. Di Martino, D. Ruch, A. Dahoun, O. Godard, and S. Patlazhan, *Quantification of Cavitation in Neat and Calcium Carbonate-Filled High-Density Polyethylene Subjected to Tension.* Journal of Engineering Materials and Technology, 2011. **133**(3): p. 030904-030904.

38. Systèmes, D. *Abaqus*. [cited 2016 15.04]; Available from: http://www.3ds.com/products-services/simulia/products/abaqus/.

39. Arruda, E.M. and M.C. Boyce, *A three-dimensional constitutive model for the large stretch behavior of rubber elastic materials.* Journal of the Mechanics and Physics of Solids, 1993. **41**(2): p. 389-412.

40.   Belytschko, T., W.K. Liu, B. Moran, and K. Elkhodary, *Nonlinear finite elements for continua and structures*. 2013: John Wiley & Sons.

41.   Jedynak, R., *Approximation of the inverse Langevin function revisited.* Rheologica Acta, 2015. **54**(1): p. 29-39.

42.   MATBASE. [cited 2016 19.01]; Available from: http://www.matbase.com/material-categories/natural-and-synthetic-polymers/commodity-polymers/material-properties-of-high-density-polyethylene-hdpe.html#properties.

43.   MATBASE. [cited 2016 11.04]; Available from: http://www.matbase.com/material-categories/natural-and-synthetic-polymers/commodity-polymers/material-properties-of-hard-polyvinyl-chloride-hard-pvc.html#properties.

"Reliability Analysis of Structural Systems using Nonlinear Finite Element Methods",
C. A. Holm, 1990:23, ISBN 82-7119-178-0.

"Uniform Stratified Flow Interaction with a Submerged Horizontal Cylinder",
Ø. Arntsen, 1990:32, ISBN 82-7119-188-8.

"Large Displacement Analysis of Flexible and Rigid Systems Considering
Displacement-Dependent Loads and Nonlinear Constraints",
K. M. Mathisen, 1990:33, ISBN 82-7119-189-6.

"Solid Mechanics and Material Models including Large Deformations",
E. Levold, 1990:56, ISBN 82-7119-214-0, ISSN 0802-3271.

"Inelastic Deformation Capacity of Flexurally-Loaded Aluminium Alloy Structures",
T. Welo, 1990:62, ISBN 82-7119-220-5, ISSN 0802-3271.

"Visualization of Results from Mechanical Engineering Analysis",
K. Aamnes, 1990:63, ISBN 82-7119-221-3, ISSN 0802-3271.

"Object-Oriented Product Modeling for Structural Design",
S. I. Dale, 1991:6, ISBN 82-7119-258-2, ISSN 0802-3271.

"Parallel Techniques for Solving Finite Element Problems on Transputer Networks",
T. H. Hansen, 1991:19, ISBN 82-7119-273-6, ISSN 0802-3271.

"Statistical Description and Estimation of Ocean Drift Ice Environments",
R. Korsnes, 1991:24, ISBN 82-7119-278-7, ISSN 0802-3271.

"Properties of concrete related to fatigue damage: with emphasis on high strength
concrete",
G. Petkovic, 1991:35, ISBN 82-7119-290-6, ISSN 0802-3271.

"Turbidity Current Modelling",
B. Brørs, 1991:38, ISBN 82-7119-293-0, ISSN 0802-3271.

"Zero-Slump Concrete: Rheology, Degree of Compaction and Strength. Effects of
Fillers as Part Cement-Replacement",
C. Sørensen, 1992:8, ISBN 82-7119-357-0, ISSN 0802-3271.

"Nonlinear Analysis of Reinforced Concrete Structures Exposed to Transient Loading",
K. V. Høiseth, 1992:15, ISBN 82-7119-364-3, ISSN 0802-3271.

"Finite Element Formulations and Solution Algorithms for Buckling and Collapse
Analysis of Thin Shells",
R. O. Bjærum, 1992:30, ISBN 82-7119-380-5, ISSN 0802-3271.

"Response Statistics of Nonlinear Dynamic Systems",
J. M. Johnsen, 1992:42, ISBN 82-7119-393-7, ISSN 0802-3271.

"Digital Models in Engineering. A Study on why and how engineers build and operate
digital models for decisison support",
J. Høyte, 1992:75, ISBN 82-7119-429-1, ISSN 0802-3271.

"Sparse Solution of Finite Element Equations",
A. C. Damhaug, 1992:76, ISBN 82-7119-430-5, ISSN 0802-3271.

"Some Aspects of Floating Ice Related to Sea Surface Operations in the Barents Sea",
S. Løset, 1992:95, ISBN 82-7119-452-6, ISSN 0802-3271.

"Modelling of Cyclic Plasticity with Application to Steel and Aluminium Structures",
O. S. Hopperstad, 1993:7, ISBN 82-7119-461-5, ISSN 0802-3271.

"The Free Formulation: Linear Theory and Extensions with Applications to Tetrahedral
Elements
with Rotational Freedoms",
G. Skeie, 1993:17, ISBN 82-7119-472-0, ISSN 0802-3271.

"Høyfast betongs motstand mot piggdekkslitasje. Analyse av resultater fra prøving i
Veisliter'n",
T. Tveter, 1993:62, ISBN 82-7119-522-0, ISSN 0802-3271.

"A Nonlinear Finite Element Based on Free Formulation Theory for Analysis of
Sandwich Structures",
O. Aamlid, 1993:72, ISBN 82-7119-534-4, ISSN 0802-3271.

"The Effect of Curing Temperature and Silica Fume on Chloride Migration and Pore
Structure of High Strength Concrete",
C. J. Hauck, 1993:90, ISBN 82-7119-553-0, ISSN 0802-3271.

"Failure of Concrete under Compressive Strain Gradients",
G. Markeset, 1993:110, ISBN 82-7119-575-1, ISSN 0802-3271.

"An experimental study of internal tidal amphidromes in Vestfjorden",
J. H. Nilsen, 1994:39, ISBN 82-7119-640-5, ISSN 0802-3271.

"Structural analysis of oil wells with emphasis on conductor design",
H. Larsen, 1994:46, ISBN 82-7119-648-0, ISSN 0802-3271.

"Adaptive methods for non-linear finite element analysis of shell structures",
K. M. Okstad, 1994:66, ISBN 82-7119-670-7, ISSN 0802-3271.

"On constitutive modelling in nonlinear analysis of concrete structures",
O. Fyrileiv, 1994:115, ISBN 82-7119-725-8, ISSN 0802-3271.

"Fluctuating wind load and response of a line-like engineering structure with emphasis on motion-induced wind forces",
J. Bogunovic Jakobsen, 1995:62, ISBN 82-7119-809-2, ISSN 0802-3271.

"An experimental study of beam-columns subjected to combined torsion, bending and axial actions",
A. Aalberg, 1995:66, ISBN 82-7119-813-0, ISSN 0802-3271.

"Scaling and cracking in unsealed freeze/thaw testing of Portland cement and silica fume concretes",
S. Jacobsen, 1995:101, ISBN 82-7119-851-3, ISSN 0802-3271.

"Damping of water waves by submerged vegetation. A case study of laminaria hyperborea",
A. M. Dubi, 1995:108, ISBN 82-7119-859-9, ISSN 0802-3271.

"The dynamics of a slope current in the Barents Sea",
Sheng Li, 1995:109, ISBN 82-7119-860-2, ISSN 0802-3271.

"Modellering av delmaterialenes betydning for betongens konsistens",
Ernst Mørtsell, 1996:12, ISBN 82-7119-894-7, ISSN 0802-3271.

"Bending of thin-walled aluminium extrusions",
Birgit Søvik Opheim, 1996:60, ISBN 82-7119-947-1, ISSN 0802-3271.

"Material modelling of aluminium for crashworthiness analysis",
Torodd Berstad, 1996:89, ISBN 82-7119-980-3, ISSN 0802-3271.

"Estimation of structural parameters from response measurements on submerged floating tunnels",
Rolf Magne Larssen, 1996:119, ISBN 82-471-0014-2, ISSN 0802-3271.

"Numerical modelling of plain and reinforced concrete by damage mechanics",
Mario A. Polanco-Loria, 1997:20, ISBN 82-471-0049-5, ISSN 0802-3271.

"Nonlinear random vibrations - numerical analysis by path integration methods",
Vibeke Moe, 1997:26, ISBN 82-471-0056-8, ISSN 0802-3271.

"Numerical prediction of vortex-induced vibration by the finite element method",
Joar Martin Dalheim, 1997:63, ISBN 82-471-0096-7, ISSN 0802-3271.

"Time domain calculations of buffeting response for wind sensitive structures",
Ketil Aas-Jakobsen, 1997:148, ISBN 82-471-0189-0, ISSN 0802-3271.

"A numerical study of flow about fixed and flexibly mounted circular cylinders",
Trond Stokka Meling, 1998:48, ISBN 82-471-0244-7, ISSN 0802-3271.

"Estimation of chloride penetration into concrete bridges in coastal areas",
Per Egil Steen, 1998:89, ISBN 82-471-0290-0, ISSN 0802-3271.

"Stress-resultant material models for reinforced concrete plates and shells",
Jan Arve Øverli, 1998:95, ISBN 82-471-0297-8, ISSN 0802-3271.

"Chloride binding in concrete. Effect of surrounding environment and concrete composition",
Claus Kenneth Larsen, 1998:101, ISBN 82-471-0337-0, ISSN 0802-3271.

"Rotational capacity of aluminium alloy beams",
Lars A. Moen, 1999:1, ISBN 82-471-0365-6, ISSN 0802-3271.

"Stretch Bending of Aluminium Extrusions",
Arild H. Clausen, 1999:29, ISBN 82-471-0396-6, ISSN 0802-3271.

"Aluminium and Steel Beams under Concentrated Loading",
Tore Tryland, 1999:30, ISBN 82-471-0397-4, ISSN 0802-3271.

"Engineering Models of Elastoplasticity and Fracture for Aluminium Alloys",
Odd-Geir Lademo, 1999:39, ISBN 82-471-0406-7, ISSN 0802-3271.

"Kapasitet og duktilitet av dybelforbindelser i trekonstruksjoner",
Jan Siem, 1999:46, ISBN 82-471-0414-8, ISSN 0802-3271.

"Etablering av distribuert ingeniørarbeid; Teknologiske og organisatoriske erfaringer fra en norsk ingeniørbedrift",
Lars Line, 1999:52, ISBN 82-471-0420-2, ISSN 0802-3271.

"Estimation of Earthquake-Induced Response",
Símon Ólafsson, 1999:73, ISBN 82-471-0443-1, ISSN 0802-3271.

"Coastal Concrete Bridges: Moisture State, Chloride Permeability and Aging Effects"
Ragnhild Holen Relling, 1999:74, ISBN 82-471-0445-8, ISSN 0802-3271.

"Capacity Assessment of Titanium Pipes Subjected to Bending and External Pressure",
Arve Bjørset, 1999:100, ISBN 82-471-0473-3, ISSN 0802-3271.

"Validation of Numerical Collapse Behaviour of Thin-Walled Corrugated Panels",
Håvar Ilstad, 1999:101, ISBN 82-471-0474-1, ISSN 0802-3271.

"Strength and Ductility of Welded Structures in Aluminium Alloys",
Miroslaw Matusiak, 1999:113, ISBN 82-471-0487-3, ISSN 0802-3271.

"Thermal Dilation and Autogenous Deformation as Driving Forces to Self-Induced
Stresses in High Performance Concrete",
Øyvind Bjøntegaard, 1999:121, ISBN 82-7984-002-8, ISSN 0802-3271.

"Some Aspects of Ski Base Sliding Friction and Ski Base Structure",
Dag Anders Moldestad, 1999:137, ISBN 82-7984-019-2, ISSN 0802-3271.

"Electrode reactions and corrosion resistance for steel in mortar and concrete",
Roy Antonsen, 2000:10, ISBN 82-7984-030-3, ISSN 0802-3271.

"Hydro-Physical Conditions in Kelp Forests and the Effect on Wave Damping and
Dune Erosion. A case study on Laminaria Hyperborea",
Stig Magnar Løvås, 2000:28, ISBN 82-7984-050-8, ISSN 0802-3271.

"Random Vibration and the Path Integral Method",
Christian Skaug, 2000:39, ISBN 82-7984-061-3, ISSN 0802-3271.

"Buckling and geometrical nonlinear beam-type analyses of timber structures",
Trond Even Eggen, 2000:56, ISBN 82-7984-081-8, ISSN 0802-3271.

"Structural Crashworthiness of Aluminium Foam-Based Components",
Arve Grønsund Hanssen, 2000:76, ISBN 82-7984-102-4, ISSN 0809-103X.

"Measurements and simulations of the consolidation in first-year sea ice ridges, and
some aspects of mechanical behaviour",
Knut V. Høyland, 2000:94, ISBN 82-7984-121-0, ISSN 0809-103X.

"Kinematics in Regular and Irregular Waves based on a Lagrangian Formulation",
Svein Helge Gjøsund, 2000-86, ISBN 82-7984-112-1, ISSN 0809-103X.

"Self-Induced Cracking Problems in Hardening Concrete Structures",
Daniela Bosnjak, 2000-121, ISBN 82-7984-151-2, ISSN 0809-103X.

"Ballistic Penetration and Perforation of Steel Plates",
Tore Børvik, 2000:124, ISBN 82-7984-154-7, ISSN 0809-103X.

"Freeze-Thaw resistance of Concrete. Effect of: Curing Conditions, Moisture Exchange
and Materials",
Terje Finnerup Rønning, 2001:14, ISBN 82-7984-165-2, ISSN 0809-103X

"Structural behaviour of post tensioned concrete structures. Flat slab. Slabs on ground",
Steinar Trygstad, 2001:52, ISBN 82-471-5314-9, ISSN 0809-103X.

"Slipforming of Vertical Concrete Structures. Friction between concrete and slipform panel",
Kjell Tore Fosså, 2001:61, ISBN 82-471-5325-4, ISSN 0809-103X.

"Some numerical methods for the simulation of laminar and turbulent incompressible flows",
Jens Holmen, 2002:6, ISBN 82-471-5396-3, ISSN 0809-103X.

"Improved Fatigue Performance of Threaded Drillstring Connections by Cold Rolling",
Steinar Kristoffersen, 2002:11, ISBN: 82-421-5402-1, ISSN 0809-103X.

"Deformations in Concrete Cantilever Bridges: Observations and Theoretical Modelling",
Peter F. Takâcs, 2002:23, ISBN 82-471-5415-3, ISSN 0809-103X.

"Stiffened aluminium plates subjected to impact loading",
Hilde Giæver Hildrum, 2002:69, ISBN 82-471-5467-6, ISSN 0809-103X.

"Full- and model scale study of wind effects on a medium-rise building in a built up area",
Jónas Thór Snæbjørnsson, 2002:95, ISBN82-471-5495-1, ISSN 0809-103X.

"Evaluation of Concepts for Loading of Hydrocarbons in Ice-infested water",
Arnor Jensen, 2002:114, ISBN 82-417-5506-0, ISSN 0809-103X.

"Numerical and Physical Modelling of Oil Spreading in Broken Ice",
Janne K. Økland Gjøsteen, 2002:130, ISBN 82-471-5523-0, ISSN 0809-103X.

"Diagnosis and protection of corroding steel in concrete",
Franz Pruckner, 20002:140, ISBN 82-471-5555-4, ISSN 0809-103X.

"Tensile and Compressive Creep of Young Concrete: Testing and Modelling",
Dawood Atrushi, 2003:17, ISBN 82-471-5565-6, ISSN 0809-103X.

"Rheology of Particle Suspensions. Fresh Concrete, Mortar and Cement Paste with Various Types of Lignosulfonates",
Jon Elvar Wallevik, 2003:18, ISBN 82-471-5566-4, ISSN 0809-103X.

"Oblique Loading of Aluminium Crash Components",
Aase Reyes, 2003:15, ISBN 82-471-5562-1, ISSN 0809-103X.

"Utilization of Ethiopian Natural Pozzolans",
Surafel Ketema Desta, 2003:26, ISSN 82-471-5574-5, ISSN:0809-103X.

"Behaviour and strength prediction of reinforced concrete structures with discontinuity regions", Helge Brå, 2004:11, ISBN 82-471-6222-9, ISSN 1503-8181.

"High-strength steel plates subjected to projectile impact. An experimental and numerical study", Sumita Dey, 2004:38, ISBN 82-471-6282-2 (printed version), ISBN 82-471-6281-4 (electronic version), ISSN 1503-8181.

"Alkali-reactive and inert fillers in concrete. Rheology of fresh mixtures and expansive reactions."
Bård M. Pedersen, 2004:92, ISBN 82-471-6401-9 (printed version), ISBN 82-471-6400-0 (electronic version), ISSN 1503-8181.

"On the Shear Capacity of Steel Girders with Large Web Openings".
Nils Christian Hagen, 2005:9 ISBN 82-471-6878-2 (printed version), ISBN 82-471-6877-4 (electronic version), ISSN 1503-8181.

"Behaviour of aluminium extrusions subjected to axial loading".
Østen Jensen, 2005:7, ISBN 82-471-6873-1 (printed version), ISBN 82-471-6872-3 (electronic version), ISSN 1503-8181.

"Thermal Aspects of corrosion of Steel in Concrete".
Jan-Magnus Østvik, 2005:5, ISBN 82-471-6869-3 (printed version), ISBN 82-471-6868 (electronic version), ISSN 1503-8181.

"Mechanical and adaptive behaviour of bone in relation to hip replacement." A study of bone remodelling and bone grafting.
Sébastien Muller, 2005:34, ISBN 82-471-6933-9 (printed version), ISBN 82-471-6932-0 (electronic version), ISSN 1503-8181.

"Analysis of geometrical nonlinearities with applications to timber structures".
Lars Wollebæk, 2005:74, ISBN 82-471-7050-5 (printed version), ISBN 82-471-7019-1 (electronic version), ISSN 1503-8181.

"Pedestrian induced lateral vibrations of slender footbridges",
Anders Rönnquist, 2005:102, ISBN 82-471-7082-5 (printed version), ISBN 82-471-7081-7 (electronic version), ISSN 1503-8181.

"Initial Strength Development of Fly Ash and Limestone Blended Cements at Various Temperatures Predicted by Ultrasonic Pulse Velocity",
Tom Ivar Fredvik, 2005:112, ISBN 82-471-7105-8 (printed version), ISBN 82-471-7103-1 (electronic version), ISSN 1503-8181.

"Behaviour and modelling of thin-walled cast components",
Cato Dørum, 2005:128, ISBN 82-471-7140-6 (printed version), ISBN 82-471-7139-2 (electronic version), ISSN 1503-8181.

"Behaviour and modelling of selfpiercing riveted connections",
Raffaele Porcaro, 2005:165, ISBN 82-471-7219-4 (printed version), ISBN 82-471-7218-6 (electronic version), ISSN 1503-8181.

"Behaviour and Modelling og Aluminium Plates subjected to Compressive Load",
Lars Rønning, 2005:154, ISBN 82-471-7169-1 (printed version), ISBN 82-471-7195-3 (electronic version), ISSN 1503-8181.

"Bumper beam-longitudinal system subjected to offset impact loading",
Satyanarayana Kokkula, 2005:193, ISBN 82-471-7280-1 (printed version), ISBN 82-471-7279-8 (electronic version), ISSN 1503-8181.

"Control of Chloride Penetration into Concrete Structures at Early Age",
Guofei Liu, 2006:46, ISBN 82-471-7838-9 (printed version), ISBN 82-471-7837-0 (electronic version), ISSN 1503-8181.

"Modelling of Welded Thin-Walled Aluminium Structures",
Ting Wang, 2006:78, ISBN 82-471-7907-5 (printed version), ISBN 82-471-7906-7 (electronic version), ISSN 1503-8181.

"Time-variant reliability of dynamic systems by importance sampling and probabilistic analysis of ice loads",
Anna Ivanova Olsen, 2006:139, ISBN 82-471-8041-3 (printed version), ISBN 82-471-8040-5 (electronic version), ISSN 1503-8181.

"Fatigue life prediction of an aluminium alloy automotive component using finite element analysis of surface topography".
Sigmund Kyrre Ås, 2006:25, ISBN 82-471-7791-9 (printed version), ISBN 82-471-7791-9 (electronic version), ISSN 1503-8181.

"Constitutive models of elastoplasticity and fracture for aluminium alloys under strain path change",
Dasharatha Achani, 2006:76, ISBN 82-471-7903-2 (printed version), ISBN 82-471-7902-4 (electronic version), ISSN 1503-8181.

"Simulations of 2D dynamic brittle fracture by the Element-free Galerkin method and linear fracture mechanics",
Tommy Karlsson, 2006:125, ISBN 82-471-8011-1 (printed version), ISBN 82-471-8010-3 (electronic version), ISSN 1503-8181.

"Penetration and Perforation of Granite Targets by Hard Projectiles",
Chong Chiang Seah, 2006:188, ISBN 82-471-8150-9 (printed version), ISBN 82-471-8149-5 (electronic version), ISSN 1503-8181.

"Deformations, strain capacity and cracking of concrete in plastic and early hardening phases",
Tor Arne Hammer, 2007:234, ISBN 978-82-471-5191-4 (printed version), ISBN 978-82-471-5207-2 (electronic version), ISSN 1503-8181.

"Crashworthiness of dual-phase high-strength steel: Material and Component behaviour", Venkatapathi Tarigopula, 2007:230, ISBN 82-471-5076-4 (printed version), ISBN 82-471-5093-1 (electronic version), ISSN 1503-8181.

"Fibre reinforcement in load carrying concrete structures",
Åse Lyslo Døssland, 2008:50, ISBN 978-82-471-6910-0 (printed version), ISBN 978-82-471-6924-7 (electronic version), ISSN 1503-8181.

"Low-velocity penetration of aluminium plates",
Frode Grytten, 2008:46, ISBN 978-82-471-6826-4 (printed version), ISBN 978-82-471-6843-1 (electronic version), ISSN 1503-8181.

"Robustness studies of structures subjected to large deformations",
Ørjan Fyllingen, 2008:24, ISBN 978-82-471-6339-9 (printed version), ISBN 978-82-471-6342-9 (electronic version), ISSN 1503-8181.

"Constitutive modelling of morsellised bone",
Knut Birger Lunde, 2008:92, ISBN 978-82-471-7829-4 (printed version), ISBN 978-82-471-7832-4 (electronic version), ISSN 1503-8181.

"Experimental Investigations of Wind Loading on a Suspension Bridge Girder",
Bjørn Isaksen, 2008:131, ISBN 978-82-471-8656-5 (printed version), ISBN 978-82-471-8673-2 (electronic version), ISSN 1503-8181.

"Cracking Risk of Concrete Structures in The Hardening Phase",
Guomin Ji, 2008:198, ISBN 978-82-471-1079-9 (printed version), ISBN 978-82-471-1080-5 (electronic version), ISSN 1503-8181.

"Modelling and numerical analysis of the porcine and human mitral apparatus",
Victorien Emile Prot, 2008:249, ISBN 978-82-471-1192-5 (printed version), ISBN 978-82-471-1193-2 (electronic version), ISSN 1503-8181.

"Strength analysis of net structures",
Heidi Moe, 2009:48, ISBN 978-82-471-1468-1 (printed version), ISBN 978-82-471-1469-8 (electronic version), ISSN1503-8181.

"Numerical analysis of ductile fracture in surface cracked shells",
Espen Berg, 2009:80, ISBN 978-82-471-1537-4 (printed version), ISBN 978-82-471-1538-1 (electronic version), ISSN 1503-8181.

"Subject specific finite element analysis of bone – for evaluation of the healing of a leg lengthening and evaluation of femoral stem design",
Sune Hansborg Pettersen, 2009:99, ISBN 978-82-471-1579-4 (printed version), ISBN 978-82-471-1580-0 (electronic version), ISSN 1503-8181.

"Evaluation of fracture parameters for notched multi-layered structures",
Lingyun Shang, 2009:137, ISBN 978-82-471-1662-3 (printed version), ISBN 978-82-471-1663-0 (electronic version), ISSN 1503-8181.

"Modelling of Dynamic Material Behaviour and Fracture of Aluminium Alloys for Structural Applications"
Yan Chen, 2009:69, ISBN 978-82-471-1515-2 (printed version), ISBN 978-82 471-1516-9 (electronic version), ISSN 1503-8181.

"Nanomechanics of polymer and composite particles"
Jianying He 2009:213, ISBN 978-82-471-1828-3 (printed version), ISBN 978-82-471-1829-0 (electronic version), ISSN 1503-8181.

"Mechanical properties of clear wood from Norway spruce"
Kristian Berbom Dahl 2009:250, ISBN 978-82-471-1911-2 (printed version) ISBN 978-82-471-1912-9 (electronic version), ISSN 1503-8181.

"Modeling of the degradation of TiB_2 mechanical properties by residual stresses and liquid Al penetration along grain boundaries"
Micol Pezzotta 2009:254, ISBN 978-82-471-1923-5 (printed version) ISBN 978-82-471-1924-2 (electronic version) ISSN 1503-8181.

"Effect of welding residual stress on fracture"
Xiabo Ren 2010:77, ISBN 978-82-471-2115-3 (printed version) ISBN 978-82-471-2116-0 (electronic version), ISSN 1503-8181.

"Pan-based carbon fiber as anode material in cathodic protection system for concrete structures"
Mahdi Chini 2010:122, ISBN 978-82-471-2210-5 (printed version) ISBN 978-82-471-2213-6 (electronic version), ISSN 1503-8181.

"Structural Behaviour of deteriorated and retrofitted concrete structures"
Irina Vasililjeva Sæther 2010:171, ISBN 978-82-471-2315-7 (printed version) ISBN 978-82-471-2316-4 (electronic version) ISSN 1503-8181.

"Prediction of local snow loads on roofs"
Vivian Meløysund 2010:247, ISBN 978-82-471-2490-1 (printed version) ISBN 978-82-471-2491-8 (electronic version) ISSN 1503-8181.

"Behaviour and modelling of polymers for crash applications"
Virgile Delhaye 2010:251, ISBN 978-82-471-2501-4 (printed version) ISBN 978-82-471-2502-1 (electronic version) ISSN 1503-8181.

"Blended cement with reduced CO_2 emission – Utilizing the Fly Ash-Limestone Synergy",
Klaartje De Weerdt 2011:32, ISBN 978-82-471-2584-7 (printed version) ISBN 978-82-471-2584-4 (electronic version) ISSN 1503-8181.

"Chloride induced reinforcement corrosion in concrete" Concept of critical chloride content – methods and mechanisms.
Ueli Angst 2011:113, ISBN 978-82-471-2769-9 (printed version) ISBN 978-82-471-2763-6 (electronic version) ISSN 1503-8181.

"A thermo-electric-Mechanical study of the carbon anode and contact interface for Energy savings in the production of aluminium".
Dag Herman Andersen 2011:157, ISBN 978-82-471-2859-6 (printed version) ISBN 978-82-471-2860-2 (electronic version) ISSN 1503-8181.

"Structural Capacity of Anchorage Ties in Masonry Veneer Walls Subjected to Earthquake". The implications of Eurocode 8 and Eurocode 6 on a typical Norwegain veneer wall.
Ahmed Mohamed Yousry Hamed 2011:181, ISBN 978-82-471-2911-1 (printed version) ISBN 978-82-471-2912-8 (electronic ver.) ISSN 1503-8181.

"Work-hardening behaviour in age-hardenable Al-Zn-Mg(-Cu) alloys".
Ida Westermann , 2011:247, ISBN 978-82-471-3056-8 (printed ver.) ISBN 978-82-471-3057-5 (electronic ver.) ISSN 1503-8181.

"Behaviour and modelling of selfpiercing riveted connections using aluminium rivets".
Nguyen-Hieu Hoang, 2011:266, ISBN 978-82-471-3097-1 (printed ver.) ISBN 978-82-471-3099-5 (electronic ver.) ISSN 1503-8181.

"Fibre reinforced concrete".
Sindre Sandbakk, 2011:297, ISBN 978-82-471-3167-1 (printed ver.) ISBN 978-82-471-3168-8 (electronic ver) ISSN 1503:8181.

"Dynamic behaviour of cablesupported bridges subjected to strong natural wind".
Ole Andre Øiseth, 2011:315, ISBN 978-82-471-3209-8 (printed ver.) ISBN 978-82-471-3210-4 (electronic ver.) ISSN 1503-8181.

"Constitutive modeling of solargrade silicon materials"
Julien Cochard, 2011:307, ISBN 978-82-471-3189-3 (printed ver). ISBN 978-82-471-3190-9 (electronic ver.) ISSN 1503-8181.

"Constitutive behavior and fracture of shape memory alloys"
Jim Stian Olsen, 2012:57, ISBN 978-82-471-3382-8 (printed ver.) ISBN 978-82-471-3383-5 (electronic ver.) ISSN 1503-8181.

"Field measurements in mechanical testing using close-range photogrammetry and digital image analysis"
Egil Fagerholt, 2012:95, ISBN 978-82-471-3466-5 (printed ver.) ISBN 978-82-471-3467-2 (electronic ver.) ISSN 1503-8181.

"Towards a better under standing of the ultimate behaviour of lightweight aggregate concrete in compression and bending",
Håvard Nedrelid, 2012:123, ISBN 978-82-471-3527-3 (printed ver.) ISBN 978-82-471-3528-0 (electronic ver.) ISSN 1503-8181.

"Numerical simulations of blood flow in the left side of the heart"
Sigrid Kaarstad Dahl, 2012:135, ISBN 978-82-471-3553-2 (printed ver.) ISBN 978-82-471-3555-6 (electronic ver.) ISSN 1503-8181.

"Moisture induced stresses in glulam"
Vanessa Angst-Nicollier, 2012:139, ISBN 978-82-471-3562-4 (printed ver.) ISBN 978-82-471-3563-1 (electronic ver.) ISSN 1503-8181.

"Biomechanical aspects of distraction osteogensis"
Valentina La Russa, 2012:250, ISBN 978-82-471-3807-6 (printed ver.) ISBN 978-82-471-3808-3 (electronic ver.) ISSN 1503-8181.

"Ductile fracture in dual-phase steel. Theoretical, experimental and numerical study"
Gaute Gruben, 2012:257, ISBN 978-82-471-3822-9 (printed ver.) ISBN 978-82-471-3823-6 (electronic ver.) ISSN 1503-8181.

"Damping in Timber Structures"
Nathalie Labonnote, 2012:263, ISBN 978-82-471-3836-6 (printed ver.) ISBN 978-82-471-3837-3 (electronic ver.) ISSN 1503-8181.

"Biomechanical modeling of fetal veins: The umbilical vein and ductus venosus bifurcation"
Paul Roger Leinan, 2012:299, ISBN 978-82-471-3915-8 (printed ver.) ISBN 978-82-471-3916-5 (electronic ver.) ISSN 1503-8181.

"Large-Deformation behaviour of thermoplastics at various stress states"
Anne Serine Ognedal, 2012:298, ISBN 978-82-471-3913-4 (printed ver.) ISBN 978-82-471-3914-1 (electronic ver.) ISSN 1503-8181.

"Hardening accelerator for fly ash blended cement"
Kien Dinh Hoang, 2012:366, ISBN 978-82-471-4063-5 (printed ver.) ISBN 978-82-471-4064-2 (electronic ver.) ISSN 1503-8181.

"From molecular structure to mechanical properties"
Jianyang Wu, 2013:186, ISBN 978-82-471-4485-5 (printed ver.) ISBN 978-82-471-4486-2 (electronic ver.) ISSN 1503-8181.

"Experimental and numerical study of hybrid concrete structures"
Linn Grepstad Nes, 2013:259, ISBN 978-82-471-4644-6 (printed ver.) ISBN 978-82-471-4645-3 (electronic ver.) ISSN 1503-8181.

"Mechanics of ultra-thin multi crystalline silicon wafers"
Saber Saffar, 2013:199, ISBN 978-82-471-4511-1 (printed ver.) ISBN 978-82-471-4513-5 (electronic ver). ISSN 1503-8181.

"Through process modelling of welded aluminium structures"
Anizahyati Alisibramulisi, 2013:325, ISBN 978-82-471-4788-7 (printed ver.) ISBN 978-82-471-4789-4 (electronic ver.) ISSN 1503-8181.

"Combined blast and fragment loading on steel plates"
Knut Gaarder Rakvåg, 2013:361, ISBN978-82-471-4872-3 (printed ver.) ISBN 978-82-4873-0 (electronic ver.). ISSN 1503-8181.

"Characterization and modelling of the anisotropic behaviour of high-strength aluminium alloy"
Marion Fourmeau, 2014:37, ISBN 978-82-326-0008-3 (printed ver.) ISBN 978-82-326-0009-0 (electronic ver.) ISSN 1503-8181.

"Behaviour of threated steel fasteners at elevated deformation rates"
Henning Fransplass, 2014:65, ISBN 978-82-326-0054-0 (printed ver.) ISBN 978-82-326-0055-7 (electronic ver.) ISSN 1503-8181.

"Sedimentation and Bleeding"
Ya Peng, 2014:89, ISBN 978-82-326-0102-8 (printed ver.) ISBN 978-82-326-0103-5 (electric ver.) ISSN 1503-8181.

"Impact against X65 offshore pipelines"
Martin Kristoffersen, 2014:362, ISBN 978-82-326-0636-8 (printed ver.) ISBN 978-82-326-0637-5 (electronic ver.) ISSN 1503-8181.

"Formability of aluminium alloy subjected to prestrain by rolling"
Dmitry Vysochinskiy, 2014:363,, ISBN 978-82-326-0638-2 (printed ver.) ISBN 978-82-326-0639-9 (electronic ver.) ISSN 1503-8181.

"Experimental and numerical study of Yielding, Work-Hardening and anisotropy in textured AA6xxx alloys using crystal plasticity models"
Mikhail Khadyko, 2015:28, ISBN 978-82-326-0724-2 (printed ver.) ISBN 978-82-326-0725-9 (electronic ver.) ISSN 1503-8181.

"Behaviour and Modelling of AA6xxx Aluminium Alloys Under a Wide Range of Temperatures and Strain Rates"
Vincent Vilamosa, 2015:63, ISBN 978-82-326-0786-0 (printed ver.) ISBN 978-82-326-0787-7 (electronic ver.) ISSN 1503-8181.

"A Probabilistic Approach in Failure Modelling of Aluminium High Pressure Die-Castings"
Octavian Knoll, 2015:137, ISBN 978-82-326-0930-7 (printed ver.) ISBN 978-82-326-0931-4 (electronic ver.) ISSN 1503-8181.

"Ice Abrasion on Marine Concrete Structures"
Egil Møen, 2015:189, ISBN 978-82-326-1034-1 (printed ver.) ISBN 978-82-326-1035-8 (electronic ver.) ISSN 1503-8181.

"Fibre Orientation in Steel-Fibre-Reinforced Concrete"
Giedrius Zirgulis, 2015:229, ISBN 978-82-326-1114-0 (printed ver.) ISBN 978-82-326-1115-7 (electronic ver.) ISSN 1503-8181.

"Effect of spatial variation and possible interference of localised corrosion on the residual capacity of a reinforced concrete beam"
Mohammad Mahdi Kioumarsi, 2015:282, ISBN 978-82-326-1220-8 (printed ver.) ISBN 978-82-1221-5 (electronic ver.) ISSN 1503-8181.

"The role of concrete resistivity in chloride-induced macro-cell corrosion"
Karla Horbostel, 2015:324, ISBN 978-82-326-1304-5 (printed ver.) ISBN 978-82-326-1305-2 (electonic ver.) ISSN 1503-8181.

"Flowable fibre-reinforced concrete for structural applications"
Elena Vidal Sarmiento, 2015-335, ISBN 978-82-326-1324-3 (printed ver.) ISBN 978-82-326-1325-0 (electronic ver.) ISSN 1503-8181.

"Development of chushed sand for concrete production with microproportioning"
Rolands Cepuritis, 2016:19, ISBN 978-82-326-1382-3 (printed ver.) ISBN 978-82-326-1383-0 (electronic ver.) ISSN 1503-8181.

"Withdrawal properties of threaded rods embedded in glued-laminated timer elements"
Haris Stamatopoulos, 2016:48, ISBN 978-82-326-1436-3 (printed ver.) ISBN 978-82-326-1437-0 (electronic ver.) ISSN 1503-8181.